Advanced characterizations of graphene-based materials for supercalacitors

Yassine Ben Cherifi

THÈSE

Pour obtenir le grade de

DOCTEUR DE L'UNIVERSITÉ GRENOBLE ALPES

École doctorale : CSV- Chimie et Sciences du Vivant
Spécialité : Chimie Physique Moléculaire et Structurale
Unité de recherche : Systèmes Moléculaires et Nano Matériaux pour l'Énergie et la Santé

Caractérisations avancées des matériaux à base de graphène pour supercondensateurs

Advanced characterizations of graphene-based materials for supercalacitors

Présentée par :

Yassine BEN CHERIFI

Direction de thèse :

Florence DUCLAIROIR DIRECTEUR DE RECHERCHE, CEA	Directrice de thèse
Hakima MENDIL-JAKANI CHERCHEURE, Université Grenoble Alpes	Co-directrice de thèse

Rapporteurs :

Sandrine DOURDAIN
DOCTEURE EN SCIENCES HDR, CEA centre de Marcoule
Encarnacion RAYMUNDO
DIRECTRICE DE RECHERCHE, CNRS délégation Centre Limousin Poitou-Charentes

Thèse soutenue publiquement le **11 mars 2024**, devant le jury composé de :

Renaud BOUCHET, PROFESSEUR DES UNIVERSITES, Grenoble INP	Président
Florence DUCLAIROIR, DIRECTRICE DE RECHERCHE, CEA centre de Grenoble	Directrice de thèse
Hakima MENDIL-JAKANI, DOCTEURE EN SCIENCES HDR, CEA centre de Grenoble	Co-directrice de thèse
Sandrine DOURDAIN, DOCTEURE EN SCIENCES HDR, CEA centre de Marcoule	Rapporteure
Encarnacion RAYMUNDO, DIRECTRICE DE RECHERCHE, CNRS délégation Centre Limousin Poitou-Charentes	Rapporteure
Cécile AUTRET-LAMBERT, MAITRESSE DE CONFERENCES HDR, Université de Tours	Examinatrice

Invités :

Stéphanie POUGET
DOCTEURE EN SCIENCES, CEA Grenoble
Lionel Dubois
DIRECTEUR DE RECHERCHE, CEA Grenoble

بِسْمِ اللَّهِ الرَّحْمَٰنِ الرَّحِيمِ

الحمد لله الذي بنعمته تتم الصالحات، وبفضله تتنزل الخيرات والبركات، وبتوفيقه تتحقق المقاصد والغايات

Acknowledgements

First of all, I would like to extend my deepest appreciation and heartfelt gratitude to my supervisors, Dr. Florence Duclairoir, Dr. Hakima Mendil-Jakani, Dr. Lionel Dubois, and Dr. Stéphanie Pouget for granting me the opportunity to work under their guidance. Working with you has been an immensely rewarding experience, contributing significantly to my professional and personal growth. I am particularly grateful for the scientific freedom you have afforded me, and I deeply appreciate your unwavering support and guidance during challenging times. I would like to make a special mention of Florence and Hakima I am deeply grateful for our long discussions about ideas and research directions “Brain storming”, as well as the hours/days spent identifying the next experiments at large facilities and proposals writing. Your assistance and help during these experiments and the challenges associated has been invaluable. I also liked our countless texts, calls and messages we've shared at all times of the day even during vacations. Your dedication and support have made a profound impact on my journey.

I would like to thank Dr. Sandrine Dourdain and Dr. Encarnacion Raymundo-Pinero for their time and effort in reviewing my thesis manuscript and Dr. Renaud Bouchet and Dr. Cécile Autret-Lambert for being part of my defense jury. I enjoyed the discussions during the defense and thank you all for the valuable advises and suggestions. I would like to thank CEA for funding my thesis and for hosting me.

I would like to acknowledge our collaborators Dr. Encarnacion Raymundo-Pinero and Dr. Conchi Ania for the gas adsorption and TPD-MS experiments and the fruitful discussions and constant support. I also thank Mr Christian Lombard. Mr. Yves Chenavier, Dr. Sandrine Schlutig, Dr. Hanako Okuno, Dr. Lionel Porcar, Dr. Maxime Dupraz, Dr. Olivier Tache, and Dr. Omar Hassan for their unwavering assistance and kind understanding all through my thesis and for the positive spirit, excellent suggestions and for the continued encouragement.

I would like to thank my colleagues at CAMPE and SyMMES for a friendly and cordial working environment. I acknowledge the support from Corine and Sarah for their administrative assistance.

Finally, I express my heartfelt gratitude towards my friends and all my family members. I thank my parents and brother & sister for their constant support, confidence and understanding all through my career and especially during the PhD.

الحمد لله

Résumé

Le mécanisme de fonctionnement d'un supercondensateur est basé sur l'électro-adsorption d'espèces électrolytiques à la surface de matériaux d'électrodes carbonés poreux polarisés. Le graphène est étudié comme matériau pour essayer d'atteindre des capacités de stockage (C_{SP}) plus élevées, car – en théorie – il présente une grande surface spécifique maximisant le nombre d'ions adsorbés, ainsi qu'une porosité hiérarchique pour favoriser la diffusion des ions. Cependant expérimentalement, la C_{SP} obtenue reste limitée car les feuillets de graphène se réagrègent. Une voie suivie pour limiter ce problème est de placer une molécule « hôte » entre deux feuillets de graphène, conduisant à l'obtention de graphène ponté (PGM). De précédent travaux ont permis de mettre en évidence de façon indirecte (électrochimiquement) que le paramètre structural d, qui correspond à la distance inter-feuillet, peut être modulé permettant d'atteindre des CSP plus élevées. Ces informations sont particulièrement importantes, et appellent à être complétées par des caractérisation directes de ces échantillons.

Aussi au cours de ces travaux de thèse, l'échelle locale de ces matériaux (oxyde de graphène GP, oxyde de graphène réduit chimiquement rGO ou de façon hydrothermale, graphène ponté PGM) a été sondée en effectuant des analyses WAXS, qui ont mis en évidence que les PGM présentent des domaines de graphène ponté qui coexistent avec des feuillets de graphène partiellement empilés. Des études de la méso-structure, réalisées par SANS, ont révélé que la structure du GO évolue fortement lors des étapes de fonctionnalisation et réduction. En effet le GO présente une morphologie en feuillet très large avec des interfaces rugueuses, qui se transforme en feuillets de plus petites dimensions post-réduction, et qui exhibe une structuration 3D post-pontage. Ces analyses SANS ont par ailleurs montré la présence de tailles caractéristiques décelables au sein des échantillons, telles que la longueur de repli R ou les longueurs de persistance Σ. Une étude SANS de porosité par l'invariant, a permis de démontrer que la méso-porosité d'un rGO est deux fois supérieure à celle d'un PGM. Malgré cette différence, les PGM ont montré des performances électrochimiques supérieures au rGO, soulignant l'importance des micropores dans le processus électrochimique.

Il est important de suivre comment cette structure est impactée lorsque ces matériaux sont soumis à des cycles de charge et de décharge rapides et répétitifs. Pour cela, des tests électrochimiques ainsi que des caractérisations *in-situ/operando* ont été effectués en électrolyte organique comprenant des cations de diamètre inférieur (TEA^+) ou supérieur (THA^+) à la

distance inter-feuillet de graphène. L'étude WAXS a permis de constater que l'échantillon ponté est bien plus stable en polarisation et en cyclage, que le rGO qui souffre d'une évolution structurale significative.

Pour aller plus loin dans l'étude des processus d'adsorption mis en jeu dans ces matériaux, une étude de SANS in-situ, basées sur les modulations de contraste liées aux modifications relatives de quantité de cations (contenant des atomes d'H) et d'anions (contenant des atomes de B) a été menée. Ainsi, on constate qu'au sein de l'échantillon ponté les ions THA^+ ions sont concentrés dans la gamme de porosité autour des 14 nm, indiquant que ces ions ne peuvent accéder à la plus petite porosité. Cet effet de blocage n'est pas observé dans le cas du cyclage dans TEA BF_4, puisque les cations TEA^+ sont distribués au sein de toute la gamme de porosité. Ainsi ces études montrent que la méso-porosité des échantillons pontés est active dans les mécanismes de transport et de stockage.

Ces travaux de thèse ont donc permis d'approfondir la compréhension de la structure et de la porosité des matériaux à base de GO, ainsi que de caractériser l'électro-diffusion et -adsorption au sein de la méso-porosité des échantillons pontés. Ces travaux constituent également une méthodologie de caractérisation qui pourrait être appliquée à l'étude d'autres matériaux, contribuant ainsi à faire progresser les travaux sur l'optimisation des supercondensateurs.

Abstract

The working principle of a supercapacitor is based on the electro-adsorption of electrolytic species on the surface of polarized porous carbon electrode materials. Graphene is being studied as a material to try to achieve higher storage capacities (C_{SP}), because – in theory – it presents a large specific surface area maximizing the number of adsorbed ions, as well as a hierarchical porosity that could promote ions diffusion. However, experimentally, the C_{SP} obtained remains limited because the graphene sheets reaggregate. One path followed to limit this problem is to place a "host" molecule between two sheets of graphene, leading to the production of pillared graphene (PGM). Previous work has indirectly (electrochemically) demonstrated that the structural parameter d, which corresponds to the inter-sheet distance, can be modulated to achieve higher C_{SP}s. This information is particularly important, and need to be further addressed by direct characterization of these samples.

Therefore during this PhD work, the local structure of these materials (graphene oxide GO, chemically or hydrothermally reduced graphene oxide rGO, pillared graphene PGM) was probed by carrying out WAXS analyses, which highlighted that PGMs exhibit pillared graphene domains that coexist with partially stacked graphene sheets. Studies of the mesostructure, carried out by SANS, revealed that the structure of GO evolves significantly during the functionalization and reduction steps. Indeed, GO presents a very large sheet size with rough interfaces, which transforms into sheets of smaller dimensions post-reduction, exhibiting 3D structure post-pillaring. These SANS analyses also showed the presence of characteristic structural features within the samples, such as the bending length R or the persistence length Σ. A porosity SANS study using the invariant demonstrated that the mesoporosity of an rGO is two times greater than that of a PGM. Despite this difference, PGM showed higher electrochemical performances, highlighting the importance of micropores in the electrochemical process.

It is important to track how this structure is impacted when these materials are subjected to rapid and repetitive charge and discharge cycles. For this, electrochemical tests as well as in-situ/operando characterizations were carried out in organic electrolyte comprising cations with a diameter smaller (TEA^+) or larger (THA^+) than the inter-graphene sheet distance. The WAXS study showed that the pillared sample is much more stable in polarization and cycling than rGO which suffers from significant structural evolution.

To go further in the study of the adsorption processes involved in these materials, a

study of SANS in-situ, based on contrast modulations linked to relative modifications in the quantity of cations (containing H atoms) and anions (containing B atoms) was carried out. It was observed that within the bridged sample the THA^+ ions are concentrated in the porosity range around 16 nm, indicating that these ions cannot access the smallest porosity. This blocking effect is not observed in the case of cycling in TEA BF_4, since the TEA^+ cations are distributed within the entire porosity range. Thus, these studies showed that the meso-porosity of the bridged samples is active in the transport and storage mechanisms.

This thesis work allowed to deepen the understanding of the structure and porosity of GO-based materials, as well as to characterize the electro-diffusion and -adsorption within the meso-porosity of the pillared samples. This work also constitutes a characterization methodology that could be applied to the study of other materials, thus contributing to advancing work on the optimization of supercapacitors.

List of Abbreviations

PGM: Pillared Graphene Material

GO: Graphene Oxide

rGO: Reduced Graphene Oxide

HR: High Resolution

XPS: X-Ray Photoelectron Spectroscopy

EA: Elemental Analysis

C/O: Carbon-to-Oxygen ratio

CV: Cyclic Voltammetry

GA: Graphene Aerogel

SEM: Scanning Electron Microscope

CNT: Carbon Nanotube

EDLC: Electrochemical Double Layer Capacitors

FPG: Fullerenes Pillared Graphene

TEM: Transmission Electron Microscope

XRD: X-Ray Diffraction

SSA: Specific Surface Area

CL: Cross-Linking

SC: Supercapacitor

C: Capacitance

CDC: Carbide-Derived Carbons

AN: Acetonitrile

SAXS: Small Angles X-Ray Scattering

SANS: Small Angles Neutron Scattering

WAXS: Wide angles X-Ray Scattering

FWHM: Full Width at Half Maximum

SLD: Scattering Length Density

CV-SANS: Contrast Variation-SANS

AC: Activated Carbon

$TEABF_4$: TetraEthyl Ammonium TetrafluoroBorate

$THABF_4$: TetraHexyl Ammonium TetrafluoroBorate

CE: Counter Electrode

WE: Working Electrode

TGA: Thermal Gravimetric Analysis

BET: Brunauer-Emmett-Teller

TPD-MS: Temperature-Programmed Desorption coupled with Mass Spectrometry

FSE: Free-Standing Electrode

AB: Acetylene Black

PTFE: Poly(TetraEluoroEthylene)

d-AN: Deuterated Acetonitrile

P(Q): Form factor

S(Q): Structure factor

Ds: Surface fractal dimension

D_m: Mass fractal dimension

INV: Invariant

R: bending length

Σ: Persistence length

Va: Envelope volume

Vc: Solid volume

CycloH: CycloHexane

d-CycloH: Deuterated CycloHexane

e_B: Solid thickness

PSD: Pore Size Distribution

nGA: Pillared Graphene aerogel

6RP: Pillared reduced powder

6P: Functionalized Powder

List of Figures

Chapter I

Figure I. 1 (a) 'Scotch tape' procedure, reported by Novoselov and Geim in 2004 (b) Optical microscope image of graphene showing the presence of flakes containing one layer (1L) and few layers 9
Figure I. 2 Schematic representation of most common graphene production methods. Each method is evaluated according to graphene quality (G), as well as the cost (C) purity (P), scalability (S) and yield (Y) of the overall process [15]. 11
Figure I. 3 Schematic representation of the oxidation and exfoliation of graphite [19] 11
Figure I. 4 Schematic representation of the reduction of GO [19] 12
Figure I. 5 The structural difference between (a) Graphene (b) GO (c) rGO [19] 13
Figure I. 6 Representation of the rGO production process via chemical reduction of GO [21] 13
Figure I. 7 Deconvolution of the C1s HR XPS spectra peak of GO and rGO reduced at different temperatures: (a) GO; (b) rGO-1 after reduction at 15 ◦C for 100 h; (c) rGO-2 after reduction at 60 ◦C for 100 h and (d) rGO-3 after reduction at 95 ◦C for 3 h [22]. 15
Figure I. 8 Representation of the rGO production process via thermal reduction of GO [30]. 16
Figure I. 9 Steps for the hydrothermal reduction of GO: (a) dispersion of GO in water, (b) GA in water after the hydrothermal reduction process performed at 180°C for 6H, (c) frozen GA (d) final GA monolith after freeze-drying [40] 18
Figure I. 10 Graphene aerogel synthesis and its morphology. (a) Schematic showing the experimental steps and synthetic conditions using graphene oxide as the precursor, (b) sample optical image illustrating the foam-type structure of the GA and (c and d) SEM images of the GA [44] 19
Figure I. 11 (a-c) SEM images at 3 different magnifications of the graphene monolith obtained from GO monolith subjected to combined ascorbic acid and thermal reductions . (d) Schematic representation of the formation mechanism of the cork-like monolith by freeze casting. [45] 20
Figure I. 12 Illustration of a radiating graphene oxide aerogel fabricated by bidirectional freezing. (a) Scheme of the fabrication process. (b) Freezing setup. (c) Two temperature gradients induced by the upper copper mold. (d) Model of the ice crystals growing along radial directions [46] 21
Figure I. 13 (a) Scanning electron microscopy (SEM) image showing a top view of a BDF G-O aerogel, (b) Side view of the aerogel, (c) Illustration showing the decreasing width of the channels [46] 22
Figure I. 14 (a) Schematic diagram of a 3D pillared CNT-graphene nanostructure. (b) Schematic representation of the fabrication process of the 3D pillared CNT-graphene architectures. Optical images of (c) graphite (d) the thermally expanded graphene layers intercalated with CNTs [51] 24
Figure I. 15 (a-c) SEM images of the 3D pillared CNT-graphene architectures under different magnifications. XRD patterns of CNT-graphene after being intercalated with CNTs of different nanotube lengths: (d) 5μm,(e) 10μm, and (f) 20μm [51] 25
Figure I. 16 (a) TEM image of the FPG. Arrows indicated fullerene. (b) XRD patterns of the FPG. (c) Ideal model of the FPG structure [52]. 26
Figure I. 17 (a) Schematic illustration of the chemical reaction between GO and amines to produce amine/rGO composites. (b) Chemical structures of the six amine spacers showing different alkyl chain length and the different heteroatoms present in the chain [59] 28
Figure I. 18 XRD spectra of (a) amine/GO and (b) amine/rGO composites; (c) comparison of d spacing values between amine/GO and amine/rGO composites (before and after the reduction); (d) nitrogen adsorption-desorption isotherms of the amine/rGO structures [59]. 29
Figure I. 19 (a) Schematic representation for the Synthesis of RPs with (b) the formula of the alkyl diamines used in H. Band et al. work [61] 30
Figure I. 20 X-ray diffraction patterns of the different RPs, rGO, and GO [61] 31
Figure I. 21 Specific power against specific energy, also called a Ragone plot, for various electrical energy storage devices [62] 32
Figure I. 22 Basic schematics for an (a) all carbon EDLC (left), (b) a pseudocapacitor (MnO_2) and (c) a lithium ion battery [70] 34
Figure I. 23 CV curves of (a) EDLC supercapacitor (b) Pseudocapacitance supercapacitor (d) battery [71] 34
Figure I. 24 (a) Correlations between normalized capacitance and average pore size in an electrolyte containing 1.5 M $TEABF_4$ dissolved in ACN. Zone I represent the condition leading to CSP decrease with SSA/pore size decrease. Zone III represents the conditions when pore size matches ion diameter and CSP increases; while zone II represents the threshold conditions. Schematic representation of solvated ions residing in pores with varying sizes (b) >2 nm, (c) 1 ─2 nm, and (d) <1nm and showing the evolution of the charge-compensation distance d

[74] 36
Figure I. 25 (a) Classification of pores based on pore width (b) Schematic illustration of an ion diffusion pattern in a typical hierarchical porous structure [77] 37
Figure I. 26 (a) SEM image of rGO (b) TEM image showing individual graphene sheets [83] 38
Figure I. 27 Pictures of a GO aqueous dispersion before and after hydrothermal reduction at 180 °C for 12 h; (b) Pictures of how mechanically strong the GA obtained was, enabling easy handling and supporting weight; (c) SEM image of the GA [84] 39
Figure I. 28 (a) 6-RPs are synthesized in two-step process: cross-linking and reduction (b) 6-GHs are synthesized in a one-step process in an auto-clave [85]. 39
Figure I. 29 XRD patterns with various pillars amount of (a) 6-RP (b) 6-GH. 40
Figure I. 30 (a) Normalized CVs of RGO and RPs obtained at a scan rate of 20 mV/s in the voltage range of 0.1 to −1.0 V vs Ag using 1 M solutions of (1) $TEABF_4$ (Φ = 0.68 nm), (2) $TPABF_4$ (Φ = 0.76 nm), (3) $TBABF_4$ (Φ = 0.82 nm), and (4) $THABF_4$ (Φ = 0.95 nm) in acetonitrile as electrolytes.(b) Ions of different sizes are sieved based on the sizes of the graphene interlayer galleries (0.78 nm for 5 RP, 0.8 nm for 6 RP and 0.86 nm for 8 RP), resulting from using pillars of different sizes [61]. 40
Figure I. 31 (a) CV curves of 6-GH in $TEPBF_4$, $TBPBF_4$, and $TOPBF_4$/ acetonitrile (AN) 1 M electrolytes recorded at 20mV/s. (b-d) 1D LT CPMAS {^{15}N-} ^{31}P zf-TEDOR NMR spectra of 6GH electrodes after negative polarization and various electrolytes (TOP^+(a),TBP^+(b), and TEP^+(c) with BF_4^-/AN), recorded using a total of 7 ms of TEDOR recoupling [86] 41
Figure I. 32 The different possible charging mechanisms for carbon pores that are initially filled with electrolyte: counter-ion adsorption, ion exchange, and co-ion desorption. [87] 43
Figure I. 33 Comparison of the ranges of pore sizes that can be probed using various types of gas adsorption methods, optical microscopy, electron microscopy, neutron and X-ray scattering. [102] 46
Figure I. 34 SAXS/WAXS profiles of (a) the ordered (CPC, graphite) and (b) disordered (AC, HC, GC) carbons. The black line represent the experimental data, red, blue, orange, and green lines represent the fitted curves [109]. 47
Figure I. 35 Simulation of a (002) peak with three different microstructures (nanocrystallite, bent, and crumpled)[109]. 48
Figure I. 36 Specific surface area deduced from SAXS (columns) and gas adsorption (dark red circles) for different carbon samples [109] 49
Figure I. 37 Qualitative representation of contrast-matching experiments with fluid saturated porous systems. (a) All pores are accessible to fluid molecules; (b) Pores are partially accessible to fluid molecules. [115] 50
Figure I. 38 Scattering intensity at Q=0.1 $Å^{-1}$ for (a) Mar-1, (b) Mar-2 and (c) Mar-3 as a function of the scattering length density (SLD) of H_2O/D_2O and toluene/d-toluene (H-TOL/D-TOL) mixtures 51
Figure I. 39 The fraction of accessible pores in three Marcellus Shale samples estimated by: (a) H_2O/D_2O contrast matching and (b) toluene/d-toluene (H-TOL/D-TOL) contrast matching 52
Figure I. 40 (a) SANS profiles of AC in its dry and immersed in different H-toluene/D-toluene mixtures form (b) Scattering intensity at Q=0.017 $Å^{-1}$ =, Q=00025 $Å^{-1}$, and Q= 0.053 $Å^{-1}$ as a function of the solvents SLDs [117]. 53
Figure I. 41 Schematic of the SANS measurements setup for in situ experimental studies of ion electrosorption phenomena in microporous carbon electrodes [119] 54
Figure I. 42 In situ neutron scattering experiments on AC electrodes immersed into 1 M TEATFB/d-AN electrolyte under an application of a potential between the WE and CE: (a) SANS patterns, (b) SANS profiles normalized by the 0 V one, (c) relative changes in the intensity of the normalized SANS profiles [119]. 55

Chapter II

Figure II. 1 Steps for acidity removal and size selection 71
Figure II. 2 TGA profile of the 6RP-0.2 sample with the difference in weight % calculated from the changes in the slopes of the degradation profile before and after the degradation step. 76
Figure II. 3 The shape related correction factor for the conductivity measurement using a four-point probe along with the CF of 3.2 corresponding to the diameter of the pellets used 77
Figure II. 4 Schematic representation of a scattering experiment [3] 81
Figure II. 5 The probed scale in SAS experiments (Q) in this study and the corresponding scale in real space (d) 82
Figure II. 6 Coherent scattering length for X-rays and neutrons, for different elements [4] 83
Figure II. 7 the probed structural properties on different scales in a biphasic system 84
Figure II. 8 Representation of the different Q-regions of the form factor [5] 85
Figure II. 9 (a) SANS profiles of different Marcellus Shales, (b) a zoon on the plateau at high Q values and the determination of the subtraction values, (c) the SANS profiles after subtraction [9] 87

Figure II. 10 (a) Typical SAXS/SANS profile of porous materials (porous glass) [10] and (b) Typical SAXS/SANS profile of a fractal system (with a fractal dimension D=1.5) [3]. 89
Figure II. 11 (a) SAXS profiles of different protein and (b) their respective Kratky representation [11] 90
Figure II. 12 Representation of (a) the real measured layer with a thickness e_P, (b) the layer visible to X-rays with a thickness e_V [14] 91
Figure II. 13 Representation of the solid phase with an effective thickness e_B [14] 92

Chapter III

Figure III. 1 Conceptual scheme of the different level of porosity in non-pillared reference graphene materials 99
Figure III. 2 X-ray diffraction (XRD) patterns of GO (red) and graphite (black) demonstrating a successful graphite exfoliation and oxidation process. 100
Figure III. 3 Synthesis protocols of (a) GA and (b) rGO and corresponding pictures of the pristine materials. 101
Figure III. 4 (a) XRD patterns of GO, GA, and rGO, and (b) an example of fitting of the G peak of rGO showing the introduction of a background between 18 and 40 2tetha values as well as a fitting peak allowing for accurate 2tetha peak position and FWHM accurate determinations 102
Figure III. 5 TEM images at 2 magnification scale of the edge of the crystals of (a) GO, (b) GA, and (c) rGO. 103
Figure III. 6 TGA response of GO, GA, and rGO under a N_2 atmosphere. 105
Figure III. 7 The decomposition products under heating of (a) GA and (b) rGO evaluated by TPD-MS. 106
Figure III. 8 (a) XPS survey scans of GO, GA, and rGO, and C1s HR XPS spectrum of (b) GO, (c) GA, and (d) rGO. 107
Figure III. 9 EA and XPS C/O ratio evolution. 108
Figure III. 10 SEM image of freeze-dried pristine GO. 109
Figure III. 11 SEM images recorded at 2 different magnifications of (a,b) GA and (c,d) rGO. 110
Figure III. 12 SEM images on (a) GA and (b) rGO showing the grinding impact on the macrostructure. 111
Figure III. 13 Conceptual model of graphene based materials showing the bending R and persistence Σ lengths, adapted from Saurel et al [22] 113
Figure III. 14 (a) SANS profile of pristine GO (b) SEM image of GO 114
Figure III. 15 (a) SANS profile of pristine GA (b) corresponding Kratky plot (c) SEM image at high magnification of GA. 116
Figure III. 16 (a) SANS profile of pristine rGO (b) corresponding Kratky plot (c) SEM image of rGO at high magnification. 117
Figure III. 17 TEM images of GA taken from different zones highlighting the 3D morphology of this material at this scale (20 to 100 nm). 119
Figure III. 18 TEM images of rGO TEM images of GA taken from different zones highlighting the 3D morphology of this materials at this scale (20 to 100 nm). 119
Figure III. 19 Grinding impact on the mesostructure of (a) GO, (b) GA, and (c) rGO studied by SANS. 120
Figure III. 20 The various volumes that can be quantified in a porous sample 121
Figure III. 21 (a) CV-SANS profiles of pristine GA at different mixtures of cyclohexane/d-cyclohexane (b) the intensity as a function of the deuterated solvent at $Q=0.007\ A^{-1}$, $Q=0.02\ A^{-1}$, and $Q=0.05\ A^{-1}$showing its uniform evolution at the different Q values and a minimum at 74% of d-CycloH. 123
Figure III. 22 (a) CV-SANS profiles of rGO at different mixtures of cyclohexane/d-cyclohexane (b) $Intensity^{1/2}$ as a function of deuterated solvent at $Q=0.007A^{-1}$ and $Q=0.02A^{-1}$showing the absence of a trend or a minimum intensity (c) image of rGO inside Hellma cell after 30 sec of the suspension. 124
Figure III. 23 The invariant determination from the area under the Kratky curves of (a) GA and (b) rGO. 126
Figure III. 24 N_2-PSD of GA and rGO. 128
Figure III. 25 C/O evolution and TGA weight loss of GO, GA, and rGO. 129
Figure III. 26 the morphologic model, the characteristic structural features (R, and Σ), and the mass and surface fractal dimensions determined from SANS of (a) GO, (b) GA, and (c) rGO. 130
Figure III. 27 (a) SANS porosity, (b) N_2 SSA, and (c) pore volume in the scale 0.6 to 30 nm of GA and rGO. .. 131

Chapter IV

Figure IV.1 Schematic representation of graphitic and pillared domains showing ions adsorption within the galleries. 138
Figure IV.2 Conceptual scheme of the different level of porosity in pillared graphene materials 139
Figure IV.3 Synthesis protocol of (a) nGAs (b) nRPs (c) the pillars used in this work with the number of carbons in the alkyl chain and (d) the equivalent number used for 6GA and 6RP synthesis. 140
Figure IV.4 (a) TGA response performed under N_2 atmosphere of GO, rGO, 6RP-0.2, and 6GA-0.05 (b) TGA profile of the 6RP sample with the difference in weight % calculated from the changes in the slopes of the

degradation profile before and after the degradation step. 142
Figure IV.5 XPS survey scan of 6GA-0.05 and 6RP-0.2 143
Figure IV.6 The decomposition products under heating evaluated by TPD-MS of (a) 1,6 diamonohexane and (b) 6RP-0.2. 144
Figure IV.7 XRD patterns of (a) 6RP-0.2 and rGO, (b) 6GA-0.05 and GA. 145
Figure IV.8 XRD patterns of different samples from the same 6RP-0.2 synthesis. 146
Figure IV.9 XRD patterns of GO and 6Ps after 2, 4, 8, and 24 hour of reaction. 148
Figure IV.10 The proposed scheme of the functionalized and pillared graphene during this first reaction. 148
Figure IV.11 XRD patterns of 6RP-0.2 after 2, 4, 8, and 24 hour of 6P-24H reduction. 149
Figure IV.12 (a) Nitrogen and (b) oxygen evolution during the first reaction step determined by XPS. 150
Figure IV.13 (a) Nitrogen and (b) oxygen evolution during the second reaction step determined by XPS. 151
Figure IV.14 XRD patterns of different samples from the same 6GA-0.05 synthesis. 152
Figure IV.15 XRD patterns of two different samples from the (a) core and (b) shell of the 6GA-0.05 aerogel, (c) SEM image of the 6GA-0.05 aerogel showing the visual difference between the core and shell. 153
Figure IV.16 XRD patterns with different diamine equivalent numbers for (a) 6GA and (b) 6RP. 155
Figure IV.17 XRD patterns of the pillared graphene aerogels using different pillars with different lengths 157
Figure IV.18 SEM images at different magnifications of (a,b) 6GA-0.05 and (c,d) 6RP-0.2. 158
Figure IV.19 SEM images of (a) 6GA-0.05 before grinding (b) 6GA-0.05 after grinding (c) 6RP-0.2 before grinding (d) 6RP-0.2 after grinding. 159
Figure IV.20 (a) SANS and (b) Kratky plot of 6GA-0.05. 161
Figure IV.21 (a) SANS and (b) Kratky plot of 6RP-0.2 162
Figure IV. 22 Grinding impact on the meso-structure studied by SANS for (a) 6GA-0.05 and (b) 6RP-0.2 before (black) and after (red) grinding 163
Figure IV. 23 SANS profiles of (a) 6GA and (b) 6RP with different equivalent number. 164
Figure IV. 24 SANS profiles of nGA-0.05 with (a) n =6 and 8, and (b) n=6,8, 10, and 12. 164
Figure IV. 25 The various volumes that can be quantified in a porous carbon sample 165
Figure IV. 26 (a) CV-SANS profiles of pristine 6GA-0.05 at different mixtures of cyclohexane/d-cyclohexane (b) the intensity as a function of the % of deuterated solvent at Q=0.007 A^{-1}, Q=0.02 A^{-1}, and Q=0.05 A^{-1}showing its uniform evolution at the different Q values and a minimum at 50% of d-CycloH 167
Figure IV. 27 (a) CV-SANS profiles of pristine 6RP0.2 at different mixtures of cyclohexane/d-cyclohexane (b) the intensity as a function of the deuterated solvent at Q=0.007 A^{-1}, Q=0.02 A^{-1}, and Q=0.05 A^{-1}showing its uniform evolution at the different Q values and a minimum at 50% of d-CycloH 168
Figure IV. 28 Schematic representation of the impact of galleries on the measured solid volume in CV-SANS. 168
Figure IV. 29 The invariant determination from the area under the Kratky curves of (a) 6GA-0.05 and (b) 6RP-0.2. 170
Figure IV. 30 N_2-PSD of 6GA-0.05, 6RP-0.2 and rGO 172
Figure IV. 31 SANS porosity, N_2 BET SSA, and the mesopores volume for GA, 6GA-0.05, rGO, and 6RP-0.2. 174
Figure IV. 32 schematic representation of (a) non-pillared sample and (b) pillared sample. 175

Chapter V

Figure V. 1 A three-electrode Swagelok® cell configuration 182
Figure V. 2 CV curves of (a) rGO (b) GA cycled at different scan rate in 1M $TEABF_4$ in acetonitrile 183
Figure V. 3 CV curves of (a) rGO (b) GA cycled at different scan rate in 3M H_2SO_4 183
Figure V. 4 (a) CV curves of rGO and GA in organic electrolyte 1M $TEABF_4$ in acetonitrile at 10 $mV.s^{-1}$ (b) SANS porosity, N_2 BET SSA, and total pore volume representation. 184
Figure V. 5 (a) CV curves of rGO and GA in aqueous electrolyte 3M H_2SO_4 at 10 $mV.s^{-1}$ (b) C/O evolution, TGA remaining weight after GO reduction, and electrochemical capacitance in the aqueous electrolyte. 185
Figure V. 6 CV curves of (a) 6GA-0.05 and (b) 6RP-0.2 cycled at different scan rate in 1M $TEABF_4$ in acetonitrile. 186
Figure V. 7 CV curves of (a) 6GA-0.05 and (b) 6RP-0.2 cycled at different scan rate in 3M H_2SO_4 electrolyte. 186
Figure V. 8 SANS porosity, N_2 BET SSA, and the electrochemical capacitance in organic electrolyte for GA, 6GA-0.05, rGO, and 6RP-0.2. 187
Figure V. 9 Rate capability of pillared and non-pillared graphene samples in (a) 1M $TEABF_4$ / AN and (b) 3M H_2SO_4 electrolytes. 188
Figure V. 10 (a) rGO (b) 6RP-0.2 cycled in 1M $TEABF_4$ and $THABF_4$ /AN at a scan rate of 10 mV/s (c) the two cations and their approximate diameter [3] 189
Figure V. 11 (a) The prototype of the operando electrochemical cell (b) the configuration of the electrodes and separator inside the cell, the beam interact only with the WE. 190

Figure V. 12 Comparison of (a) SANS and (b) SAXS profiles of pristine rGO 191
Figure V. 13 Comparison of (a) SANS and (b) SAXS profiles of pristine 6RP-0.2 192
Figure V. 14 SAXS profile of (a) 6RP-0.2 powder, (b) AB, (c) PTFE, (d) 6RP-0.2 FSE calculated from the different volume fraction of the three materials (e) Kratky plot of 6RP-0.2 FSE..... 194
Figure V. 15 (a) SAXS profile and (b) Kratky plot of rGO FSE..... 195
Figure V. 16 XRD profiles of rGO and 6RP-0.2 FSEs..... 196
Figure V. 17 WAXS profiles of (a) rGO and (b) 6RP-0.2 FSEs 196
Figure V. 18 (a) SAXS and (b) WAXS profiles of 6RP-0.2 FSE recorded during cycling in 1M $TEABF_4$ /AN, (C) SAXS and (d) WAXS profiles of 6RP-0.2 FSE recorded during cycling in 1M $THABF_4$ /AN 198
Figure V. 19 Subtraction of the first WAXS profile from the last one of 6RP-0.2 FSE cycled in 1M $THABF_4$ / AN. 199
Figure V. 20 (a) SAXS and (b) WAXS profiles of 6RP-0.2 FSE recorded during polarization at -1.3V vs Ag in 1M $TEABF_4$/ AN, (c) SAXS and (d) WAXS profiles of 6RP-0.2 FSE recorded during polarization at -1.3V vs Ag in 1M $THABF_4$/ AN. 200
Figure V. 21 (a) Kratky plots of the first and last SAXS profiles of the polarization of 6RP-0.2 FSE at -1.3V vs Ag in 1M $THABF_4$ /AN (b) subtraction of the first WAXS profile from the last one for 6RP-0.2 FSE polarized at -1.3V vs Ag in 1M $THABF_4$ /AN..... 201
Figure V. 22 (a) SAXS and (b) WAXS profiles of rGO FSE during polarization at -1.3V vs Ag in 1M $TEABF_4$ /AN, (c) SAXS and (d) WAXS profiles of rGO FSE during polarization at -1.3V vs Ag in 1M $THABF_4$ /AN. 202
Figure V. 23 (a) Kratky plots of the first and last SAXS profiles of the polarization of rGO FSE at -1.3V vs Ag in 1M $TEABF_4$ /AN, (b) subtraction of the first WAXS profile from the last one of rGO FSE polarized at -1.3V vs Ag in 1M $TEABF_4$ /AN, (c) Kratky plots of the first and last SAXS profiles of the polarization of rGO FSE at -1.3V vs Ag in 1M $THABF_4$ /AN (d) subtraction of the first WAXS profile from the last one of rGO FSE polarized at -1.3V vs Ag in 1M $THABF_4$ /AN...... 203
Figure V. 24 The expected variations in contrast $\Delta\rho$ or intensity after anions and cations adsorption within the porosity. 205
Figure V. 25 the normalized scattering profiles to the OCV without signal processing of 6RP-02 FSE polarized in 1M $TEABF_4$ /AN at (a) -1.3V followed by +1.5V, (b) +1.5 V followed by -1.3V, and in 1M $THABF_4$ /AN at (c) -1.3V followed by +1.5V, (d) +1.5 V followed by -1.3V..... 206
Figure V. 26 SANS profiles of 6RP-02 FSE polarized in 1M $TEABF_4$ / d-AN at (a) -1.3V followed by +1.5V and (b) +1.5V followed by -1.3V, and the normalized scattering profiles to the OCV of 6RP-02 FSE polarized in 1M $TEABF_4$ /d-AN at (c) -1.3V followed by +1.5V and (d) +1.5V followed by -1.3V. 208
Figure V. 27 SANS profiles of 6RP-02 FSE polarized in 1M $THABF_4$ /d-AN at (a) -1.3V followed by +1.5V and (b) +1.5V followed by -1.3V, and the normalized scattering profiles to the OCV of 6RP-02 FSE polarized in 1M $THABF_4$ /d-AN at (c) -1.3V followed by +1.5V and (d) +1.5V followed by -1.3V...... 210
Figure V. 28 (a) The different polarization potentials displayed on a CV curve, (b) the normalized scattering profiles to the OCV of 6RP-0.2 FSE polarized at these different potentials, R refer to return. 212

List of Tables

Chapter I

Table I.1 List of the main reducing agents for graphene oxide towards chemically reduced graphene oxide……14
Table I.2 Comparative analysis of capacitors, supercapacitors, and batteries for the storage of electrical energy [68]…… 29
Table I.3: Comparative properties of neutron and X-ray small angle scattering [108]…….. 43

Chapter II

Table II.1: The different pillars used for nGAs synthesis and their respective weights…….. 68
Table II.2: Power law of the scattered intensity from simple structures in the intermediate-Q region……..81

Chapter III

Table III. 1: XRD fitting data (peak-position, d-spacing and FWHM values) and crystal stack height calculated from Scherrer equation along with the number of layers/crystal determined, the error bars were determined from the standard deviation between five measures……99
Table III. 2: Atomic percentages extracted from XPS and EA and C/O ratio of the GO, GA, and rGO……102
Table III.3: Summary of characteristic sizes and mass/surface fractal dimension determined by SANS…….113
Table III.4: The envelope density of GA and rGO……116
Table III.5: The solvent mixtures used for CV-SANS and the corresponding SLD……..117
Table III.6: Envelope and solid density as well as envelope, solid, and pores volumes of GA and rGO…….120
Table III.7: The different parameters used to estimate the mesoporosity of GA and rGO……121

Chapter IV

Table IV.1: XPS atomic concentration extracted from and EA mass concentration of the 6GA-0.05 and 6RP-0.2 ……...137
Table IV.2: XRD fitting data and the crystal stack height calculated from Scherrer equation……140
Table IV.3: XRD fitting data and the percentages of the cross-linked and the graphitic domains of 4 different samples of 6GA-0.05 single batch……146
Table IV.4: XRD fitting data and the percentages of the cross-linked and the graphitic domains of different 6GA-0.05 samples extracted from the core and the shell of the aerogel……147
Table IV.5 Atomic percentages extracted from XPS and EA of the different 6GAs……148
Table IV.6 Atomic percentages extracted from XPS and EA of the 6GAs……148
Table IV.7 Atomic percentages extracted from XPS and EA of the different nGA-0.05 (n=6, 8, 10, and 12)….150
Table IV.8: Summary of characteristic sizes and mass/surface fractal dimension of the graphene-based materials determined by SANS……156
Table IV.9: The envelope density pillared and reference graphene-based materials……159
Table IV.10: The solvent mixtures used for CV-SANS and the corresponding SLD……160
Table IV.10: Solid, envelope, and pores volumes of the pillared and reference graphene-based materials…….163
Table IV.11: The different parameters used to estimate the mesoporosity of pillared and reference graphene-based materials……164

Table of contents

General introduction……...1

Chapter I: Bibliography

1 Background on graphene 8

2 Graphene-based-materials 11

2.1 Graphene oxide 11

2.2 Reduced graphene oxide 12

2.2.1 Chemical reduction 13

2.2.2 Thermal reduction 16

2.2.3 Electrochemical reduction 17

2.2.4 Hydrothermal reduction 17

2.3 Strategies to avoid the graphene sheets restacking 22

2.3.1 Carbon nanotubes CNTs 23

2.3.2 Fullerenes 25

2.3.3 Nanoparticles 26

2.3.4 Organic molecules: alkyl diamines 27

3 Graphene based materials for energy storage applications 31

3.1 Supercapacitors 31

3.2 The importance of electrode materials porosity in SCs 34

3.3. Graphene-based materials in SCs 37

4 Multi-scale structure and porosity characterization 45

5 Interest of small angle scattering techniques in characterizing the mesoscale 47

6 Aim of the PhD 55

7 References: 57

Chapter II: Materials and Methods

1 Material synthesis 70

1.1 GO synthesis 70

1.2 rGO synthesis 72

1.3 GA synthesis 72

1.4 6RPs synthesis 72

1.5 nGAs synthesis 73

2 Basic characterization 73

2.1 X-ray diffraction (XRD) 73

2.2 X-Ray Photoelectron Spectroscopy (XPS) 74

2.3 Elemental Analysis (EA) 74
2.4 Thermal Gravimetric Analysis (TGA) 75
2.5 Scanning Electron Microscopy (SEM) 76
2.6 Transmission Electron Microscopy (TEM) 76
2.7 Conductivity measurement 76
2.8 N_2 and H_2 adsorption isotherms 77
2.9 Temperature-programmed desorption coupled with mass spectrometry (TPD-MS) 78
3 Electrochemistry 78
3.1 Free standing electrodes preparation 78
3.2 The studied electrolytes 78
3.3 Electrochemical program and data treatment 79
4 Standard deviation 79
5 Advanced characterizations instruments setup 79
5.1 SANS at D22 (Institut Laue Langevin (ILL)) 79
5.2 SAXS/WAXS at D2AM (European Synchrotron Radiation Facility (ESRF)) 80
6 Principle of small angle scattering 81
7 The structural features probed by SAS techniques 84
7.1 Form factor P(Q) 85
7.1.1 Low-Q regime “Guinier region” 85
7.1.2 Intermediate-Q region 86
7.1.3 Porod region “scattering by the interface”: 86
7.2 Structure factor S(Q): 87
8 The fundamental basis of SAS used in this study 88
8.1 SAS profiles of porous and fractal materials 88
8.2 Kratky representation 89
8.3 SAS porosity using the invariant 90
8.4 Contrast variation small angle neutrons scattering (CV-SANS) 93
9 References: 94

Chapter III: Chemical and structural studies of reduced graphene oxide-based materials

1 Objectives and approaches 98
2 Nanoscale structure investigation 99
3 Reduction efficiency and chemical composition 104
4 Macrostructure investigation and its evolution after GO reduction 109
5 Understanding the mesostructure and porosity: interest of small angle scattering 111

5.1 Mass and surface fractal dimension determination 112
5.2 Characteristic sizes 113
5.3 Investigation of the mesoscale morphology of GO 113
5.4 Comparison of the impact of the reduction method on materials morphology at the mesoscale 114
5.4.1 Study of the mesoscale morphology of GA by SANS and SEM 114
5.4.2 Study of the mesoscale morphology of rGO by SANS and SEM 116
5.5 Discussion on the impact of reduction method on the mesoscale morphology 117
5.6 Impact of grinding on the mesoscale morphology 120
6 Density and porosity investigation 120
6.1 Envelope density 120
6.2 Solid density, interest of neutrons 122
6.2.1 Solid density of GA investigated by CV-SANS 122
6.2.2 Solid density of rGO investigated by CV-SANS 123
6.3 Mesoporosity investigation 125
7 Conclusions 128
8 References 132

Chapter IV: Chemical and structural studies of pillared graphene materials

1 Objectives and approaches 138
2 Overview on the studied pillared graphene materials 140
3 Reduction efficiency and chemical composition of 6RP-0.2 and 6GA-0.05 141
4 Nano-porosity investigation 144
5 Pillaring homogeneity investigation 147
5.1 Pillaring homogeneity in 6RP-0.2 147
5.2 Pillaring homogeneity in 6GA-0.05 151
6 Investigation of impact of the equivalent number of pillars on the nanostructure and chemical properties of 6RP and 6GA 153
7 Pillars length impacts on the nanostructure and chemical properties of nGA-0.05 155
8 Macro-structure investigation and its evolution compared to non-pillared materials 157
9 Understanding the meso structure and porosity of pillared graphene materials, interest of small angle scattering 159
9.1 Investigation of the meso-scale morphology of 6GA-0.05 159
9.2 Investigation of the mesoscale morphology of 6RP-0.2 161

9.3 Impact of grinding on the meso-scale morphology 162
9.4 Impact of pillars density and length on the meso-scale morphology of pillared samples 163
10 Density and porosity investigation 165
10.1 Envelope density 165
10.2 Solid density, interest of neutrons 166
10.2.1 Solid density of 6GA-0.05 investigated by CV-SANS 166
10.2.2 Solid density of 6RP-0.2 investigated by CV-SANS 167
10.3 Mesoporosity investigation 169
11 Conclusion: 172
12 References: 176

Chapter V: Insights into the electrochemical behavior of graphene-based materials

1 Objectives and approaches 180
2 Electrochemical performances of graphene-based materials 181
2.1 The electrochemical performances of reference materials: rGO and GA 181
2.2 The electrochemical performances of pillared graphene materials: 6RP-0.2 and 6GA-0.05 185
3 Understanding the adsorption/desorption mechanisms in graphene-based materials 189
3.1 Unveiling the structural evolution of graphene-based materials during SC operation by *in-situ/operando* SAXS-WAXS study 191
3.1.1 *Operando* SAXS-WAXS study on 6RP-0.2 FSE during cycling 196
3.1.2 *In-situ* SAXS-WAXS study on 6RP-0.2 FSE during polarization 199
3.1.3 *In-situ* SAXS-WAXS study on rGO FSE during polarization 201
3.2 Unveiling the localization of ions within the porosity of graphene-based materials during SC operation by *in-situ* SANS study 204
3.2.1 *In-situ* SANS on 6RP-0.2 during polarization in 1M $TEABF_4$ /AN 206
3.2.2 *In-situ* SANS on 6RP-0.2 during polarization in 1M $THABF_4$ /AN 209
3.2.3 *In-situ* SANS on 6RP-0.2 during polarization at different potentials in 1M $TEABF_4$ /AN 211
4 Conclusion 212
5 References 216
General conclusion and perspectives……...……..218

General introduction

Carbon based materials are of interest in a wide variety of applications ranging from fuel cells, to filtration devices, or to hydrogen storage and supercapacitors etc. Their specific macroscopic (shape and size of particles, density, thermal and electric conductivity, etc.) and microscopic properties (porosity, chemical functionalization, etc.) can be tuned to target specific application. There is a large range of carbon materials that can be created by changing the carbon precursor and by controlling the synthesis chemistry. Moreover, research on carbon-based materials is very dynamic and has recently been growing. Their low cost, high electrical conductivity, surface functionality and their nano and microstructures properties make them a good choice of materials for energy storage technologies: supercapacitors and batteries [1].

Among various carbons, activated carbons (ACs) have been widely studied for SCs applications owing to their high specific surface areas (SSA), low material costs, and their tunable porous structures [2]. This porous structure triggers lot of researches to understand the capacitance to porosity relationship. Furthermore, studies on carbide-derived carbons (CDCs) revealed that in addition to high surface areas, matching pore sizes to electrolytic ion sizes also enables to reach high capacitances [3]. The problem of ACs is that their porous structure is not hierarchical which limit the ions diffusion and hence their capacitance as a supercapacitor electrode. Among other carbon derivatives tested, graphene has been studied as an electrode material candidate due to its high theoretical SSA, high electrical conductivity, hierarchical porous structure that should theoretically lead to high capacitance. Indeed, graphene is expected to display an electrochemical double layer specific capacitance of 550 F/g [4]. However, graphene produced by the up-scalable chemical exfoliation of graphite, yielding reduced Graphene Oxide (rGO), which is not a single rGO sheet but rather a stack of rGO sheets. Since stacking impedes the exploitation of the surface area of graphene, numerous three-dimensional (3D) assemblies of graphene such as aerogels are being investigated to address this issue, with particular focus on optimizing the material porosity and surface area. However, the graphitic stacking in reduced graphene-based materials has an inter-layer spacing very slightly higher than graphite which is too narrow to accommodate electrolytic ions in supercapacitors (SCs). In order to prevent the graphene sheets from restacking, the strategy of pillaring has been introduced to limit this effect using organic linkers locking apart graphene sheets (**Figure 1**) [5]. These molecular pillars are covalently grafted on graphene, in order to prevent molecular spillage over time promoting expanded graphene structure stability. This opens the door to a

new tailor-able family of graphene-based materials incorporating alkyl-diamine linkers of different lengths yielding a 2D porosity accessible to electrolytic ions, thereby potentially increasing the storage performances of supercapacitors.

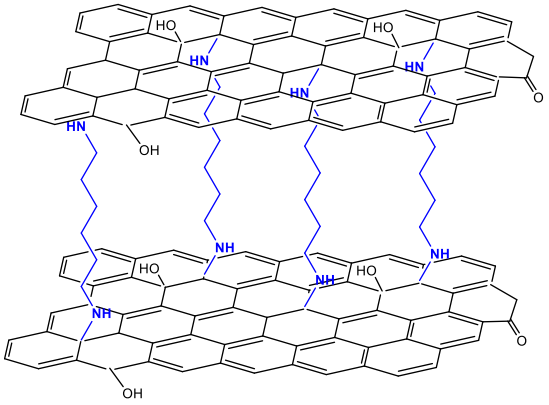

Figure 1 schematic representation of a cross linking (CL) or pillaring using hexamethylene diamine as an organic pillar.

The ability to tune the structure and properties of graphene-based materials represent a big advantage in optimizing their structural, electronic, and chemical properties, thereby enhancing their electrochemical performance. This level of control can be achieved through a variety of means, including selecting specific reduction methods, incorporating pillaring techniques, or introducing functionalization. Research mainly focused on the development of these materials and on the study of their electrochemical performances. While studies correlating electrochemical performances and chemical or structural properties can be found in the literature. However, and to the best of our knowledge, the multi-scale comprehensive characterization of graphene-based materials has not been addressed, particularly in terms of their mesostructural and morphological properties. For a better understanding of these materials, their structural characterization should be completed by unveiling their mesoscale structural features; all the more that hierarchical porosity is a pre-requisite property for SC operation. It is also important to recognize that understanding their multiscale structural and chemical properties is pivotal to adapt the design of these materials in order to reach higher performances. Therefore, to fully harness the potential of graphene-based materials, a comprehensive approach that integrates structural and morphological analysis, electrochemical investigation, and physicochemical characterization is essential. As these materials are subjected to fast and repetitive charge and discharge cycles, revealing how they interact with ions during these processes and how their structure and morphology are impacted is fundamental. It not only would shed light on the long-term stability and durability of these graphene-based materials, but it would also provides a fundamental knowledge of these

materials for further enhancements in the design and utilization in SCs. All together, these perspectives would not only enhance our understanding of these materials but it would also unlock new avenues for advancements in supercapacitor technology.

Therefore, this thesis aims at understanding the structure of these graphene-based materials and the adsorption/desorption mechanisms, in order to gain fundamental knowledge and in fine to optimize their design as supercapacitors electrodes. To reach such objective, a multi-scale advanced characterization methodology has been devised. Considering the complexity of the structure and porosity of these materials, this methodology consists in i) a thorough characterization of the sample microstructure and hierarchical porosities, ii) analyzing their electrochemical performances, and iii) studying their behavior and evolutions in real time during SC operation.

During the first part of this PhD, the characterization methodology that was used involving a multiscale characterization that required the combination of different characterization techniques (**Figure 2**). XRD allowed probing the crystalline nature of materials, providing insight on the local structure, crystal size, and interlayer spacing. In contrast, SEM provided morphologic images at a meso to macroscale resolution (> 10 nm), providing a visual observation into the morphology, surface features, and the macro-porosity of the material. Gas adsorption, particularly the BET method, was used to quantify surface area and porosity, giving indication of the ability of the materials to adsorb and store ions. However, the morphology and the internal structure of the mesoscale can not be observed using the gas sorption techniques. Indeed, Small-angle X-ray scattering (SAXS) and small-angle neutron scattering (SANS) were highly valuable, offering the possibility to characterize the sample structure at the mesoscale and macroscale. In addition, SAS techniques have the unique advantage to get access to the whole porosity as they can probe both open and closed porosities. In addition, their physicochemical properties, notably the degree of reduction and pillaring efficiency were assessed using TGA, XPS, EA, and TPD-MS. Through this study, a comprehensive analysis of graphene-based materials was conducted, encompassing the determination of both porosity and chemical properties. The acquired insights into these aspects served as a foundation for a deeper understanding of the electrochemical performances of the graphene-based materials.

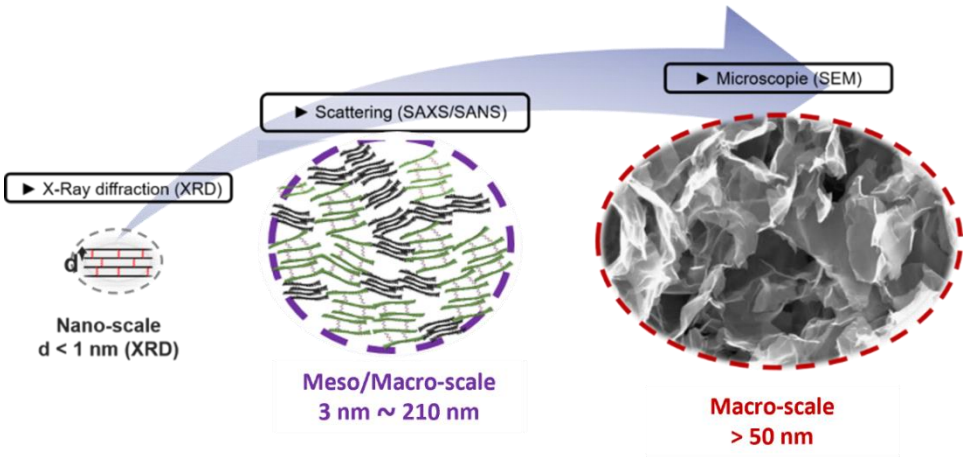

Figure 2 Multi-scale approach used to study the graphene based materials.

The second part of this thesis was dedicated to understanding the materials behavior in real time as a supercapacitor electrode. The influence of the physicochemical properties and structure or porosity of graphene-based materials on their electrochemical performances was studied. Furthermore, an advanced *in-situ/operando* SAXS/WAXS study using a synchrotron radiation was performed to reveal the structural evolution during cycling and polarization of the graphene-based materials. Since the electrochemical process in SCs is very fast, a synchrotron beam was necessary to perform operando measurements. In addition, we took advantage of the sensitivity of SANS to the adsorbed ions and performed an *in-situ* SANS experiment to reveal the location of ions inside the pore of different sizes.

This thesis work allowed to deepen the understanding of the structure and porosity of GO-based materials, as well as to characterize the electro-diffusion and -adsorption within the mesoporosity of the pillared samples. This work also constitutes a characterization methodology that could be applied to the study of other materials, thus contributing to advancing work on the optimization of supercapacitors.

References:

[1] L. Li Zhang et X. S. Zhao, « Carbon-based materials as supercapacitor electrodes », *Chemical Society Reviews*, vol. 38, nº 9, Art. nº 9, 2009, doi: 10.1039/B813846J.
[2] J. Gamby, P. L. Taberna, P. Simon, J. F. Fauvarque, et M. Chesneau, « Studies and characterisations of various activated carbons used for carbon/carbon supercapacitors », *Journal of Power Sources*, vol. 101, nº 1, Art. nº 1, oct. 2001, doi: 10.1016/S0378-7753(01)00707-8.
[3] J. Chmiola, G. Yushin, Y. Gogotsi, C. Portet, P. Simon, et P. L. Taberna, « Anomalous Increase in Carbon Capacitance at Pore Sizes Less Than 1 Nanometer », *Science*, vol. 313, nº 5794, Art. nº 5794, sept. 2006, doi: 10.1126/science.1132195.
[4] J. Chen, C. Li, et G. Shi, « Graphene Materials for Electrochemical Capacitors », *J. Phys. Chem. Lett.*, vol. 4, nº 8, Art. nº 8, avr. 2013, doi: 10.1021/jz400160k.
[5] H. Banda *et al.*, « Sparsely Pillared Graphene Materials for High-Performance Supercapacitors: Improving Ion Transport and Storage Capacity », *ACS Nano*, vol. 13, nº 2, Art. nº 2, févr. 2019, doi: 10.1021/acsnano.8b07102.

CHAPTER I: BIBLIOGRAPHY

1 Background on graphene

Graphene, was first isolated in 2004, as a one-atom-thick sheet of sp^2 carbon atoms arranged in a hexagonal lattice making it the first single layer fully exfoliated two-dimensional material [1]. Its unique atomic structure gives rise to a wide range of properties such as high electrical conductivity. The electron mobility in graphene is extremely high exceeding 2×10^5 cm^2 v^{-1} s^{-1}, [2] making it a good candidate in the field of electronics. Graphene is also an outstanding thermal conductor. It dissipates heat more efficiently than copper [3]. Moreover, it is remarkably strong with a tensile strength of 130 GPa, outperforming steel with a tensile strength of 505 MPa, despite its extremely low thickness and due to the strong carbon-carbon bonds [4]. Additionally, a single layer graphene exhibits nearly perfect transparency, absorbing only 2.3% of light. Since graphene combines high electrical conductivity and transparency, it is a material of high interest for optoelectronics and photovoltaics applications [5]. Furthermore, it exhibits a very high intrinsic theoretical specific surface area (2600 m^2/g) making it a promising candidate for next-generation energy storage applications, particularly supercapacitors [6]. Despite the current challenges faced in developing scalable production method and integration within existing technologies, graphene continues to be at the forefront of material science research.

The synthesis method used to produce graphene depends on the required quality, quantity and application. Several synthesis methods for graphene have been developed with different set of advantages and challenges. Each method yields a certain quantity of graphene with a given quality (*i.e.* graphene with various density of defects, or of surface oxygen groups, with different lateral sizes or with different number of layers). One of the earliest methods, that was devised, is the mechanical exfoliation of graphite or "scotch-tape method" (**Figure I.1 a, b**) [1]. It involves the peeling off of graphene layers from graphite using an adhesive; however, this technique suffers from difficulties in scalability and consistency.

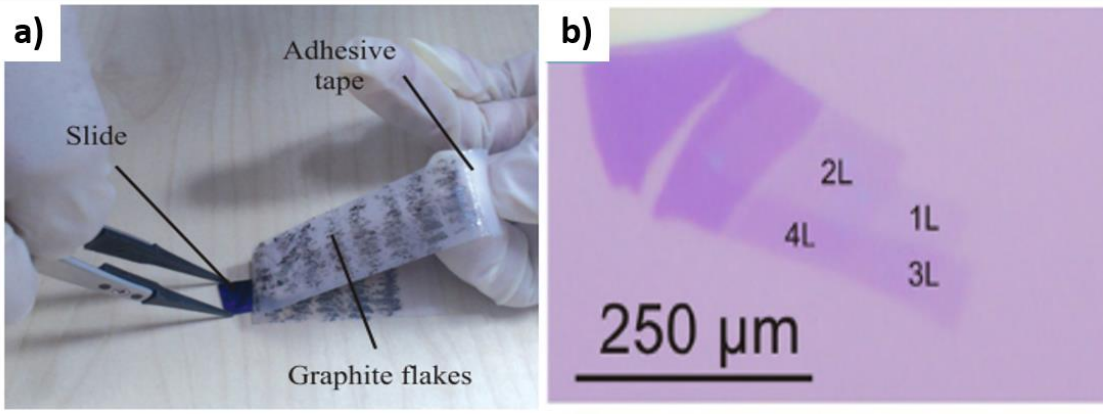

Figure I. 1 (a) 'Scotch tape' procedure, reported by Novoselov and Geim in 2004 (b) Optical microscope image of graphene showing the presence of flakes containing one layer (1L) and few layers (2L, 3L, 4L) [7] [8].

Chemical vapor deposition (CVD) is another widely used method that involves the decomposition of hydrocarbon gases on a metal substrate, typically copper or nickel. Using this method the production of large-area, high-quality graphene films is possible up to 30 square inches [9]. Other graphene synthesis methods include epitaxial growth, relying on the high temperature sublimation of the silicon atoms of silicon carbide, leaving behind a layer of C atoms rearranging in graphene [10]. However, these methods are expensive and transferring the CVD graphene films onto a different substrate can be challenging as it often involves the underlying metallic substrate dissolution [11] and it is impossible to transfer graphene grown on SiC.

The graphene production methods presented so far lie under two denominations: the top-down method that involves the use of graphite as starting material that will be thinned down to its most divided state graphene (scotch-tape method), and the bottom-up methods consisting of graphene grown from carbon containing substrate (epitaxial growth) or gases (CVD growth). Even though new advances in the development of such graphene production methods are being made, they still yield a limited amount of material that is not compatible with graphene use in more mass-demanding applications. Hence when larger amounts of graphene are required, another top-down production method is used: the liquid phase exfoliation.

This latter method consists in thinning down graphite in liquid medium involving various techniques such as electrochemical exfoliation, ions intercalation, or oxidizing graphite using a strong chemical oxidation and then exfoliating it into graphene oxide (GO) [12]. During this latter oxidation process, the sp^2 carbons network of graphene is modified with oxygen-containing functional groups [13]. To restore the Csp^2 network and for a bulk production of

graphene, the chemical reduction of graphene oxide is a commonly used technique [14]. This technique opens the way towards graphene-based-materials.

The methods employed for graphene production play a crucial role in determining the properties of the final graphene-based material [15] (**Figure I.2**). Mechanical exfoliation, epitaxial growth on silicon carbide (SiC), and bottom-up synthesis from organic precursors have limitations in terms of scalability and cost-effectiveness. However, they are still valuable for fundamental research and for applications not requiring mass amount of material. The graphene obtained from these methods is also very interesting as it presents a very high quality evidenced by low numbers of defects and surface groups. Other methods used for bulk graphene production involve the various liquid-phase exfoliation processes, including the widely employed (electro-)chemical exfoliation of graphite or the reduction of graphene oxide route. The liquid-phase exfoliation of graphite (electrochemically or by ions intercalation or by sheer-force exfoliation) leads to high-quality graphene sheets dispersed in a liquid media. However, the low yields associated with these exfoliation processes often result in a significant amount of non-exfoliated graphite [16]. In turn, the reduction of graphene oxide is considered as a well-established technique for mass production of graphene-based materials. However, the resulting graphene consists of few-layer partially-reduced graphene oxide (rGO) rather than single-layer graphene. The quality of graphene produced this way is often lower (*i.e.* stacks of few rGO layers, high density of surface functionalities and defects, Csp^2 domains of small dimensions) than that achieved for graphene obtained with other methods.

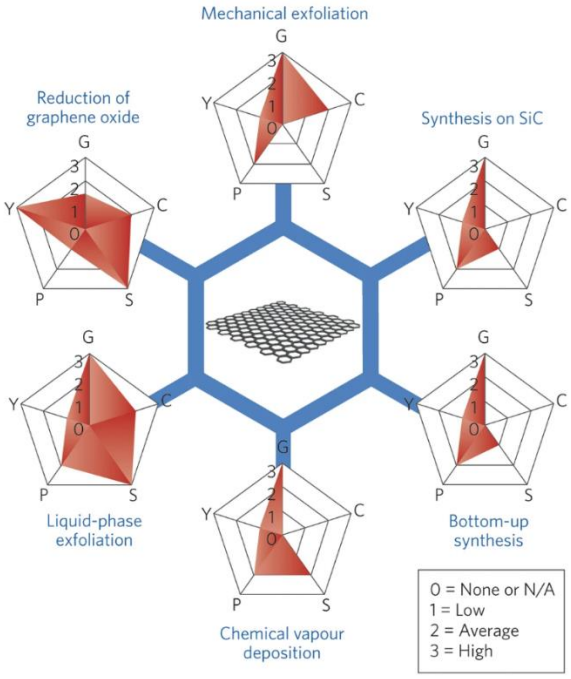

Figure I. 2 Schematic representation of most common graphene production methods. Each method is evaluated according to graphene quality (G), as well as the cost (C) purity (P), scalability (S) and yield (Y) of the overall process [15].

2 Graphene-based-materials

2.1 Graphene oxide

Graphene Oxide (GO) is an oxidized form of graphene containing oxygen functional groups such as hydroxyl, carboxyl, carbonyl and epoxy groups on its surface and edges [17]. GO is produced from the oxidation and exfoliation of graphite using the Hummers' method [18] (**Figure I.3**).

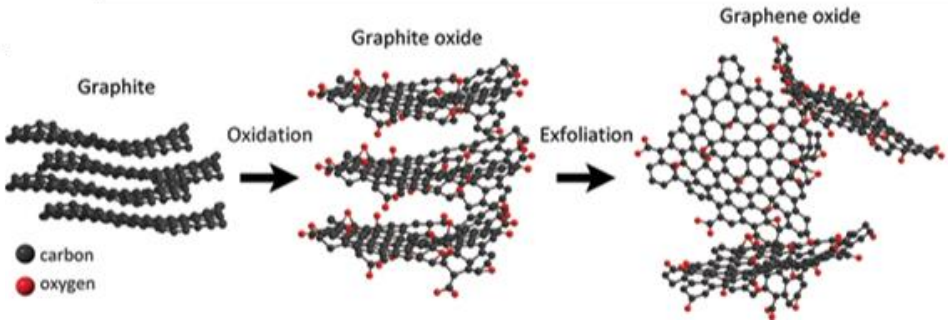

Figure I. 3 Schematic representation of the oxidation and exfoliation of graphite [19]

The introduction of oxygen groups in graphene makes it hydrophilic, allowing its efficient dispersion in water. However, these oxygen groups disrupt the Csp^2 bonding

network leading to a significant decrease in the electrical conductivity. GO must be reduced to decrease the amount of O groups, restore the sp^2 carbons network, and produce reduced graphene oxide (rGO) (**Figure I.4**), displaying an electrical conductivity reaching 2000 S/m, which is much higher than that of GO, but still lower than that of high quality graphene (>10 MS/m) [20].

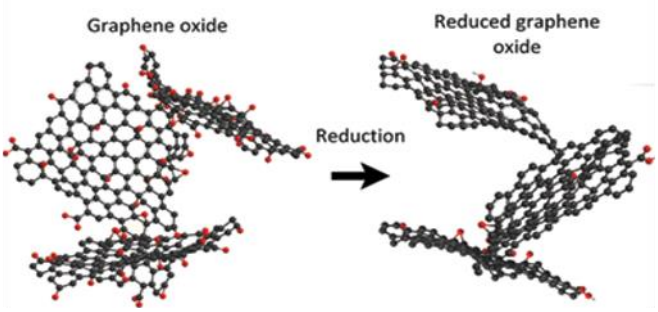

Figure I. 4 Schematic representation of the reduction of GO [19]

2.2 Reduced graphene oxide

The reduction of GO partially eliminates the oxygen-containing functional groups that had been introduced during the graphite chemical exfoliation. However, the properties of rGO are significantly different from those of graphene (without defect or oxygen functionalities see **Figure I.5 a**). Indeed, residual defects and functional groups remain after the reduction process (**Figure I.5 c**). The presence of these residual elements disrupts the pure sp^2 carbon lattice structure of graphene, leading to a drop in electrical conductivity, thermal conductivity, and mechanical strength when compared to pure single layer graphene. This surface chemistry modification makes rGO less hydrophilic than GO, but less hydrophobic than graphene. rGO properties can be fine-tuned by choosing a specific reduction method, and/or by using potential functionalization routes, which offer opportunities for designing the material for specific applications.

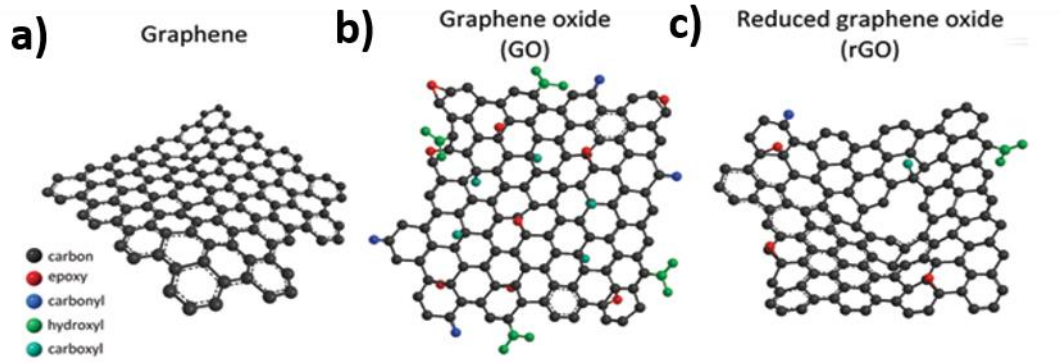

Figure I. 5 The structural difference between (a) Graphene (b) GO (c) rGO [19]

2.2.1 Chemical reduction

Chemical reduction is indeed the most common process used to reduce GO. This method involves the use of reducing agents that react with the oxygen containing groups in GO. The most frequently used reducing agents are hydrazine, sodium borohydride, and ascorbic acid (**Figure I.6**), which act to eliminate oxygen functional groups and restore the π-conjugated network of graphene. While this method is easy to perform and scalable, it often leaves residues from the reducing agents such as the introduction of N from hydrazine in the graphene layers, which may affect the properties of the resulting rGO [21].

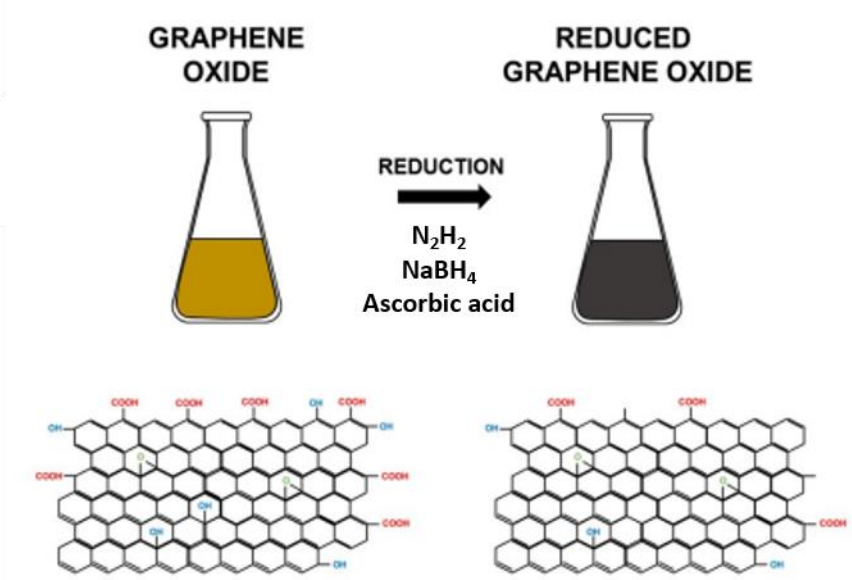

Figure I. 6 Representation of the rGO production process via chemical reduction of GO [21]

Reduction using hydrazine (N_2H_2) is very efficient, as the strong reducing nature of hydrazine allows for the substantial removal of oxygen groups from GO, restoring its

conductive properties (**Table I.1**). Nevertheless, hydrazine is highly toxic and hazardous, necessitating careful handling and disposal [14].

Peng-Gang Ren *et al* [22] studied the efficiency of hydrazine reduction at different temperatures and reaction time. The started GO was prepared following the Hummer's method, then reduced under stirring using hydrazine hydrate with a Hydrazine/GO weight ratio of 1:1 at different temperatures (15, 60, 80 and 95°C) in order to identify the most efficient reduction parameters. At the end, the rGO powder was isolated by filtration and dried at 60°C for 24h. XPS characterization was employed to track the evolution of the reaction by monitoring the amount of oxygen functional groups within the material. **Figure I.7** displays the C1s high-resolution (HR) XPS spectra and its deconvolution for GO and the different rGO. For GO, two distinct peaks were observed at binding energies of approximately 284 and 286 eV. These were attributed to graphitic C=C/(C–C) and to C-O of the different oxygen-related functional groups, respectively. The deconvolution of the C1s peak of GO, shows five peaks at 284.4, 285.7, 286.7, 288.0, and 289.1 eV, corresponding to the C–C/C=C bonds as well as C–OH, C-O of epoxide, C=O (carbonyl), and O=C–OH (carboxylate) functional groups, respectively. The dominant oxygen-related group in GO appears to be the epoxide group (C–O–C). Although rGO's C1s HR XPS spectrum presents similar functional groups as GO, most peaks exhibit lower intensities, with the exception of the one at 285.7 eV which was assigned to the overlap between the C–N peak which originate from the insertion of N of the hydrazine in the graphene matrix (285.9 eV) and the C–OH (285.7 eV) peaks.

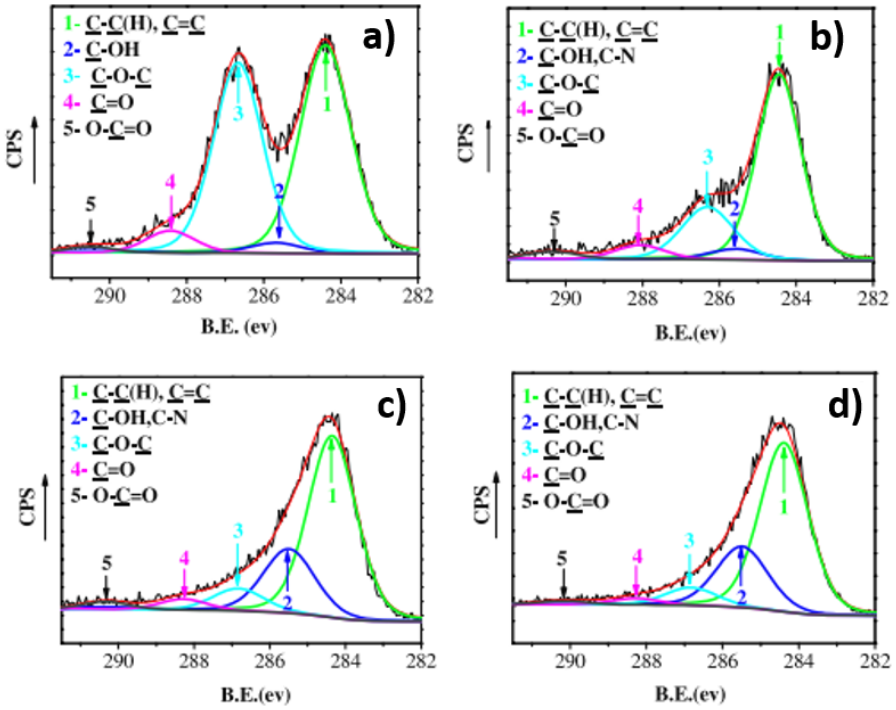

Figure I. 7 Deconvolution of the C1s HR XPS spectra peak of GO and rGO reduced at different temperatures: (a) GO; (b) rGO-1 after reduction at 15 ◦C for 100 h; (c) rGO-2 after reduction at 60 ◦C for 100 h and (d) rGO-3 after reduction at 95 ◦C for 3 h [22].

The Carbon-to-Oxygen ratio (C/O) was determined from XPS data and elemental analysis (EA) to assess the efficiency of the reduction process using hydrazine. The C/O atomic ratio from XPS data increases from 3.0 for GO to 6.4, 10.9, 13.1 and 15.1 for rGO at 15, 60, 80 and 95 ◦C reaction temperatures, respectively. Although there is a slight difference compared with EA data (1.65 for GO, 6.87 at 15 ◦C, 8.13 at 60 ◦C, 11.08 at 80 ◦C and 13.25 at 95 ◦C) a similar trend is observed. Hence the most reduced sample is obtained when using a 95°C reaction temperature

Another reducing agent is sodium borohydride ($NaBH_4$), which is less toxic than hydrazine and offers a relatively good reduction efficiency with a reached C/O ratio of 8.6. It can result in a significant restoration of the graphene structure [23]. However, it tends to be less efficient than hydrazine at removing certain types of oxygen groups, particularly carboxyl groups, leading to a less conductive sample with a conductivity that does not exceed 100 S/m while that of graphene reduced with hydrazine hydrate shows a conductivity value exceeding 2000 S/m (**Table I.1**).

Ascorbic acid (vitamin C), compared to the first two agents is the most environmentally friendly agent for the reduction of GO. The reduction using ascorbic acid is efficient, without the need

for toxic substances [24]. However, the reduction process with ascorbic acid can be slower reaching 48 hours of reaction compared to the other agents, and is less efficient than that involving the use of hydrazine hydrate as hinted by the lower conductivity reached with rGO-VitC samples (**Table I.1**). Various literature studies investigated GO reduction using other chemical reducing agents such as hydrogen sulfide, sodium citrate, sugars … [25]. The aforementioned discussed examples were chosen as they were the most used and efficient ones.

Table I.1 List of the main reducing agents for graphene oxide towards chemically reduced graphene oxide

Agent	Conditions	Conductivity ($S.m^{-1}$)	C/O ratio	Ref
$NaBH_4$	80°C, 1h	82	4.8	[26]
	RT, 2h	45	8.6	[23]
Hydrazine hydrate	100°C, 24h	2420	10.3	[14]
	80°C, 12h	1700	11	[27]
Ascorbic acid	RT, 48h	800	-	[24]

2.2.2 Thermal reduction

Thermal reduction consists of heating GO to high temperatures surpassing 500°C (**Figure I.8**), usually in an inert atmosphere or under vacuum. The heating induces the decomposition and removal of the oxygen-containing functional groups, leading to the restoration/establishment of graphene conjugated network, thereby restoring rGO electrical and thermal properties [28] [29].

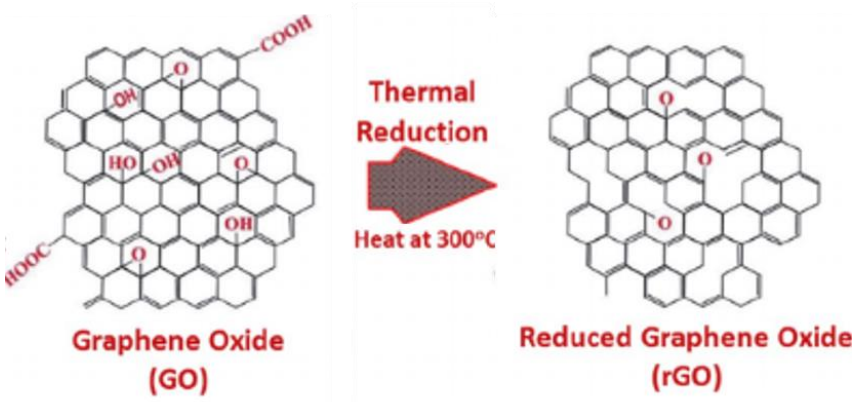

Figure I. 8 Representation of the rGO production process via thermal reduction of GO [30].

Chen *et al*. [31] showed that the thermal reduction of graphene oxide, achieved by vacuum-assisted thermal expansion at 250, 600, 800, and 1000 °C for 20 min, results in a decrease in the oxygen content from 27% to 3%, and in an increase in the C/O ratio from 2.5 to 33 as the annealing temperature is increased from 250 to 1000°C as shown by XPS.

Thermal reduction can produce rGO with better electrical conductivity (up to ~10^5 S/m) [32] than rGO reduced with hydrazine showing a better removal of the oxygen functional groups specially at high temperatures. However, this process requires high energy input and results in a higher level of defects in the graphene lattice due to the intense heat [33].

2.2.3 Electrochemical reduction

An alternative approach to the chemical and thermal GO reduction is the electrochemical reduction method. GO is reduced by applying an electric potential in a three electrodes setup with a calomel reference electrode, titanium mesh counter electrode, and glassy carbon working electrode immersed in a solution containing a suspension of GO and an electrolyte (0.5M $NaNO_3$ [34] 0.5M NaCl [35], 0.1M KCl [36]). The reduction process can be performed with cyclic voltammetry (CV) [37], or at a constant potential [38]. This technique allows for the rapid and clean reduction of GO without the need for chemical reducing agents. However, electrochemically reduced GO generally exhibits low electrical conductivity (around ~20 S/m [37]) due to its lower efficiency in removing the oxygen containing groups with a C/O ratio not exceeding 8. Additionally, the process can be complex requiring a careful control of the electrochemical conditions.

2.2.4 Hydrothermal reduction

Hydrothermal reduction is another efficient reduction method used to produce rGO. This process consists of exposing (GO) water dispersions to high pressure and temperature conditions, typically within an autoclave [39]. The hydrothermal process produces a 3D monolithic structure through the interconnection of graphene sheets (**Figure I.9 b)**. To preserve this 3D shape, the hydrothermal process is usually followed by a freeze-drying step (**Figure I.9 c**). The final material is called graphene aerogels (GA) (**Figure I.9 d**) [40].

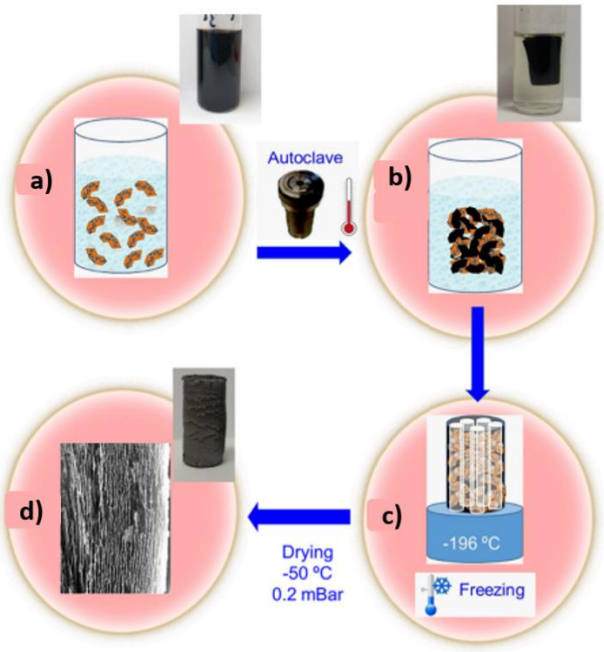

Figure I. 9 Steps for the hydrothermal reduction of GO: (a) dispersion of GO in water, (b) GA in water after the hydrothermal reduction process performed at 180°C for 6H, (c) frozen GA (d) final GA monolith after freeze-drying [40]

During the reduction process, the oxygen-containing functional groups on the GO sheets are removed, restoring the π-conjugated structure characteristic of graphene, and increasing the electrical conductivity of the material. However, the GA conductivity does not exceed 20 S/m with a reached C/O ratio of 7 [41], which is lower than that achieved by thermal reduction and reduction using reducing agents. These materials are lightweight and highly macroporous. It was observed that their conductivity is affected by their density, as the conductivity increases from 11.74 S/m to 704 S/m upon compression of the material ($\varepsilon \approx$ 80%) [42].

GA, compared to the other rGOs, present a higher porosity due to their 3D morphological network. This 3D macrostructure could be tuned trough controlling the synthesis parameters and the drying method [43]. M. A. Riaz *et al*. [44] hydrothermally synthesized GA (2h, 160°C) and freeze-dried it for 24h (**Figure I.10 a**). The SEM images (**Figure I.10 c-d**) show randomly oriented graphene sheets and an interconnected hierarchical multi scale porosity forming a 3D porous network with abundant voids.

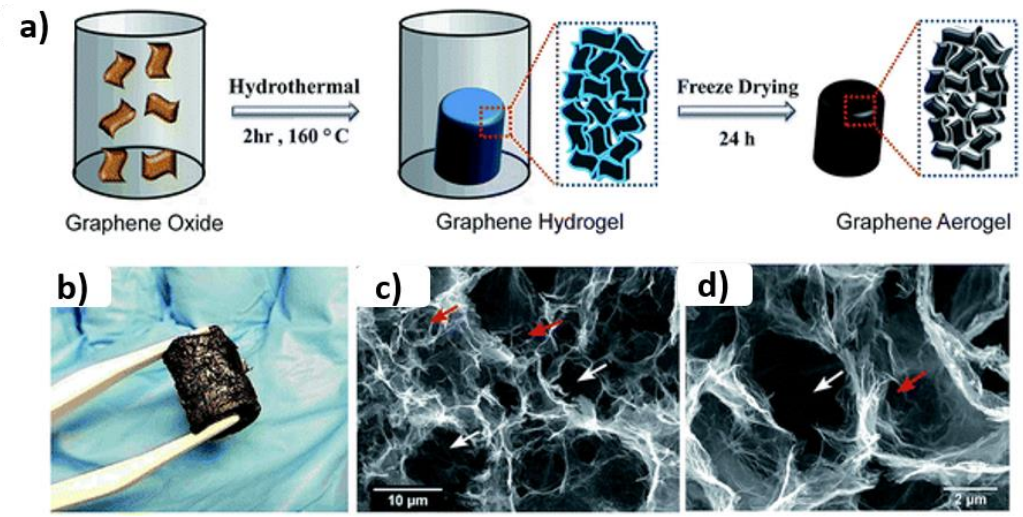

Figure I. 10 Graphene aerogel synthesis and its morphology. (a) Schematic showing the experimental steps and synthetic conditions using graphene oxide as the precursor, (b) sample optical image illustrating the foam-type structure of the GA and (c and d) SEM images of the GA [44]

It is noteworthy that hydrothermal process is not the only process yielding monolithic structures. The macrostructure of graphene aerogels can be tailored by carefully controlling the freezing process, which significantly influences the arrangement of graphene oxide sheets within the monolith. Indeed Qiu *et al*. [45] prepared GA by freeze casting of a graphene oxide (GO) dispersion trying to assemble graphene sheets into cork-like monoliths. The GO monolith was partially reduced using ascorbic acid, then the solution was frozen in a dry ice bath, followed by thawing. The sample was further reduced, freeze-dried again and finally annealed at 200°C. In such studies, SEM observations are essential to gain insights into graphene sheet arrangement within the monolith and its porosity. The SEM images (**Figure I.11 a,b,c**) show that the monolith exhibits a honeycomb-like cellular structure with the cell dimension in the order of tens of micrometers and the cell walls are slightly corrugated and well oriented in a nearly parallel manner. Using this synthesis method, they obtained a density value that varies from 0.0005 g/cm^3 (corresponding to a porosity of 99.98%) to 0.005 g/cm^3, showing the highly macro-porous structure of these materials.

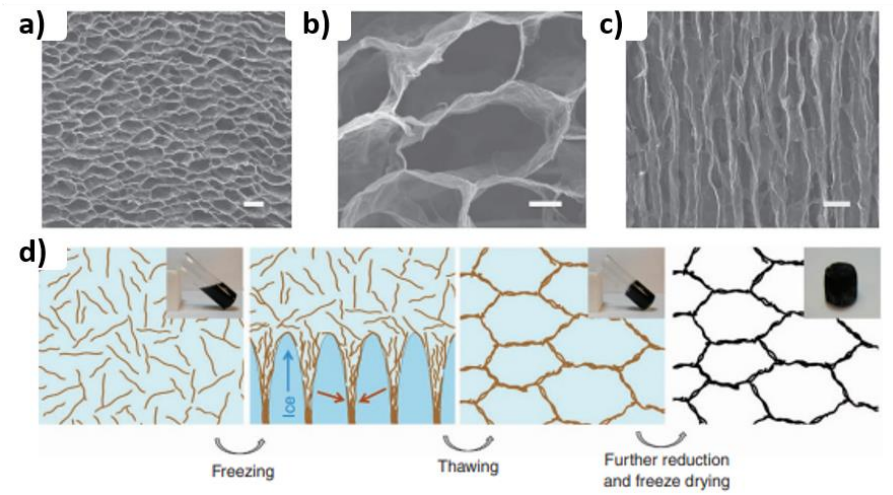

Figure I. 11 (a-c) SEM images at 3 different magnifications of the graphene monolith obtained from GO monolith subjected to combined ascorbic acid and thermal reductions . (d) Schematic representation of the formation mechanism of the cork-like monolith by freeze casting. [45]

Another example reported by Wang *et al* [46] shows the assembly of graphene oxide (GO) building blocks into a vertically and radially aligned structure obtained by a bidirectional freeze-casting approach. The GO dispersion was frozen in a copper container, with its bottom part immersed in liquid nitrogen (**Figure I.12 b**). Hence, when GO is poured into the container, it is subjected to two temperature gradients: one in the radial directions of the copper rod and the other along the Z-axis (**Figure I.12 c**), and hence the freezing progress in these two directions. The ice crystals were influenced by these two temperature gradients and at the end of the freezing step, the ice crystals within the copper mold were radially aligned. The ice was then removed by sublimations resulting in a radially aligned graphene aerogel.

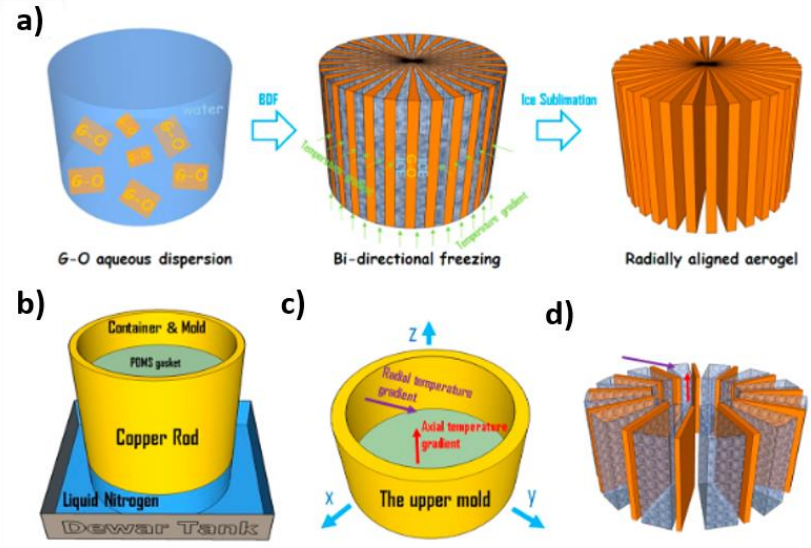

Figure I. 12 Illustration of a radiating graphene oxide aerogel fabricated by bidirectional freezing. (a) Scheme of the fabrication process. (b) Freezing setup. (c) Two temperature gradients induced by the upper copper mold. (d) Model of the ice crystals growing along radial directions [46]

The macrostructure of this GO aerogel was investigated using SEM. The obtained image of the cross section of the aerogel (**Figure I.12 a**) shows that the GO sheets are lamellar and ordered along radial directions, indicating that the ice crystals had lamellar shape during freezing. **Figure 13 c** shows that the distance between the lamellae decreases when closer to the center of the mold, because the crystals grow preferentially from the edge to the center of the copper container during freezing. As a result, the GO aerogel has a pore channel width that decreases from the edge to the center. The BET surface area was measured to be 45.9 m^2/g using N_2, with a pore size distribution varying from 1.7 to 5.6nm. After reduction, these assemblies preserve this 3D macrostructure and showed higher absorption capacities than traditional aerogels.

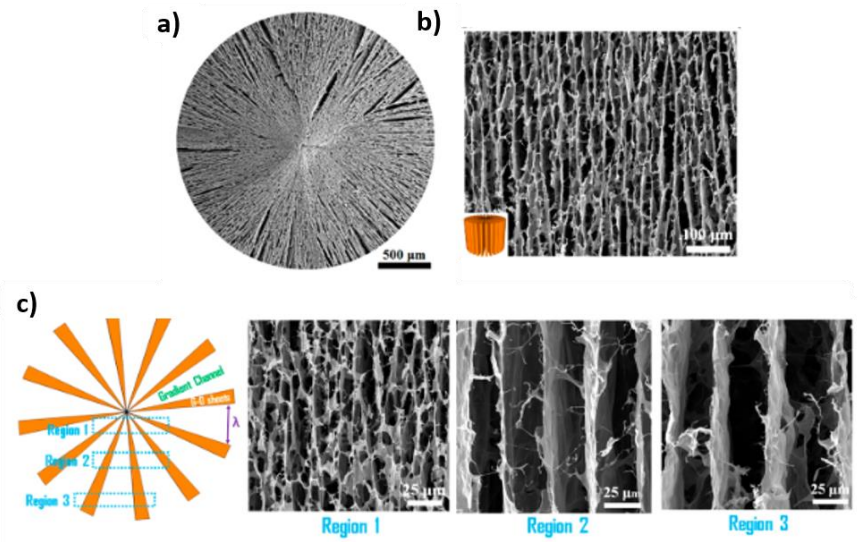

Figure I. 13 (a) Scanning electron microscopy (SEM) image showing a top view of a BDF G-O aerogel, (b) Side view of the aerogel, (c) Illustration showing the decreasing width of the channels [46]

The aforementioned reduction techniques yield rGOs with different reduction degrees and moderate to high electrical conductivities. Moreover, rGO has an intrinsically high surface area ranging from 500 to 800 m^2/g [47], which is beneficial for various applications such as energy storage, catalysis, and adsorption. However, the accessible surface area of rGO is often significantly lower than the theoretical value of graphene (2600 m^2/g). The origin of this limitation is the problem of restacking or agglomeration of rGO sheets, due to strong π-π interactions and van der Waals forces [48]. The restacking of rGO sheets results in the limitation of the access to both sides of single layer graphene; hence the number of active sites available for interaction with other substances (such as ions in energy storage applications) is also decreased and the diffusion of substances through the rGO structure is limited [49]. Strategies to prevent restacking of the graphene sheets have involved the introduction of spacers or pillars' between the rGO sheets, or functionalization of the rGO sheets to reduce the strength of the interlayer interactions [50]. These avenues are presented in the below sub-section.

2.3 Strategies to avoid the graphene sheets restacking

Pillared graphene materials represent a solution that aims to preserve the high surface area of individual graphene sheets through limiting the issue of restacking or aggregation of the graphene sheets. These materials have essentially a three-dimensional (3D) architecture, formed by inserting 'pillars' between individual layers of graphene, creating a more open structure and thus increasing the accessible surface area. The 'pillars' can be of various types, such as carbon nanotubes, fullerenes, nanoparticles, or organic molecules. In this part, examples

of pillared graphene materials will be presented, and the impact of the increased specific surface area and the creation of new pores will be discussed directly in connection with the intended purpose and the targeted application by the authors of the paper.

2.3.1 Carbon nanotubes CNTs

Carbon nanotubes (CNTs), with their hollow cylindrical structure, have emerged as promising candidates to be used as spacers between graphene sheets. Inserting CNTs between graphene sheets prevents restacking and increases the active surface area. For instance, hybrid materials constructed with vertically aligned CNTs sandwiched between graphene layers have demonstrated an increase in adsorption sites and enhanced electrolytic ions diffusion and showed improved specific capacitance and rate capability in hybrid supercapacitors [51].

The fabrication process of the 3D pillared CNT-graphene structures consisted of soaking a piece of highly ordered graphite in a mixture of sulfuric and nitric acids (3:1 volume ratio) (**Figure I.14 b**). This was followed by heating to 900°C under argon atmosphere. This resulted in the evaporation of the acid molecules trapped between the graphene layers, triggering a significant expansion along the graphite c-axis (**Figure I.14 b**). The thermally-expanded graphene was then exposed to heat within a tube furnace at a temperature ranging from 1000-1200°C under a flow of Ar and H_2 gases, passing through silicon tetrachloride ($SiCl_4$). This step created a SiO_2 layer that facilitated the CNTs growth. The SiO_2 layer is essential to achieve uniform CNT growth. Without it, the growth can be inhomogeneous due to issues arising from surface tension inconsistencies. In the final stage, the CNT-graphene 3D structure was created by decomposing FePc at temperatures between 800-1000°C in an Ar/H_2 environment. The resulting 3D CNT-graphene formations exhibited a notable increase in weight and underwent a substantial volume expansion compared to the initial graphite (**Figure I.14 c, d**).

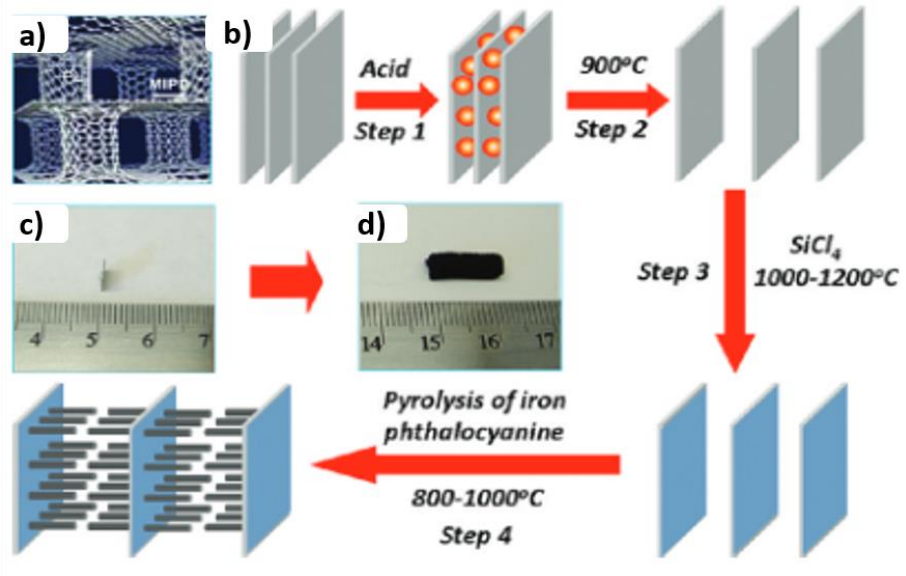

Figure I. 14 (a) Schematic diagram of a 3D pillared CNT-graphene nanostructure. (b) Schematic representation of the fabrication process of the 3D pillared CNT-graphene architectures. Optical images of (c) graphite (d) the thermally expanded graphene layers intercalated with CNTs [51]

The CNTs grew from both sides of adjacent graphene sheets as shown in the SEM images (**Figure I.15 a, b, c**). The XRD patterns of CNT-graphene with CNTs of lengths 5 and 10 µm show a shift of the (002) peak and the appearance of a broad band at $2\theta = 19°$. Such a band suggests the formation of regions with expanded stacking and disordered graphene sheets. When CNT pillars extending up to 20 µm are introduced within the graphitic structure, the 19° peak significantly increased compared to the sharp peak around 27°. This confirms the idea that longer CNT pillars tend to disrupt the stacked graphene layers, making them more disordered (**Figure I.15 f**). Compared to rGO, CNT-graphene electrode in Electrochemical Double Layer Capacitors (EDLC) exhibited approximatively similar specific capacitance around 110 F/g at 10 mV/s indicating that the porosity was not optimized using CNT as a spacer [51].

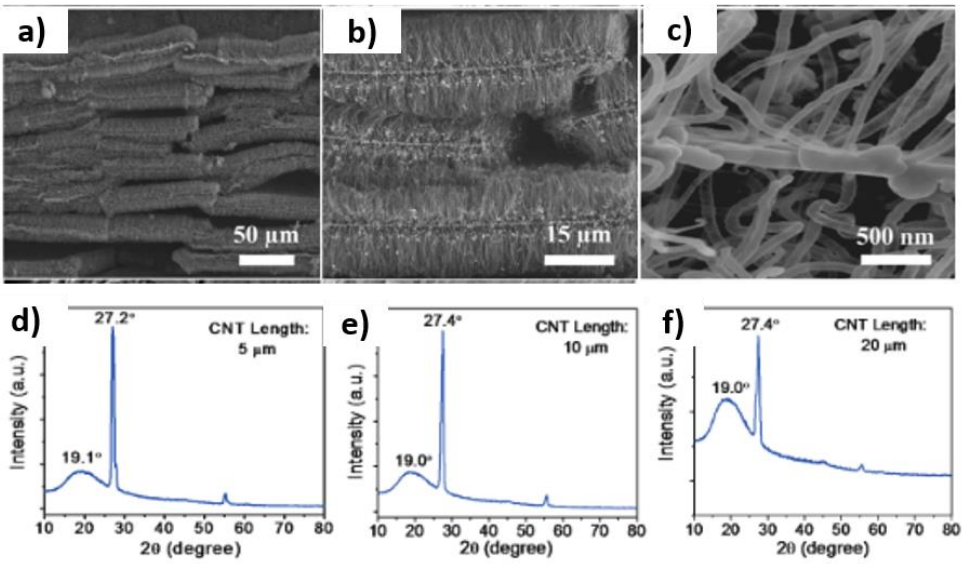

Figure I. 15 (a-c) SEM images of the 3D pillared CNT-graphene architectures under different magnifications. XRD patterns of CNT-graphene after being intercalated with CNTs of different nanotube lengths: (d) 5µm,(e) 10µm, and (f) 20µm [51]

2.3.2 Fullerenes

Fullerenes, which are carbon-based spherical structures, can be inserted between graphene layers, creating a steric hindrance that prevents restacking and increase the active surface area. Haraguchi *et al.* [52] studied the water vapor adsorption properties of different fullerenes pillared graphene (FPG) porous materials by modifying the fullerene content. Graphene was prepared via CVD and mixed with a dispersion of fullerene in toluene. The fullerene molecules were observed between graphene sheets using TEM observations (**Figure I.16 a**). XRD pattern (**Figure I.16 b**) of the FPG shows broad peaks at 20° and 25° corresponding to interlayer distances of 0.47 nm and 0.36 nm, corresponding to the spacing between graphene sheets with and without fullerene insertion, respectively. In addition, a peak below 5° is observed due to the expansion of the interlayer distances between graphene sheets confirming fullerene insertion between two graphene layers (**Figure I.16 c**). Graphene structures pillared with fullerenes revealed different water vapor adsorption capacities depending on the fullerene concentration. The porous graphene with approximately 25 ± 8% fullerenes showed the highest water vapor adsorption at 40% relative humidity (RH), showing an increase of the adsorption active porosity. In contrast, when the fullerene content was increased to 50%, there was a decrease in water vapor adsorption suggesting that an excess of fullerene molecules blocks the accessible porosity, which limit the water vapor adsorption.

Thus, for optimal adsorption capacity and uniform pore distribution, graphene with a fullerene content of 25 ± 8% was found to be the most effective.

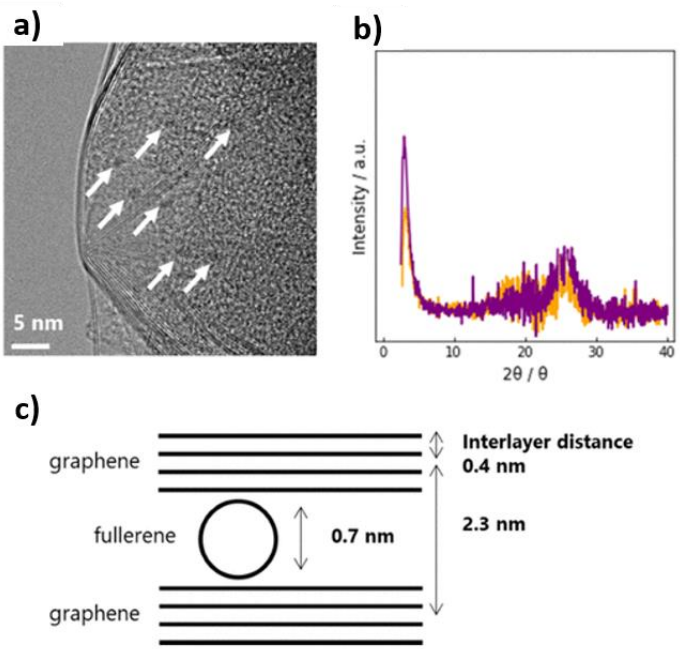

Figure I. 16 (a) TEM image of the FPG. Arrows indicated fullerene. (b) XRD patterns of the FPG. (c) Ideal model of the FPG structure [52].

2.3.3 Nanoparticles

Nanoparticles have also been used as pillars for graphene-based materials, inducing separation between graphene sheets and preventing their restacking. These nanostructured pillars typically consist of metal or metal oxide nanoparticles such as gold, silver, titanium dioxide, or iron oxide [47]. When introduced between graphene sheets, these nanoparticles separate the sheets, enabling the creation of architectures that increase the graphene specific surface area [53].

Compared to fullerenes, nanoparticles exhibit a broader spectrum in terms of size, morphology, and composition. While fullerenes offer predominantly carbon-based spherical structures, nanoparticles can range from spherical to rod-like or even more irregular shapes [54]. Such diversity facilitates the formulation of nanoparticle-pillared graphene materials for specific needs, from energy storage to catalysis, by selecting an appropriate nanoparticle type.

As revealed previously, CNTs, fullerenes, and nanoparticles can indeed provide effective interlayer spacing in graphene-based materials. However, the use of these materials as spacers to prevent graphene sheets from restacking has its limitations and challenges.

Achieving a uniform dispersion of nanoparticles and fullerenes throughout the graphene matrix can be complicated. Indeed, aggregation of these particles may occur, affecting their ability to serve as effective spacers [55]. Furthermore, CNTs as spacers for preventing graphene restacking can be expensive due to the complex preparation protocol involved. Moreover, the high density of CNTs within the graphene sheets may also have implications for porosity at this scale, potentially limiting its accessibility [56]. Beside these nanostructured pillars, another class of pillars exists: the organic pillars that will be less subjected to aggregation. These pillars have also been used to prepare pillared graphene materials that have been used for different applications such as hydrogen storage [57] and supercapacitors [58].

2.3.4 Organic molecules: alkyl diamines

Compared to the other pillaring techniques, chosen organic molecules can react with the oxygen groups present on the graphene oxide and establish covalent bonds with GO. Due to their diversity in structure and functionality, they have been widely studied as pillaring agents to tune the properties of pillared graphene structures [59]. Various synthetic pathways have been proposed in the literature for the synthesis of pillared graphene materials, including methods such as pillaring through diazonium grafting, amine reactivity, and silylation reactions. Herein, a specific emphasis is placed on alkyl diamines, and relevant examples from the literature are presented. Bo, S. *et al* [60] studied six different alkyl diamine pillars of different lengths and different functionalities on the alkyl chain (**Figure I.17**). The preparation of the materials involved a two-step hydrothermal synthesis starting from GO water dispersion. The first step, carried out at 90°C for 3 hours, was performed to establish the chemical covalent bond between GO and amines. This step was followed by a reduction reaction carried out at 180 °C for 12 hours to restore the sp^2 hybridized graphene structure.

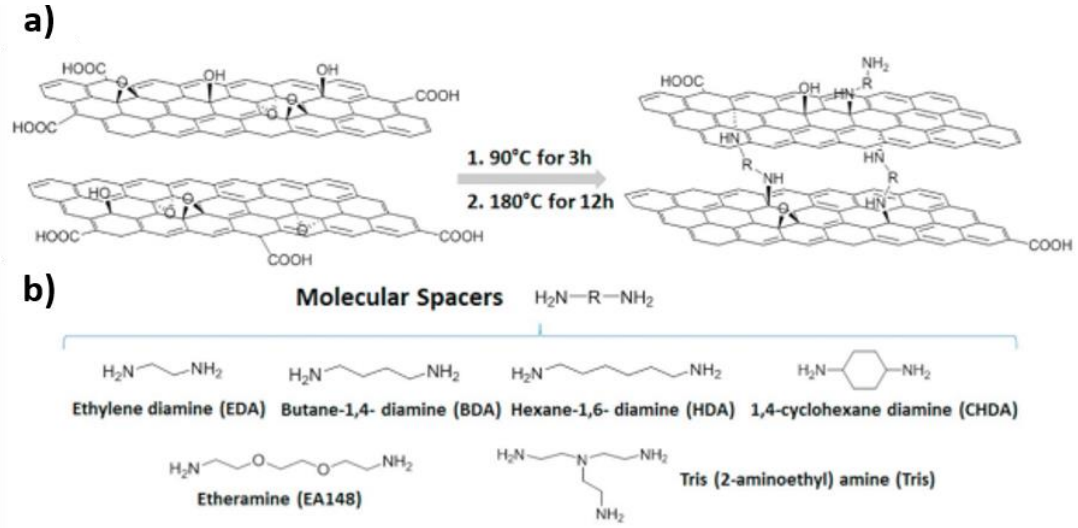

Figure I. 17 (a) Schematic illustration of the chemical reaction between GO and amines to produce amine/rGO composites. (b) Chemical structures of the six amine spacers showing different alkyl chain length and the different heteroatoms present in the chain [60]

In this study, the XRD patterns after the first reaction step (**Figure I.18 a**) showed a 2θ peak at 10.9° for the GO aerogel (GOA – without pillars), corresponding to an interlayer distance of 0.82 nm. After ethylenediamine (EDA) intercalation, the 2θ angle of EDA/GO shifted to 10° *i.e.* to a lower d-spacing. As the alkyl chain length increased, the 2θ angle shifted to 9.3° for BDA/GO and 8.4° for HDA/GO. CHDA mirrored HDA with a 2θ of 8.5° representing a d-spacing of 1.04 nm. For molecules (EA148 and Tris) with larger structures, the complicated molecular interactions could affect the interlayer spacing. For instance, EA148, characterized by its hydrophilic ether groups, is likely adopting a coiled or helical shape rather than a linear one [61]. As a result, the interlayer spacing of EA148/GO is not aligned with its chain length. Notably, Tris/GO exhibited the highest d-spacing at 1.22 nm, representing a 48.8% increase relative to GOA. After the reduction step, multiple free-standing amine/rGO films were prepared for supercapacitor testing. The XRD patterns (**Figure I.18 b**) displayed a distinct peak at 18° attributed to the PTFE binder. The reference sample rGO showed a broad peak at 24.8° (d=0.36 nm), attributed to the restacking of the graphene sheets. The diffractogramms of the diamine/rGO samples showed the appearance of new peaks below 11° indicating the increase in the graphene interlayer spacing resulting from the grafting of spacers with oriented molecular configuration. For these reduced samples, it was also observed that the interlayer spacing increased with increasing alkyl chain length. The peak near 2θ = 24° represents the partial rGO restacking in certain domains of the materials. The absence or low intensity of the peak in HDA/rGO and EA148/rGO suggests a more disordered functionalized graphene structure. **Figure I.18 c** summarizes the interlayer spacing values both before and

after GO reduction. The results show that EDA, BDA, HDA, and CHDA functionalized/pillared graphene samples exhibit minimal change in d-spacing during the reduction process, indicating the formation of a stable 3D graphene assembly. The slight decrease in d-spacing could be attributed to the intrinsic shrinkage of the graphene sheets driven by the intermolecular interactions and less electrostatic repulsions after partial removal of the oxygen containing functionalities. In addition, BET specific surface area (SSA) using N_2 gas (**Figure I.18 d**) showed that the SSA increased from 129 m^2 /g (rGO) to 327 m^2 /g (Tris/rGO) after amine-based spacers grafting. This study confirmed that the SSA increases by limiting rGO restacking after implementing organic pillars within the material. Furthermore, all pillared materials showed a higher specific capacitance by at least 50% than that of rGO in both aqueous and organic electrolytes in supercapacitors applications.

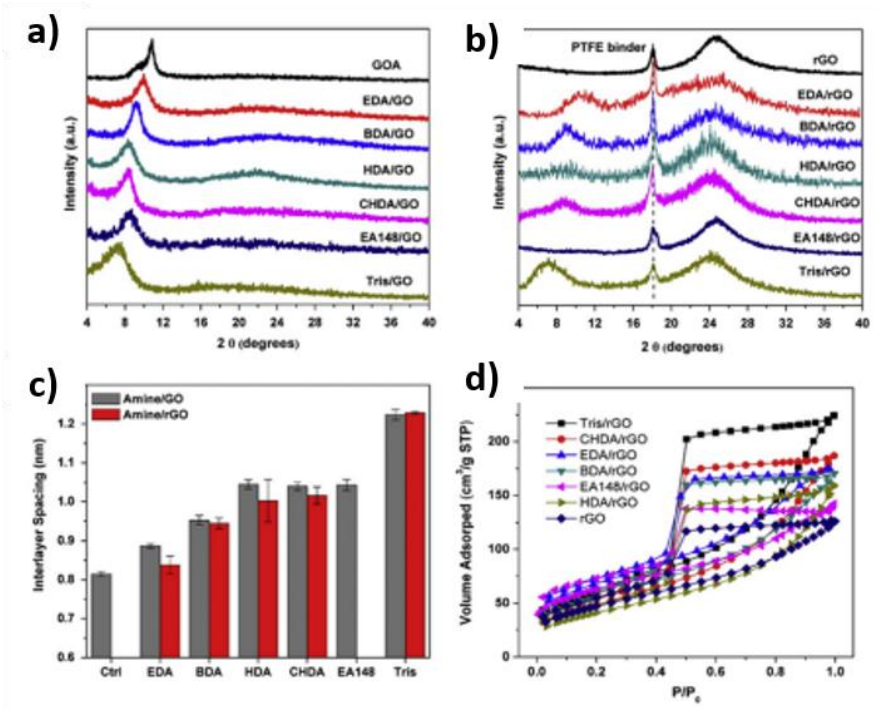

Figure I. 18 XRD spectra of (a) amine/GO and (b) amine/rGO composites; (c) comparison of d spacing values between amine/GO and amine/rGO composites (before and after the reduction); (d) nitrogen adsorption-desorption isotherms of the amine/rGO structures [60].

Another example of organic pillared graphene assemblies was reported by Banda, H. *et al.* [62]. The pillared graphene materials (RPs) were obtained following a two-step synthesis. The first step involved graphene functionalization/pillaring with different alkyl diamines displaying increasing alkyl chain length. The second step consisted in a reduction using hydrazine hydrate (**Figure I.19**). The aim of this work was to limit graphene restacking by increasing and locking the distance between graphene sheets.

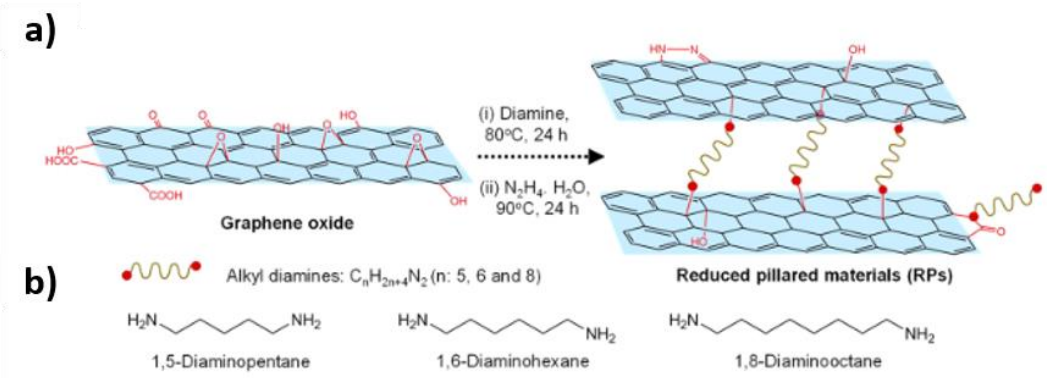

Figure I. 19 (a) Schematic representation for the Synthesis of RPs with (b) the formula of the alkyl diamines used in H. Band et al. work [62]

XRD results revealed the presence of rGO (002 peak at 28°), indicating that there is always a restacked graphitic portion as shown in **Figure I.20.** However, the diffractogramm also revealed the appearance of new peaks at low 2θ values, assigned to the cross-linking (CL) (pillaring). The d-spacing values were found to be 0.78 nm, 0.8 nm, and 0.86 nm for samples incorporating alkyl diamines of 5 carbons (5 RP), 6 carbons (6 RP), and 8 carbons (8 RP) respectively. This CL peak is absent in the non-pillared rGO, even when reduced with an identical reducing agent (hydrazine hydrate). This observation confirms that the CL peak originates from the insertion of diamines between the graphene layers. Moreover, the alignment of d-spacing values with the length of the pillars, coupled with the increased spacing for the longer aliphatic pillars, provides clear evidence of the successful pillaring. This study revealed an enhancement of the specific capacitance by 20% for the pillared samples compared to rGO in 1M $TEABF_4$ in acetonitrile electrolyte in supercapacitor cell. This finding highlights the creation of new adsorptions sites for ions adsorption by incorporating pillars and partially preventing rGO restacking.

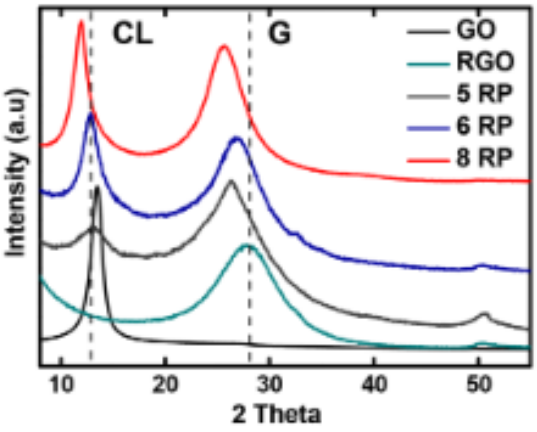

Figure I. 20 X-ray diffraction patterns of the different RPs, rGO, and GO [62]

Sections 2.2 and 2.3 respectively showed how it is possible to tune the physicochemical and structural properties of graphene-based materials, by adjusting the parameters of the reduction reaction (reaction time, temperature, reducing agent …), by modulating the GA drying conditions or by functionalization or implementation of a spacer to increase the accessible surface area. These graphene-based materials engineering steps enable their use in a wide range of fields, from electronics to energy storage. More specifically, in this PhD, the focus is placed on the use of chemically and structurally tuned graphene-based materials as electrodes for supercapacitors.

3 Graphene based materials for energy storage applications

Graphene-based materials have been extensively studied as electrode materials for supercapacitors due to their high electronic conductivity, large surface area, chemical stability, and tunable porosity by implementing functionalization or pillaring [6]. The first part of this sub-chapter focuses on giving details about what are supercapacitors, while the second part shows how graphene-based materials are beneficially used for this application.

3.1 Supercapacitors

Supercapacitors (SCs), also known as ultracapacitors or electrochemical capacitors (ECs), stand as a unique class of energy storage devices that bridge the gap between conventional capacitors and batteries (**Figure I.21**) [63].

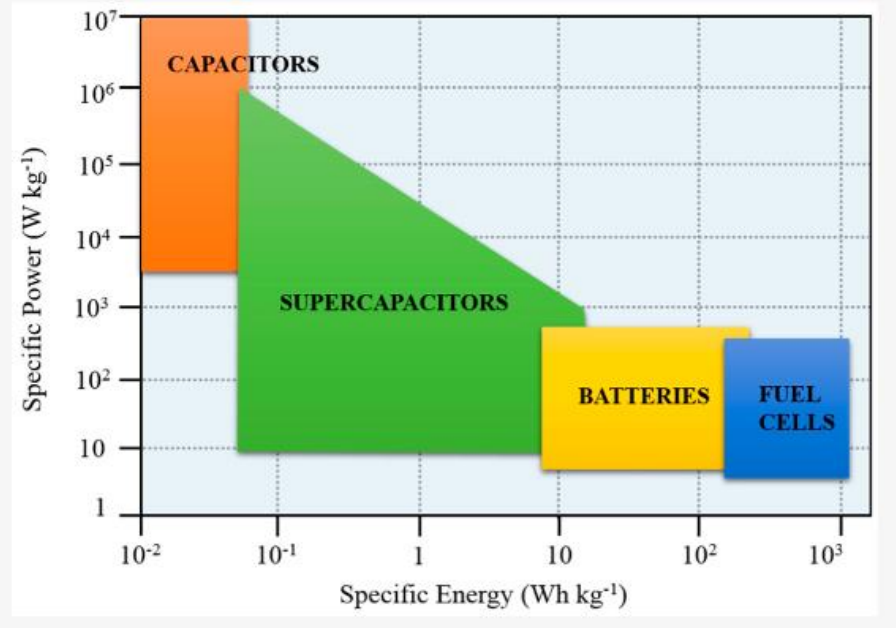

Figure I. 21 Specific power against specific energy, also called a Ragone plot, for various electrical energy storage devices [63]

When comparing batteries and SCs, batteries are known for their high energy densities but are often criticized for their limited life time, slower charging rates, and lower power densities. In contrast, SCs exhibit high power densities, rapid charging capabilities, and extended life time [64]. However, they face a drawback in terms of limited energy densities and higher costs per kWh compared to batteries. Despite the initial cost difference, the extended cycle life of SCs contributes to a lower price per kWh per cycle compared to batteries [65]. SCs consist of two porous and conductive electrodes with high surface areas (mainly carbonaceous materials), an electrolyte, current collectors, and a separator. When an external potential is applied to charge the SC, charges accumulate on the electrodes, initiating the diffusion and adsorption of electrolytic ions to neutralize these charges electrostatically. During discharge, the reverse process occurs, with electrons flowing into the external circuit and ions diffusing back into the bulk electrolyte. They store energy through the electrostatic separation of charges, a process that similar to conventional capacitors [66].

The difference in performances between batteries and SCs can be explained by their different electrochemical storage mechanisms. In batteries, a reversible redox reaction takes place at the cathode and anode during the charge–discharge phase. Although Li-ion batteries produce a high energy density and greater capacity due to the faradic nature of the charge storage, they display a lower power density and poor cycle life due to their slow storage processes. On the other hand, the performance of a supercapacitor depends on the specific

surface area and scale of porosity of its electrode, that will dictate the amount and kinetics of the electro-adsorption and desorption of charged ions from the electrolyte within the pores [67]. Supercapacitors (SCs) can provide high power densities in the range of 500–10000 W/kg. In addition, SCs are cost-effective, have a long cycle life (often exceeding 500000 cycles), and present a safer alternative compared to conventional batteries. Given these advantages, SCs are becoming increasingly popular in various fields, including consumer electronics, digital cameras, computers, security systems, regenerative braking, electric and hybrid vehicles, buses and trains [68]. A comparative analysis of capacitors, SCs, and batteries for the electrical energy storage is shown in **Table I.2**.

Table I.2 Comparative analysis of capacitors, supercapacitors, and batteries for the storage of electrical energy [69].

Properties	Capacitor	Super-Capacitor	Battery
Specific energy (Wh/kg)	<0.1	1–10	10–100
Specific power (W/kg)	10,000	500–10,000	<1000
Discharge time (s)	10^{-6} to 10^{-3}	S to min	0.3–3 h
Charge time (s)	10^{-6} to 10^{-3}	S to min	1–5 h
Coulombic efficiency (%)	About 100	85–98	70–85
Lifecycle (cycles)	Almost infinite	>500,000	~1000

Supercapacitors can be categorized into two types based on their energy storage mechanisms. The first category, known as Electrochemical Double Layer Capacitors (EDLCs), stores energy through the adsorption and desorption of electrolytic ions at the surface of porous carbon-based electrode materials. In this mechanism, there is no charge transfer occurring across the electrode-electrolyte interface (non-faradaic process) (**Figure I.22 a**). The second type, called pseudocapacitors, rely on both the electrochemical double-layer charge storage mechanism and additional faradaic processes. The faradic process is highly reversible in nature, occurs at or near the surface between the electrode materials, that are typically transition metal oxides, hydroxides, or conducting polymers like polyaniline and the electrolyte (**Figure I.22 b**). Such faradaic reactions might include redox reactions or battery-like intercalation/de-intercalation mechanisms (**Figure I.22 c**) [70].

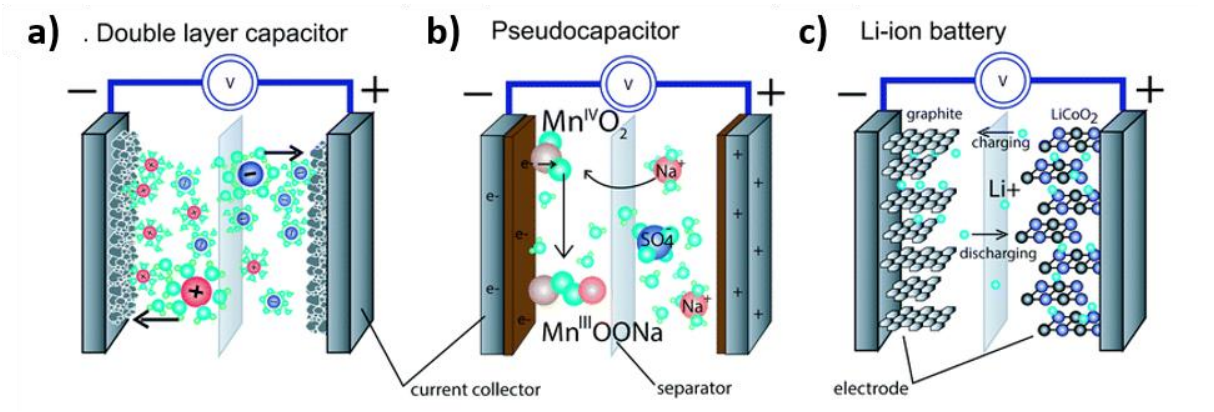

Figure I. 22 Basic schematics for an (a) all carbon EDLC (left), (b) a pseudocapacitor (MnO_2) and (c) a lithium ion battery [71]

The distinct charge storage mechanisms in these three different energy storage devices is manifested in each of their electrochemical signatures, as illustrated in **Figure I.23**. EDLC typically exhibit a characteristic rectangular shape in their Cyclic Voltammogram (CV). In turn, batteries display well-defined oxidation and reduction peaks, often with a substantial voltage separation attributed to phase changes. Classifying pseudocapacitors as supercapacitors pose a challenge due to their faradic charge storage nature involving rapid surface or near-surface redox reactions. Despite this, pseudocapacitors exhibit a notable EDLC contribution, differentiating them from batteries. Moreover, their redox reactions are highly reversible and fast, with minimal voltage separation between oxidation and reduction peaks. Importantly, the overall CV shape closely resembles the rectangular profile associated with EDLCs [72].

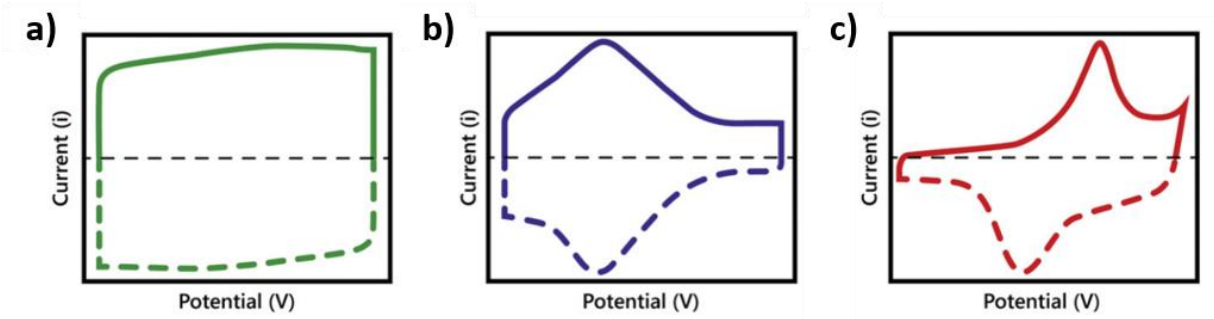

Figure I. 23 CV curves of (a) EDLC supercapacitor (b) Pseudocapacitance supercapacitor (d) battery [72]

3.2 The importance of electrode materials porosity in SCs

The EDLC capacitance (C) for a storage mechanism based on the adsorption/desorption of ions on the surface and the porosity of the polarized electrodes can be obtained by: [66]

$$C = \frac{\varepsilon_0 \varepsilon_r A}{d} \quad \text{(I. 1)}$$

Where ε_r, ε_0, d, and A represent the permittivity of the vacuum (in F/m), relative dielectric constant of the electrolyte solution (no unit), the distance of the electrolyte ions to the electrode surface (in m), and the ion-accessible surface area of the electrode material (in m^2), respectively.

Another critical performance parameter of SCs is the energy density (E), which can be calculated using: [73]

$$E = \frac{1}{2} C V^2 \quad \text{(I. 2)}$$

Where C and V are the capacitance (in F) and the applied voltage window (in V), respectively.

Based on **Equation (I.1),** we might expect a direct relationship between specific capacitance and specific surface area, suggesting that increasing the specific surface area of porous carbons could lead to an enhancement in specific capacity. However, experimental data have not established a straightforward relationship between specific capacitance and specific surface area. Increasing the specific surface area of porous carbons would not significantly enhance the specific capacitance value. Indeed it seems that increasing the specific surface area is not the only porosity related parameter that is at play when it comes to reaching higher capacitance. J. Gamby *et al.* showed that given an average EDL capacitance value of 20 $\mu F.cm^{-2}$ and a porous carbon with a specific surface area of 920 m^2/g, the expected theoretical specific capacitance should be up to 184 F/g. However, the real specific capacitance achieved in this case was only 80 F/g, indicating that only 44% of the specific surface area actually contributed to the capacitance [74]. So, this example highlights that accessibility of electrolytic ions to adsorption-active surface area is triggered by the wide scale porosity of the sample. Indeed, it was postulated that electro-adsorption takes place in the micropores, but meso and macropores (*i.e.* hierarchical pore size distribution) are also necessary for electrolytic ions to navigate and reach these adsorption sites. Hence, the pore structure properties (pore size, their distribution, shape, and accessibility) present crucial parameters that influence the capacitance of porous carbons. This porous structure controls the movement and transfer of ions, which in turn significantly affects both the capacitance and rate capabilities of the material. Additionally, the relationship between ions and pore size has been investigated. Chmiola *et al.* [75] reported an

anomalous increase in capacitance for carbide-derived carbons (CDCs) when the pore size was less than 1 nm (**Figure I.24**). Indeed, as the pore size decreased, there was a drop in the electrochemical double layer (EDL) capacitance. Interestingly, when the pore size was further reduced to match the size of the desolvated ions, a significant increase in capacitance was observed. This was associated with the proximity between ions and pore walls leading to very tiny charge separation distance d (see **Equation (I.1)**).

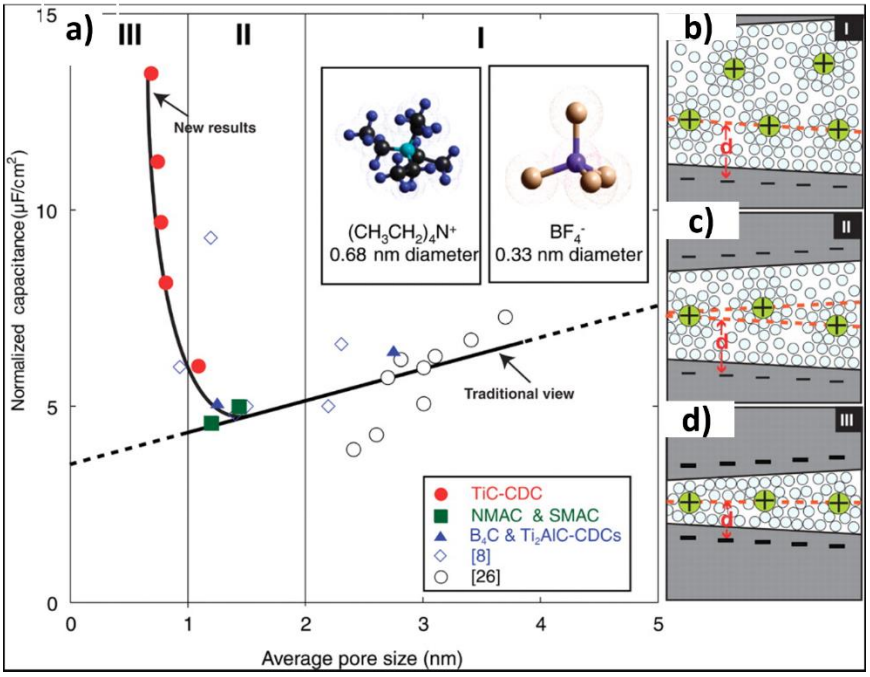

Figure I. 24 (a) Correlations between normalized capacitance and average pore size in an electrolyte containing 1.5 M TEABF$_4$ dissolved in ACN. Zone I represent the condition leading to CSP decrease with SSA/pore size decrease. Zone III represents the conditions when pore size matches ion diameter and CSP increases; while zone II represents the threshold conditions. Schematic representation of solvated ions residing in pores with varying sizes (b) >2 nm, (c) 1 ─2 nm, and (d) <1nm and showing the evolution of the charge-compensation distance d [75]

Raymundo-Pinero *et al*. [76] found comparable results with microporous carbon in both aqueous and non-aqueous solutions. This enhancement in EDLC capacitance for pores smaller than 1 nm broke the conventional understanding of electrolyte ion adsorption and EDL formation within porous carbons [77].

For supercapacitors that rely on ion diffusion for operation, different pores types should be at least interconnected with each other and be accessible for ions. This interconnection between pores of different sizes is called hierarchical porosity. **Figure I.25** illustrates a typical ion diffusion path in a hierarchical porous structure: ions enter first the largest pores (macropores > 50 nm) that serves as reservoir for electrolytic ions, and then flow into smaller ones (2 nm < mesopores < 50 nm) that are subdivided from the larger pores. This

pattern continues until the ions reach the smallest pores (micropores < 2 nm) where the final adsorption occurs [78]. As a consequence, hierarchical porous carbons, characterized by their multi-scale pores structure connectivity, have demonstrated superior performance in SCs applications compared to traditional carbon materials [79, 80]. Several hierarchical carbon-based materials have revealed exceptional gravimetric capacitance, surpassing 300 F/g. The hierarchical structure, which incorporates a range of pore sizes, contributes to enhanced electrochemical performance, showing the importance of the pore structure in SCs storage mechanism [81 - 83].

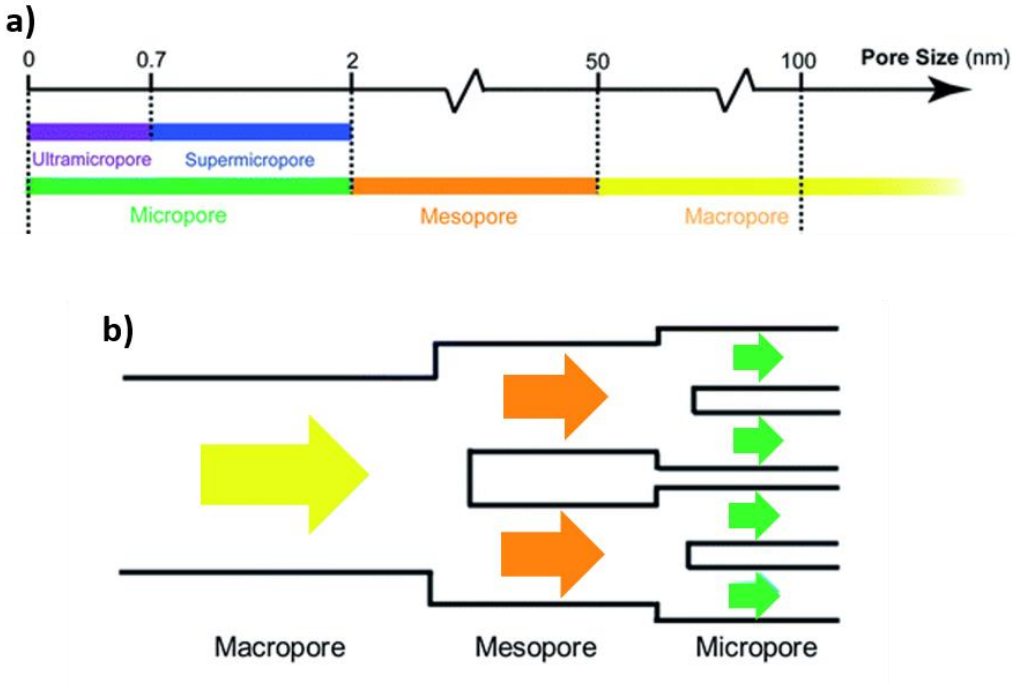

Figure I. 25 (a) Classification of pores based on pore width (b) Schematic illustration of an ion diffusion pattern in a typical hierarchical porous structure [78]

As a result, more and more attention has been paid to the study of the sub-nanometer hierarchically porous carbon. For example, graphene-based materials are specifically being considered for their hierarchical pore distribution and the possibility to tune their structure (functionalization/pillaring) to match the pores size to ions size [62].

3.3 Graphene-based materials in SCs

Graphene-based materials have been extensively studied as material electrodes for supercapacitors because of their attractive physicochemical properties (high electronic conductivity, large surface area, mechanical flexibility, and chemical stability), and their hierarchical pore distribution providing enhanced ion accessibility [84]. Furthermore, the

ability to enhance these properties by introducing functionalization or pillaring further favors its suitability compared to other carbonaceous materials. Moreover, the versatility of graphene allows for its combination with other materials like metal oxides, polymers or conductive nanoparticles improving the specific capacitance and cycling stability. For instance, hybrid structures of graphene with MnO_2 or CoO_2 have demonstrated improved electrochemical performance, by combining the high surface area of graphene with the pseudocapacitive properties of the metal oxides [85]. In addition, the functionalization or doping of graphene with heteroatoms (for example nitrogen) can modify its physicochemical properties, further boosting its capacitive performance [86].

Stoller, M. *et al.* [87] studied the electrochemical performances of rGO prepared from the hydrazine hydrate reduction of graphene oxide (GO). This rGO exhibited a specific capacitance of 99 F/g and 82 F/g at a current density of 0.01 A/g and a scan rate of 20 mV/s, in 1 M $TEABF_4$ in acetonitrile (AN) and 1 M $TEABF_4$ in propylene carbonate (PC), respectively. These electrochemical performances are comparable to those of activated carbon (100-120 F/g in 1.5M $TEABF_4$ in AN) [77]. However, the exposed surface area of rGO to the electrolyte was limited due to the restacking of the graphene sheets during its reduction (**Figure I.26 a, b**) suggesting that if the entire surface area of the graphene was accessible to electrolyte ions, there could be a significant improvement in capacitance performance.

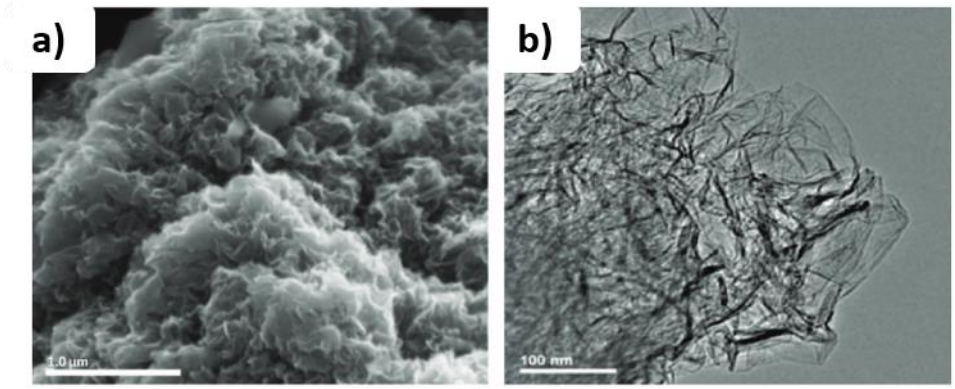

Figure I. 26 (a) SEM image of rGO (b) TEM image showing individual graphene sheets [87]

In another example Shi *et al.* [88] synthesized graphene aerogels via a hydrothermal method followed by a freeze-drying step. The capacitance values reached were as high as 175 F/g in a 5M KOH aqueous electrolyte and at a scan rate of 10 mV/s, showing an increase of about 60% compared to rGO reduced with hydrazine hydrate. This increase in the capacitance was attributed to the macroporous 3D network structure of the graphene aerogels (**Figure I.27**).

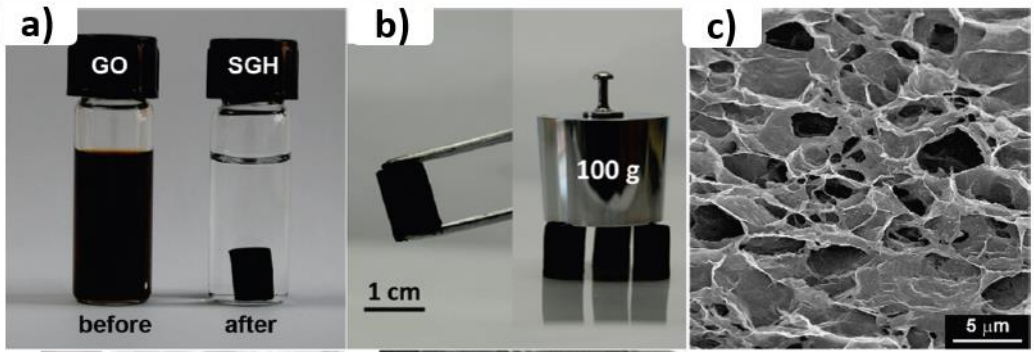

Figure I. 27 Pictures of a GO aqueous dispersion before and after hydrothermal reduction at 180 °C for 12 h; (b) Pictures of how mechanically strong the GA obtained was, enabling easy handling and supporting weight; (c) SEM image of the GA [88]

Pillared reduced graphene powder (6RP) and pillared graphene hydrogel (6GH) were studied by Banda *et al.* [89] using 1,6-diaminohexane as organic pillars reacting with GO. In the case of 6RP, the functionalization was followed by a reduction step using hydrazine hydrate, and in the case of 6GH, the two steps were carried out simultaneously in a hydrothermal process (**Figure I.28**).

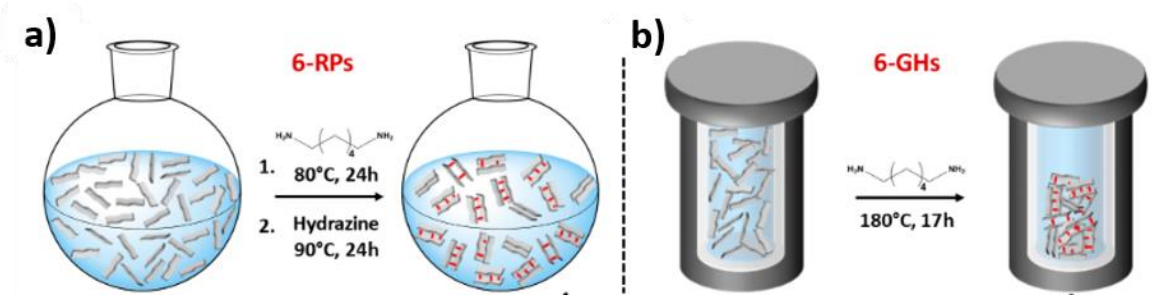

Figure I. 28 (a) 6-RPs are synthesized in two-step process: cross-linking and reduction (b) 6-GHs are synthesized in a one-step process in an auto-clave [89].

Different pillars densities have been investigated in an attempt to optimize the electrochemical performance of these materials. XRD shows the successful pillaring by the presence of two distinct diffraction peaks around 25−27° and 11−13°. The peaks at higher angles correspond to graphite stacking and indicate a degree of reduction close to that of rGO. The peaks below 20°, corresponding to diamine intercalation and cross-linking (CL) within the graphene sheets, shifts to smaller angles (higher d-spacing) when increasing the amount of pillars used (**Figure I.29**). The optimized 6GH and 6RP reveal a capacitance of 230 F/g and 205 F/g, respectively, at a scan rate of 10 mV/s in 1 M $TEABF_4$ in AN. The higher values for 6GH were mainly attributed to better ion accessibility and less restacking due to the

macroporous 3D structure. Both pillared materials show a remarkable improvement over rGO, which has a capacitance of 100 F/g, proving once again the successful pillaring strategy.

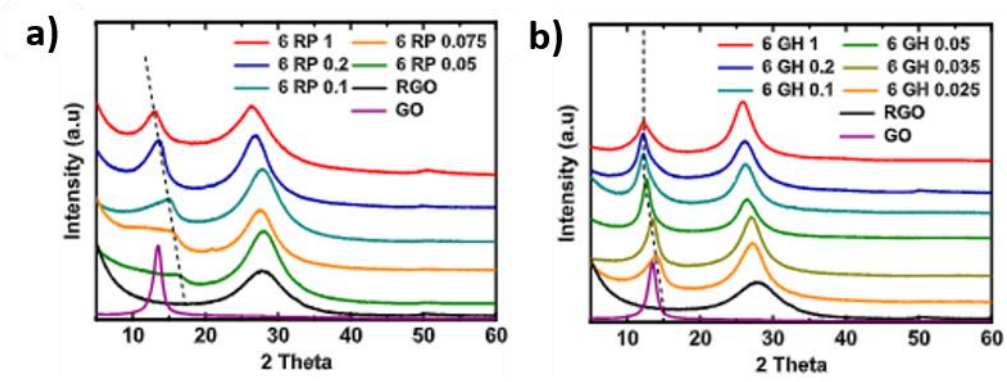

Figure I. 29 XRD patterns with various pillars amount of (a) 6-RP (b) 6-GH.

In the course of related electrochemical studies, ion-sieving behavior was observed in these graphene-derived materials [62]. CV was performed on four different graphene materials: rGO (without pillar), and three pillared graphene materials (nRP) with n=5, 6 and 8 corresponding to the number of carbons in the alkyl chain. The pillars created an interlayer distance of 0.78 nm, 0.8 nm and 0.86 nm respectively. Different cations with various sizes were tested (**Figure I.30 b**). A clear dependence between the d-spacing of the interlayer galleries and the electrolytic ion sizes was observed. Ions with sizes smaller than d-spacing can get access to the newly created pores, also called graphene galleries, whereas larger ions cannot access the surface area inside the galleries (**Figure I.30 a**). This study highlights that larger ions experience less adsorption within the porosity formed by pillaring (galleries).

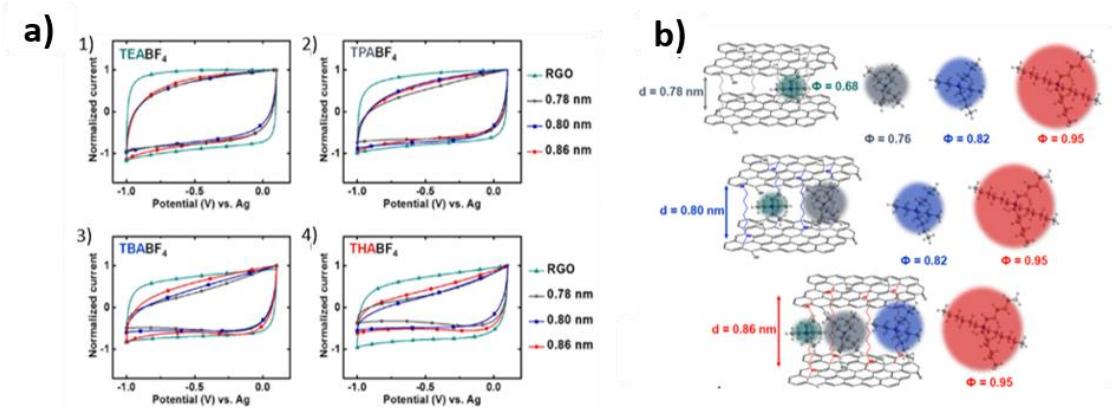

Figure I. 30 (a) Normalized CVs of RGO and RPs obtained at a scan rate of 20 mV/s in the voltage range of 0.1 to −1.0 V vs Ag using 1 M solutions of (1) $TEABF_4$ (Φ = 0.68 nm), (2) $TPABF_4$ (Φ = 0.76 nm), (3) $TBABF_4$ (Φ = 0.82 nm), and (4) $THABF_4$ (Φ = 0.95 nm) in acetonitrile as electrolytes.(b) Ions of different sizes are sieved based on the sizes of the graphene interlayer galleries (0.78 nm for 5 RP, 0.8 nm for 6 RP and 0.86 nm for 8 RP), resulting from using pillars of different sizes [62].

Therefore, in the course of the previous work, a combination of electrochemical and ex-situ solid-state NMR (ssNMR) studies were conducted on a ^{15}N pillared graphene material with a d-spacing of 0.78 nm to assess the proximity of the cations of different sizes to the nitrogen within the pillars [90]. **Figure I.31 a** shows a lower current on the CV curves under negative potential when larger electrolytic cations (tetraoctyl phosphonium TOP^+ and tetrabutyl phosphonium TBP^+) were used, indicating less adsorption of these cations in the material's porosity. When small tetraethyl phosphonium TEP^+ was used, the CV was quasi-rectangular showing optimum adsorption at the material surface. These CVs are indirect proof that provide insights on the amount of adsorbed electrolytic ions at the electrode material surface. **Figure I.31 b-d** reveal the double-polarization transfer (H→N→P) ssNMR spectra of three different electrodes polarized at -1.3V in the three electrolytes. When the pillared material is polarized at -1.3V vs Ag in $TEP^+BF_4^-$/ACN or $TBP^+BF_4^-$/ACN, clear ^{31}P signals originating from the adsorbed cations interacting with the ^{15}N of the pillar are observed (**Figure I.31 c, d**), revealing proximity between these cations and nitrogen atoms in the pillars. However, when the polarization occurred in the presence of $TOP^+BF_4^-$/ACN, no signal was observed for the ^{31}P (**Figure I.31 b**) suggesting the absence of TOP^+ ions in proximity to nitrogen from the pillars in the electrode; thus the large TOP^+ ions were not adsorbed within the pillared graphene galleries. This study confirms the non-adsorption within the galleries of large ions when their diameter is higher than the d-spacing of the pillared graphene.

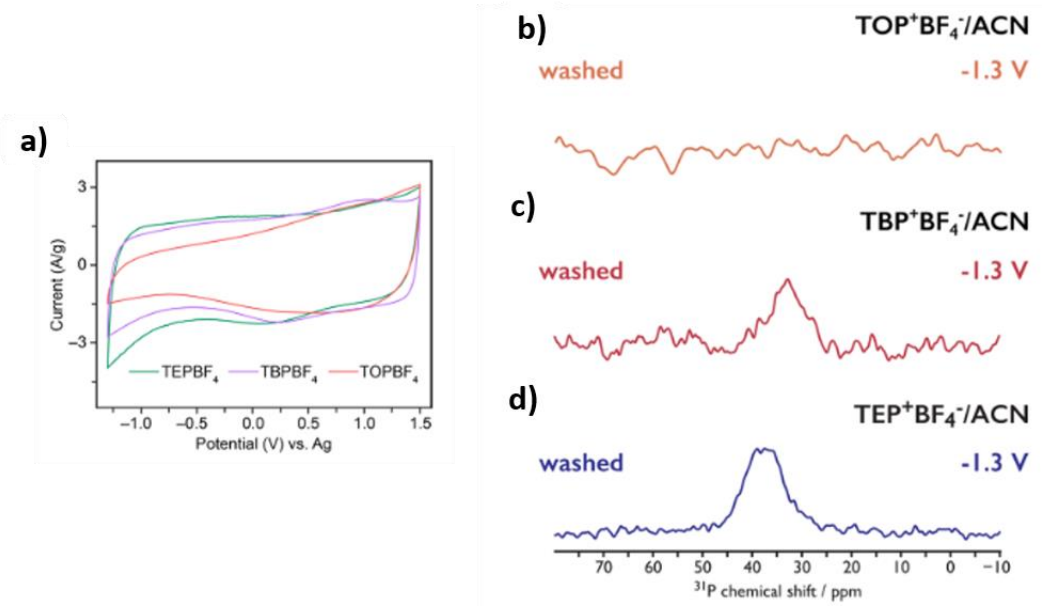

Figure I. 31 (a) CV curves of 6-GH in $TEPBF_4$, $TBPBF_4$, and $TOPBF_4$ / acetonitrile (AN) 1 M electrolytes recorded at 20mV/s. (b-d) 1D LT CPMAS {^{15}N-} ^{31}P zf-TEDOR NMR spectra of 6GH electrodes after negative polarization and various electrolytes (TOP^+(a),TBP^+(b), and TEP^+(c) with BF_4^-/AN), recorded using a total of 7 ms of TEDOR recoupling [90]

Despite the insights gained from electrochemical and *ex-situ* ssNMR measurements, it is essential to recognize their indirect nature in probing the adsorbed ions. Direct characterization methods, notably *in-situ/operando* measurements, are essential to understand the adsorption mechanisms in supercapacitors. Indeed, Clare P. Grey *et al.* [91] employed a combination of *in-situ* ssNMR characterizations and molecular dynamics simulations to investigate the charge storage mechanism during the charging process of supercapacitors using a carbon electrode and 1.5M $TEABF_4$ organic electrolyte. Their findings revealed substantial ion adsorption into the carbon pores even without an externally applied voltage. The charging process involved three possible mechanisms: adsorption of oppositely charged ions, desorption of similarly charged ions, and ion exchange. These mechanisms operated simultaneously during charging. Additionally, they introduced the charging mechanism parameter, denoted as X(V, V_0) that provides insights on the amount of adsorbed ions within the micropores at the applied potential, to quantitatively compare the various energy storage mechanisms. This parameter is defined as:

$$X(V,V_0) = \frac{\mathrm{N(V)} - N(V_0)}{\left(N_{counter}\ (V) - N_{co}\ (V)\right) - \left(N_{counter}\ (V_0) - N_{co}\ (V_0)\right)} = \frac{\mathrm{N(V)} - N(V_0)}{(|Q_{ionic}(\mathrm{V}) - Q_{ionic}(V_0)|)/e} \quad (I.3)$$

Where N(V) is the total number of in-pore ions at a charging voltage V, $N(V_0)$ is the total number of in-pore ions at the initial voltage V_0 (typically 0V or OCV), and $N_{counter}(V)$ and $N_{co}(V)$ are the number of in-pore counter-ions and co-ions, respectively, at a voltage V. $Q_{ionic}(V)$ and $Q_{ionic}(V_0)$ are then the net in-pore ionic charges at the two voltages, and e is the elementary charge.

As illustrated in **Figure I.32**, the charging mechanism parameter X serves as a quantitative measure where X=+1 indicates the adsorption of ions with a charge opposite to the applied potential, X=0 denotes ion exchange, and X=−1 implies the desorption of ions with the same charge as the applied one. Intermediate values, such as $0<X<1$ or $-1<X<0$, suggest the coexistence of two energy storage mechanisms. For instance, X=0.7 indicates a charging process characterized by a predominant mechanism involving the adsorption of ions with the opposite sign to the applied potential, alongside with a smaller contribution of the ion exchange mechanisms. It is important to acknowledge that in the context of initially empty pores, the charging process must start with counter-ion adsorption (X=1), as there are no co-ions within

the pores available for desorption. In scenarios involving empty pores, charging could further favor the ion pairs adsorption into the empty carbon pores. Consequently, in these unique cases, the parameter X can take values greater than 1.

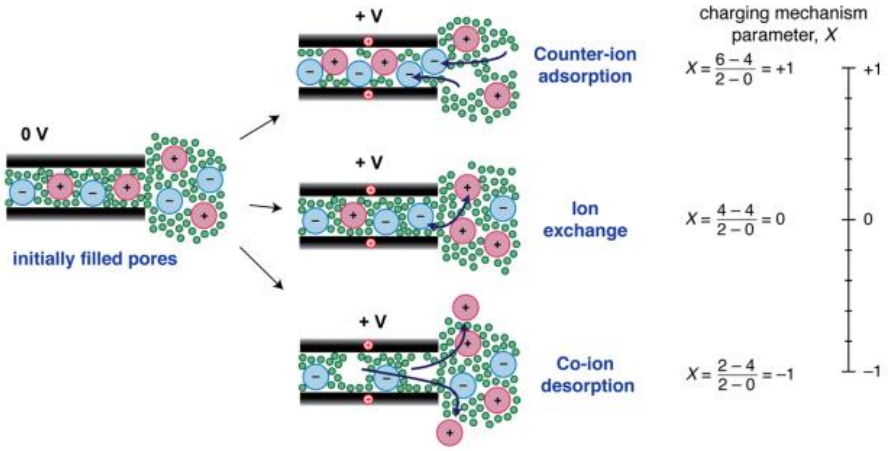

Figure I. 32 The different possible charging mechanisms for carbon pores that are initially filled with electrolyte: counter-ion adsorption, ion exchange, and co-ion desorption. [91]

These aforementioned models provide valuable insights; however, they may not fully capture the complexity of the pore structure or the oxygen groups that are present on the surface of the porous carbon electrode. These models primarily focus on electrostatic capacitance, neglecting Faradaic capacitance. Numerous questions persist regarding the reality of the device charging process such as the distribution of ions under a certain potential in the pores of different scales as they could be immobilized at another porosity level even before reaching micropores, leading to an incomplete representation of the energy storage mechanism in supercapacitors. Consequently, there is still a need for a comprehensive investigation into the charge storage mechanism within the multi-scale pore structure of carbonaceous materials. This underscores the importance of employing advanced techniques, notably techniques that enable probing the mesoscale such as small angle X-ray/neutrons scattering (SAXS/SANS) to precisely investigate the localization of ions within the diverse scales of porosity. This will help in providing additional insights that could be used to understand the adsorption/desorption mechanisms in SCs.

As evoked earlier, in this PhD, the focus is placed on the chemically and structurally tuned graphene-based materials. The ability to tune the structure and properties of graphene-based materials is one of the keys to their versatile applications in diverse fields such as electronics [92 - 95], energy storage [96, 97] and catalysis [98 - 100]. The characterization of these graphene-based materials is crucial for understanding their properties and performance in

these various applications. As shown previously in **Section 2.3**, the local microscale was extensively addressed either for rGO or for pillared graphene materials. XRD was used to reveal the restacking of graphene sheet after GO reduction and the evidence of pillaring for pillared samples. TEM was also used to investigate the micro scale morphology of graphene-based materials. Finally, ssNMR was performed, giving evidence of the adsorption of ions within the galleries in SCs applications. In SCs the structure and porosity of graphene-based materials are crucial factors in determining their electrochemical performances [101]. The specific capacitance, energy density, and power density of a supercapacitor are highly dependent on the structural characteristics of the electrode materials. Firstly, the porosity of graphene-based materials is critical because it directly impacts the available surface area for the storage mechanisms. High porosity, particularly in the form of interconnected pores (hierarchical porous structure), enhances the ions diffusion as well as their adsorption on the active sites, which contribute to increasing the capacitance. However, the pore size distribution should be optimized to strike a balance between maximizing surface area and ensuring efficient ion transport. In general, smaller pores increase the surface area, while larger pores facilitate rapid ion diffusion [102]. Secondly, the structural characteristics of graphene-based materials, including stacked-layer thickness, interlayer spacing, and degree of disorder, significantly influence their electrochemical performance. As it was shown in the previous (**Section 2.4.3**), properly engineered interlayer spacing allows reduced restacking of graphene layers, leading to enhanced ion adsorption and diffusion, thereby improving charge storage capacity. [103] Moreover, the introduction of defects or functional groups can create additional active sites for pseudocapacitive reactions, further boosting the specific capacitance [104]. However, and to the best of our knowledge, the multi-scale comprehensive characterization of graphene-based materials has not been addressed yet in the literature, particularly in terms of their mesostructural and morphological properties. To address this issue and for a better understanding of these materials, their structural characterization should be completed by unveiling their mesoscale structural features, which play a noticeable role in SCs applications [105]. Therefore, the aim of this PhD work is to better understand the multi scale structure and porosity of these materials and to reveal their behaviour in real time SCs testing. The underlying objective of such work is to get insights into the adsorption/desorption mechanisms within the whole sample porosity scales in order to open new avenues, enabling the optimization of their design to achieve better electrochemical performances. To help reach this objective, it is necessary to correlate the outputs from different characterization techniques that enable probing

different scales. More specifically, it is necessary to unveil these graphene-based samples mesoscale structural features. To study this scale, scattering techniques are quite well adapted but have not been used so much to specifically study such type of materials. The next section of this chapter will describe how these techniques bridge the mesoscale gap in structural characterizations and how they are valuable to complement the multi-scale structure and porosity characterizations.

4 Multi-scale structure and porosity characterization

The multi-scale structure and porosity characterization studies we intend to conduct in this PhD work will enable to uncover the structure-performance relationships. Addressing this link is essential for optimizing the design and tailoring of graphene-based materials for SCs and advancing the fundamental research of graphene.

Figure I.33 gathers the different structural/morphological (XRD, SAXS, SANS, SEM, and TEM) and porosity (gas adsorption) characterization techniques with their probed scales [106]. SEM delivers topographic images at a resolution ranging from the meso to macroscale (>10 nm), providing visual observations of the morphology, the surface features, and macroporosity of the material. On the other hand, XRD allows probing the crystalline nature of materials, providing insight into lattice parameters, phase identification, crystal size, and interlayer spacing. Gas adsorption, particularly the BET method, is used to quantify the surface area, porosity of materials, and pore size distribution giving insight into their capacity for adsorption and storage. However, the morphology and the internal structure of the micro/mesoscale (ranging from 1 to 200 nm) is not accessible using these techniques. TEM, small-angle X-ray scattering (SAXS) and small-angle neutron scattering (SANS) are highly valuable techniques for their capabilities in structural characterization at these microscale and mesoscale. One of the primary advantages of SAXS and SANS is their non-destructive nature, allowing for in-depth probing of materials without causing any damage. In addition, addressing the porosity, they provide access to materials closed and open porosity in contrast to gas adsorption techniques [107]. SAXS/SANS may also provide insight into pore size distribution, the morphology of materials such as characteristic object shapes and sizes [108], solid density and yield real-space information about the hierarchical structures in complex systems like polymers and graphene-based materials [109]. Unlike many other characterization methods, SAXS and SANS are versatile enough to be applied to samples in various states – whether solid

or liquid. They are also suitable for a wide range of environmental conditions, enabling *in-situ* and *operando* studies [110].

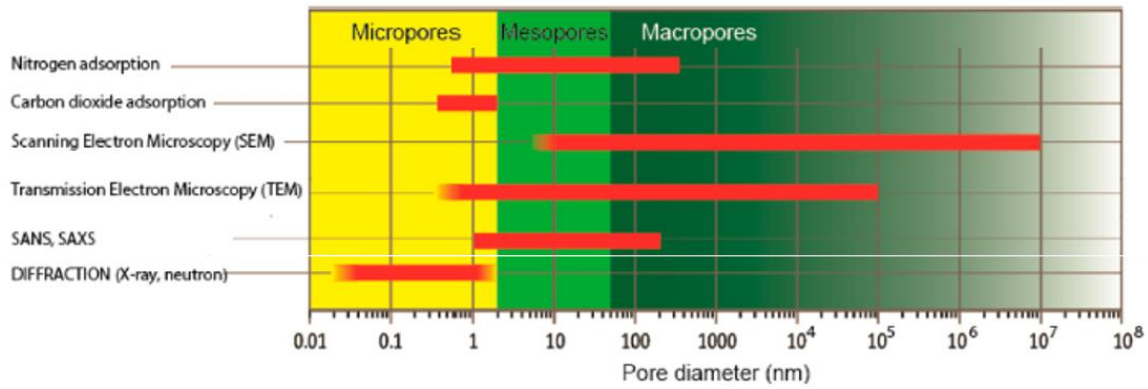

Figure I. 33 Comparison of the ranges of pore sizes that can be probed using various types of gas adsorption methods, optical microscopy, electron microscopy, neutron and X-ray scattering. [106]

The main differences between SAXS and SANS are summarized in **Table I.3**. While SAXS leverages the difference in electron densities, SANS relies on the variations in nuclear scattering lengths. The unique sensitivity of neutrons to light elements and the isotopes of elements is their greatest advantage over X-ray, making them complementary methods that, when used together, provide comprehensive structural information [111]. Given these capabilities, the complementary nature of the basic (XRD, SEM, TEM, BET …) and advanced techniques (SAXS, SANS) used for structural characterization ensures a multi-dimensional and a multi-scale vision of the materials. These versatility and complementarity between techniques result in revealing their complete structure and morphology.

Table I.3: Comparative properties of neutron and X-ray small angle scattering [112]

Parameter	Neutron	X-ray
Radiation is scattered by	Nuclei	Electrons
Radiation Sources	Steady state reactors Spallation neutron sources	Synchrotron sources Laboratory generation (Cu or Mo Kα)
SAS: Typical scattering vectors (Q)	0.001–0.5 $Å^{-1}$	0.005–1 $Å^{-1}$
USAS: Typical scattering vectors (Q)	2.0×10^{-5}-0.001 $Å^{-1}$	0.0001–0.05 $Å^{-1}$
Typical sample thickness (mm)	<1	<0.2
Typical counting time per sample	Minutes to hours	Seconds to minutes
Effect of isotopic substitution	Significant	Negligible
Absolute intensity calibration	Direct beam flux method	Standard sample method

5 Interest of small angle scattering techniques in characterizing the mesoscale

In the frame of this PhD, we wanted to apply this multi-scale characterization approach on graphene-based materials including *ex-situ*, *in-situ* and *operando* characterizations to address the questions arising from the adsorption/desorption mechanisms that are at play at different porosity scale from the nanoscale to the mesoscale. It is noteworthy that the relevance of small angle scattering techniques in probing the mesoscale of carbonaceous materials is further stressed by the existing literature work on the study of carbon materials. Indeed, D. Saurel *et al*. [113] studied various ordered carbonaceous materials such as graphite, non-porous carbon as well as disordered ones like activated carbon (AC), carbide derived carbon (CDC), glassy carbon (GC), and hard carbon (HC) to investigate the role and potential of SAXS and WAXS (wide angle X-ray scattering: equivalent to XRD) in understanding the microstructure of these materials. The SAXS/WAXS profiles show a broadening of the (002) peak of the disordered carbons (**Figure I.34 b**) in comparison to graphite and non-porous carbon which exhibit a sharp (002) peak (**Figure I.34 a**).

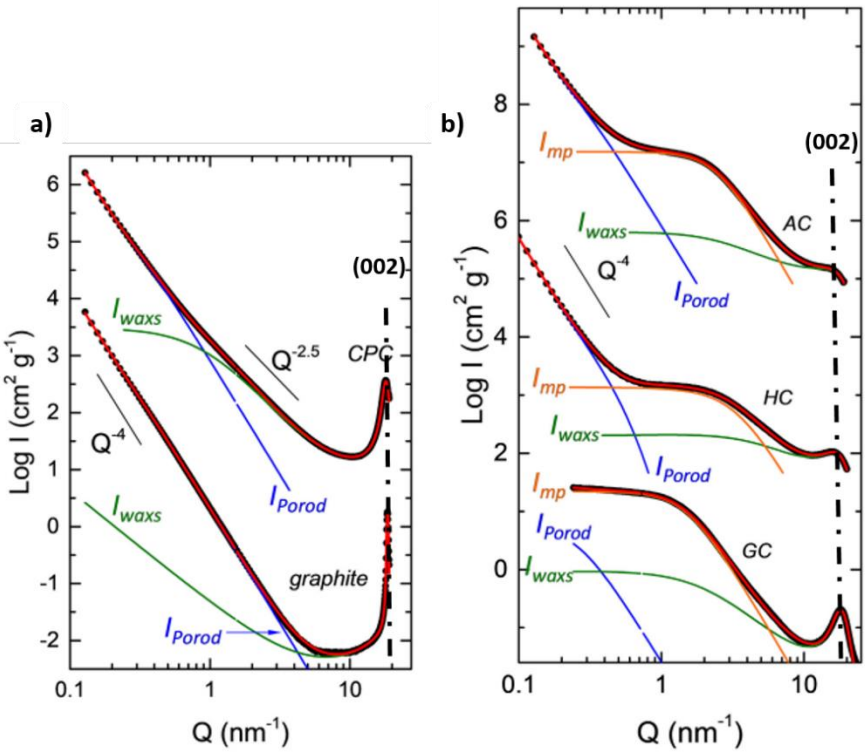

Figure I. 34 SAXS/WAXS profiles of (a) the ordered (CPC, graphite) and (b) disordered (AC, HC, GC) carbons. The black line represent the experimental data, red, blue, orange, and green lines represent the fitted curves [113].

In order to understand how material microstructure affects the (002) peak, a simulation was conducted for the (002) peak using three different microstructures (nanocrystallite, bent, and crumpled). **Figure I.35** illustrates that the bent and crumpled microstructures induce a broadening of the (002) peak, while the nanocrystallite model preserves this (002) peak sharpness (low FWHM). Experimentally AC, HC, and GC profiles are closer to that of a nano-curved layered structure (bent or crumpled) challenging the traditional models (nanocrystallite).

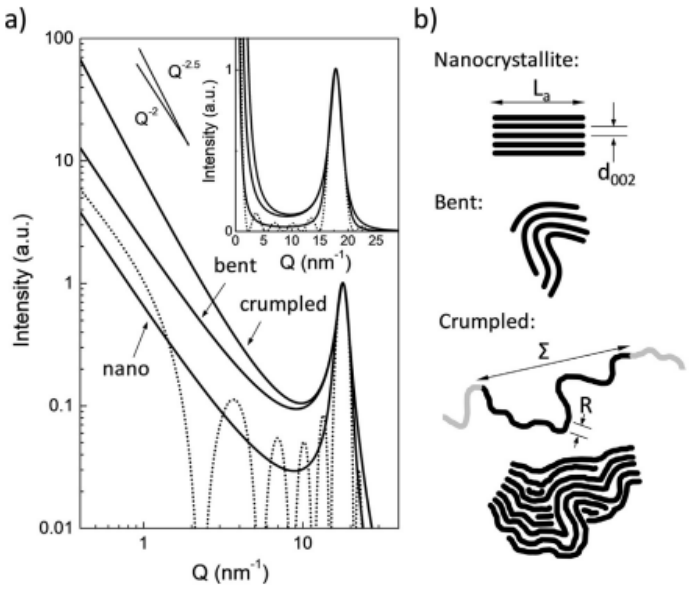

Figure I. 35 Simulation of a (002) peak with three different microstructures (nanocrystallite, bent, and crumpled)[113].

In addition, the specific surface area (SSA) was calculated based on the SAXS fitted data. A surface area of 493 m^2/g for GC and 792 m^2/g for HC were measured which may seem surprising at first sight since GC is known to exhibit zero BET SSA and HC has a rather modest N_2 BET SSA of 30 m^2/g. However, X-rays can penetrate into the bulk of particles. Thus, the measured SAXS SSA includes closed pores that are inaccessible to gas adsorption because it is totally closed, or connected to the surface via narrow paths that prevent N_2 diffusion. **Figure I.36** summarizes the comparison of SAXS and BET SSA for all the studied samples.

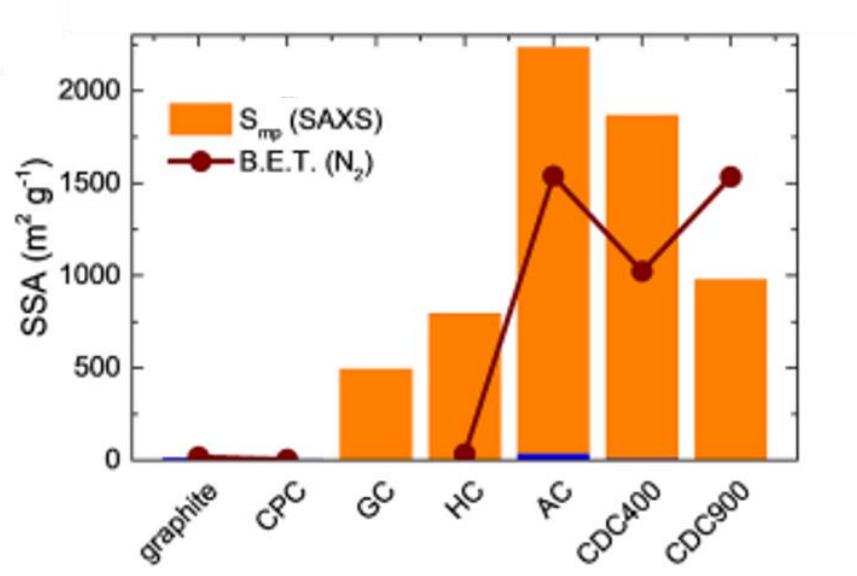

Figure I. 36 Specific surface area deduced from SAXS (columns) and gas adsorption (dark red circles) for different carbon samples [113]

In term of characterizing the material structure, SAXS and SANS are similar. However, the variation of scattering cross-section of elements across the periodic table is very different for neutrons and X-rays. For X-rays, it is proportional to the electrons density while for neutrons it varies irregularly with the atomic number. The principle of SAXS and SANS is the same, but each technique has its own specificity allowing to obtain complementary information on the microstructure of materials. Neutrons can be scattered by all atomic nuclei and the magnitude of the neutron waves scattered by a given nucleus is defined by the scattering length density (SLD or ρ) which is dependent, in the case of a molecule, by its neutron coherent length and volume [114]. In structural studies of biphasic materials, the scattering intensity is dependent on this SLD but also on different factors that are related to the sample such as its structure and its form; hence the scattering intensity is given by:

$$I(Q) = \varphi V p \Delta\rho^2 P(q) S(q) \qquad (I.3)$$

With:

φ the particle volume fraction.

$\Delta\rho = \rho_1 - \rho_2$ contrast: difference in the SLD between the particles (ρ_1) and the medium (ρ_2).

P(q): form factor.

S(q): structure factor.

One key distinction between neutron and X-ray scattering lies in their respective sensitivities to isotopic variations. For example, in neutron scattering, there is a marked difference in the SLD values for H_2O and D_2O [115, 116]. This allows the use of contrast-variation fluids such as water (H_2O), deuterated water (D_2O), toluene (C_7H_8), deuterated toluene (C_7D_8), and deuterated methane (CD_4) and also other deuterated solvents to study the fluid accessibility within the porosity of the material [117, 118]. In the context provided, contrast refers to the difference in the SLD between the solvent and the particle of interest ($\Delta\rho$). Isotopic substitution in the solvent is suggested as a method to modulate this contrast. When the SLD value of the fluid mixture matches with that of the sample, the remaining scattering is attributed to the inaccessible porosity (**Figure I.37 b**). If all the pores are accessible, the scattering intensity reduces to zero (**Figure I.37 a**). This technique (contrast-variation small-angle neutron scattering (CV-SANS)) is widely used to investigate the open and closed porosity in porous materials, as well as to study the accessibility of solvent to open pores.

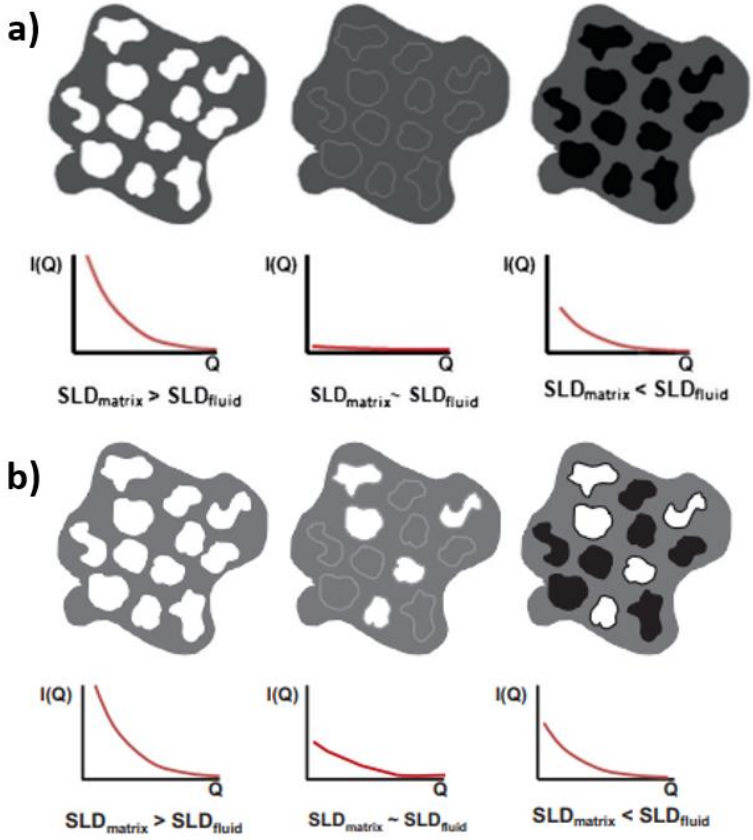

Figure I. 37 Qualitative representation of contrast-matching experiments with fluid saturated porous systems. (a) All pores are accessible to fluid molecules; (b) Pores are partially accessible to fluid molecules. [119]

This technique could be used on all porous materials. Indeed, Bahadur *et al*. [120] investigated the accessibility of water and toluene in Marcellus Shale samples with various

mineral compositions. Three different Marcellus Shales, representing quartz-rich (Mar-1), clay-rich (Mar-2), and carbonate-rich (Mar-3), were examined using CV-SANS at ambient temperature and pressure. As explained just above, changing the solvents relative composition will result in the modulation of the phase contrast parameter. If the solvent accesses the full porosity, the scattered intensity becomes null when the solvent composition SLD matches that of the solid phase. Different compositions of water, deuterated water (H_2O/D_2O) and toluene, deuterated toluene (H-TOL/D-TOL) are used to probe the open and closed porosity of these three shale samples. **Figure I.38** shows the relationship between the normalized scattering intensity at an arbitrarily chosen Q (Q=0.1 $Å^{-1}$) and the scattering length density (SLD) of the added liquids. It is observed that scattering intensity from the samples initially decreases with increasing amounts of deuterated solvent in the mixture (*i.e.* increasing SLD), and then increases again in a parabolic shape. In addition, the penetrating abilities of water and toluene are different in the three samples, as shown by different minimum scattering intensities. The contrast matching SLD of shale obtained by toluene/d-toluene (SLD ~ 4 x 10^{10} cm^{-2}) is higher than the contrast matching SLD obtained by H_2O/D_2O (SLD ~3.5 x 10^{10} cm^{-2}). These results reveal the difference in accessibility mechanisms of water and toluene within the porosity of the different samples due to their different sizes and to the different chemical interactions. However, there is always a residual intensity, which means that all samples contain some amount of closed or inaccessible pores.

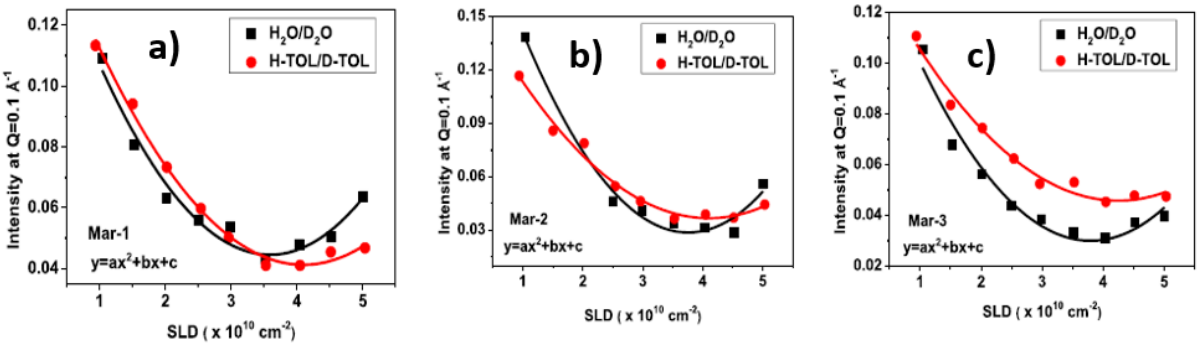

Figure I. 38 Scattering intensity at Q=0.1 $Å^{-1}$ for (a) Mar-1, (b) Mar-2 and (c) Mar-3 as a function of the scattering length density (SLD) of H_2O/D_2O and toluene/d-toluene (H-TOL/D-TOL) mixtures

To investigate the accessibility of water and toluene in the different porosity scales, the fraction of closed porosity was calculated from the residual intensity (**Figure I.39**). It is evident that the accessibility of pores to water and toluene varies with pore size and that the three samples show similar trends in their pore volume accessibility. Water was accessible to 70-80% of the larger pores across all samples. However, accessibility decreases in intermediate

range of pore size (approximately 5-80 nm radius), reaching its lowest values around a pore size of 25 nm, especially in the quartz-rich sample (Mar-1), suggesting that there is more closed porosity or greater heterogeneity around this size range, compared to other size ranges. Interestingly, this trend reverses in even smaller pores (less than 2.5 nm radius), where water accessibility increases again to about 70-80% in all samples. The accessibility of toluene was similar to that of water, except in the smallest pore sizes, where it significantly decreases, especially in the clay-rich sample (Mar-3), which may be related to an abundance of closed pores or simply that the toluene molecule is too large (kinetic diameter ~6.7 Å) to fit into the smallest pores. These results suggest that the mineral content (quartz and clay) of shale layers could significantly influence the accessibility of pores to water and toluene.

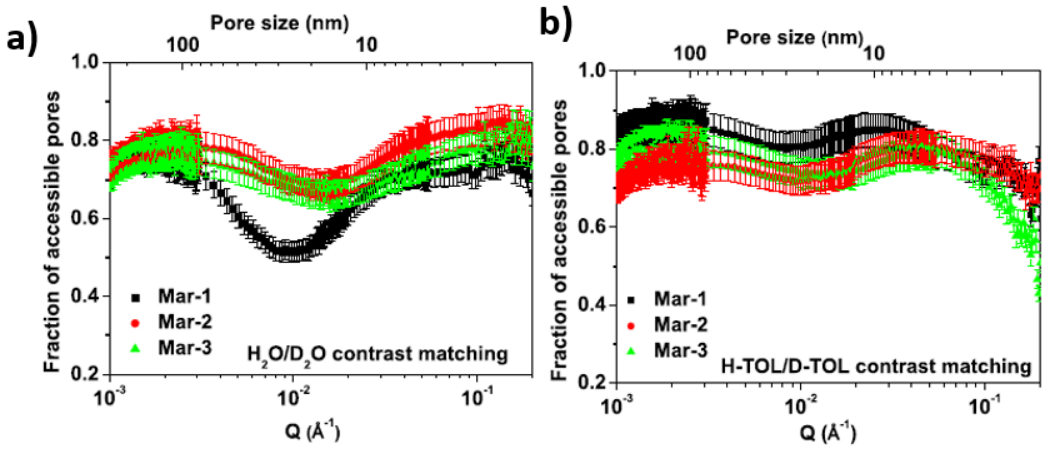

Figure I. 39 The fraction of accessible pores in three Marcellus Shale samples estimated by: (a) H_2O/D_2O contrast matching and (b) toluene/d-toluene (H-TOL/D-TOL) contrast matching

The previous example shows that CV-SANS is a very powerful technique to investigate the accessibility of solvents within the mesoporosity scale. This technique could also be used to determine the solid density of a porous material. Indeed, Z. Mileeva *et al*. [121] investigated the porosity of an activated carbon (AC) using CV-SANS technique. The scattering was modulated by filling the pores with different mixtures of hydrogenated and deuterated toluene. Mixtures containing 100% of hydrogenated toluene, 80, 85, 90, and 100% of deuterated toluene were used. **Figure I.40 a** shows the SANS profiles of the AC in its dry state and immersed in the different mixtures. The scattering intensity decreases while increasing the amount of the deuterated toluene reaching its minimum at 100% of deuterated toluene (red curve). **Figure I.40 b** shows the relationship between the normalized scattering intensity at arbitrarily chosen Q (Q=0.017, 0.025, and 0.053 $Å^{-1}$) and the scattering length density (SLD) of the added liquids for the measured curves (dots) and its fitting (red curve). The fitting reveals an increase in the intensity above the point measured at 100% of deuterated toluene in a

parabolic shape. The solid density of the AC can then be calculated from the matching SLD giving 1.86 g/cm^3 using:

$$SLD = \frac{\sum_i b_i \boldsymbol{d} Na}{M} \quad (I.4)$$

With:

b_i: atomic neutron coherent scattering length.

d: the solid density

Na: Avogadro number (6.02×10^{23})

M: molecular weight of the material

The solid density is very important and can be used to estimate the material porosity knowing its apparent density. Moreover, as shown previously, the small angles scattering techniques are used to determine the materials SSA, for this purpose, a normalization of the scattering intensity to the absolute intensity is imperative, and accurate normalization relies on knowledge of the real density of the solid material.

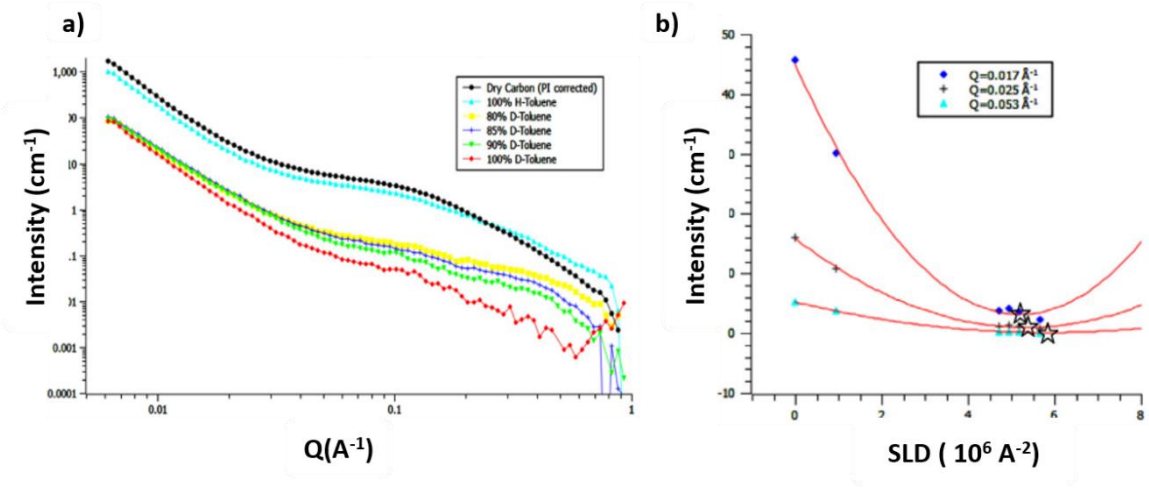

Figure I. 40 (a) SANS profiles of AC in its dry and immersed in different H-toluene/D-toluene mixtures form (b) Scattering intensity at Q=0.017 Å^{-1} =, Q=00025 Å^{-1}, and Q= 0.053 Å^{-1} as a function of the solvents SLDs [121].

The previous examples showed how SAXS and SANS technique can be advantageously used to understand the mesostructure of carbon samples as well as their solid density and mesoporosity. These techniques have been applied to the study of carbons in supercapacitors notably in *in-situ/operando* modes. Indeed, thanks to the enhanced scattering contrasts, neutrons scattering is a unique tool to reveal the diffusion and electro adsorption of electrolyte ions in material pores of different sizes [122]. As shown previously, the sensitivity of neutrons to the variations in nuclear scattering lengths, makes the SANS a powerful

technique to probe the variation of the nature and amount of adsorbed species and their concentration within the porosity of the material. Boukhalfa *et al.* [123] studied the electroadsorption of organic electrolytic ions in an activated carbon (AC) of different sizes using *in-situ* SANS. A 1 M solution of tetraethylammonium tetrafluoroborate ($TEABF_4$) salt in deuterated acetonitrile (d-AN) was used in an activated carbon with a pore size distribution similar to that of the carbons used in commercial double layer capacitors. d-AN was used so that the only external hydrogen source is the cations (TEA^+). The working and counter electrodes (WE and CE) were positioned inside a quartz cuvette side-to-side at a distance of ~3-5 mm from each other so that the incoming neutron beam hits only the working electrode (WE) (**Figure I.41**) When a positive potential was applied, there is a noticeable reduction in the scattering intensity. Conversely, the application of a negative potential leads to a clear increase in scattering intensity as shown in **Figure 42 a**. Under negative potential, H-containing TEA^+ cations are electrostatically adsorbed into the pores to neutralize the charge that leads to an increase of the scattered intensity, whereas under positive potential, H-rich cations are desorbed and replaced by anions that do not contain hydrogen, and hence the scattering intensity decreases. Indeed, around 20% of the BF_4^- anions consist of neutron-absorbing B^{10} isotopes, which result in an attenuation of the neutron scattering intensity when these anions are present within the pores.

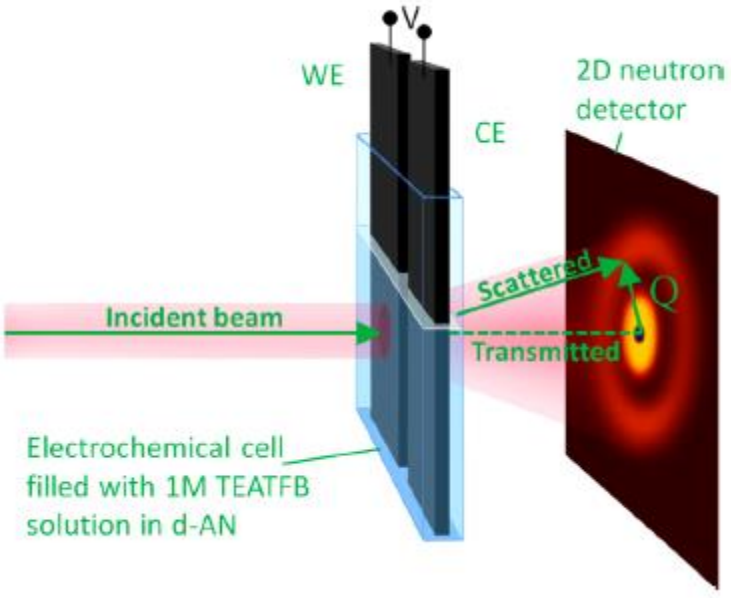

Figure I. 41 Schematic of the SANS measurements setup for in situ experimental studies of ion electrosorption phenomena in microporous carbon electrodes [123]

To better understand the ion adsorption in pores of different sizes, the SANS intensities were compared to a baseline established at zero voltage (**Figure I.42 b**). When a potential of -2 V is applied, the scattering intensity increases by about 10%, which suggests a hydrogen (H) enrichment within the pores. Conversely, at a potential of +2 V, the scattering intensity decreases by about 7%, reflecting a hydrogen depletion. Slightly higher increase in scattering intensity at negative potentials compared to the decrease at positive potentials could be attributed to a slightly higher initial concentration of BF_4^- anions in the carbon pores. The smallest pores (Q > 0.2 $Å^{-1}$) in activated carbon (AC) display even greater ion adsorption capacity as shown by their higher scattering intensities, signifying increased H concentration and a lower ^{10}B concentration at negative potentials; while at positive potentials lower scattering intensities are observed for these pores, indicating a lower H concentration and a higher ^{10}B concentration. **Figure I.42 c** shows the relative changes in normalized scattering intensities at both negative and positive potentials, and illustrates more clearly the impact of pore size on ion electroadsorption.

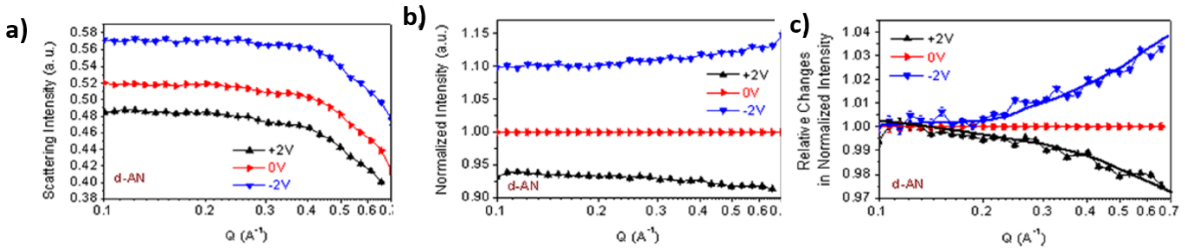

Figure I. 42 In-situ neutron scattering experiments on AC electrodes immersed into 1 M TEATFB/d-AN electrolyte under an application of a potential between the WE and CE: (a) SANS patterns, (b) SANS profiles normalized by the 0 V one, (c) relative changes in the intensity of the normalized SANS profiles [123].

This finding supports many previously reported results that have highlighted the potential for enhanced ion adsorption in the small (micro) pores of many porous carbon materials [76, 75].

6 Aim of the PhD

These above cited examples highlighted the versatility of SAXS and SANS and their complementarity in probing the mesoscale structure, in studying the wetting and accessibility of solvents within the mesoporosity and determining the solid density, and also in probing *in-situ* the adsorption of ions within the pores of different sizes under different applied potential in SCs. These instances emphasize that standard and advanced characterization (notably in *ex-situ*, *in-situ*, and *operando* conditions) work hand in hand to get a clear picture of the multi-scale structure and porosity of graphene-based materials. We also understand that *in-situ* SANS

could bring added value to the adsorption mechanisms in SCs within an extended scale. Therefore to study graphene-based materials we decide to define a methodology counting i) the investigation of the reduction impact on the physicochemical and multi-scale structural properties of rGO using two reduction methods, hydrothermal reduction and reduction using hydrazine hydrate, ii) the study of the influence of functionalization/pillaring on the multi-scale structure, morphology, and porosity of pillared graphene materials, underscoring their characteristics at different scales, and iii) the understanding of the electrochemical properties of both references (non-pillared) and pillared graphene materials by establishing a correlation between their structural and chemical properties to their electrochemical performances. The corresponding parts of this PhD work are further described below.

Accordingly, in the 1st part of this PhD, the different graphene-based materials were synthesized, and a fundamental study was carried out on reduced graphene oxide including chemically reduced GO using hydrazine hydrate (rGO), and hydrothermally reduced GO, namely graphene aerogels (GA). The aim of this study is to understand the impact of the reduction technique on the graphene samples multi-scale structure/porosity using a correlation between local structural characterizations techniques (XRD, TEM), macrostructural observations (SEM), and advanced mesostructural characterization (SANS). In addition, a physicochemical study was conducted to assess the samples chemical properties notably their reduction degree. This part of the work also enabled defining and qualifying the methodology used to get access to these characterization details.

Following-up from this work, in the 2nd part of this PhD, this characterization methodology was conducted on pillared graphene materials including pillared graphene aerogels (nGA) and reduced pillared powders (nRP) synthesized using various alkyl diamines with different lengths as a pillar in different concentrations. The primary impacts on the multi-scale structure and on the materials chemistry of pillaring were identified and compared to those of reduced graphene materials.

In the third part of this PhD, a dedicated effort was made to understand the behavior of these materials cycled as a supercapacitor electrode. Electrochemical testing was carried out on the samples to test their electrochemical performances. Therefore, physicochemical properties, morphological features, and electrochemical behavior were compared in order to find possible correlations and to highlight different chemical or structural features. Additionally, an advanced *in-situ/operando* SAXS/WAXS study, using synchrotron radiation,

was conducted to unveil the structural evolution during cycling and polarization of the graphene-based materials. Additionally, we took advantage of the SANS contrast modulation and performed an *in-situ* SANS experiment to uncover the location of ions within pores of different sizes. The integration of these datasets aimed to provide insights into the adsorption/desorption mechanisms in graphene-based materials.

7 References:

[1] K. S. Novoselov *et al.*, "Electric Field Effect in Atomically Thin Carbon Films," *Science*, vol. 306, no. 5696, pp. 666–669, Oct. 2004, doi: 10.1126/science.1102896.

[2] S. V. Morozov *et al.*, "Giant Intrinsic Carrier Mobilities in Graphene and Its Bilayer," *Phys. Rev. Lett.*, vol. 100, no. 1, p. 016602, Jan. 2008, doi: 10.1103/PhysRevLett.100.016602.

[3] A. A. Balandin *et al.*, "Superior Thermal Conductivity of Single-Layer Graphene," *Nano Lett.*, vol. 8, no. 3, pp. 902–907, Mar. 2008, doi: 10.1021/nl0731872.

[4] C. Lee, X. Wei, J. W. Kysar, and J. Hone, "Measurement of the Elastic Properties and Intrinsic Strength of Monolayer Graphene," *Science*, vol. 321, no. 5887, pp. 385–388, Jul. 2008, doi: 10.1126/science.1157996.

[5] R. R. Nair *et al.*, "Fine Structure Constant Defines Visual Transparency of Graphene," *Science*, vol. 320, no. 5881, pp. 1308–1308, Jun. 2008, doi: 10.1126/science.1156965.

[6] A. S. Lemine, M. M. Zagho, T. M. Altahtamouni, and N. Bensalah, "Graphene a promising electrode material for supercapacitors—A review," *International Journal of Energy Research*, vol. 42, no. 14, pp. 4284–4300, 2018, doi: 10.1002/er.4170.

[7] E. P. Randviir, D. A. C. Brownson, and C. E. Banks, "A decade of graphene research: production, applications and outlook," *Materials Today*, vol. 17, no. 9, pp. 426–432, Nov. 2014, doi: 10.1016/j.mattod.2014.06.001.

[8] M. Lazzeri and A. Barreiro, "Carbon-Based Nanoscience," *Elements*, vol. 10, pp. 447–452, Dec. 2014, doi: 10.2113/gselements.10.6.447.

[9] S. Bae *et al.*, "Roll-to-roll production of 30-inch graphene films for transparent electrodes," *Nature Nanotech*, vol. 5, no. 8, Art. no. 8, Aug. 2010, doi: 10.1038/nnano.2010.132.

[10] V. Yu. Aristov *et al.*, "Graphene Synthesis on Cubic SiC/Si Wafers. Perspectives for Mass Production of Graphene-Based Electronic Devices," *Nano Lett.*, vol. 10, no. 3, pp. 992–995, Mar. 2010, doi: 10.1021/nl904115h.

[11] W. Norimatsu and M. Kusunoki, "Epitaxial graphene on SiC{0001}: advances and perspectives," *Physical Chemistry Chemical Physics*, vol. 16, no. 8, pp. 3501–3511, 2014, doi: 10.1039/C3CP54523G.

[12] Y. Hernandez *et al.*, "High-yield production of graphene by liquid-phase exfoliation of graphite," *Nature Nanotech*, vol. 3, no. 9, Art. no. 9, Sep. 2008, doi: 10.1038/nnano.2008.215.

[13] S. Mao, H. Pu, and J. Chen, "Graphene oxide and its reduction : modeling and experimental progress," *RSC Advances*, vol. 2, no. 7, pp. 2643–2662, 2012, doi: 10.1039/C2RA00663D.

[14] S. Stankovich *et al.*, "Synthesis of graphene-based nanosheets via chemical reduction of exfoliated graphite oxide," *Carbon*, vol. 45, no. 7, pp. 1558–1565, Jun. 2007, doi: 10.1016/j.carbon.2007.02.034.

[15] R. Raccichini, A. Varzi, S. Passerini, and B. Scrosati, "The role of graphene for electrochemical energy storage," *Nature Mater*, vol. 14, no. 3, Art. no. 3, Mar. 2015, doi: 10.1038/nmat4170.

[16] K. R. Paton *et al.*, "Scalable production of large quantities of defect-free few-layer graphene by shear exfoliation in liquids," *Nature Mater*, vol. 13, no. 6, Art. no. 6, Jun. 2014, doi: 10.1038/nmat3944.

[17] D. R. Dreyer, A. D. Todd, and C. W. Bielawski, "Harnessing the chemistry of graphene oxide," *Chemical Society Reviews*, vol. 43, no. 15, pp. 5288–5301, 2014, doi: 10.1039/C4CS00060A.

[18] W. S. Hummers and R. E. Offeman, "Preparation of Graphitic Oxide," *J. Am. Chem. Soc.*, vol. 80, no. 6, pp. 1339–1339, Mar. 1958, doi: 10.1021/ja01539a017.

[19] E. J.-C. Amieva *et al.*, "Graphene-Based Materials Functionalization with Natural Polymeric Biomolecules," in *Recent Advances in Graphene Research*, IntechOpen, 2016. doi: 10.5772/64001.

[20] S. Pei and H.-M. Cheng, "The reduction of graphene oxide," *Carbon*, vol. 50, no. 9, pp. 3210–3228, Aug. 2012, doi: 10.1016/j.carbon.2011.11.010.

[21] A. N. Ghulam, O. A. L. dos Santos, L. Hazeem, B. Pizzorno Backx, M. Bououdina, and S. Bellucci, "Graphene Oxide (GO) Materials—Applications and Toxicity on Living Organisms and Environment," *JFB*, vol. 13, no. 2, p. 77, Jun. 2022, doi: 10.3390/jfb13020077.

[22] P.-G. Ren, D.-X. Yan, X. Ji, T. Chen, and Z.-M. Li, "Temperature dependence of graphene oxide reduced by hydrazine hydrate," *Nanotechnology*, vol. 22, no. 5, p. 055705, Dec. 2010, doi: 10.1088/0957-4484/22/5/055705.

[23] H.-J. Shin *et al.*, "Efficient Reduction of Graphite Oxide by Sodium Borohydride and Its Effect on Electrical Conductance," *Advanced Functional Materials*, vol. 19, no. 12, pp. 1987–1992, 2009, doi: 10.1002/adfm.200900167.

[24] J. Zhang, H. Yang, G. Shen, P. Cheng, J. Zhang, and S. Guo, "Reduction of graphene oxide via l - ascorbic acid," *Chemical Communications*, vol. 46, no. 7, pp. 1112–1114, 2010, doi: 10.1039/B917705A.

[25] K. K. H. De Silva, H.-H. Huang, R. K. Joshi, and M. Yoshimura, "Chemical reduction of graphene oxide using green reductants," *Carbon*, vol. 119, pp. 190–199, Aug. 2017, doi: 10.1016/j.carbon.2017.04.025.

[26] W. Gao, L. B. Alemany, L. Ci, and P. M. Ajayan, "New insights into the structure and reduction of graphite oxide," *Nature Chem*, vol. 1, no. 5, Art. no. 5, Aug. 2009, doi: 10.1038/nchem.281.

[27] S. Park *et al.*, "Colloidal Suspensions of Highly Reduced Graphene Oxide in a Wide Variety of Organic Solvents," *Nano Lett.*, vol. 9, no. 4, pp. 1593–1597, Apr. 2009, doi: 10.1021/nl803798y.

[28] S. Mikhailov, *Physics and Applications of Graphene: Experiments*. BoD – Books on Demand, 2011.

[29] A. E. F. Oliveira, G. B. Braga, C. R. T. Tarley, and A. C. Pereira, "Thermally reduced graphene oxide: synthesis, studies and characterization," *J Mater Sci*, vol. 53, no. 17, pp. 12005–12015, Sep. 2018, doi: 10.1007/s10853-018-2473-3.

[30] A. Raza *et al.*, "A comparative study of dirac 2D materials, TMDCs and 2D insulators with regard to their structures and photocatalytic/sonophotocatalytic behavior," *Applied Nanoscience*, vol. 10, Jun. 2020, doi: 10.1007/s13204-020-01475-y.

[31] C.-M. Chen, Q. Zhang, M.-G. Yang, C.-H. Huang, Y.-G. Yang, and M.-Z. Wang, "Structural evolution during annealing of thermally reduced graphene nanosheets for application in supercapacitors," *Carbon*, vol. 50, no. 10, pp. 3572–3584, Aug. 2012, doi: 10.1016/j.carbon.2012.03.029.

[32] H. A. Becerril, J. Mao, Z. Liu, R. M. Stoltenberg, Z. Bao, and Y. Chen, "Evaluation of Solution-Processed Reduced Graphene Oxide Films as Transparent Conductors," *ACS Nano*, vol. 2, no. 3, pp. 463–470, Mar. 2008, doi: 10.1021/nn700375n.

[33] C. Gómez-Navarro *et al.*, "Atomic Structure of Reduced Graphene Oxide," *Nano Lett.*, vol. 10, no. 4, pp. 1144–1148, Apr. 2010, doi: 10.1021/nl9031617.

[34] X.-Y. Peng, X.-X. Liu, D. Diamond, and K. T. Lau, "Synthesis of electrochemically-reduced graphene oxide film with controllable size and thickness and its use in supercapacitor," *Carbon*, vol. 49, no. 11, pp. 3488–3496, Sep. 2011, doi: 10.1016/j.carbon.2011.04.047.

[35] Z. Wang, X. Zhou, J. Zhang, F. Boey, and H. Zhang, "Direct Electrochemical Reduction of Single-Layer Graphene Oxide and Subsequent Functionalization with Glucose Oxidase," *J. Phys. Chem. C*, vol. 113, no. 32, pp. 14071–14075, Aug. 2009, doi: 10.1021/jp906348x.

[36] D. Wang, W. Yan, S. H. Vijapur, and G. G. Botte, "Electrochemically reduced graphene oxide–nickel nanocomposites for urea electrolysis," *Electrochimica Acta*, vol. 89, pp. 732–736, Feb. 2013, doi: 10.1016/j.electacta.2012.11.046.

[37] M. Hilder, B. Winther-Jensen, D. Li, M. Forsyth, and D. R. MacFarlane, "Direct electro-deposition of graphene from aqueous suspensions," *Phys. Chem. Chem. Phys.*, vol. 13, no. 20, pp. 9187–9193, May 2011, doi: 10.1039/C1CP20173E.

[38] H.-H. Chang, C.-K. Chang, Y.-C. Tsai, and C.-S. Liao, "Electrochemically synthesized graphene/polypyrrole composites and their use in supercapacitor," *Carbon*, vol. 50, no. 6, pp. 2331–2336, May 2012, doi: 10.1016/j.carbon.2012.01.056.

[39] X. Zheng *et al.*, "Hydrothermal reduction of graphene oxide; effect on surface-enhanced Raman scattering," *Journal of Raman Spectroscopy*, vol. 48, no. 1, pp. 97–103, 2017, doi: 10.1002/jrs.4998.

[40] E. Garcia-Bordejé, A. M. Benito, and W. K. Maser, "Graphene aerogels via hydrothermal gelation of graphene oxide colloids: Fine-tuning of its porous and chemical properties and catalytic applications," *Advances in Colloid and Interface Science*, vol. 292, p. 102420, Jun. 2021, doi: 10.1016/j.cis.2021.102420.

[41] L. Xu *et al.*, "Superhydrophobic and superoleophilic graphene aerogel prepared by facile chemical reduction," *Journal of Materials Chemistry A*, vol. 3, no. 14, pp. 7498–7504, 2015, doi: 10.1039/C5TA00383K.

[42] I. K. Moon, S. Yoon, K.-Y. Chun, and J. Oh, "Highly Elastic and Conductive N-Doped Monolithic Graphene Aerogels for Multifunctional Applications," *Advanced Functional Materials*, vol. 25, no. 45, pp. 6976–6984, 2015, doi: 10.1002/adfm.201502395.

[43] K. Trembecka-Wójciga, J. J. Sobczak, and N. Sobczak, "A comprehensive review of graphene-based aerogels for biomedical applications. The impact of synthesis parameters onto material microstructure and porosity," *Archiv.Civ.Mech.Eng*, vol. 23, no. 2, p. 133, Apr. 2023, doi: 10.1007/s43452-023-00650-6.

[44] M. A. Riaz, P. Hadi, I. H. Abidi, A. Tyagi, X. Ou, and Z. Luo, "Recyclable 3D graphene aerogel with bimodal pore structure for ultrafast and selective oil sorption from water," *RSC Adv.*, vol. 7, no. 47, pp. 29722–29731, Jun. 2017, doi: 10.1039/C7RA02886E.

[45] L. Qiu, J. Z. Liu, S. L. Y. Chang, Y. Wu, and D. Li, "Biomimetic superelastic graphene-based cellular monoliths," *Nat Commun*, vol. 3, no. 1, Art. no. 1, Dec. 2012, doi: 10.1038/ncomms2251.

[46] C. Wang *et al.*, "Freeze-Casting Produces a Graphene Oxide Aerogel with a Radial and Centrosymmetric Structure," *ACS Nano*, vol. 12, no. 6, pp. 5816–5825, Jun. 2018, doi: 10.1021/acsnano.8b01747.

[47] S. Tamang, S. Rai, R. Bhujel, N. K. Bhattacharyya, B. P. Swain, and J. Biswas, "A concise review on GO, rGO and metal oxide/rGO composites: Fabrication and their supercapacitor and catalytic applications," *Journal of Alloys and Compounds*, vol. 947, p. 169588, Jun. 2023, doi: 10.1016/j.jallcom.2023.169588.

[48] J. H. Lee *et al.*, "Restacking-Inhibited 3D Reduced Graphene Oxide for High Performance Supercapacitor Electrodes," *ACS Nano*, vol. 7, no. 10, pp. 9366–9374, Oct. 2013, doi: 10.1021/nn4040734.

[49] Y. Zhu *et al.*, "Graphene and Graphene Oxide: Synthesis, Properties, and Applications," *Advanced Materials*, vol. 22, no. 35, pp. 3906–3924, 2010, doi: 10.1002/adma.201001068.

[50] D. Chen, H. Feng, and J. Li, "Graphene Oxide: Preparation, Functionalization, and Electrochemical Applications," *Chem. Rev.*, vol. 112, no. 11, pp. 6027–6053, Nov. 2012, doi: 10.1021/cr300115g.

[51] F. Du, D. Yu, L. Dai, S. Ganguli, V. Varshney, and A. K. Roy, "Preparation of Tunable 3D Pillared Carbon Nanotube–Graphene Networks for High-Performance Capacitance," *Chem. Mater.*, vol. 23, no. 21, pp. 4810–4816, Nov. 2011, doi: 10.1021/cm2021214.

[52] K. Haraguchi, S. Iwakami, and T. Ohba, "Fabrication of Fullerene-Pillared Porous Graphene and Its Water Vapor Adsorption," *J. Phys. Chem. C*, vol. 127, no. 25, pp. 12333–12341, Jun. 2023, doi: 10.1021/acs.jpcc.3c02394.

[53] Z.-S. Wu, G. Zhou, L.-C. Yin, W. Ren, F. Li, and H.-M. Cheng, "Graphene/metal oxide composite electrode materials for energy storage," *Nano Energy*, vol. 1, no. 1, pp. 107–131, Jan. 2012, doi: 10.1016/j.nanoen.2011.11.001.

[54] X. Huang, F. Boey, and H. Zhang, "A brief review on graphene-nanoparticle composites," *COSMOS*, vol. 06, no. 02, pp. 159–166, Dec. 2010, doi: 10.1142/S0219607710000607.

[55] L. Dai, "Functionalization of Graphene for Efficient Energy Conversion and Storage," *Acc. Chem. Res.*, vol. 46, no. 1, pp. 31–42, Jan. 2013, doi: 10.1021/ar300122m.

[56] J. Li and M. Östling, "Prevention of Graphene Restacking for Performance Boost of Supercapacitors—A Review," *Crystals*, vol. 3, no. 1, Art. no. 1, Mar. 2013, doi: 10.3390/cryst3010163.

[57] V. Jain and B. Kandasubramanian, "Functionalized graphene materials for hydrogen storage," *J Mater Sci*, vol. 55, no. 5, pp. 1865–1903, Feb. 2020, doi: 10.1007/s10853-019-04150-y.

[58] Y. Xie *et al.*, "Graphene covalently functionalized by cross-linking reaction of bifunctional pillar organic molecule for high capacitance," *Journal of Energy Storage*, vol. 38, p. 102530, Jun. 2021, doi: 10.1016/j.est.2021.102530.

[59] F. Ma *et al.*, "Organic Molecule-Functionalized Reduced Graphene Oxide for All-Carbon Asymmetric Supercapacitor Applications," *ACS Appl. Energy Mater.*, vol. 4, no. 6, pp. 5493–5503, Jun. 2021, doi: 10.1021/acsaem.1c00150.

[60] B. Song *et al.*, "Systematic study on structural and electronic properties of diamine/triamine functionalized graphene networks for supercapacitor application," *Nano Energy*, vol. 31, pp. 183–193, Jan. 2017, doi: 10.1016/j.nanoen.2016.10.057.

[61] K. Tasaki, "Poly(oxyethylene)−Water Interactions: A Molecular Dynamics Study," *J. Am. Chem. Soc.*, vol. 118, no. 35, pp. 8459–8469, Jan. 1996, doi: 10.1021/ja951005c.

[62] H. Banda *et al.*, "Ion Sieving Effects in Chemically Tuned Pillared Graphene Materials for Electrochemical Capacitors," *Chem. Mater.*, vol. 30, no. 9, pp. 3040–3047, May 2018, doi: 10.1021/acs.chemmater.8b00759.

[63] S. Kulandaivalu and Y. Sulaiman, "Recent Advances in Layer-by-Layer Assembled Conducting Polymer Based Composites for Supercapacitors," *Energies*, vol. 12, no. 11, Art. no. 11, Jan. 2019, doi: 10.3390/en12112107.

[64] S. Boukhalfa, K. Evanoff, and G. Yushin, "Atomic layer deposition of vanadium oxide on carbon nanotubes for high-power supercapacitor electrodes," *Energy & Environmental Science*, vol. 5, no. 5, pp. 6872–6879, 2012, doi: 10.1039/C2EE21110F.

[65] A. Burke, "Ultracapacitors: why, how, and where is the technology," *Journal of Power Sources*, vol. 91, no. 1, pp. 37–50, Nov. 2000, doi: 10.1016/S0378-7753(00)00485-7.

[66] L. Li Zhang and X. S. Zhao, "Carbon-based materials as supercapacitor electrodes," *Chemical Society Reviews*, vol. 38, no. 9, pp. 2520–2531, 2009, doi: 10.1039/B813846J.

[67] N. P. Shetti, S. Dias, and K. R. Reddy, "Nanostructured organic and inorganic materials for Li-ion batteries: A review," *Materials Science in Semiconductor Processing*, vol. 104, p. 104684, Dec. 2019, doi: 10.1016/j.mssp.2019.104684.

[68] Z. Lin *et al.*, "Materials for supercapacitors: When Li-ion battery power is not enough," *Materials Today*, vol. 21, no. 4, pp. 419–436, May 2018, doi: 10.1016/j.mattod.2018.01.035.

[69] M. Yaseen *et al.*, "A Review of Supercapacitors: Materials Design, Modification, and Applications," *Energies*, vol. 14, no. 22, Art. no. 22, Jan. 2021, doi: 10.3390/en14227779.

[70] U. Gulzar *et al.*, "Next-Generation Textiles: From Embedded Supercapacitors to Lithium Ion Batteries," *J. Mater. Chem. A*, vol. 4, pp. 16771–16800, Sep. 2016, doi: 10.1039/C6TA06437J.

[71] K. Jost, G. Dion, and Y. Gogotsi, "Textile energy storage in perspective," *Journal of Materials Chemistry A*, vol. 2, no. 28, pp. 10776–10787, 2014, doi: 10.1039/C4TA00203B.

[72] T. S. Mathis, N. Kurra, X. Wang, D. Pinto, P. Simon, and Y. Gogotsi, "Energy Storage Data Reporting in Perspective—Guidelines for Interpreting the Performance of Electrochemical Energy Storage Systems," *Advanced Energy Materials*, vol. 9, no. 39, p. 1902007, 2019, doi: 10.1002/aenm.201902007.

[73] A. González, E. Goikolea, J. A. Barrena, and R. Mysyk, "Review on supercapacitors: Technologies and materials," *Renewable and Sustainable Energy Reviews*, vol. 58, pp. 1189–1206, May 2016, doi: 10.1016/j.rser.2015.12.249.

[74] J. Gamby, P. L. Taberna, P. Simon, J. F. Fauvarque, and M. Chesneau, "Studies and characterisations of various activated carbons used for carbon/carbon supercapacitors," *Journal of Power Sources*, vol. 101, no. 1, pp. 109–116, Oct. 2001, doi: 10.1016/S0378-7753(01)00707-8.

[75] J. Chmiola, G. Yushin, Y. Gogotsi, C. Portet, P. Simon, and P. L. Taberna, "Anomalous Increase in Carbon Capacitance at Pore Sizes Less Than 1 Nanometer," *Science*, vol. 313, no. 5794, pp. 1760–1763, Sep. 2006, doi: 10.1126/science.1132195.

[76] E. Raymundo-Piñero, K. Kierzek, J. Machnikowski, and F. Béguin, "Relationship between the nanoporous texture of activated carbons and their capacitance properties in different electrolytes," *Carbon*, vol. 44, no. 12, pp. 2498–2507, Oct. 2006, doi: 10.1016/j.carbon.2006.05.022.

[77] P. Simon and Y. Gogotsi, "Materials for electrochemical capacitors," *Nature Mater*, vol. 7, no. 11, Art. no. 11, Nov. 2008, doi: 10.1038/nmat2297.

[78] T. Liu, F. Zhang, Y. Song, and Y. Li, "Revitalizing carbon supercapacitor electrodes with hierarchical porous structures," *Journal of Materials Chemistry A*, vol. 5, no. 34, pp. 17705–17733, 2017, doi: 10.1039/C7TA05646J.

[79] L. Qie *et al.*, "Synthesis of functionalized 3D hierarchical porous carbon for high-performance supercapacitors," *Energy & Environmental Science*, vol. 6, no. 8, pp. 2497–2504, 2013, doi: 10.1039/C3EE41638K.

[80] J. Li *et al.*, "Fabrication of high performance structural N-doped hierarchical porous carbon for supercapacitors," *Carbon*, vol. 164, pp. 42–50, Aug. 2020, doi: 10.1016/j.carbon.2020.03.044.

[81] X. J. Li *et al.*, "Excellent Capacitive Performance of a Three-Dimensional Hierarchical Porous Graphene/Carbon Composite with a Superhigh Surface Area," *Chemistry – A European Journal*, vol. 20, no. 41, pp. 13314–13320, 2014, doi: 10.1002/chem.201402897.

[82] H. Feng *et al.*, "Three-dimensional honeycomb-like hierarchically structured carbon for high-performance supercapacitors derived from high-ash-content sewage sludge," *Journal of Materials Chemistry A*, vol. 3, no. 29, pp. 15225–15234, 2015, doi: 10.1039/C5TA03217B.

[83] B. You, J. Jiang, and S. Fan, "Three-Dimensional Hierarchically Porous All-Carbon Foams for Supercapacitor," *ACS Appl. Mater. Interfaces*, vol. 6, no. 17, pp. 15302–15308, Sep. 2014, doi: 10.1021/am503783t.

[84] L. Dong, Z. Chen, D. Yang, and H. Lu, "Hierarchically structured graphene-based supercapacitor electrodes," *RSC Advances*, vol. 3, no. 44, pp. 21183–21191, 2013, doi: 10.1039/C3RA44357D.

[85] Z.-S. Wu *et al.*, "Graphene Anchored with Co3O4 Nanoparticles as Anode of Lithium Ion Batteries with Enhanced Reversible Capacity and Cyclic Performance," *ACS Nano*, vol. 4, no. 6, pp. 3187–3194, Jun. 2010, doi: 10.1021/nn100740x.

[86] H. M. Jeong *et al.*, "Nitrogen-Doped Graphene for High-Performance Ultracapacitors and the Importance of Nitrogen-Doped Sites at Basal Planes," *Nano Lett.*, vol. 11, no. 6, pp. 2472–2477, Jun. 2011, doi: 10.1021/nl2009058.

[87] M. D. Stoller, S. Park, Y. Zhu, J. An, and R. S. Ruoff, "Graphene-Based Ultracapacitors," *Nano Lett.*, vol. 8, no. 10, pp. 3498–3502, Oct. 2008, doi: 10.1021/nl802558y.

[88] Y. Xu, K. Sheng, C. Li, and G. Shi, "Self-Assembled Graphene Hydrogel via a One-Step Hydrothermal Process," *ACS Nano*, vol. 4, no. 7, pp. 4324–4330, Jul. 2010, doi: 10.1021/nn101187z.

[89] H. Banda *et al.*, "Sparsely Pillared Graphene Materials for High-Performance Supercapacitors: Improving Ion Transport and Storage Capacity," *ACS Nano*, vol. 13, no. 2, pp. 1443–1453, Feb. 2019, doi: 10.1021/acsnano.8b07102.

[90] D. Lee *et al.*, "Revealing Electrolytic Ion Sorption in Layered Graphene Galleries through Low-Temperature Solid-State NMR," *Chem. Mater.*, vol. 35, no. 10, pp. 3841–3848, May 2023, doi: 10.1021/acs.chemmater.2c03502.

[91] A. C. Forse, C. Merlet, J. M. Griffin, and C. P. Grey, "New Perspectives on the Charging Mechanisms of Supercapacitors," *J. Am. Chem. Soc.*, vol. 138, no. 18, pp. 5731–5744, May 2016, doi: 10.1021/jacs.6b02115.

[92] G. Eda and M. Chhowalla, "Chemically Derived Graphene Oxide: Towards Large-Area Thin-Film Electronics and Optoelectronics," *Advanced Materials*, vol. 22, no. 22, pp. 2392–2415, 2010, doi: 10.1002/adma.200903689.

[93] G. Eda, G. Fanchini, and M. Chhowalla, "Large-area ultrathin films of reduced graphene oxide as a transparent and flexible electronic material," *Nature Nanotech*, vol. 3, no. 5, Art. no. 5, May 2008, doi: 10.1038/nnano.2008.83.

[94] F. Bonaccorso *et al.*, "Graphene, related two-dimensional crystals, and hybrid systems for energy conversion and storage," *Science*, vol. 347, no. 6217, p. 1246501, Jan. 2015, doi: 10.1126/science.1246501.

[95] D. S. Hecht, L. Hu, and G. Irvin, "Emerging Transparent Electrodes Based on Thin Films of Carbon Nanotubes, Graphene, and Metallic Nanostructures," *Advanced Materials*, vol. 23, no. 13, pp. 1482–1513, 2011, doi: 10.1002/adma.201003188.

[96] Y. Fang *et al.*, "Two-Dimensional Mesoporous Carbon Nanosheets and Their Derived Graphene Nanosheets: Synthesis and Efficient Lithium Ion Storage," *J. Am. Chem. Soc.*, vol. 135, no. 4, pp. 1524–1530, Jan. 2013, doi: 10.1021/ja310849c.

[97] Y.-X. Wang, S.-L. Chou, H.-K. Liu, and S.-X. Dou, "Reduced graphene oxide with superior cycling stability and rate capability for sodium storage," *Carbon*, vol. 57, pp. 202–208, Jun. 2013, doi: 10.1016/j.carbon.2013.01.064.

[98] H. Su and Y. H. Hu, "Recent advances in graphene-based materials for fuel cell applications," *Energy Science & Engineering*, vol. 9, no. 7, pp. 958–983, 2021, doi: 10.1002/ese3.833.

[99] S. Li, C. Cheng, and A. Thomas, "Carbon-Based Microbial-Fuel-Cell Electrodes: From Conductive Supports to Active Catalysts," *Advanced Materials*, vol. 29, no. 8, p. 1602547, 2017, doi: 10.1002/adma.201602547.

[100] S. Hu *et al.*, "Proton transport through one-atom-thick crystals," *Nature*, vol. 516, no. 7530, Art. no. 7530, Dec. 2014, doi: 10.1038/nature14015.

[101] C.-F. Liu, Y.-C. Liu, T.-Y. Yi, and C.-C. Hu, "Carbon materials for high-voltage supercapacitors," *Carbon*, vol. 145, pp. 529–548, Apr. 2019, doi: 10.1016/j.carbon.2018.12.009.

[102] E. Frackowiak, Q. Abbas, and F. Béguin, "Carbon/carbon supercapacitors," *Journal of Energy Chemistry*, vol. 22, no. 2, pp. 226–240, Mar. 2013, doi: 10.1016/S2095-4956(13)60028-5.

[103] H. Banda *et al.*, "Investigation of ion transport in chemically tuned pillared graphene materials through electrochemical impedance analysis," *Electrochimica Acta*, vol. 296, pp. 882–890, Feb. 2019, doi: 10.1016/j.electacta.2018.11.122.

[104] H. Zhang, D. Yang, A. Lau, T. Ma, H. Lin, and B. Jia, "Hybridized Graphene for Supercapacitors: Beyond the Limitation of Pure Graphene," *Small*, vol. 17, no. 12, p. 2007311, 2021, doi: 10.1002/smll.202007311.

[105] R. Mendoza, J. Oliva, and V. Rodriguez-Gonzalez, "Effect of the micro-, meso- and macropores on the electrochemical performance of supercapacitors: A review," *International Journal of Energy Research*, vol. 46, no. 6, pp. 6989–7020, 2022, doi: 10.1002/er.7670.

[106] J. Bahadur, A. P. Radlinski, Y. B. Melnichenko, M. Mastalerz, and A. Schimmelmann, "Small-Angle and Ultrasmall-Angle Neutron Scattering (SANS/USANS) Study of New Albany Shale: A Treatise on Microporosity," *Energy Fuels*, vol. 29, no. 2, pp. 567–576, Feb. 2015, doi: 10.1021/ef502211w.

[107] D. Lombardo, P. Calandra, and M. A. Kiselev, "Structural Characterization of Biomaterials by Means of Small Angle X-rays and Neutron Scattering (SAXS and SANS), and Light Scattering Experiments," *Molecules*, vol. 25, no. 23, Art. no. 23, Jan. 2020, doi: 10.3390/molecules25235624.

[108] J. Ilavsky and P. R. Jemian, "Irena: tool suite for modeling and analysis of small-angle scattering," *J Appl Cryst*, vol. 42, no. 2, pp. 347–353, Apr. 2009, doi: 10.1107/S0021889809002222.

[109] D. Yamaguchi, N. Miyamoto, S. Koizumi, T. Nakato, and T. Hashimoto, "Hierarchical structure of niobate nanosheets in aqueous solution," *J Appl Cryst*, vol. 40, no. s1, pp. s101–s105, Apr. 2007, doi: 10.1107/S0021889807011727.

[110] A. Yaghmur and I. Hamad, "Microfluidic Nanomaterial Synthesis and In Situ SAXS, WAXS, or SANS Characterization: Manipulation of Size Characteristics and Online Elucidation of Dynamic Structural Transitions," *Molecules*, vol. 27, no. 14, Art. no. 14, Jan. 2022, doi: 10.3390/molecules27144602.

[111] M. Ballauff, "SAXS and SANS studies of polymer colloids," *Current Opinion in Colloid & Interface Science*, vol. 6, no. 2, pp. 132–139, May 2001, doi: 10.1016/S1359-0294(01)00072-3.

[112] "Pore characterization of shales: A review of small angle scattering technique," *Journal of Natural Gas Science and Engineering*, vol. 78, p. 103294, Jun. 2020, doi: 10.1016/j.jngse.2020.103294.

[113] D. Saurel *et al.*, "A SAXS outlook on disordered carbonaceous materials for electrochemical energy storage," *Energy Storage Materials*, vol. 21, pp. 162–173, Sep. 2019, doi: 10.1016/j.ensm.2019.05.007.

[114] B. Jacrot and G. Zaccai, "Determination of molecular weight by neutron scattering," *Biopolymers*, vol. 20, no. 11, pp. 2413–2426, 1981, doi: 10.1002/bip.1981.360201110.

[115] L. F. Ruppert *et al.*, "A USANS/SANS Study of the Accessibility of Pores in the Barnett Shale to Methane and Water," *Energy Fuels*, vol. 27, no. 2, pp. 772–779, Feb. 2013, doi: 10.1021/ef301859s.

[116] L. M. Anovitz and D. R. Cole, "Characterization and Analysis of Porosity and Pore Structures," *Reviews in Mineralogy and Geochemistry*, vol. 80, no. 1, pp. 61–164, Jan. 2015, doi: 10.2138/rmg.2015.80.04.

[117] M. Sun *et al.*, "Pore connectivity and water accessibility in Upper Permian transitional shales, southern China," *Marine and Petroleum Geology*, vol. 107, pp. 407–422, Sep. 2019, doi: 10.1016/j.marpetgeo.2019.05.035.

[118] C. R. Clarkson *et al.*, "Characterization of tight gas reservoir pore structure using USANS/SANS and gas adsorption analysis," *Fuel*, vol. 95, pp. 371–385, May 2012, doi: 10.1016/j.fuel.2011.12.010.

[119] Y. B. Melnichenko *et al.*, "Accessibility of pores in coal to methane and carbon dioxide," *Fuel*, vol. 91, no. 1, pp. 200–208, Jan. 2012, doi: 10.1016/j.fuel.2011.06.026.

[120] J. Bahadur, L. F. Ruppert, V. Pipich, R. Sakurovs, and Y. B. Melnichenko, "Porosity of the Marcellus Shale: A contrast matching small-angle neutron scattering study," *International Journal of Coal Geology*, vol. 188, pp. 156–164, Mar. 2018, doi: 10.1016/j.coal.2018.02.002.

[121] Z. Mileeva, D. K. Ross, D. Wilkinson, S. M. King, T. A. Ryan, and H. Sharrock, "The use of small angle neutron scattering with contrast matching and variable adsorbate partial pressures in the study of porosity in activated carbons," *Carbon*, vol. 50, no. 14, pp. 5062–5075, Nov. 2012, doi: 10.1016/j.carbon.2012.06.046.

[122] S. Boukhalfa, L. He, Y. B. Melnichenko, and G. Yushin, "Small-Angle Neutron Scattering for In Situ Probing of Ion Adsorption Inside Micropores," *Angew. Chem. Int. Ed.*, vol. 52, no. 17, pp. 4618–4622, Apr. 2013, doi: 10.1002/anie.201209141.

[123] S. Boukhalfa *et al.*, "*In Situ* Small Angle Neutron Scattering Revealing Ion Sorption in Microporous Carbon Electrical Double Layer Capacitors," *ACS Nano*, vol. 8, no. 3, pp. 2495–2503, Mar. 2014, doi: 10.1021/nn406077n.

CHAPTER II:
Materials and Methods

In this chapter, the syntheses of the studied materials are detailed along with the various characterization techniques employed and presented in **Chapters III, IV** and **V**. The synthesis procedures of the following samples are detailed:

- Graphene Oxide (GO)
- Chemically Reduced Graphene Oxide with hydrazine hydrate (rGO)
- Hydrothermally reduced Graphene Oxide (GA)
- Pillared Graphene Materials:
    - Pillared reduced powder (6RPs)
    - Pillared aerogels (nGAs)

The characterization techniques are detailed in terms of the specifications of the instruments used and the conditions of the measurements. The techniques include:

- X-ray Phototelectron Spectroscopy (XPS)
- Elemental Analysis (EA)
- Thermal Gravimetric Analysis (TGA)
- X-ray Diffraction (XRD)
- Scanning Electron Microscopy (SEM)
- Transmission Electron Microscopy (TEM)
- Conductivity measurement
- Gaz sorption analysis
- TPD-MS measurements
- Electrochemical analysis
- Small angles neutron scattering (SANS)
- Small angles X-ray scattering (SAXS)
- Wide angles X-ray scattering (WAXS)

The focus of the second part of this chapter is to provide fundamental details and specifications of the scattering methods used in this study. In addition, the data treatments and the structural and physical features accessible through these techniques are outlined.

1 Material synthesis

1.1 GO synthesis

Graphite nanopowder (CAS #7782-42-5 - 400 nm APS, 99.9% purity) was purchased from Nanostructured & Amorphous Materials Inc. and washed with hexane and ethyl acetate prior to use to remove any possible contaminants adsorbed on the surface of the graphite sheets. Concentrated sulfuric acid (CAS #7664-93-9 - 95-97%) and hydrochloric acid (CAS #7647-01-0 - 37% solution) were purchased from Sigma Aldrich, sodium nitrate (CAS #7631-99-4 - 99.7%) and hydrogen peroxide (CAS #7722-84-1 - 30% solution) were purchased from VWR Chemical and potassium permanganate (CAS #7722-64-7 - 99%) was purchased from OSI France and used as received without further purification.

3.0 g of graphite was added to a 1L beaker in an ice bath, followed by 90 mL of concentrated sulfuric acid. The mixture was cooled down to 4 °C using an ice batch and kept under stirring. 1.5 g of sodium nitrate was added and the mixture was left to stir for 2 h, while ensuring the temperature did not exceed 5°C. Then, 9.1 g of potassium permanganate was very slowly and carefully added to the reaction medium, controlling that the temperature would not rise above 4-5°C. The mixture was left to stir for 90 min while maintaining the temperature between 0 and 3°C. The beaker was then removed from the ice bath and left to reach room temperature. Afterwards, 100 ml of milliQ water (18MΩ) was added slowly using a Pasteur pipette, controlling that the temperature would not exceed 95°C. The temperature was then set to 95°C and the mixture stirred for 2 h. The color changed from purple to brown as the 100 mL of milliQ water was added. Another 300 mL of milliQ water was added to the mixture and the mixture was stirred at 95°C for a further 90 minutes. The heating was stopped and the mixture allowed to cool down to room temperature. Then, 30 ml of 30% hydrogen peroxide solution was added to further oxidize the graphite and facilitate its exfoliation and the mixture was stirred for 30 min before adding 450 mL of milliQ water was added and the mixture left overnight with stirring.

Then, the brown mixture was then filtered under vacuum on cellulose filter paper using fritted funnels. The precipitate was collected and redispersed in a 1L beaker using 900 mL of milliQ water. This suspension was then sonicated for 1 h in a water sonication bath. Afterwards, 100 mL of 37% hydrochloric acid was added to remove the metallic impurities and the mixture was stirred overnight.

The subsequent centrifugation and redispersion steps are summarized in **Figure II.1** and described in detail below. Most of these steps were carried out to wash away remaining starting materials or by-products and to adjust the pH to a less acidic value (2.6). The final centrifugation step is a size selection step aiming at separating exfoliated GO from larger GO aggregates as well as non-oxidized graphite or less oxidized large graphene oxide sheets.

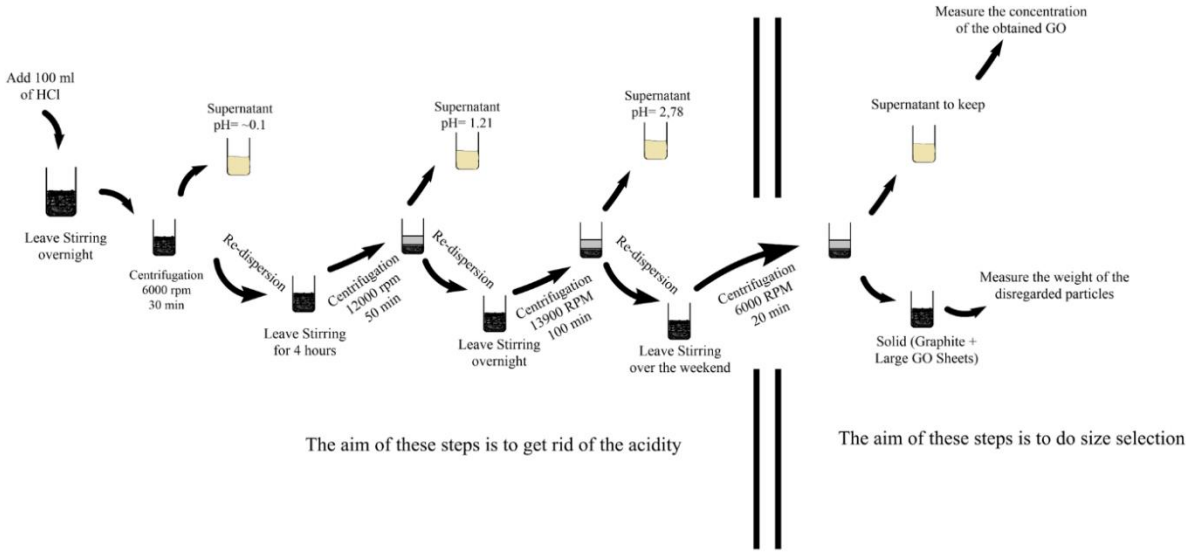

Figure II. 1 Steps for acidity removal and size selection

So, the above mixture was centrifuged at 6000 rpm for 30 min and the precipitate was collected and re-dispersed using a volume of milliQ water between 800 and 1400 ml before being left to stir for approximatively 3h. The pH of the supernatant of the 1st centrifugation was measured to be 0.32 before being discarded. Another centrifugation was done, at 12000 rpm for 50 min. The pH of the supernatant was found to be 1.46, the precipitate was re-dispersed in a volume of milliQ water between 800 and 1400 ml and then left to stir overnight.

Further centrifugation at 13900 rpm for 100 min was then performed, the pH of the supernatant was measured (2.7) and the precipitate was redispersed with a volume of milliQ water between 800 and 1000 mL. The mixture was then stirred over the week-end.

Finally, the mixture was centrifuged at 6000 rpm for 20 min. Afterwards, the supernatant was kept while the precipitate was discarded. A 25 ml aliquot was pipetted out from the supernatant for freeze-drying. The freeze-dried sample was weighed and the concentration was determined.

The concentration was adjusted to 5 mg/mL by either adding water or evaporating water in case the concentration was higher or lower than 5 mg/mL. The GO in water dispersion was stored in a bottle in a dark place away from light to avoid self-reduction of epoxides.

1.2 rGO synthesis

Hydrazine hydrate (CAS #10217-52-4 - 50-60%) was purchased from Sigma Aldrich and used as received without further purification.

12.5 mL of hydrazine hydrate was added to 75 mL of 5 mg/mL GO in water dispersion and the mixture was stirred at 90°C for 24 h with a condenser connected to the round bottom flask. The mixture was then filtered under vacuum on ash-free cellulose filter paper (ash content < 0.01 %) using a P4 fritted glass funnel. The resulting powder was then washed with large volumes of milliQ water to remove any traces of hydrazine, then washed with ethanol, followed by a final wash with absolute ethanol. The sample was then dried overnight at 80°C in an oven under the fume hood. The product was weighed and found to be 175 mg. The sample was stored in a desiccator with silica beads.

1.3 GA synthesis

30 mL of 5 mg/mL GO in water dispersion was added to the inner Teflon container of an autoclave. The Teflon container was then placed in a water sonication bath for 15 min before placed in the hydrothermal autoclave reactor. The reactor was heated at 180°C for 17 h. The product was then washed for 30 min in a P3 fritted glass funnel with no filter paper and no vacuum, keeping the product covered with water. The product was then frozen in liquid nitrogen for 10 min and transferred to a freeze-dryer for 2 days. The weight of the self-standing monolith was 77 mg. The sample was stored in a desiccator with silica beads

1.4 6RPs synthesis

The synthesis was performed in two steps: chemical functionalization followed by chemical reduction. Three different diamine equivalent numbers were used for the preparation of 6RP: 0.2, 1, and 2 equivalents. For the functionalization, 0.435 g (3.74 mmol), 2.175 g (18.7 mmol), and 4.35 g (37.4 mmol) of 1,6-diaminohexane were dissolved in 50 mL of absolute ethanol in a 100 mL round bottom flask for 6RP-0.2, 6RP-1, and 6RP-2 respectively. Then, 50 mL of 5 mg/mL GO in water dispersion was added and the mixture was stirred at 80°C for 24 h with a water condenser connected to the round bottom flask. The mixture was then filtered under vacuum on an ash-free cellulose filter paper (ash content < 0.01 %) using a P4 fritted

glass funnel. The solid sample was then washed with ethanol, milliQ water and finally absolute ethanol before being drying for 1 h at 80°C in an oven.

The functionalized samples were then transferred to a round bottom flask. 10 mL of hydrazine hydrate was added to the samples and the mixtures were left to stir at 90°C for 24 h with a condenser connected to the round bottom flask. The mixtures were then filtered under vacuum on an ash-free cellulose filter paper (ash content < 0.01 %) using a P4 fritted glass funnel. The samples were then washed with large volumes of milliQ water to remove any traces of hydrazine, then were washed with ethanol, followed by a final wash with absolute ethanol. The samples were then dried overnight at 80°C in an oven under the fume hood. The products were weighed and found to be ~130 mg.

1.5 nGAs synthesis

30 mL of 5 mg/mL GO in water dispersion was added to the Teflon inner container of an autoclave. Various alkyl diamines were added in different quantities depending on their length and the equivalent number as shown in **Table.II.1**. The Teflon container was then placed in a water sonication bath for 15 minutes before being placed in the hydrothermal autoclave reactor. The reactor was heated at 180°C for 17 h. The product was then washed for 30 min in a P3 fritted glass funnel without filter paper and no vacuum, while maintaining the product always covered with clean water. The product was then frozen using liquid nitrogen for 10 min and transferred to a freeze-dryer for 2 days. The sample was stored in a desiccator with silica beads

Table II.1: The different pillars used for nGAs synthesis and their respective weights.

Sample	Alkyl diamine	Weight (mg)
6GA-0.05	1,6 diaminohexane	65.2
6GA-0.5	1,6 diaminohexane	652
6GA-1	1,6 diaminohexane	1304
8GA-0.05	1,8 diaminooctane	80.7
10GA-0.05	1,10 diaminodecane	96.3
12GA-0.05	1,12 diaminododecane	112

2 Basic characterization

2.1 X-ray diffraction (XRD)

X-ray Diffraction (XRD) experiments were conducted using a Panalytical X'pert PRO X-ray diffractometer with a Co Kα radiation source (λ=1.798 Å). The measurements were performed in a θ-θ goniometer configuration in reflection mode. Sample analysis were conducted on pellets with a diameter of 6 mm and a sample weight of approximately 5 mg. These pellets were prepared by pressing the samples in a mold under 2 Tons for 10 min.

Prior to measurements, alignment procedures were carried out using a 1/32 fixed slit, a 4 mm fixed mask, a 5 mm fixed mask, and a programmable beam attenuator Fe 0.1 m with an attenuation factor of 84.96 on the incident beam side and a 0.27 attenuation slit on the detector side to protect it during alignment. A ponctual 0-D detector was used. Alignments were conducted for 2θ (angle between incident and reflected beams), Ω (angle between incident beam and sample's surface), and z (the height of the sample holder stage).

During the measurements, the 1/32 fixed slit was replaced by a 1/8 fixed slit, the attenuator was stopped, and the 0.27 slit was removed. The measurement range was from 3° to 60° with a step size of 0.05°. Diffractograms of all the samples were fitted using HighScore to extract the d-spacing, peak position, and full width at half maximum (FWHM) of the peaks. Origin software was used for plotting the diffractograms.

2.2 X-Ray Photoelectron Spectroscopy (XPS)

XPS analysis was conducted using a PHI Versa Probe II spectrometer equipped with a monochromatized Al Kα X-ray source (1486.6 eV) with a 200 µm beam size. The samples were mounted on a conductive Cu double- sided tape surrounded by stainless steel (SS) rings to facilitate surface charge state replenishment. For insulating samples like graphene oxide (GO), double charge compensation was applied using an electron-neutralizer and an ion-gun. Analyses were performed on areas averaging 200 µm² under ultra-high vacuum conditions.

The survey spectra were acquired with a pass energy of 117.4 eV covering a range from 0 to 1100 eV. High-resolution spectra were obtained with a pass energy of 23.5 eV within specific ranges: 276 to 298 eV for C1s, 523 to 545 eV for O1s, and 389 to 411 eV for N1s. SXI photoelectron images were recorded for each sample. All the spectra were calibrated using the the C1s sp2 peak at 284.3 eV. Peak fitting was performed using Multipak software, and Origin

software was used for plotting the survey and high-resolution spectra along with their fitted peaks

2.3 Elemental Analysis (EA)

EA experiments were performed on a UNICUBE® organic elemental analyzer (C, H, N and S) by Elementar. The samples were loaded into tin boats and their masses were maintained between 1.5 and 2 mg. Three sample-loaded tin boats were prepared for each sample for statistical analysis. The samples were then introduced in the oven under He gas, then burnt at 1150°C in the presence of O_2, and the resulting gases were treated in a reduction tube at 850°C. The resulting gases were then passed through an adsorption column where thermal programmed desorption took place at the following temperatures: 40°C for N_2, 60°C for CO_2, 150°C for H_2O and 210°C for SO_2. A thermal conductivity detector quantified the amounts of each element from the difference between the thermal conductivity of pure He gas and a mixture of He gas and the gas carrying the element of interest (e.g. CO_2 for detection of C). The oxygen amount was then assumed to correspond to the remaining weight percentage, after confirming with XPS the presence of only C, N and O in the sample. Origin software was used for plotting histograms of the C, H, N and O content of each sample.

2.4 Thermal Gravimetric Analysis (TGA)

TGA experiments were carried out using a Setaram TGA 92 instrument. The experiments were performed under Ar gas from 30°C to 800°C with a heating ramp of 5 °C/min. Stabilization was carried out at 30°C for 30 min prior to heating to reach a stable mass prior to the analysis. The number of moles of pillars per gram of sample was calculated from the weight loss recorded between the changes in the slopes of the degradation profile before and after the degradation step of the pillars, as shown for 6RP in **Figure II.2**. This weight loss was then corrected by subtracting the weight loss of rGO in the same temperature region to account for the contribution of the reduced graphene oxide support to the oxygen loss. Origin software was used to plot the degradation profiles.

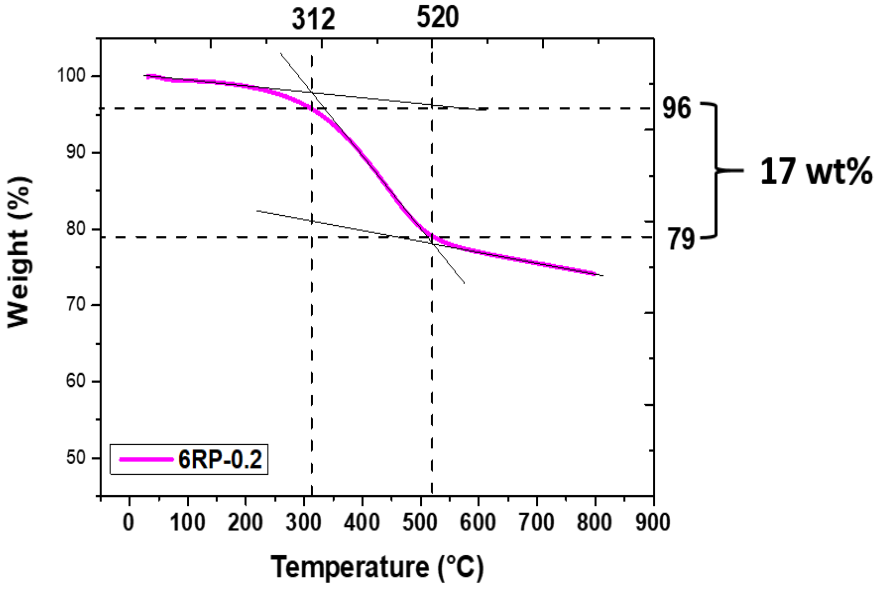

Figure II. 2 TGA profile of the 6RP-0.2 sample with the difference in weight % calculated from the changes in the slopes of the degradation profile before and after the degradation step.

2.5 Scanning Electron Microscopy (SEM)

SEM Images were obtained using a Zeiss Ultra 55 electron microscope with an accelerating voltage of 3 keV. The samples were mounted on the sample holder using a double-sided conductive copper tape. No conductive layer was sputtered. The Working Distance (WD) was adjusted for each sample. An in-lens detector was used to detect Secondary Electrons (SE). SmartSEM software was used for instrument control the and data acquisition.

2.6 Transmission Electron Microscopy (TEM)

TEM images were obtained by monochromatic TEM imaging using a Titan Ultimate (Thermo Fisher) operating at 80 keV with an aberration corrector. The samples were dispersed in 1-propanol using an ultra-water bath sonication system. A titanium wire was folded to form a loop, which is dipped in the solution to extract a small drop. The loop was then placed in contact with a Lacey carbon-coated copper grid, resulting in the transfer of the drop onto the grid, which is then left to air dry before transferred to the microscope equipment.

2.7 Conductivity measurement

Conductivity measurements were done using the four-point probe method. A low intensity current flows between the outer two probes, and the voltage is measured across the two inner probes. The samples analyzed were in the form of pellets of a diameter of 6 mm,

weighing around 10-12 mg. The pellets were done through pressing the samples in a mold under 2 Tons for 10 minutes. The conductivity was calculated according to the following equations:

$$R_s = \frac{V}{I} * CF \qquad (II.1)$$

$$\rho = R_s W \qquad (II.2)$$

$$\sigma = \frac{1}{\rho} \qquad (II.3)$$

Where R_s is the sheet resistance ($\Omega/square$), V is the measured voltage (V), I is the applied current (A), CF is a shape-related correction factor, ρ is the resistivity ($\Omega.m$), W is the thickness of the sample (m) and σ is the conductivity (S/m). The shape-related correction factor is based on the ratio between different shape and probe related parameters as shown in (**Figure II.3**). Such a correction factor was found to be 3.2 for these pellets of 6 mm diameter.

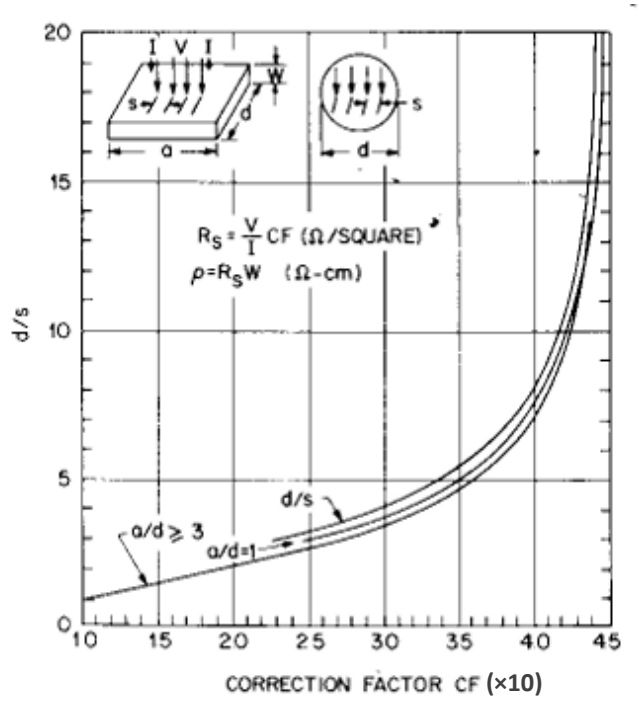

Figure II. 3 The shape related correction factor for the conductivity measurement using a four-point probe along with the CF of 3.2 corresponding to the diameter of the pellets used

2.8 N_2 and H_2 adsorption isotherms

High resolution N_2 and H_2 adsorption/desorption isotherms (performed in CEMTHI Orléans by Pr Encarnacion Raymundo and DR. Conchi Ania) were carried out at 77 K in a volumetric analyzer (3Flex, Micromeritics), equipped with a turbo molecular vacuum pump

and three pressure transducers, allowing accurate measurements between 10^{-6} and 1 bar. The samples were previously outgassed under a dynamic vacuum (ca. 10^{-5} mbar) at 77 K for 24 h. Ultrahigh purity N_2 (99.9992 %) was supplied by Air Products. The Brunauer-Emmett-Teller theory was used to calculate the specific surface area (SBET); the total pore volume was evaluated at relative pressure of 0.99 for all the materials. The micropore volume was estimated using the Dubinin-Raduskevich method [1]. The pore size distribution was calculated from the high-resolution gas adsorption data using the 2D-NLDFT-HS method [2].

2.9 Temperature-programmed desorption coupled with mass spectrometry (TPD-MS)

TPD-MS (performed in CEMTHI Orléans by Pr Encarnacion Raymundo and DR. Conchi Ania) was performed under inert atmosphere (Ar, 100 mL/min). The sample (around 10 mg) was placed in a thermo-balance and heat treated up to 900 °C at a rate of 10 ^{o}C min^{-1}. The decomposition products (gas evolved) were monitored by on-line mass spectrometry (Skimmer, Netzsch, Germany).

3 Electrochemistry

3.1 Free standing electrodes preparation

Free-standing electrodes (FSE) were prepared as follows: 80 wt% active material, 5 wt% PTFE as a binder, and 15 wt% acetylene black (AB) as a conductive additive. These products were placed in a 100 mL beaker. A minimum amount of absolute ethanol was added to disperse the powders. The mixture was stirred with a magnetic stirrer for approximately 30 min. This was followed by manual stirring with a glass rod until a paste was formed (approximately 1 h). The paste was then spread on a glass plate and flattened with a glass rod. This paste was then placed in an oven at 80°C for 24 h. This dry paste was then cut into 8 mm diameter FSE discs. The counter electrode was prepared similarly with YP50 (activated carbon) as active materials. In electrochemical testing, the weight of the counter electrode was at least 8 time the weight of the working electrode. In this way the working electrode was not the limiting factor.

.

3.2 The studied electrolytes

The electrolytes used in this works were 3M H_2SO_4, 1M $TEABF_4$ in AN, 1M $THABF_4$ in acetonitrile (AN), 1M $TEABF_4$ in deuterated acetonitrile (d-AN), and 1M $THABF_4$ in d-AN.

Concentrated sulfuric acid was added to milliQ water to reach the desired concentration for the aqueous 3M H_2SO_4 electrolyte. The salts of the organic electrolytes were weighed and dissolved in AN and d-AN. $TEABF_4$ and $THABF_4$ stands for tetraethylammonium tetrafluoroborate and tetrahexylammonium tetrafluoroborate

3.3 Electrochemical program and data treatment

The FSE was cycled by Cyclic Voltammetry (CV) at 50 mV/s for 300 cycles to reach stabilization and allow electro-wetting. After the stabilization step, the samples were cycled using CV at 5, 10, 20, 50, and 100 mV/s for 10 cycles at each scan rate.

The specific capacitance in F/g was calculated from the CVs according to the following equation:

$$C_s = \frac{\int_{V_1}^{V_2} I\, dV}{2 * \Delta V * m * v} \qquad (II.4)$$

Where C_s is the specific capacitance (F/g), V_1 and V_2 are the limits of the potential window (V), I is the current response (A), ΔV is the potential window (V), m is the mass of the electrode (g) and v is the scan rate. The nominator of **Equation (II.4)** means integrating the whole area enclosed by the CV curve, accordingly, a factor of 2 is added to the denominator.

4 Standard deviation

In this PhD thesis, the values reported for XRD, XPS, EA and electrochemistry were the average of at least three measurements (more than 6 for XRD) and the standard deviation was determined based on these values. Reporting the average values along with their respective standard deviation rather than selecting the highest values was chosen to promote scientific rigor and avoid misinterpretation. However, the impact of the difference in GO batches could not be avoided.

5 Advanced characterizations instruments setup

5.1 SANS at D22 (Institut Laue Langevin (ILL))

The instrument used in this work was the D22 large dynamic range small-angle diffractometer. The neutron wavelength is controlled by a velocity selector (Anatole), which selects neutrons based on their velocity with a resolution of $\Delta\lambda/\lambda = 10\%$ for a wavelength range

from 4.5 to 40 Å. Dynamic collimation compensates for beam divergence, allowing a source-to-sample distance ranging from 1.4 to 17.6 m and a total Q range of 4×10^{-4} to 1.05×10^{-1} $Å^{-1}$. The instrument is operated using the in-house software Nomad. In this PhD work, the measurements were performed within two sample-to-detectors distances (5.6 and 17.7 m) to cover a Q range of 0.003 $Å^{-1} < Q < 0.2$ $Å^{-1}$ (*i.e.* from 3 nm to 210 nm). Three sets of experiments were performed at D22:

- On pristine dry materials: the materials were placed inside a DSC aluminum cell (aluminum is transparent to neutrons), positioned between two Quartz windows and placed in a 18 position sample holder.
- On suspensions of pristine materials: pristine materials were dispersed in different mixtures of hydrogenated and deuterated cyclohexane then introduced inside a 1 mm quartz Hellma cell, and placed in a 22 position sample holder. (This experiment was also conducted on SANS-I at Paul Sherrer Institut (PSI) within the same Q-range).
- *In-situ* measurements of FSE during polarization. The electrochemical cell **(see Chapter V Section 3)** was mounted on a sample holder using a Teflon screw to avoid any current leakage and short-circuit. A 5 channels VSP Biologic potentiostat was used for the electrochemical measurements.

The collected scattering profiles were corrected to the absolute intensity (cm^{-1}) by i) subtraction of the empty cell as shown in **Equation (II.5),** and ii) normalization by the solid thickness as shown in **Section 8.3**. Furthermore, in SANS the scattering from hydrogen lead to incoherent scattering, which should be subtracted as shown in **Section 7.1.3.**

$$I_c = \left(\frac{1}{T_s T_{ec}}(I_s - I_{cd})\right) - \left(\frac{1}{T_{ec}}(I_{ec} - I_{cd})\right) \qquad (II.5)$$

Equation (II.5) shows the correction of the measured data. This correction involves the measurement of cadmium plate which completely absorbs the beam (corresponds to the electronic noise of the detector, noted Cd), empty beam (used for the calculation of the transmission), empty cell (corresponds to the contribution of the empty cell in the transmission and scattering, noted ec), water (used to calculate the efficiency of the detector and compensate for geometrical effects) and finally the sample (noted s).

5.2 SAXS/WAXS at D2AM (European Synchrotron Radiation Facility (ESRF))

Synchrotron radiation is a form of electromagnetic radiation emitted by accelerated relativistic particles such as electrons or positrons. The ESRF operates with electron energies close to 6 GeV, producing photons across a wide range of wavelengths, from the visible to the very hard X-ray regime, approximately 2.5×10^{-12} m.

The D2AM beam line is equipped with two detectors that allow simultaneous SAXS and WAXS acquisition over an energy range from 6 keV to 45 keV and a beam size ranging from 30 μm^2 to 5 mm^2. Two sets of experiments were conducted on this beam line:

- *Ex-situ* measurements on solid pristine materials: the materials were placed between two Kapton windows and placed in a 20 position sample holder.
- *In-situ* and *operando* measurements on FSE: the electrochemical cell **(see Chapter V Section 3)** was held on a holder with a Teflon screw to avoid any current leakage. A 5 channel VSP Biologic potentiostat was used for the electrochemical measurements.

For these two experiments, the scattering profiles were recorded simultaneously on both detectors (SAXS and WAXS). The measured Q range was: $0.003\ Å^{-1} < Q < 0.2\ Å^{-1}$ for SAXS and $0.5\ Å^{-1} < Q < 3\ Å^{-1}$ for WAXS.

6 Principle of small angle scattering

Small angle scattering techniques (X-rays, neutrons) measure nanoscale heterogeneities. In a scattering experiment, the interaction between a monochromatic beam of wavelength λ and the atoms of the sample is studied. As a result of this interaction, the wave is scattered in all directions in space (**Figure II.4**). The interaction responsible for the small angle scattering is the photon-electron interaction for X-rays (SAXS), and the neutron-nucleus interaction for neutrons (SANS).

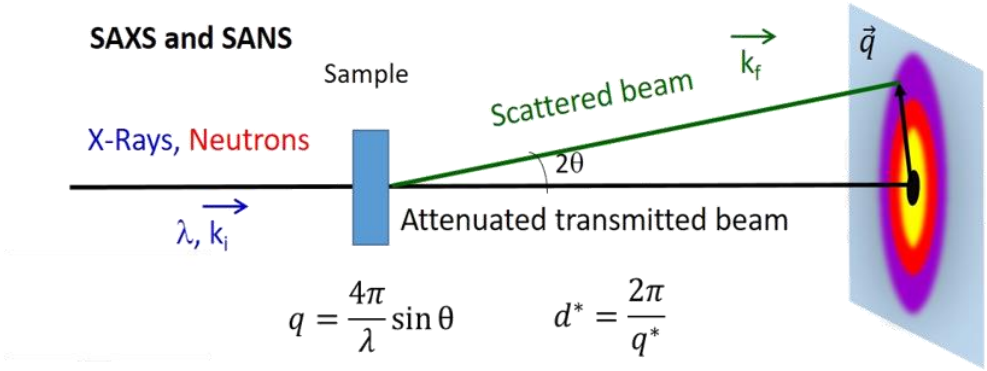

Figure II. 4 Schematic representation of a scattering experiment [3]

The scattered intensity collected on a 2D detector is expressed as a function of the scattering vector Q:

$$Q = k_f - k_i \qquad (II.6)$$

Where k_i and k_f are the scattering vectors of the incident and scattered waves, respectively. Since the scattering is elastic, the magnitudes of the vectors k_i and k_f are identical and equal to $2\pi/\lambda$, where λ is the wavelength. Therefore, the magnitude of the vector q is thus determined by the equation:

$$\|Q\| = Q = \frac{2\pi}{\lambda}\sin(\theta) \qquad (II.7)$$

With 2θ the scattering angle.

The magnitude of the vector Q is inversely proportional to the probed distance (d) in real space following the equation:

$$d = \frac{2\pi}{Q} \qquad (II.8)$$

The probed Q values (reciprocal space) and corresponding distances (real space) in this work are illustrated in **Figure II.5**.

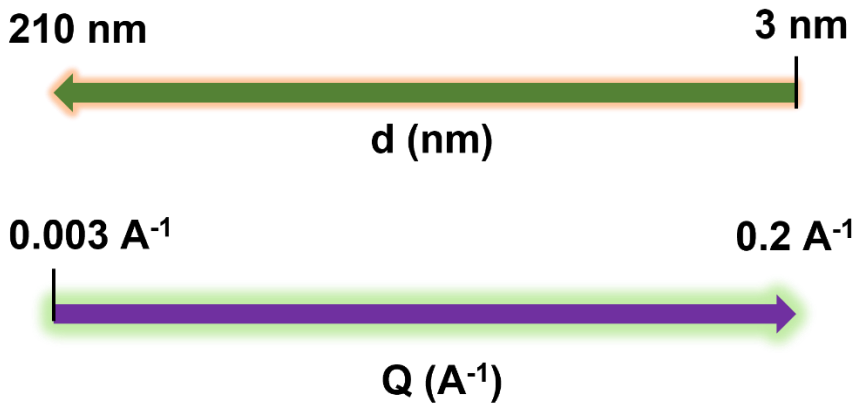

Figure II. 5 The probed scale in SAS experiments (Q) in this study and the corresponding scale in real space (d)

The scattered intensity is associated with the material's structure and the type of radiation employed. The scattering capability of a material's element is characterized by the scattering length density $\rho(r)$:

$$\rho(r) = \sum \rho_i\,(r) b_i \qquad (II.9)$$

Where $\rho_i(r)$ represents the local density of the scattering element, and b_i is the characteristic coherent scattering length for neutrons and electrons in the case of X-rays. The diffusion length for an electron is equal to the Thomson scattering length ($b_e = 2.82\times10^{-15}$ m). For neutrons, the neutron-nucleus interaction is influenced by the magnetic and nuclear forces. The scattering is therefore isotropic and can be characterized by the coherent scattering length b_i, which for neutrons, unlike X-rays, shows irregular variations between different elements. It also shows variations from one isotope to another, as illustrated in **Figure II.6** [4]**.**

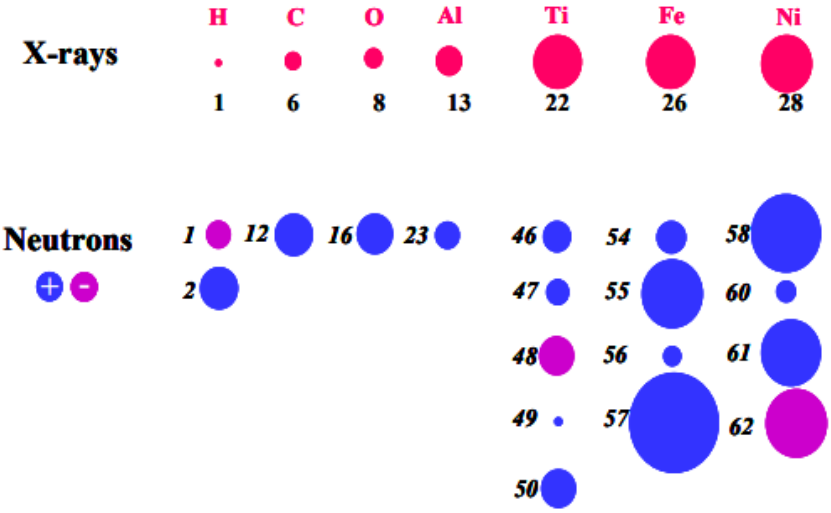

Figure II. 6 Coherent scattering length for X-rays and neutrons, for different elements [4]

A very advantageous feature of neutron scattering is its sensitivity to light elements, making it well suited to study the hydrogen. Another interesting aspect arises from the variations in scattering length between different isotopes, which allows the use of isotopic substitution for contrast variation techniques. More details on this aspect are given in **Section 8.4**.

The total scattered amplitude, which represent the Fourier transform of the fluctuations of the SLD, is expressed in the form of an integral over the volume of the sample:

$$A(Q) = \int_v \rho(r) e^{iq.r}\, dr \qquad (II.10)$$

Experimentally, the amplitude of the scattered signal is not measured, but its intensity is recorded. The scattered intensity per unit volume is obtained by multiplying the scattered amplitude by its conjugate:

$$I(Q) = \frac{A(Q)A^*(Q)}{V} = \frac{1}{V} \iint_{vi\ vj} \rho(r_i)\rho(r_j) e^{iq.(r_i - r_j)} dr_i dr_j \qquad (II.11)$$

In the case of condensed and dispersed particles consisting of homogeneous isotropic scattering centers, for a two-phase system, the scattered intensity I(Q) is proportional to the structure factor S(Q), which describes correlations between objects and their organization, and the form factor P(Q), characterizes the structure of these objects and contains information about the particles shape. For N_p centrosymmetric particles of volume V, the intensity per unit volume V is given by:

$$I(Q) = \varphi V_p \Delta\rho^2 P(Q) S(Q) \qquad (II.12)$$

With:

φ the particle volume fraction.

$\Delta\rho = \rho_1 - \rho_2$ contrast: difference in the SLD between the particles (ρ_1) and the medium (ρ_2).

P(Q): form factor.

S(Q): structure factor.

As shown previously, the scale of the observation window in real space is inversely proportional to the magnitude of the vector q. Consequently, the probed scale depends on the q value (**Figure II.7**): the size and internal structure of the objects (purple circle), or the interface between two mediums (blue circle) can be investigated, and the distances in the real space can be determined directly using **Equation (II.8).**

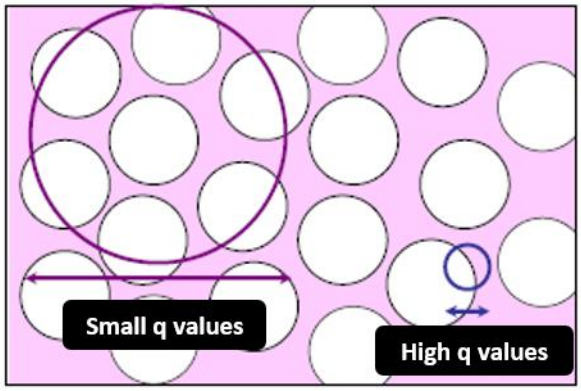

Figure II. 7 the probed structural properties on different scales in a biphasic system

7 The structural features probed by SAS techniques

As shown in **Equation (II.12),** in small-angle scattering (SAS), for a two-phase system, the scattering intensity is proportional to the product of the form factor P(Q) and the structure factor S(Q). These components help to describe the scattering behavior of particles or structures in a sample. The form factor represents the inherent scattering shape of an individual particle or structural element within the sample. The structure factor accounts for the interactions between scattering elements in the sample. It includes information about the spatial arrangement, correlations, and interference effects between multiple scattering elements.

7.1 Form factor P(Q)

The form factor P(q) describes the shape of the scattering object (size, form, polydispersity) and it varies depending on the probed scale (**Figure II.8**).

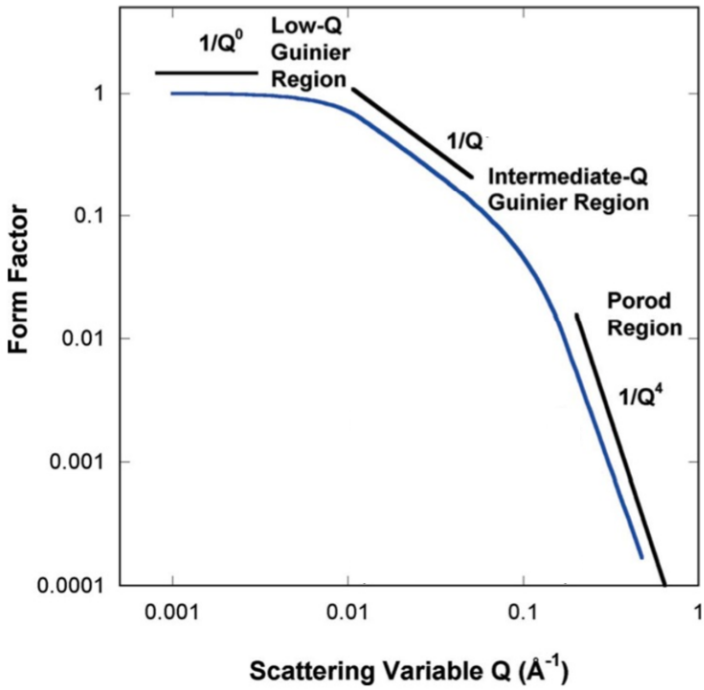

Figure II. 8 Representation of the different Q-regions of the form factor [5]

7.1.1 Low-Q regime "Guinier region"

Considering the case of N homogeneous particles with a defined gyration radius R_g (the distance from the center of mass of the body and the surface), for $q << 1/R_g$ (the probed scale is bigger than the size of the particles) the scattered intensity shows a plateau in the small angle region (**Figure II.8**), which represent the particle size (R_g) which can be determined using the equation:

$$I(Q)\alpha\varphi V_{part} \exp\left(-\frac{(qR_g)^2}{3}\right) \qquad (II.13)$$

Where φ is the volume fraction of particles, and V_{part} is the volume of a particle. R_g can be determined by plotting the intensity as a function of Q^2, the radious of gyration can be calculated from the slope. For a sphere of radius R or a rod of length L, the radius of gyration is given by:

$$R_g = \sqrt{\frac{3}{5}}\,R^2\ (Sphere) \quad R_g = \sqrt{\frac{L^2}{12}}\ (Rod) \qquad (II.14)$$

The geometric radius R and length L can then be calculated. If the material lacks a clearly defined isolated object at this scale, such as in the case of an interconnected network, the scattering intensity at small angles follows a power-law pattern and does not show a plateau. This scenario is conceivable if the objects are very large and extend beyond the observation window (*i.e.* in our case beyond 210 nm).

7.1.2 Intermediate-Q region

The scattering in this region reflects the shape of the internal structure of the object (**Figure II.9**). The scattered intensity by an object with defined dimensions or by a fractal structure with dimension D_m is given by the following formula [6]:

$$I(Q) \alpha\ Q^{-Dm} \qquad (II.15)$$

Table II.2 gathers the expected scattering dimension from simple objects [7].

Table II.2: Power law of the scattered intensity from simple structures in the intermediate-Q region.

	Dimension	Power law
Rod-like particle, filament (R<<L)	$D = 1$	q^{-1}
Disc, thin wafer	$D = 2$	q^{-2}
Ideal polymer, Gaussian chain	$\nu = 1/2$	q^{-2}
Swollen polymer or excluded volume	$D = 1/\nu$	
	$\nu = 3/5$	$q^{-5/3}$

7.1.3 Porod region "scattering by the interface":

At high Q values (blue circle in **Figure II.7)**, the intensity is scattered by the interface between medium 1 and medium 2. The scattered intensity is described by the Porod's law [5].

$$\lim_{q\to\infty} I(Q) = \frac{2\pi(\rho_1 - \rho_2)^2}{q^4}\frac{S}{V} \qquad (II.16)$$

Where S is the total surface area developed within the volume V. The Q^{-4} law (**Figure II.9**) allows the measurement of the specific surface area (SSA) of the object and this is valid only when the interface is smooth and well-defined. In the case of objects with non-smooth surfaces, the roughness can be characterized by a fractal surface dimension D_S ranging between 2 and 3. The scattered intensity is then expressed in the following form [8]:

$$I(Q) \alpha\, Q^{6-D_s} \qquad (II.17)$$

The exponent of the power law, 6-D_S, is therefore 4 for D_S = 2, corresponding to an object with smooth contours, and 3 for D_S = 3 in the extreme case of an object with extremely rough contours. In this study, all the graphene-based materials feature a rough interface (Ds > 2), which hinders the determination of specific surface area (SSA) using small-angle scattering. Furthermore, in SANS, the incident neutron beam interacts with hydrogen nuclei within the sample, leading to incoherent scattering. As an example, **Figure II.9** shows SANS profiles showing such incoherent scattering at high Q values [9] as evidenced by the plateau at high Q values (**Figure II.9 a**). Such incoherent scattering poses challenges in determining the slope in the Porod region and, consequently, complicates the estimation of the surface fractal dimension (Ds). Indeed, this scattering does not contribute to the structural information obtained through SANS, therefore, a subtraction of the incoherent scattering from the total scattering signal is necessary in order to extract the slope at Porod region. The intensity of the final point of the highest Q of the plateau (**Figure II.9 b**) is subtracted from the total intensity of the profile and the slope at high Q values is extracted (**Figure II.9 c)**.

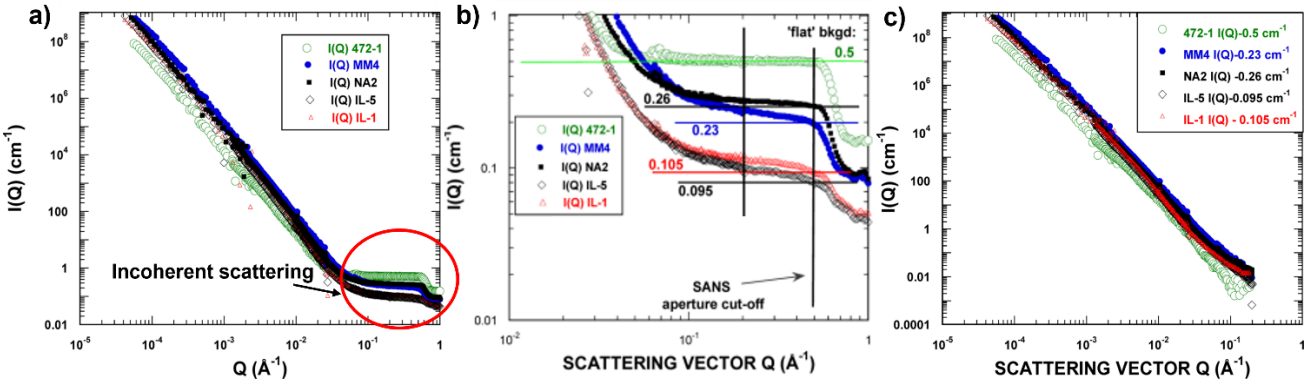

Figure II. 9 (a) SANS profiles of different samples, (b) a zoon on the plateau at high Q values and the determination of the subtraction values, (c) the SANS profiles after subtraction [9]

7.2 Structure factor S(Q):

The structure factor provides information about the organization of scattered objects in terms of interparticle interferences. In the case of a nano-organized material, the structure factor S(Q) contains clear correlation peaks in the scattering profile. The Q position is associated to the mean separation distances d between scattering objects within the sample ($d^*=2\pi/Q$). In dilute systems, where there is no interaction between objects, the structure factor tends to 1 (S(Q) →1), and will not contribute to the scattering profile. In this case, the features within the scattering profile are attributed to the morphological characteristics (form factor). If

the scattering profile of a non-dilute system does not show any peaks or bumps, it is always recommended to assess whether the contribution of S(Q) is hindered by F(Q). The best way to investigate the contribution from S(Q) is to perform SAS experiments on different dilution of the materials and observe the evolution of the scattering profiles. In such experiment, two possible scenarios may arise: i) if the scattering profiles are altered after dilution, it indicates that there is a significant contribution from S(Q) that was removed after dilution, or ii) if the scattering profiles remain unchanged, in this case, there is no substantial contribution from S(Q). In this PhD work, the scattering profiles of the diluted materials were investigated. The materials were diluted in propanol, which allowed obtaining stable dispersion for graphene-based materials among the different solvents tested (water, ethanol, acetonitrile, cyclohexane). Four different dilutions of mg of material per mL of solvent, were studied: 1:1, 1:10, 1:20, and 1:50. Unfortunately, the scattering profiles of all these dilutions showed quasi-zero intensity, which might be due to i) the sedimentation of the solid, ii) insufficient counting time. Given the absence of any peak or bump in SAS profiles of graphene-based materials within the probed scale ($0.003\ Å^{-1} < Q < 0.2\ Å^{-1}$), the contribution of S(Q) is considered to be very low compared to P(Q). Therefore, the features observed within the scattering profiles of these materials are likely to be primarily correlated with the form factor.

8 The fundamental basis of SAS used in this study

8.1 SAS profiles of porous and fractal materials

In this PhD, graphene-based materials are recognized as porous fractal materials as will be presented in **Chapter III Section 5**. The definition of fractal structure refers to a structure that is characterized by self-similarity within some spatial range. It is an "infinitely fragmented" geometric object whose details can be observed at any chosen scale. It is relevant at this stage to introduce the typical SAS profiles of a porous and fractal material with fractal pore structure (correlated pores) as they will serve as the fundamental basis in understanding the SAS profiles of graphene-based materials in the following chapters. **Figure II.11** shows the two typical SAS profiles of a porous and a fractal material. The scattering profile of a porous material (**Figure II.10 a**) exhibits a typical signal of pores at the intermediate-Q range, illustrated by the quasi plateau that indicates a well-defined pore size in this region (non-correlated pores).

At high-Q values, the profile follows a power-law regime, with the slope (6-Ds) dependent of the interface quality. At small angles (Guinier region), in this example, the power-law regime indicates the absence of well-defined size objects in this scale. Conversely, the SAS profile of a fractal material with correlated pores (**Figure II.10 b**) presents a succession of power laws with breaks in slopes that describe the characteristic sizes within the material at the probed scale (ξ and r for example in **Figure II.10 b**). In this example, the profile shows a plateau at small angles indicating that at the probed scale a well-defined object size in probed and can be determined using Guinier model as shown in the previous section. Determining characteristic sizes from scattering profiles can be challenging when the amplitude of break in slopes is low. In such instances, the use of a Kratky presentation becomes essential.

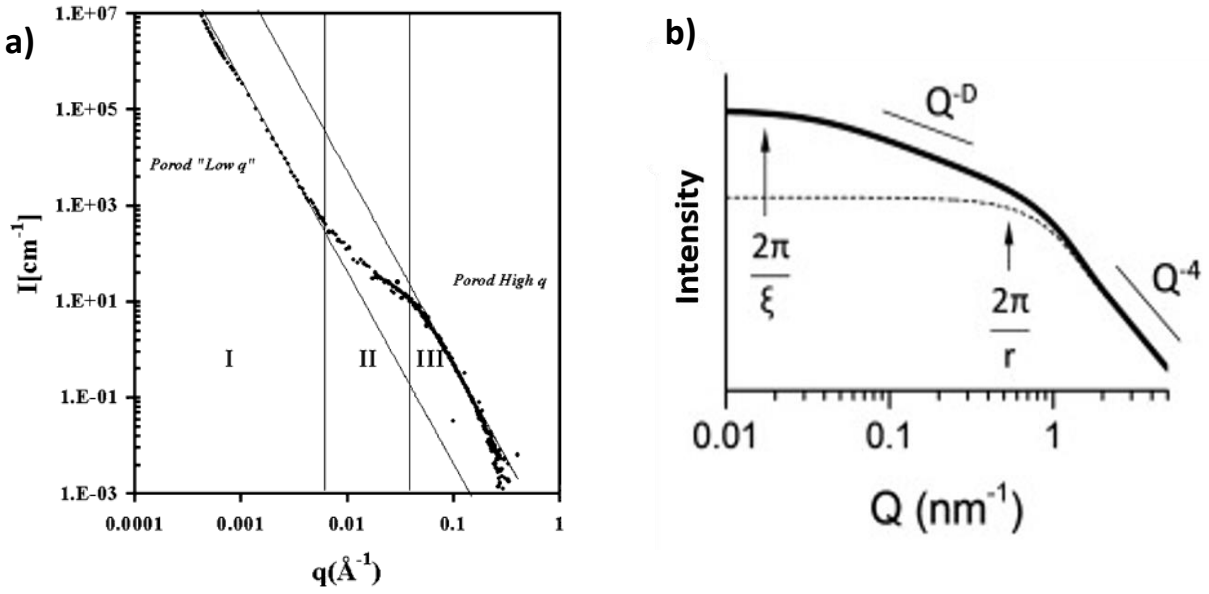

Figure II. 10 (a) Typical SAXS/SANS profile of porous materials (porous glass) [10] *and (b) Typical SAXS/SANS profile of a fractal system (with a fractal dimension D=1.5)* [3].

8.2 Kratky representation

The Kratky plot is a graphical representation commonly used in small angle scattering analysis, which consists in plotting $I(Q)\times Q^2$ vs Q. This representation is particularly valuable for highlighting breaks in slopes within a scattering profile. These breaks may appear more pronounced or, in certain cases, show as peaks. **Figure II.11** shows an example of Kratky presentation on the scattering profiles of three different proteins [11]. As depicted in **Figure II.11 a**, the conventional presentation (I(Q) vs Q) of the scattering profiles does not reveal any distinct break in slopes. However, after applying the Kratky presentation, a peak becomes evident (**Figure II.11 b**).

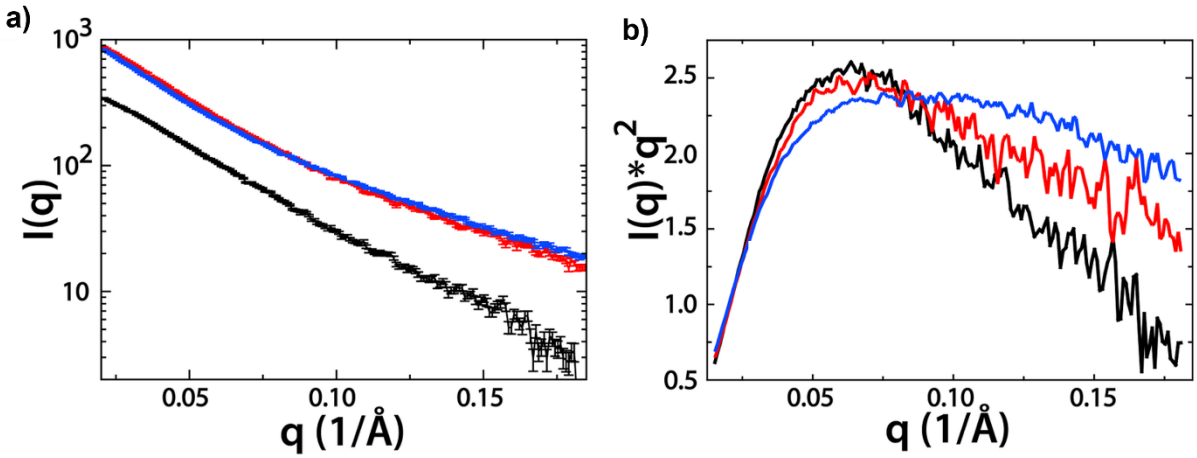

Figure II. 11 (a) SAXS profiles of different protein and (b) their respective Kratky representation [11]

8.3 SAS porosity using the invariant

One of the most useful capabilities of SAS is the identification of the changes in morphological structure including porosity, through analysis of the invariant (INV). The invariant describes a characteristic of small-angle scattering in which the total scattering from a two-phase morphology depends only on the amounts of the two phases and their contrast [12]. Here, if φ is the volume fraction of a given component, and $\Delta\rho = \rho_1 - \rho_2$ is the contrast, then INV can be found using the following equation:

$$INV = \int_0^\infty I_{measured}(Q)Q^2 dQ = 2\pi^2\varphi(1-\varphi)\Delta\rho^2 \qquad (II.18)$$

The absence of structural parameters in **Equation (II.18)** shows that the invariant is a quantity independent of changes even when the morphology is disturbed [13].

In In a porous system, the two phases are the solid phase and the pores, and the volume fraction of pores could be estimated using the invariant (INV). However, as the invariant is calculated for q = 0→∞, the total porosity of the material cannot be determined (during this PhD work Q range 0.003–0.2 $Å^{-1}$). **Equation (II.18)** provides information only on pores within a range inversely proportional to the accessible q range. To facilitate analysis, the powder is represented as a two-layer conformation (**Figure II.12**). One layer consists of the material and the pores visible to the beam, with a thickness e_V and volume V. The other layer, with thickness (e_P - e_V), contains only the pores not visible to the beam.

The accessible porosity in this case is defined as the ratio of the pore volume (V_p) to the total volume of the visible part to the beam (V) and can be calculated using:

$$\varphi^* = \frac{V_p}{V} \qquad (II.19)$$

Equation (II.18) is directly applicable to the layer visible to the beam by replacing the integration limits with the experimentally accessible Q limits and replacing the total porosity with the visible porosity φ^*. This results in a specific invariant denoted INV^*, defined as:

$$INV^* = \int_{0.003}^{0.2} I_{measured}(Q)Q^2 dQ = 2\pi^2\varphi^*(1-\varphi^*)\Delta\rho^2 \qquad (II.20)$$

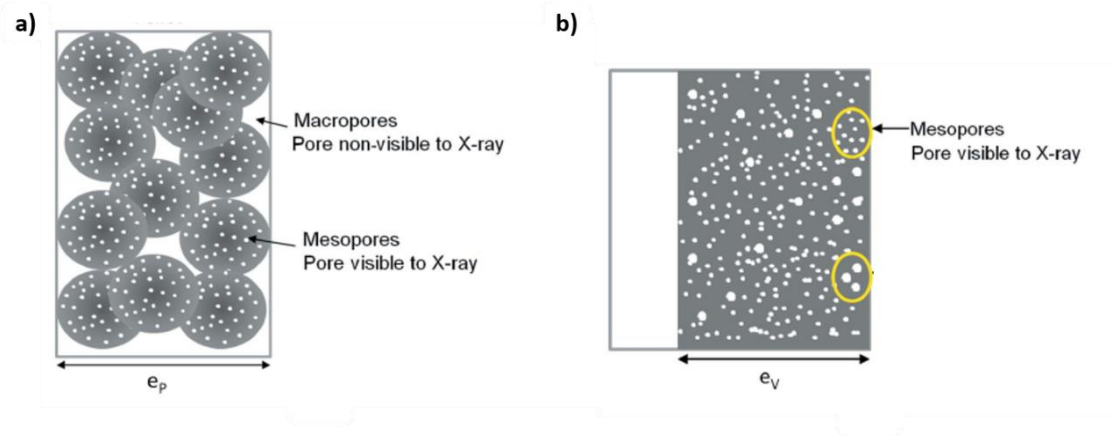

Figure II. 12 Representation of (a) the real measured layer with a thickness e_P, (b) the layer visible to X-rays with a thickness e_V [14]

As demonstrated by Spalla *et al.* [10], a significant challenge in powder materials lies in the unknown values of e_P and e_V. However, an effective thickness (solid thickness) (**Figure II.13**), denoted as e_B, can be derived from the transmission (T) and the absorption coefficient of the solid material (μ_{solid}).

$$e_B = \frac{-\ln(T)}{\mu_{solid}} \qquad (II.21)$$

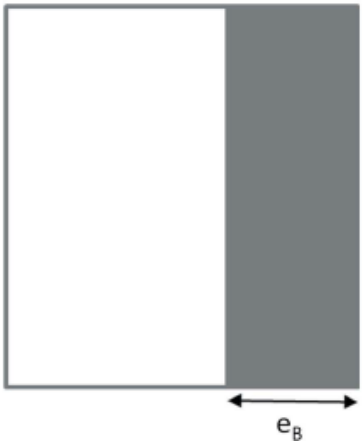

Figure II. 13 Representation of the solid phase with an effective thickness e_B [14]

Following the work of Spalla *et al*. [10], the absolute intensity in the probed q range can be determined using a normalization to the probed solid thickness (e_B) and the volume fraction of the solid (1- φ^*):

$$I_{abs}(Q) = \frac{I_{measured}}{e_B}\,(1-\varphi^*) \qquad (II.22)$$

By replacing $I_{measured}$ in **Equation (II.20)** by I_{abs} we obtain an expression with measurable and known parameters:

$$\int_{0.003}^{0.2} \frac{I_{abs}}{e_B}(S)(1-\varphi^*)Q^2dQ = 2\pi^2\varphi^*(1-\varphi^*)\Delta\rho^2 \qquad (II.23)$$

The invariant can then be derived as:

$$INV^* = \int_{0.003}^{0.2} \frac{I_{abs}}{e_B}(Q)Q^2dQ = 2\pi^2\varphi^*\Delta\rho^2 \qquad (II.24)$$

The porosity can be calculated from the invariant extracted from the absolute intensity after its normalization by the solid thickness.

However, in SAS experiments involving porous media, an additional challenge lies in accurately calculating the scattering length density (SLD) (ρ) of the solid phase. This parameter is dependent on the solid density of the solid phase (excluding pores), as indicated by the **Equation (II.25).** Since this density is unknown, a precise technique for determining both the SLD and the solid density of the solid phase is contrast variation SANS (CV-SANS).

$$\rho = \frac{\sum_i b_i \boldsymbol{d} Na}{M} \qquad (II.25)$$

With:

bi: atomic scattering length

d: the density of the solid phase

Na: Avogadro number 6,022 × 10^{23} mol^{-1}

M: the molecular weight of the material

8.4 Contrast variation small angle neutrons scattering (CV-SANS)

SANS is known for its sensitivity to isotope substitution. This unlocks the possibility to modulate the contrast through the variations in scattering lengths between hydrogen and deuterium. In porous materials, this feature is typically used to modulate the contrast of solvents in CV-SANS experiments. Indeed, this experiment consists in recording the SANS profiles of materials equilibrated with different hydrogenated and deuterated solvent mixtures to vary the contrast between the solid phase and the solvent. It is possible to continuously adjust the scattering length density (SLD) of the solvent in order to match out the SLD of a the solid, making it invisible to neutrons. In this situation, the contrast at matching point is defined as:

$$\Delta\rho_{matching\ point} = \rho_{solid} - \rho_{solvent} = 0 \qquad (II.26)$$

In this work, CV-SANS experiments were conducted, and the SLD of the solid phase and solid density were determined, and then used to calculate the porosity using the invariant.

9 References:

[1] "Adsorption by Powders and Porous Solids - 2nd Edition." Accessed: Jan. 09, 2024. [Online]. Available: https://shop.elsevier.com/books/adsorption-by-powders-and-porous-solids/rouquerol/978-0-08-097035-6

[2] J. Jagiello and J. P. Olivier, "2D-NLDFT adsorption models for carbon slit-shaped pores with surface energetical heterogeneity and geometrical corrugation," *Carbon*, vol. 55, pp. 70–80, Apr. 2013, doi: 10.1016/j.carbon.2012.12.011.

[3] D. Saurel *et al.*, "A SAXS outlook on disordered carbonaceous materials for electrochemical energy storage," *Energy Storage Materials*, vol. 21, pp. 162–173, Sep. 2019, doi: 10.1016/j.ensm.2019.05.007.

[4] G. E. Bacon, *X-Ray and Neutron Diffraction: The Commonwealth and International Library: Selected Readings in Physics*. Elsevier, 2013.

[5] B. Hammouda, "A new Guinier–Porod model," *J Appl Cryst*, vol. 43, no. 4, pp. 716–719, Aug. 2010, doi: 10.1107/S0021889810015773.

[6] J. Teixeira, "Small-angle scattering by fractal systems," *J Appl Cryst*, vol. 21, no. 6, Art. no. 6, Dec. 1988, doi: 10.1107/S0021889888000263.

[7] P. W. Schmidt, "Small-angle scattering studies of disordered, porous and fractal systems," *J Appl Cryst*, vol. 24, no. 5, Art. no. 5, Oct. 1991, doi: 10.1107/S0021889891003400.

[8] H. D. Bale and P. W. Schmidt, "Small-Angle X-Ray-Scattering Investigation of Submicroscopic Porosity with Fractal Properties," *Phys. Rev. Lett.*, vol. 53, no. 6, pp. 596–599, Aug. 1984, doi: 10.1103/PhysRevLett.53.596.

[9] J. Bahadur, A. P. Radlinski, Y. B. Melnichenko, M. Mastalerz, and A. Schimmelmann, "Small-Angle and Ultrasmall-Angle Neutron Scattering (SANS/USANS) Study of New Albany Shale: A Treatise on Microporosity," *Energy Fuels*, vol. 29, no. 2, Art. no. 2, Feb. 2015, doi: 10.1021/ef502211w.

[10] O. Spalla, S. Lyonnard, and F. Testard, "Analysis of the small-angle intensity scattered by a porous and granular medium," *J Appl Cryst*, vol. 36, no. 2, Art. no. 2, Apr. 2003, doi: 10.1107/S0021889803002279.

[11] M. Jamros, L. Oliveira, P. Whitford, J. Onuchic, J. Adams, and P. Jennings, "Substrate-Specific Reorganization of the Conformational Ensemble of CSK Implicates Novel Modes of Kinase Function," *PLoS computational biology*, vol. 8, p. e1002695, Sep. 2012, doi: 10.1371/journal.pcbi.1002695.

[12] G. Porod, "Die Röntgenkleinwinkelstreuung von dichtgepackten kolloiden Systemen," *Kolloid-Zeitschrift*, vol. 124, no. 2, pp. 83–114, Nov. 1951, doi: 10.1007/BF01512792.

[13] F. L. Beyer, K. A. Masser, and J. L. Lenhart, "Application of the small-angle scattering invariant to morphological behavior in ballistic materials," *Journal of Applied Polymer Science*, vol. 138, no. 21, p. 50478, 2021, doi: 10.1002/app.50478.

[14] E. A. Chavez Panduro *et al.*, "Small-angle X-ray scattering analysis of porous powders of CaCO3," *J Appl Cryst*, vol. 45, no. 5, Art. no. 5, Oct. 2012, doi: 10.1107/S0021889812032219.

CHAPTER III:

Chemical and structural studies of reduced graphene oxide-based materials

1 Objectives and approaches

As discussed in chapter I, graphene-based materials have gained considerable attention due to their potential as electrode materials for supercapacitors [1, 2]. So far, previous research has primarily focused on the synthesis and the study of the electrochemical performances of these materials, with limited attention paid to the correlation between their structure and storage properties in SCs. However, the correlation between the structural and chemical properties of graphene-based materials and their use in supercapacitor applications is the key to further optimizing the design and the engineering of these materials to enhance their electrochemical performance

In this chapter, two methods of reducing GO were studied, namely *via* hydrazine hydrate reduction (rGO) and hydrothermal reduction (GA). Each reduction method has a specific impact on the structure, porosity [3, 4], and chemical properties of these materials [5, 6]. In this Chapter the thorough characterization of these materials is presented, while the correlation to their electrochemical performances is presented in **Chapter V**. As these materials appear in two distinct forms (powder for rGO and aerogel for GA), we will compare their respective morphological and structural features, including porosity at all relevant length scale ranging from nano- to macroscale to investigate the scales that are mainly involved in electrolytic ion diffusion and adsorption during SC operation. **Figure III.1** shows the different porosity scales in rGO and the characterization techniques that will be used to probe these scales. The term "nanoscale" refers to a porosity scale smaller than 1 nm and will be characterized using XRD, which directly probes the inter-layer distance. The term "microscale" refers to porosity in the range of 1 to 2 nm, while the "mesoscale" encompasses a porosity scale ranging from 2 to 50 nm. The microscale and mesoscale porosities will be characterized using XRD and SAS techniques respectively. The "macro-scale" includes all porosities larger than 50 nm and will be mainly probed by SEM. In this PhD work, the probed length scale in SAS techniques is ranging from 3 to 210 nm. This indicates that the SAS techniques extend over the mesoscale and include also a part of the macro scale, specifically in the range of 50 to 210 nm. It is noteworthy to remind that both XRD and SANS allow covering an extended Q-range (0.2 to 210 nm). In order to make it easier to read and compare the structural information, the XRD data will be represented as a function of Q($Å^{-1}$) rather than in 2θ, which is traditionally used.

Additionally, the effect of reduction method on their chemical properties and reduction efficiency will be evaluated, as the presence of remaining oxygen functionalities might add

pseudo-capacitive contribution to the storage mechanism. Finally, this fundamental study will evaluate the effects of the aforementioned properties on their electrochemical performances as will be presented in **Chapter V**.

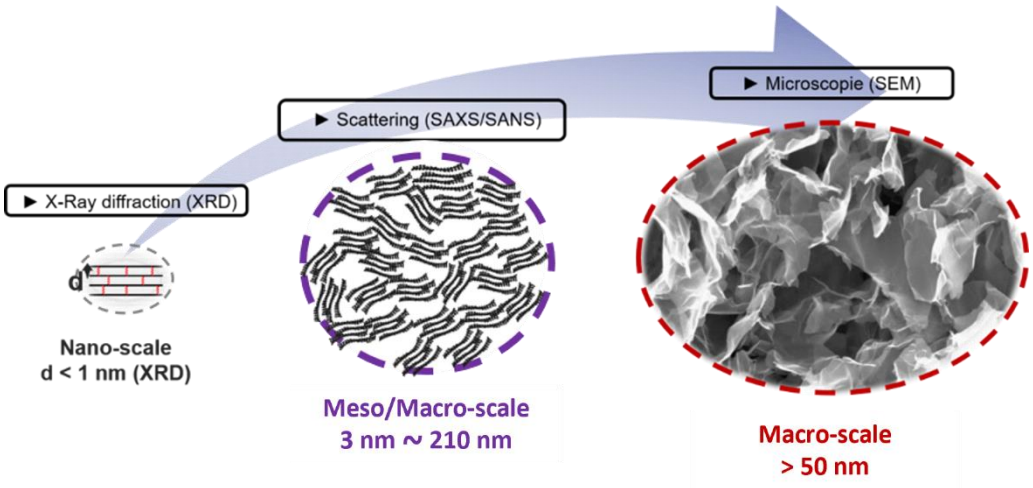

Figure III. 1 Conceptual scheme of the different level of porosity in non-pillared reference graphene materials

2 Nanoscale structure investigation

The study of the nanoscale structure and porosity refers to the XRD characterization of the local scale of the samples. At such scale, this analytical method allows to study the degree of oxidation and reduction for rGO-based samples that has an impact on the inter-graphene sheet distance. Hence in this part, the peak position will be used to study this oxidation/reduction extent since it enables the determination of the inter-layer distance using Bragg's law [7].

For the synthesis of rGO and GA, the required starting material is graphene oxide (GO). Its preparation involves a two-step process including graphite oxidation with potassium permanganate ($KMnO_4$) and subsequent exfoliation by sonication [8] (more details in **Chapter II: Materials and methods**). XRD analysis was performed to confirm the efficient graphite exfoliation. **Figure III.2** shows the XRD patterns of GO and graphite. GO (red curve) presents a **single sharp peak at Q=0.77 $Å^{-1}$ associated with a d-spacing (interlayer distance) of 0.8 nm**, attributed to the exfoliated GO. The absence of a graphitic peak expected at Q=1.86 $Å^{-1}$ (d-spacing =0.33 nm) corresponding to the (002) orientation, shows that the sample synthesis process did not leave any unreacted graphite particles, thus achieving effective graphite oxidation.

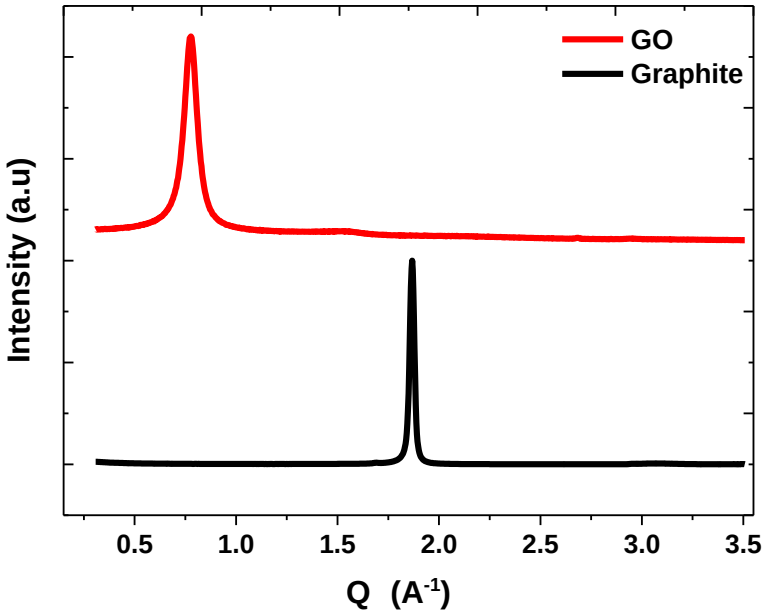

Figure III. 2 X-ray diffraction (XRD) patterns of GO (red) and graphite (black) demonstrating a successful graphite exfoliation and oxidation process.

Figure III. 3 provides an overview of the two synthesis protocols applied for the reduction of GO. GA was synthesized following a hydrothermal process in which GO is introduced in an autoclave heated at 180°C for 17h [9]. During this process, GO sheets are thermally reduced and the newly formed graphene sheets self-assemble into a three-dimensional network. The assembly process involves the formation of a stable structure of interconnected graphene sheets, resulting in the production of an aerogel (also known as a monolith). In contrast, rGO was formed by reducing GO with hydrazine hydrate under stirring and heating at 90°C for 24h. This reaction involves the reaction of hydrazine with the oxygen-containing functionalities on the GO surface, leading to the subsequent partial restoration of the Csp2 conjugated network, yielding rGO powder as the final product.

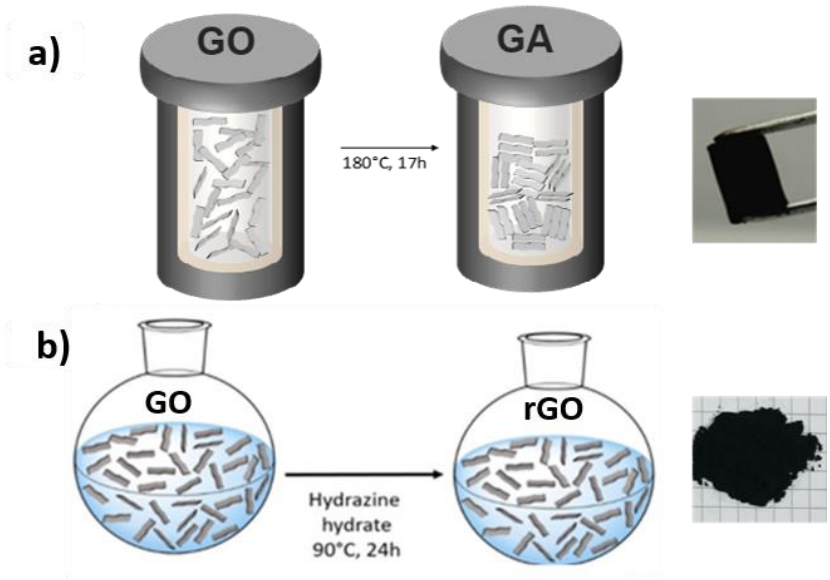

Figure III. 3 Synthesis protocols of (a) GA and (b) rGO and corresponding pictures of the pristine materials.

As shown previously, these two different GO reduction methods result in two different product textures and macroscopic morphologies (aerogel and powder). These two materials exhibit clear visual differences in terms of shape and density. rGO is a dense and fine powder, whereas GA appears as a lightweight aerogel with very low density and high macroporosity. These densities are of high interest to understand their impact on the electrochemical performances of these materials and part of this work is devoted to their determination, as it will be presented below. To verify the successful reduction of GO, XRD analysis was performed (**Figure III. 4**). The diffraction peak associated with GO (Q=0.77 $Å^{-1}$) has completely disappeared, showing that the reduction of GO was successfully achieved in both samples.

The XRD patterns of the two samples show a **single diffraction peak corresponding to the graphitic (002) orientation at Q=1.7 $Å^{-1}$, associated with an interlayer distance of 0.36 nm**, close to that of graphite (d=0.33 nm). This observation is explained by the restacking of some extent of rGO sheets during the reduction process, resulting in a graphitic signal (G). The G peak in these new structures is significantly broader than that of graphite (**Figure III.4**). In addition, the rGO peak is found to be broader than that of GA (FWHM = 6.7 for rGO and FWHM = 4.9 for GA). The broadness of a XRD peak is mainly influenced by two factors related to the crystal structure. The first is the crystal size. Indeed, as crystal size decreases, the number of diffracting planes contributing to the diffraction pattern decreases, resulting in broadened peak [10]. The second factor is micro-strain, which represents the presence of local distortions or non-uniformities in the crystal lattice. This strain contributes to the broadening of diffraction

peaks by causing variations in the inter-planar spacing within the crystal [11]. Thus, in the case of these two samples, FWHM differences could be evidenced by variation in number of rGO restacked layers, or by micro-strains occurring between sheets. To distinguish between the two hypotheses, TEM observations at the edge of the graphene stacks were performed.

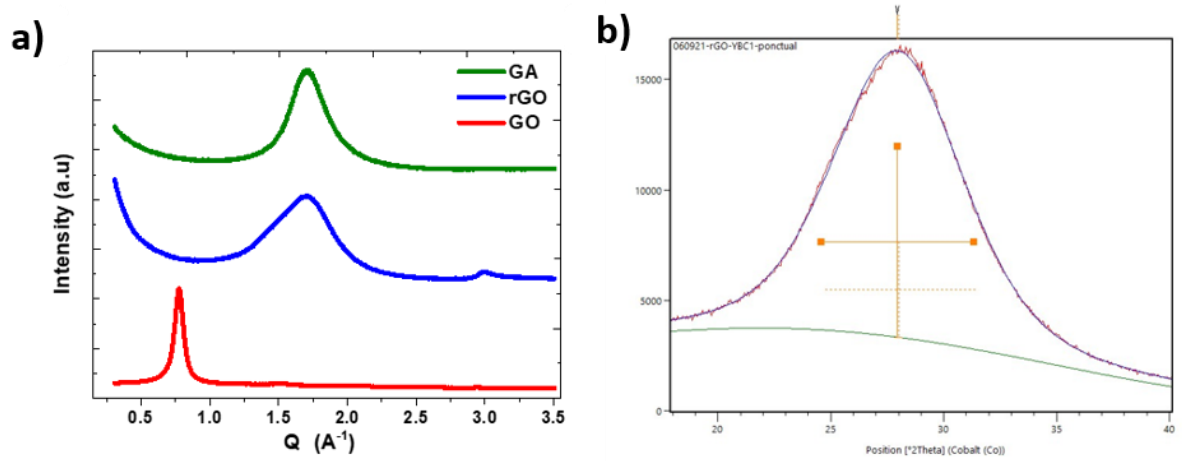

Figure III. 4 (a) XRD patterns of GO, GA, and rGO, and (b) an example of fitting of the G peak of rGO showing the introduction of a background between 18 and 40 2tetha values as well as a fitting peak allowing for accurate 2tetha peak position and FWHM accurate determinations

TEM study was carried out to gain further insight into these structural stacking differences between rGO and GA. Indeed, TEM is a powerful imaging technique that uses an electron beam to observe the inner structure of materials at nanoscale resolution. It has proven to be invaluable in the study of various materials, providing detailed insights into their morphology and crystal structure [12]. In addition, TEM enables direct imaging of graphene sheets, allowing to visualize the number of layers per stack [13]. Consequently, it represents a powerful tool for assessing the size of the stacked graphene domains, potentially confirming one of the two previously proposed hypotheses regarding XRD peak broadening. TEM observations at the edge of the stacks (**Figure III. 5**) show that the number of stacked graphene layers varies between 9 to 12, 4 to 7, and 2 to 4 for GO, GA, and rGO respectively.

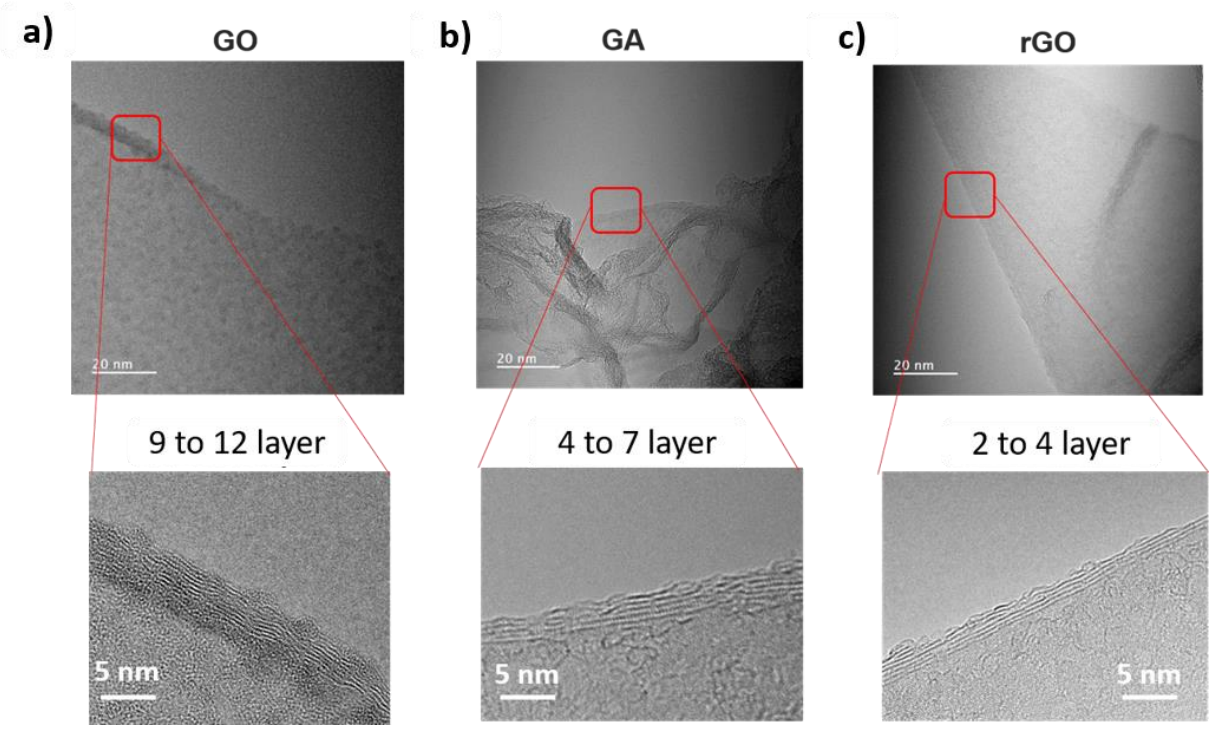

Figure III. 5 TEM images at 2 magnification scale of the edge of the stackss of (a) GO, (b) GA, and (c) rGO.

These observations show a higher number of restacked graphene layers in GA than in rGO, which suggests that the XRD peak broadness might rather originate from the difference in stack size (number of stacked layer) than strain.

Therefore, the XRD data were fitted and the stack height was estimated using the Scherrer equation [10] (neglecting strain). The XRD fitting data and calculation results are presented in **Table III. 1.**

$$L_c = \frac{k_1 \lambda}{FWHM.cos\theta_1} \qquad (III.1)$$

With:

ƛ radiation wavelength of Cobalt (0.1789 nm).

K_1, form factor (k=1).

FWHM, full width at half maximum of the diffraction peak (rad).

Table III. 1: XRD fitting data (peak-position, d-spacing and FWHM values) and stack height calculated from Scherrer equation along with the number of layers/stack determined, the error bars were determined from the standard deviation between five measures.

Sample	Peak position (°)	d-spacing (nm)	FWHM	Crystal Stack Height (nm)	Number of layers/stack
Graphite	30.8 ±0.3	0.34 ±0.01	0.4	20.5	61
GO	12.6 ±0.3	0.8 ±0.01	1.2	7.5	9
GA	28.2 ±0.3	0.36 ±0.01	4.9	2.1	6
rGO	27.9 ±0.3	0.37 ±0.01	6.7	1.5	4

The number of layers per stack was determined by dividing the size of the stack by the d-spacing. This showed a decrease from 61 layers per stack for graphite down to 6 and 4 for GA and rGO respectively. These results are in a good agreement with the TEM observations suggesting a slightly higher number of restacked graphene layers in GA compared to rGO, and **confirming that the XRD peaks broadness originates mainly from the difference in the stack height rather than distortions.**

The XRD results showed that both reduction methods were efficient. However, the reduction degree may vary between GA and rGO. It appears essential to examine their chemical properties to further understand their reduction degree, which may affect their electrochemical performances.

3 Reduction efficiency and chemical composition

The reduction efficiency was also assessed chemically by TGA, XPS, elemental analysis (EA), and TPD-MS. TGA allows to track the weight loss of the sample while being subjected to an increasing temperature ramp. In the case of GO-based samples, this analysis allows to track the mass loss associated with the thermal degradation of the oxygen containing functions. Such mass loss can therefore be qualitatively related to the amount of these oxygen functions and, in turn, this amount of oxygen functionalities can be used to compare the degree of oxidation and reduction between samples. TGA were performed on all samples at a heating rate of 5°C/min from 30 to 800°C under N_2 atmosphere (**Figure III. 6**). The GO thermogram exhibits three distinct weight loss processes: the first is due to the evaporation of adsorbed water below 100°C, and the second is associated with the elimination of surface oxygen functional groups at around 200°C.

Beyond 200°C, a steady weight loss is typically attributed to the gradual removal of stable oxygen functional groups [14]. In contrast, rGO shows a marginal weight loss of *ca.* 10% over the entire temperature range, indicating that the majority of the oxygen functional groups were removed during the synthesis process and that GO was successfully reduced. GA displays a similar behavior than rGO but with a more pronounced weight loss of *ca.* 30%. **This indicates that GA contains more oxygenated groups than rGO and therefore GA is less reduced than rGO**.

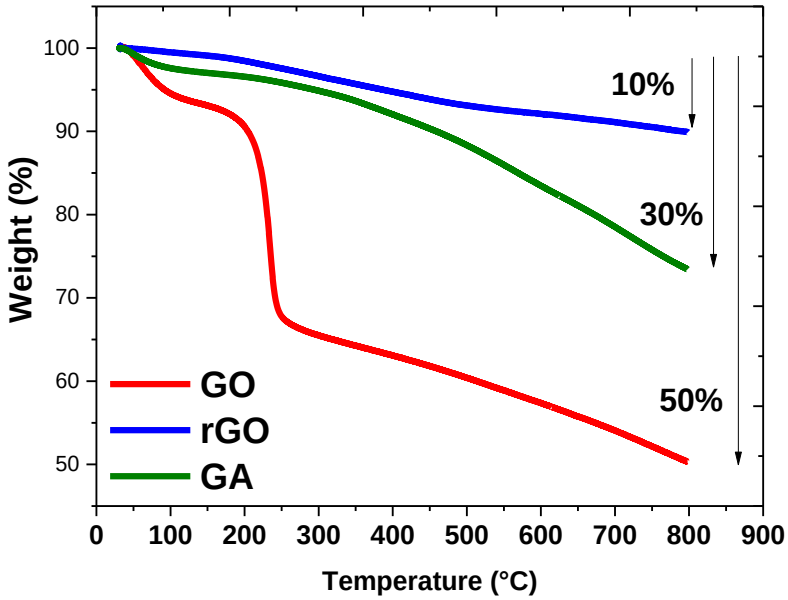

Figure III. 6 TGA response of GO, GA, and rGO under a N_2 atmosphere.

This thermogravimetric analysis was combined with temperature-programmed desorption coupled to mass spectrometry (TPD-MS), carried out by the CEMHTI Laboratory in Orléans (by Pr Encarnacion Raymundo and DR. Conchi Ania), to identify the decomposition products generated under thermal treatment.

TPD-MS analyses were performed under an inert atmosphere (Ar). **Figure III.7** shows the removal of H_2O at a lower temperature (~30 °C), followed by CO_2 emission (~100°C), mainly due to the decomposition of carboxylic and oxalic groups, and CO emission (300°C), due to the decomposition of more stable carbonyl and hydroxyl groups for both materials [15], [16]. The emission of water, CO_2, and CO was higher in GA compared to rGO, indicating the presence of more oxygen functional groups in GA; **thereby confirming that rGO is more reduced than GA and showing that hydrazine reduction is the most efficient**.

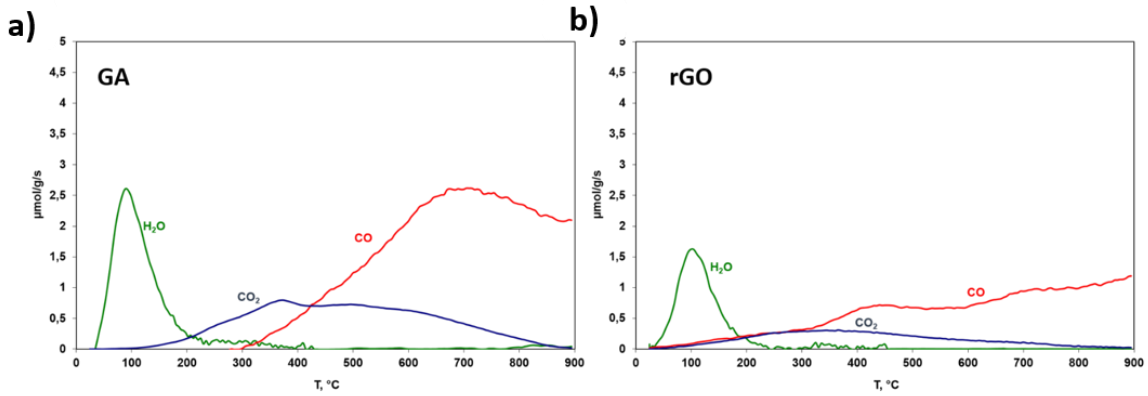

Figure III. 7 The decomposition products under heating of (a) GA and (b) rGO evaluated by TPD-MS.

TGA provided further qualitative evidence that rGO is more reduced than GA. In turns, XPS and EA analyses were performed to try to get more quantitative analysis about the amount of oxygen containing functionalities as their amount can be correlated to the conductivity of the sample as well as to pseudocapacitive behavior in electrochemistry. The XPS survey spectrum of GO, GA, and rGO (**Figure III.8 a**) show a lower O1s peak intensity compared to C1s in reduced samples compared to GO, indicating a successful reduction of GO. In addition, the XPS survey spectrum of rGO shows the presence of the expected signal for N1s at approximately 400 eV, which stems from the hydrazine used in the reduction process of GO. Furthermore, the high resolution (HR) XPS C1s spectrum was recorded to track the evolution of the amount of oxygen functional groups within the material. **Figure II.8 b, c, d** displays the C1s (HR) XPS spectra and its deconvolution for GO, GA and rGO respectively. For GO, two distinct peaks are observed at binding energies of approximately 284 and 286 eV attributed to carbon-carbon bonds (C=C and C–C) and carbon-oxygen bonds of the different oxygen-related functional groups, respectively. In turns, GA and rGO C1s HR XPS spectra present similar functional groups as GO. However, most carbon-oxygen bonds peaks exhibit lower intensities, indicating an elimination of the majority of the oxygen functional groups and thereby a successful reduction of GO. In addition, rGO C1s HR spectrum shows a new peak at 285 eV, which is assigned to the C–N bonds peak originating from hydrazine hydrate used for its reduction. Moreover, the HR XPS O1s and N1s spectra were also recorded and the atomic concentration of each element was determined to calculate C/O ratios, which indicate the degree of reduction. These data are gathered in **Table III. 2** alongside with the EA atomic concentration and C/O ratio.

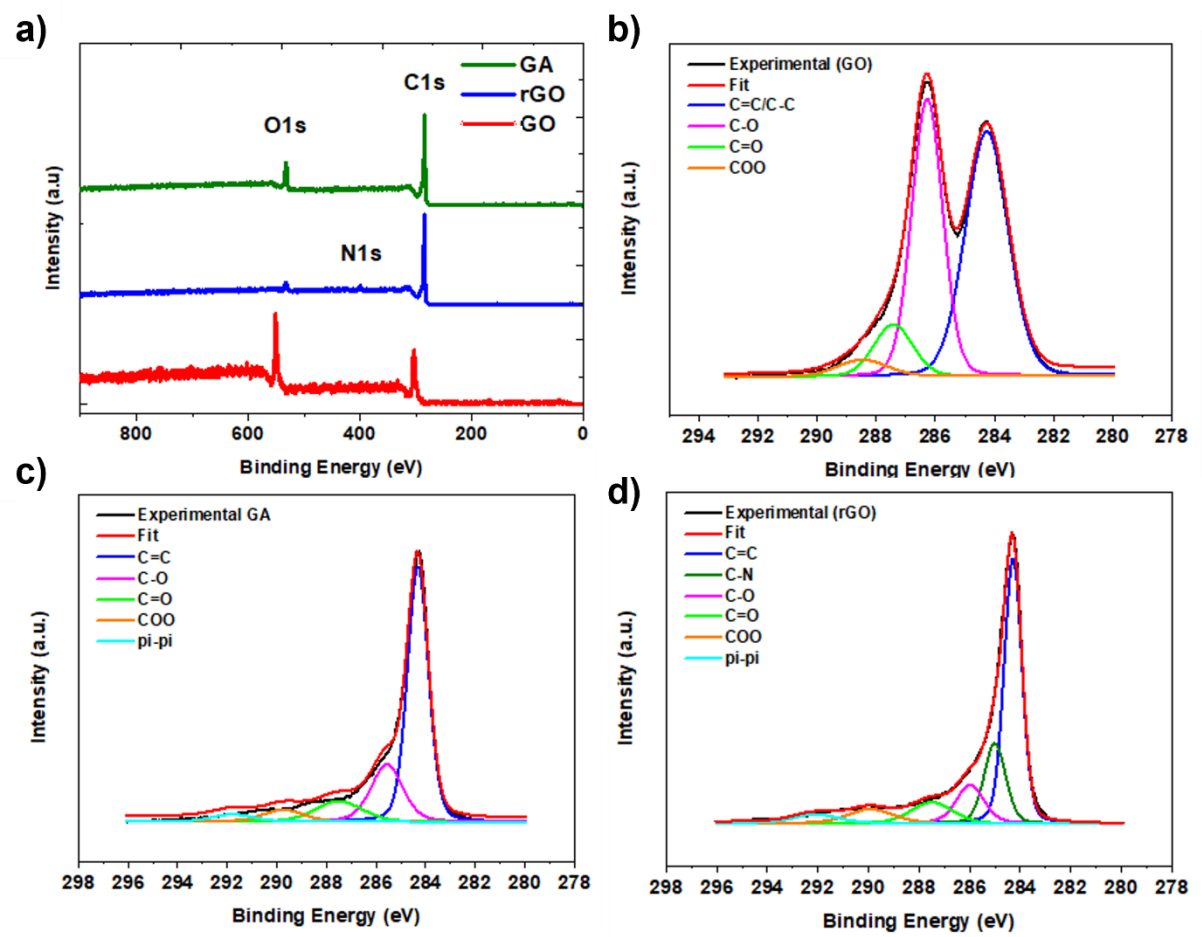

Figure III. 8 (a) XPS survey scans of GO, GA, and rGO, and C1s HR XPS spectrum of (b) GO, (c) GA, and (d) rGO.

Table III. 2: Atomic percentages extracted from XPS and EA and C/O ratio of the GO, GA, and rGO.

	Materials	%C	%H	%N	%O	C/O
EA ±0.3	**RGO**	83.8	0.9	5.0	10.2	8.2
	GA	78.6	1.4	2.3	17.6	4.4
	GO	49.4	2.6	0.1	47.6	1.0
XPS ±%	**RGO**	89.2	-	4.1	6.6	13.4
	GA	86.8	-	2.4	11	7.9
	GO	70.6	-	0.3	29	2.4

Both techniques show similar trends as shown in **Figure III. 9**. For instance, rGO shows the highest C/O ratio, followed by GA. These results corroborate the TGA and TPD-MS and confirm that rGO is more reduced than GA.

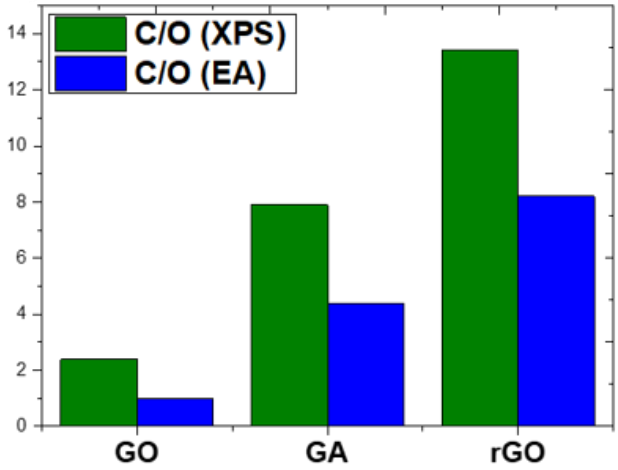

Figure III. 9 EA and XPS C/O ratio evolution for GO, GA, and rGO.

Conductivity plays a crucial role in energy storage applications. High electrical conductivity facilitates efficient electron transport within the energy storage device, enabling faster charge and discharge rates. This enhances the ability of the material to store and release energy rapidly [17]. In the case of rGO-based samples, this conductivity value is also an indicator of the degree of reduction. Therefore, the conductivity of GO, GA and rGO samples were determined. The conductivities of the pellets were measured using a four-probe system. GO exhibits complete insulation with a conductivity of 0 S/m, indicating that GO could not be used as an active material in supercapacitors. The conductivities recorded for GA and rGO were about 108 ± 5 S/m and 1662 ± 18 S/m respectively. This means that rGO has 15 times higher conductivity than GA, indicating that rGO is indeed more reduced than GA. This shows that the hydrazine reduction has resulted in a highly reduced and conductive material compared to hydrothermal reduction. Therefore, it is expected that rGO could have better electrochemical performances. However, conductivity and reduction degree are not the only parameters that control electrochemical performances. In fact, in addition to the physicochemical properties, the structural features including the porosity, play a major role in enhancing the electrochemical performances [18]. Indeed, the nano-/microporosity increases the active surface area available for ion adsorption, contributing to increased charge storage capacity. Mesoporosity provides pathways for ions to access the interior of the electrode material. This accessibility is crucial for efficient ion adsorption and contributes to fast charge and discharge rates. **Therefore, a**

comprehensive analysis of their multi-scale structure and porosity is essential to gain an in-depth understanding of the parameters governing their electrochemical performances.

4 Macrostructure investigation and its evolution after GO reduction

The macroscale structure and morphology of these materials were investigated by SEM. The morphology of the freeze-dried pristine GO (**Figure III.10**) shows a flat and very large graphene sheet morphology. The lateral size of a GO sheet was estimated to be ranging between 1 and 10 µm. Due to the insulating properties of GO, obtaining clear SEM images was very challenging, despite the deposition of a carbon-coating (5 nm).

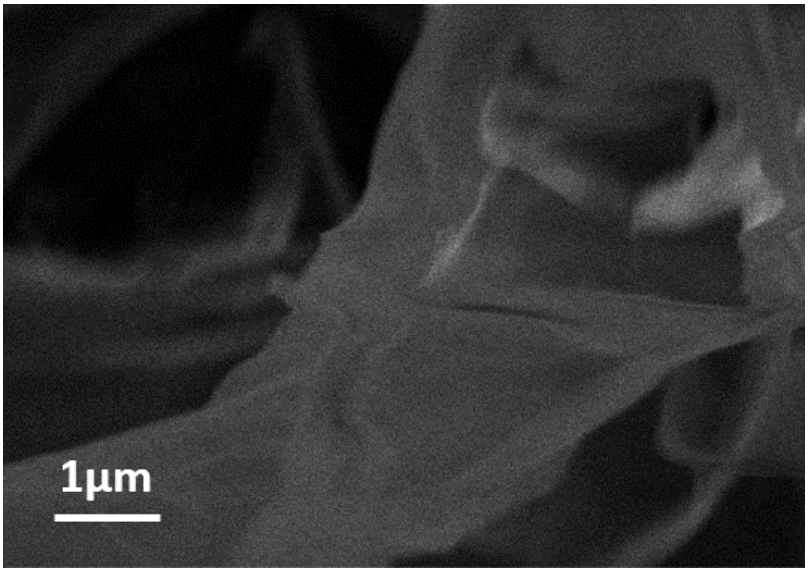

Figure III. 10 SEM image of freeze-dried pristine GO.

After the reduction process, the SEM observations (**Figure III.11**) show significant differences in the macrostructure of pristine GA and rGO. GA shows a highly macroporous network with large voids between the graphene layers (~1 µm). In addition, there is a significant decrease of the size of graphene sheets compared to freeze-dried GO. Conversely, rGO exhibits a densely packed, crumpled and aggregated morphology with less macroporosity than that observed in GA. The lower porosity in rGO may be attributed to the stirring used during synthesis, which may promote folding of the graphene sheets. Both materials present a highly interconnected network, which is fractal-like structure, characterized by a similar structure at all scales. It is an "infinitely fragmented" geometric object whose details can be observed at any chosen scale.

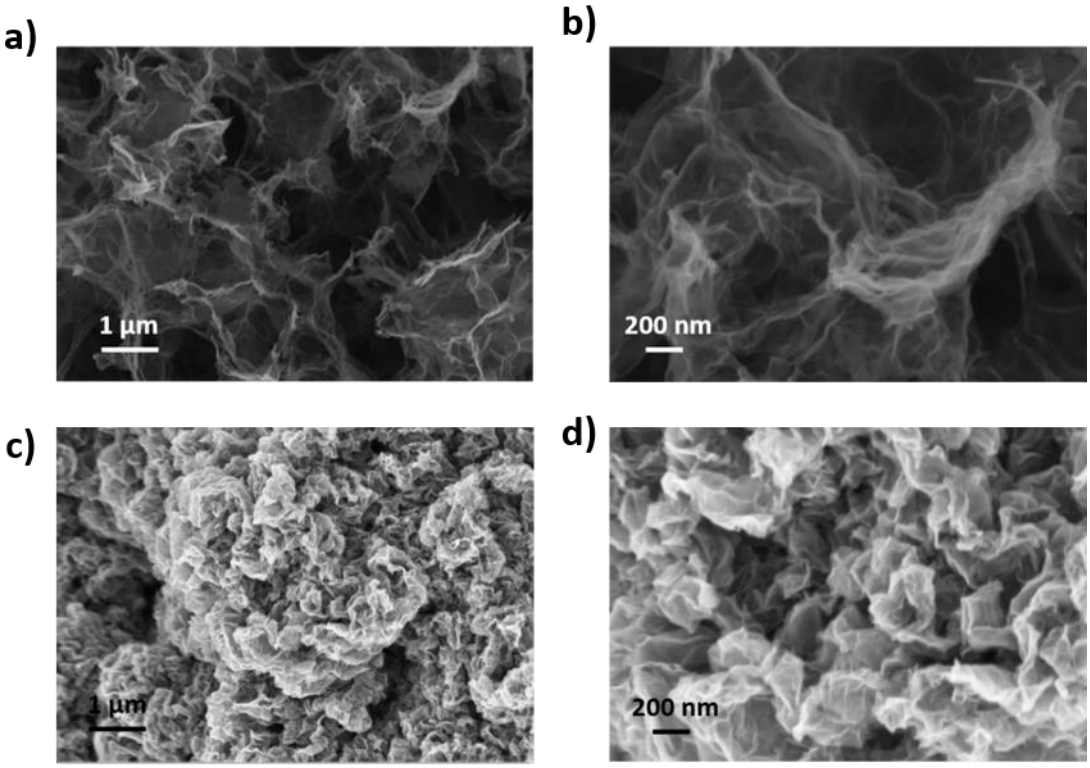

Figure III. 11 SEM images recorded at 2 different magnifications of (a,b) GA and (c,d) rGO.

This study shows that GA and rGO samples are macroporous and that GA presents a higher macroporous volume. These images therefore demonstrate that both samples have a porosity adapted for bulk electrolyte diffusion. However, at this stage, it is important to note that in order to achieve improved and reproducible electrochemical performances of electrode materials for supercapacitors, it is necessary to obtain a thin and homogeneous powder. Grinding is therefore one of the essential steps in electrode preparation and its impact on the material structure is a key factor in understanding electrochemical behavior. The impact of grinding on the macrostructure was studied by SEM (**Figure III.12**). The SEM images show that grinding destroys the external macrostructure and porosity of both GA and rGO. Consequently, the resulting materials possess a comparable macrostructure. In addition, the grinding process creates walls on the outer surface of these materials by sheets flattening, which could potentially modify the access to their macroporosity.

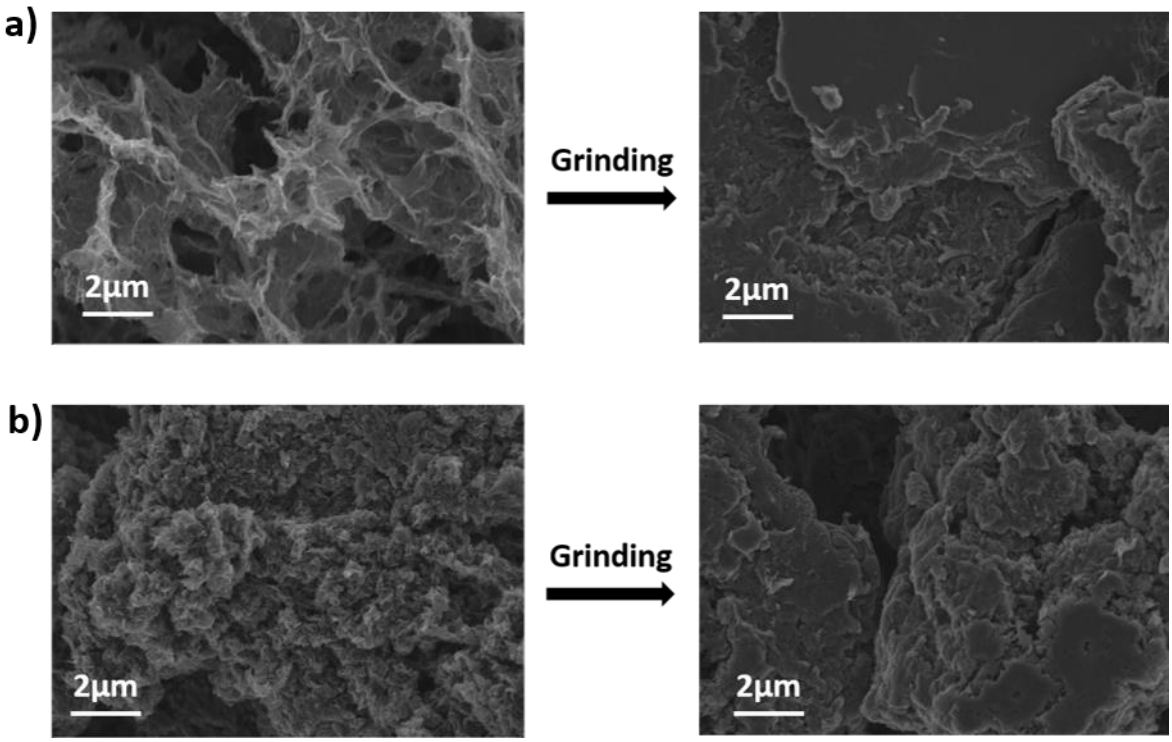

Figure III. 12 SEM images on (a) GA and (b) rGO showing the grinding impact on the macrostructure.

This SEM analysis shows that both GA and rGO samples display an open macroporosity that was highly modified after grinding, which may affect their capabilities to store ions as electrolytic ion reservoirs.

Still, in the context of SCs, the mesostructure of the material plays a pivotal role. The presence of mesopores increases the effective surface area available for charge storage. An optimal mesoscale structure ensures efficient ion transport and accessibility of active sites, contributing to superior electrochemical performances [19, 20].

5 Understanding the mesostructure and porosity: interest of small angle scattering

Real-space imaging techniques, such as SEM and TEM are valuable tools for visualizing nanostructures. However, they do not always provide a clear picture of the order of magnitude of the structures observed in high aspect ratio nanomaterials, such as those based on graphene. TEM, examines the isolated objects (divided matter), so, it is not possible to observe the porosity of the sample or the assembly of structures. On the other hand, with SEM, we observe the bulk material, but it is not possible to quantify features such as porosity at a specific scale. It is therefore important to consider the limitations of these techniques when analyzing such materials. **Scattering techniques were used to capture structure over a wide range of**

length scales and these results were compared, when possible, with real-space images. Indeed, small-angle scattering techniques are a highly relevant method for characterizing the porosity of disordered media, such as carbonaceous materials, and show a valuable complementarity with real-space imaging techniques.

GO, GA and rGO are high aspect ratio graphene-based samples, but because they are not single layers and also because they are used as powder, they actually consist of assemblies of GO- or rGO-based structures with varying tunable porosity and density. Their mesoscale morphology was investigated using SANS. The scattering profiles provide insights into the structural features inherent to the material [21]. In order to gain a deeper understanding of these features, prior knowledge of the material structure is important as it complements the SAS results, helping to make consistent assumptions and ultimately leading to a clearer view of the sample mesoscale. **As discussed above, SEM observations of GA and rGO revealed a porous fractal-like structure of interconnected crumpled and wrinkled graphene sheets, characterized by a similar structure at all scales**.

It is worth reminding here the typical small angle scattering (SAS) profile properties of porous and fractal materials discussed in **Chapter II section 8.1**. The SAS profile of porous materials with a well-defined pore size distribution is characterized by a plateau in the intermediate-Q range, indicating a characteristic size at the probed length scale (pores in this case). However, this plateau disappears in the case of correlated (inter-connected) pores, with no longer well-defined size and exhibiting a fractal structure, [22]. Furthermore, SAS profiles of fractal materials are characterized by their mass fractal scattering (D_m) [23, 24], which can be obtained directly from the slope of the scattering decay in the intermediate-Q range. The mass fractal scattering dimension reflects the typical shape of the scattering object. In addition, at high Q values, the intensity is scattered by the solid/air interface. The interface roughness can be characterized by a fractal surface dimension D_S as shown in **Chapter II section 7.1.3**.

5.1 Mass and surface fractal dimension determination

Mass and surface fractals are easily observed in the small-angle scattering region. Indeed, for mass fractals, the scattered intensity is expressed as follows:

$$I(Q) \alpha\ Q^{-D_m} \qquad (III.2)$$

and, for surface fractals, the equation (III.2) applies:

$$I(Q) \alpha\ Q^{6-D_s} \qquad (III.3)$$

These dependencies should extend for at least a decade in Q, with the I(Q) *vs.* Q representation (log-log) resulting in a distinct straight line for both types of fractals dimensions.

As shown in **Chapter II section 7.1.3**, if the exponent (slope) is between ≤ -1 and ≥ -3, it indicates $-D_m$ revealing that we are dealing with *mass fractals*. If the exponent is between ≤ -3 and ≥ -4, it refers to (-6 + Ds), which indicates *surface fractals* (high Q range, Porod's regime) [25] where Ds = 2 represents a perfectly smooth surface (Q^{-4}), and values approaching 3 represent a "very rough" surface (Q^{-3}). This is often a simple way of identifying and distinguishing between the presence of two types of fractal structure in a system.

5.2 Characteristic sizes

Soft carbons could be modelled as an interconnected network of crumpled carbon layers as shown by Saurel *et al*. [22]. This model, presented in **Figure III.13,** could also be applied to study graphene-based materials, as they present an interconnected crumpled graphene sheet structure. R (bending length) represents the smallest flat section of the layers. The layers are crumpled between R and Σ, and the distribution of radii of curvature follows a fractal exponent. Below R, the layers can be considered flat. Σ denotes the fractal cut-off length (persistence length), beyond which the fractal correlation vanishes but it does not necessarily corresponds to a restricted expansion of the crumpled layers. Rather, it signifies that, beyond this length, their curvatures are random [26].

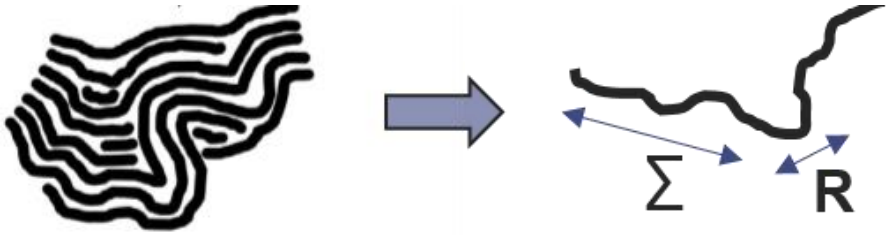

Figure III. 13 Conceptual model of graphene based materials showing the bending R and persistence Σ lengths, adapted from Saurel et al [22]

Considering the previous model applied to the fractal nature of these graphene-based materials, and their hierarchical porous structure with correlated pores, the expected scattering profile for such a fractal model is anticipated to follow a power-law relationship Q^{-Dm} at intermediate and small angles and Q^{6-Ds} at high Q values with break in slopes characterizing the bending and the persistence length.

5.3 Investigation of the mesoscale morphology of GO

The SANS profile of the pristine freeze-dried GO (**Figure III.14 a**) shows **a single power-law decay with a slope of - 3.6 over the whole Q-range** (0.003 - 0.2 $Å^{-1}$ corresponding to a scale of 3 - 210 nm), indicating that we are probing the same structure without any modification in this wide range of scales. In addition, the scattering profile does not present any plateau in the small or intermediate Q-range that characterizes a distinctive size [25]. **Figure III.14 b** shows the SEM image of GO at low magnification (scale: 10 × 10 µm), revealing a structure with very large graphene sheets.

The red square depicted in the SEM image indicates the range of length scale probed in SANS, *i.e.*, 210 × 210 nm^2. This comparison enables the understanding of the observed GO SANS profile. Only the interfaces of the object with high aspect ratios are probed in the SANS scale, *i.e.*, **the scattering entity appears infinite to the neutrons**. No typical structural feature such as peaks, bumps, or breaks in slope are observed. The $Q^{-3.6}$ power law indicates rough air-particle interfaces with a surface fractal dimension Ds of 2.4. Since our probing scale is located within the large graphene sheet of GO, it is not possible to estimate the mass fractal dimension. Similarly, both the bending and persistence length remain beyond the investigation scale. At the probed scale, the GO morphology could be represented as a large rough graphene layer, as depicted by the zig-zag black line in the SANS profile (**Figure III.14 a**).

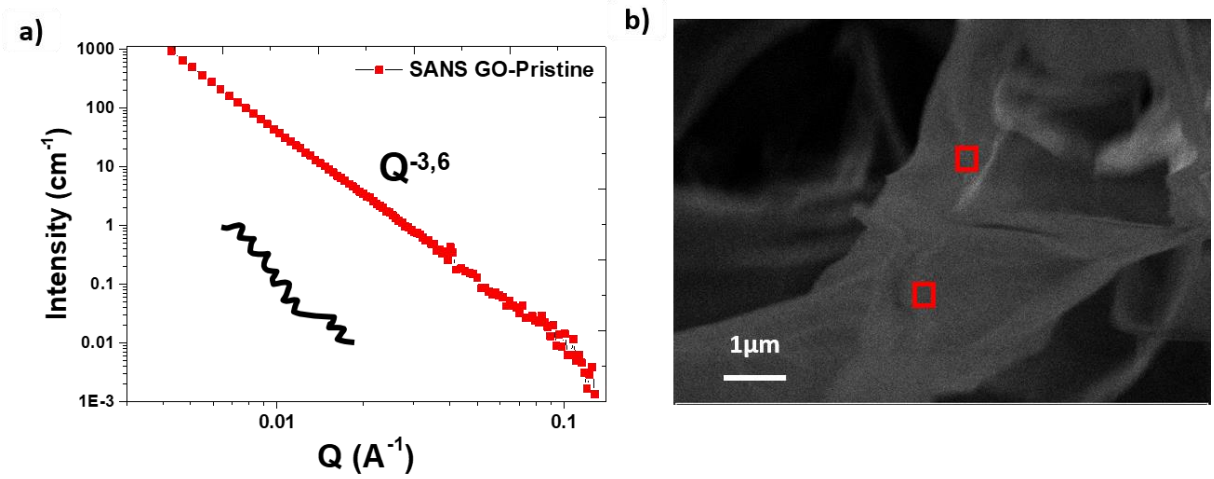

Figure III. 14 (a) SANS profile of pristine GO (b) SEM image of GO

In order to study the morphological evolution at the mesoscale after GO reduction, GA and rGO were studied using SANS and correlated to SEM/TEM observations to establish a link between real-space images and scattering techniques.

5.4 Comparison of the impact of the reduction method on materials morphology at the mesoscale

5.4.1 Study of the mesoscale morphology of GA by SANS and SEM

It is observed that the SANS profiles of the reduced materials are characterized by a series of power-law decays separated by breaks in slopes. Such a shape of the scattering profile is characteristic of a porous two-phase system (carbon matrix and pores) with fractal structure [22, 27, 28]. More specifically, the SANS profile of GA (**Figure III.15 a) lacks distinct structural features (bump/peak)**, yet a break in slope is discernible albeit not easily observable at $Q^* \sim 0.011$ Å^{-1}. The corresponding so-called Kratky representation which consists of plotting $I(Q)Q^2$ against Q (**Figure III.15 b)** is plotted as it allows breaks in slope to be observed as more or less well-defined maxima. This representation allows better visualization of the slope discontinuities, associated with characteristic distances within the material. **In this case, the distance $d^* \sim 57$ nm ($d^*=2\pi/Q^*$) can be assigned to the bending length (R) of the crumpled graphene layers within GA**. In addition, a slope of ~- 3.4 at high Q values indicates a **surface fractal dimension D_s of 2.6, which indicates that the air/particles interface of GA is rough**. Moreover, the GA shows a Q^{-3} slope at small angle, which could be attributed to **mass fractal scattering with high structural compacity or to the scattering from 3D crumpled graphene layers. Figure III.15 c** shows a high magnification SEM image of GA capturing a large bent graphene sheet, highlighted by a red line. Comparing the size of the bending on the image (~50 nm) with that of the SANS break in slope ($d^* \sim 57$ nm), they are very close, supporting the idea that the break in slope may indeed originate from this characteristic bending length.

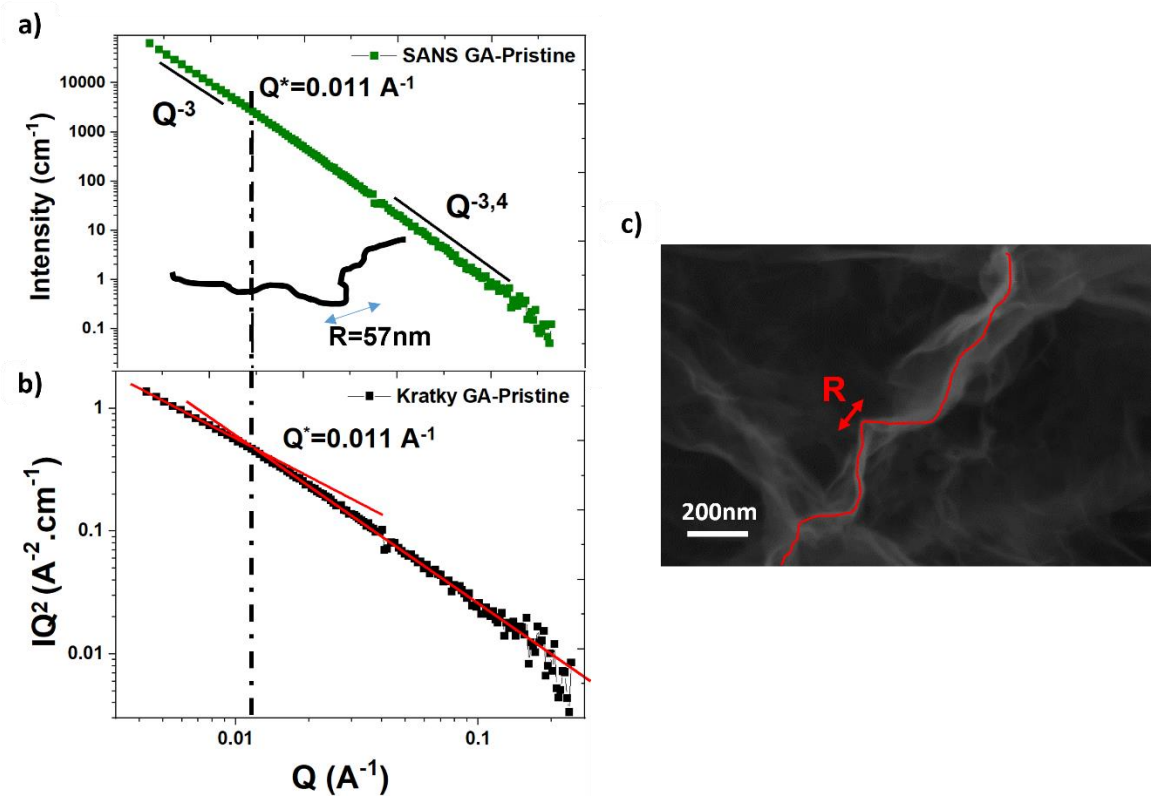

Figure III. 15 (a) SANS profile of pristine GA (b) corresponding Kratky plot (c) SEM image at high magnification of GA.

5.4.2 Study of the mesoscale morphology of rGO by SANS and SEM

Figure III.16 a displays the SANS profile of rGO showing a sequence of power-law decays with (i) a $Q^{-2.5}$ dependency at small angles (although observed in a limited Q-range), (ii) a Q^{-2} in the intermediate-Q range (Q^{-Dm} type: shape of the object) and (iii) a Q^{-3} in the large Q-range (Q^{6-Ds} type: surface fractal scattering). The small angle $Q^{-2.5}$ dependence can be assigned to the scattering from a mixture of 3D crumpled particles and 2D flat restacked graphene domains. The Q^{-2} slope in the intermediate Q-range can be attributed to the scattering from 2D shaped objects (restacked graphene sheets). The Q^{-3} slope in the large Q-range is the typical signature of extremely rough interfaces. It is noteworthy that the surfaces of rGO are rougher compared to GA (Q^{-3} *vs* $Q^{-3.4}$ in the Porod's regime respectively). The power laws are separated by two breaks in slope at Q*=0.053 $Å^{-1}$ and Q**=0.006 $Å^{-}$ (better determination of these values is provided by the Kratky plot, see **Figure III.16. b**). **These discontinuities are associated with the bending and cut-off/persistence length of the crumpled layers of rGO, which are about 12 nm (d*) and 105 nm (d**), respectively**. The high magnification SEM image (**Figure III.16 c**) shows that the graphene layers have a highly crumpled structure, with many bends within a single layer (indicated by the red lines on the SEM image). Importantly, the

bending and persistence lengths on the SEM image (R~20 nm and Σ~100 nm) are very close to those derived from the SANS breaks in slope, supporting previous hypotheses about the origin of these breaks in the SANS profile.

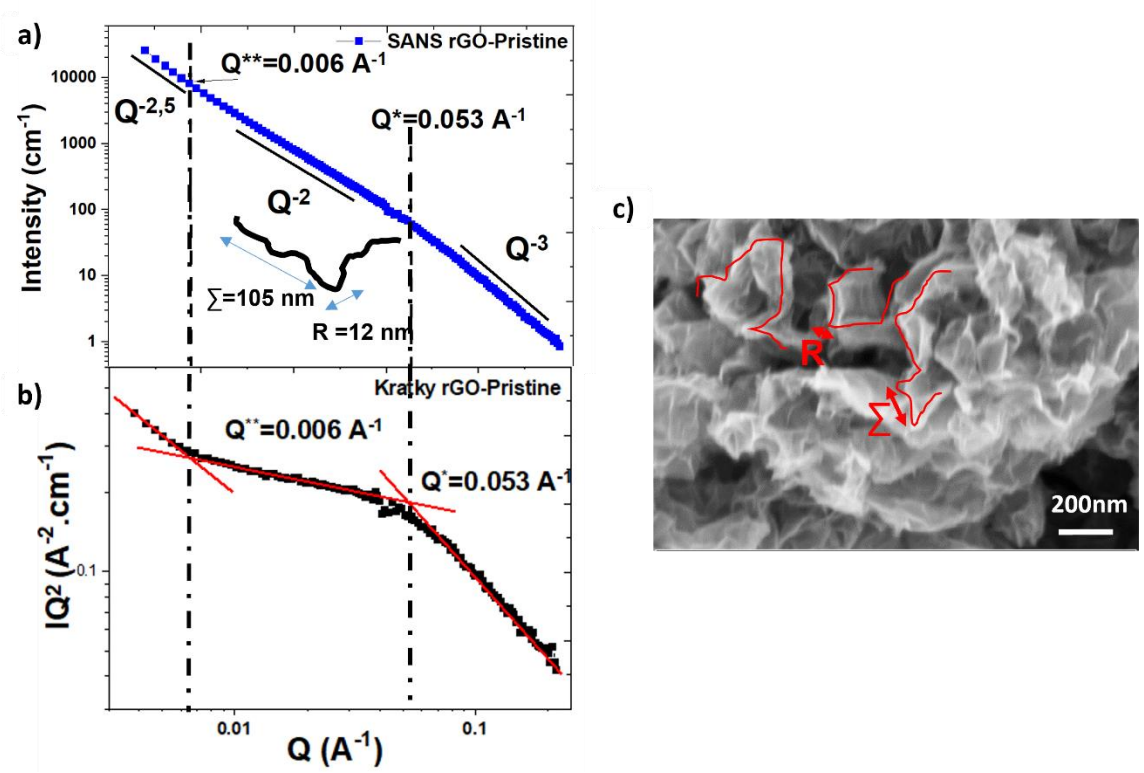

Figure III. 16 (a) SANS profile of pristine rGO (b) corresponding Kratky plot (c) SEM image of rGO at high magnification.

5.5 Discussion on the impact of reduction method on the mesoscale morphology

The scattering profiles of GA and rGO show that the mesoscale morphology of GO was modified after its reduction using either hydrazine hydrate or hydrothermal reduction. The single power-law decay profile of GO was no longer observed. Furthermore, the difference in scattering profiles between GA and rGO indicates that the reduction methods used have a significant impact on the mesoscale morphology. The SANS profile of GA shows a single break in slope, associated with a characteristic distance attributed to the bending length within the crumpled graphene layers of GA, which was estimated to be about 52 nm. The SEM observation was very helpful in confirming these findings. As a reminder, the SANS profile of rGO shows two breaks in slopes at Q*=0.053 $Å^{-1}$ and Q**=0.006 $Å^{-1}$, associated with the bending length R and the persistence length Σ which are about 12 nm and 105 nm, respectively. The high-magnification SEM observations of rGO corroborate these SANS results. The interface roughness extracted from the slope Q-values (6-Ds) shows a surface fractal dimension of 2.4,

2.6, and 3 for GO, GA, and rGO respectively. The interface roughness increases with the surface fractal dimension. rGO has the roughest interface, followed by GA and then GO. The SEM images confirm these results. They show that rGO has a high roughness due to its crumpled structure and high density of bends. In contrast, GA has a lower density of bends and less crumpled graphene sheet structure, resulting in a smoother interface. In contrast, GO, has an extended and flat graphene sheet morphology, causing the length of the bends to exceed the probed length scale, resulting in a smoother interface. These structural features are summarized in **Table III.3**.

As a brief reminder, at small angles, GA presents a Q^{-3} slope, which is attributed to mass fractal scattering within the 3D graphene structure. Additionally, rGO presents a Q^{-2} slope at the intermediate-Q range, likely arising from the scattering of 2D-shaped objects (lamellar), specifically restacked graphene sheets. However, SEM observations of the highly crumpled morphology of rGO raises doubts about the 2D mass fractal scattering instead of the expected 3D mass fractal. Additionally, GA, which has larger and flatter graphene sheets, does not exhibit 2D mass fractal scattering in the intermediate-Q range, which contradicts expected patterns. Therefore, investigating the morphology of objects on a smaller scale range (from 10 to 100 nm) is crucial to gain a more comprehensive understanding of the object morphology. For this purpose, TEM observations were conducted.

Table III.3: Summary of characteristic sizes and mass/surface fractal dimension determined by SANS

Materials	R (nm)	Σ (nm)	D_m	Ds
GO	-	-	-	2.4
GA	57	-	3	2.6
rGO	12	105	2	3

TEM observations in the intermediate-Q range scale (10 - 100 nm) of GA (**Figure III.17**) reveal a fractal network of interconnected graphene sheets with a distinct 3D shape due to the bent graphene layers**. These observations support the morphological interpretations derived from SANS, which indicate the absence of a 2D mass fractal morphology at this scale**. In contrast, the TEM images of rGO (**Figure III.18**) show a structure of 2D flat graphene sheets at this local scale, which is consistent with the results obtained from SANS. The complementarity of SANS and microscopic techniques was useful in confirming our

morphological interpretations and highlighting the significance of the SAS technique in establishing a connection between the different probed length scales.

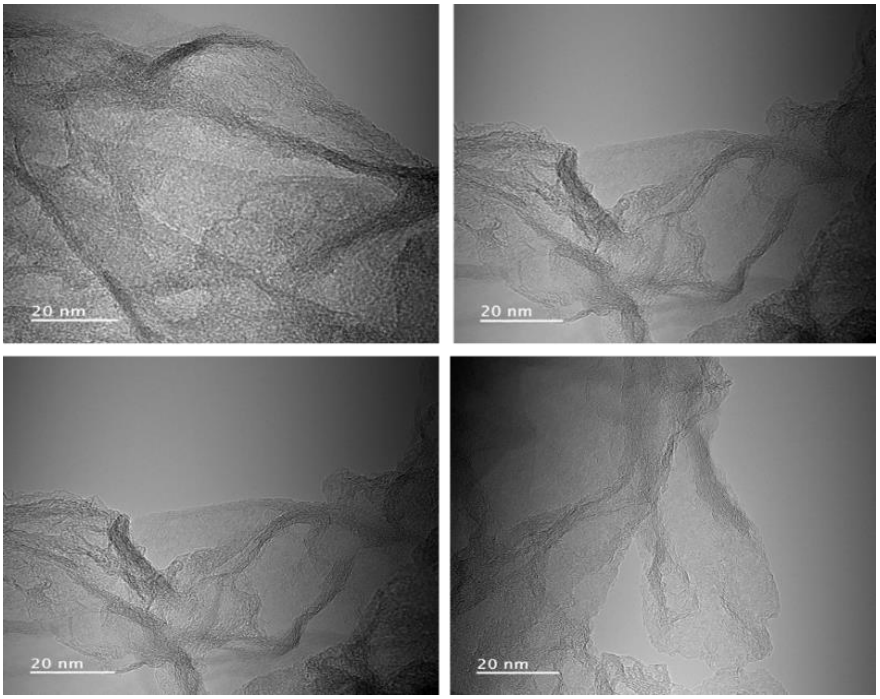

Figure III. 17 TEM images of GA taken from different zones highlighting the 3D morphology of this material at this scale (20 to 100 nm).

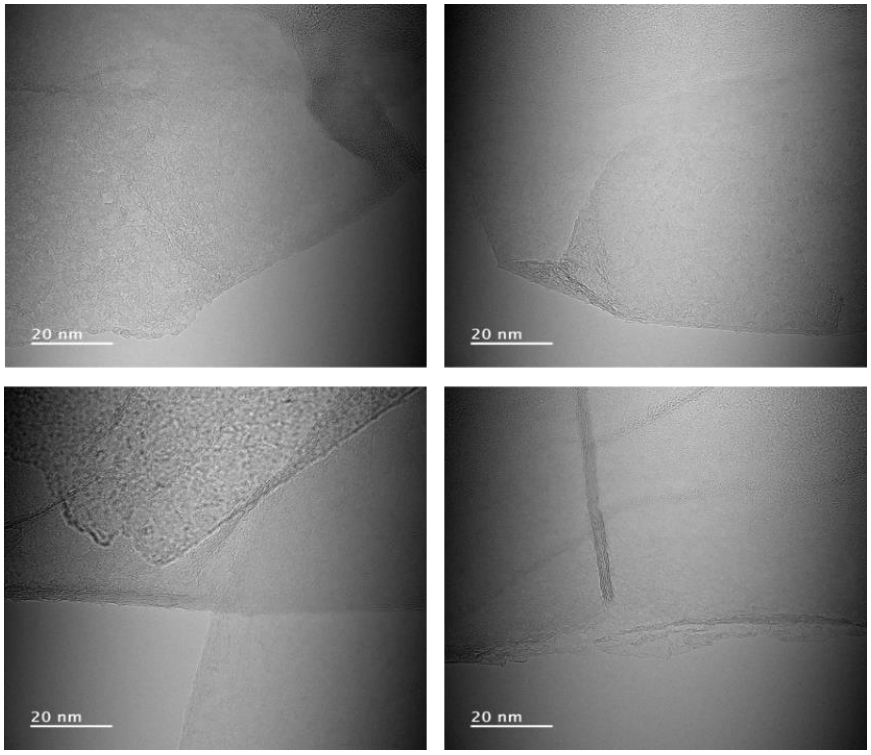

Figure III. 18 TEM images of rGO TEM images of GA taken from different zones highlighting the 3D morphology of this materials at this scale (20 to 100 nm).

5.6 Impact of grinding on the mesoscale morphology

Until now, the focus has been dedicated on studying pristine materials, providing valuable insights into understanding bare graphene-based materials. However, within the scope of this project, these materials have also been employed as electrode materials for supercapacitors, and the electrode preparation process involves grinding the material. Therefore, the potential impact of grinding on the mesoscale structure and porosity has been investigated. This investigation is particularly crucial because these materials are used and engineered to exhibit mesoporosity. Therefore, it is essential to explore the potential changes in their mesoscale structure and porosity induced by the grinding process. The study of the grinding impact on the mesostructure was conducted by SANS on both pristine and powder (after grinding) materials (**Figure III.19**). Despite the significant impact of grinding on the macrostructure, as shown previously by SEM, the SANS profiles of all samples remained almost unchanged after grinding. **This indicates that the materials' mesoscale morphology and structure (including bending and persistence lengths) were preserved**. This result bears significance because the micro/mesoscale structure and porosity are key factors in electrochemical storage [19].

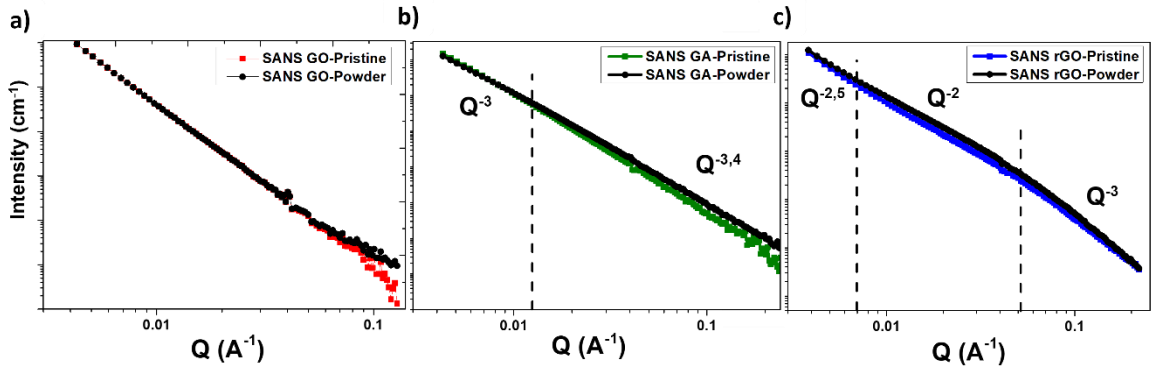

Figure III. 19 Grinding impact on the mesostructure of (a) GO, (b) GA, and (c) rGO studied by SANS.

6 Density and porosity investigation

6.1 Envelope density

Material density is a crucial property for energy storage applications. High material density, combined with optimized porosity, facilitates the storage of more energy in a given volume, enabling the design of more compact energy storage devices. Density is defined as the ratio of an object's mass to its volume. Determining the volume of a material (to calculate its density) is a complex process that heavily relies on its shape and porosity. The measurement of volume can be affected by surface irregularities and small fractures and fissures. In addition,

the presence of closed porosity can impact the volume measured using gas pycnometry techniques.

Figure III.20 illustrates the three different volumes that could be measured in porous materials. The total volume of the material envelope (V_A), which includes both the solid volume and all the porosity (case A); in this case, the porosity is completely under-estimated. The apparent or skeletal volume (V_B) represents the solid volume containing closed porosity accessible by gas pycnometry (case B). Lastly, the true or absolute volume (V_C) refers to the solid volume containing no porosity (case C). These volumes yield different densities and offer valuable insights into the porosity of the material.

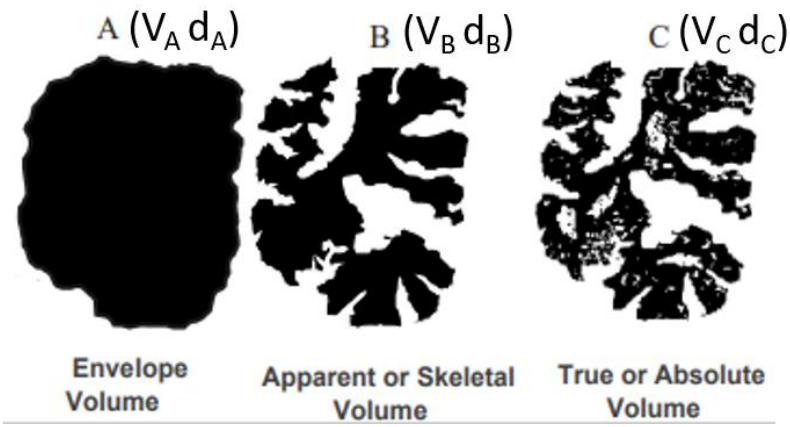

Figure III. 20 The various volumes that can be quantified in a porous sample

The volume of the envelope (V_A) was determined by filling completely a Hellma 1 mm quartz cell with the pristine material. Compression was avoided to preserve the macro porosity of the materials. The envelope density was calculated by weighing the materials within the cell and using the known volume of the cell (**Table III.4**).

Table III.4: The envelope density of GA and rGO.

Material	Envelope density (d_A)
GA	0.04 ±0.005
rGO	0.2 ±0.02

The envelope density between GA and rGO is significantly different, as shown in **Table III.4**. The envelope density of rGO is five times higher than that of GA. These results underscore the substantial difference in the occupied volume within the Hellma cell between

GA and rGO. The low density of pristine GA demonstrates a higher occupied volume compared to rGO, which may be due to its higher macroporosity as shown previously by SEM observations in **Section 4.**

6.2 Solid density, interest of neutrons

Determining the solid density is crucial in quantifying the overall porosity of the material (open *vs* closed). Contrast Variation-SANS (CV-SANS) is one of the most suitable techniques for determining this density [29] (more details can be found in **Chapter I and II**).

Our initial CV-SANS study was carried out on pristine materials on the SANS-I spectrometer (Paul Scherrer Institut (PSI)-Villigen) and complementary measurements were conducted on the D22 spectrometer at ILL. A high SLD solvent was needed based on the materials SLD calculated using the closest solid density to our materials, which is graphite density (d= 2.3 g/cm^3, SLD~ 7 10^{10} cm^{-2}). Considering that the graphene-based materials are exfoliated graphite their final density is expected to be lower than that of graphite, so their SLD should be lower than ~ 7 10^{10} cm^{-2} and cyclohexane was found to be a good solvent to try matching our materials. The materials were placed in Hellma 1 mm quartz cells and immersed in different mixtures of cyclohexane (CycloH) and deuterated cyclohexane (d-CycloH) (**Table III.5**) to adjust the scattering contrast between the solid and the solvent. This solvent was chosen because it covers a wide SLD range reaching a maximum of 6.7 10^{10} cm^{-2} for 100% d-CycloH (higher than d-toluene and d-acetonitrile for example), and exhibits low viscosity.

Table III.5: The solvent mixtures used for CV-SANS and the corresponding SLD.

% d – CycloHexane (d-CycloH) (% vol.)	**SLD (10^{10} cm^{-2})**
60	3.9
80	5.2
90	5.9
100	6.7

6.2.1 Solid density of GA investigated by CV-SANS

The combined CV-SANS profiles recorded at PSI and ILL of pristine 6GA-0.05 (**Figure III.21 a**) show a gradual decrease in intensity as the amount of d-CycloH decreases. **The minimum intensity is observed at a mixture containing 74% of d-CycloH, beyond**

which the intensity increases as the amount of deuterated solvent decreases. At 74% of d-CycloH, the intensity is almost zero in the high Q values domain (above Q=0.02 $Å^{-1}$) and shows a slight increase in small angles range (below Q=0.02 $Å^{-1}$).

The evolution of the intensity was plotted against the amount of d-CycloH for different Q values (Q=0.007 $Å^{-1}$, Q=0.02 $Å^{-1}$, and Q=0.05 $Å^{-1}$) in order to check the uniformity of the structure at different length scales. The Intensity as a function of the percentage of deuterated solvent (%vol) reveals a **uniform evolution of the intensity at all the Q values with a minimum intensity close to zero at Q=0.02 $Å^{-1}$ and Q=0.05 $Å^{-1}$ recorded at 74% of d-CycloH** (**Figure III.21 b**). However, a slight increase in the intensity is observed at Q=0.007 $Å^{-1}$ at the matching point. This residual intensity at small angles is attributed to the potential presence of closed pores in the material or scattering from hydrogen-rich domains [30]. **This uniform relationship indicates a matching point at 74% deuterated solvent**, which corresponds to a Scattering Length Density (SLD) of 4.9 10^{10} cm^{-2}. The GA solid density determined from the matching SLD and the molecular weight calculated from the EA chemical formula is found to be d_C= 1.56 g/cm^3

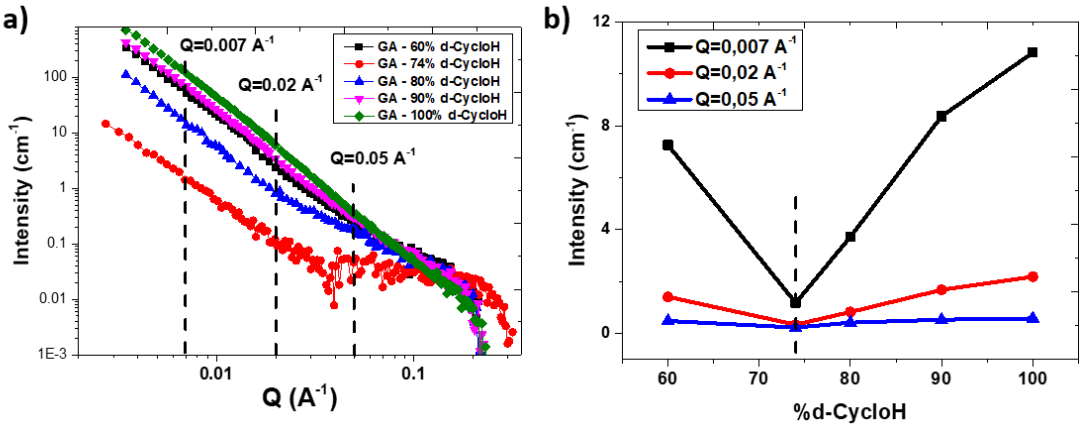

Figure III. 21 (a) CV-SANS profiles of pristine GA at different mixtures of cyclohexane/d-cyclohexane (b) the intensity as a function of the deuterated solvent at Q=0.007 A^{-1}, Q=0.02 A^{-1}, and Q=0.05 A^{-1}showing its uniform evolution at the different Q values and a minimum at 74% of d-CycloH.

6.2.2 Solid density of rGO investigated by CV-SANS

Unlike aerogels, the suspensions of rGO in the solvent mixture suffer from precipitation. The dense rGO powder sediments quickly (in less than 30 sec) and remains at the bottom of the quartz cells (**Figure III.22 c**), while the recording of the scattering profile can take more than 30 min. Depending on the area probed by the beam, there may be some powder-rich or solvent-rich domains. The CV-SANS profiles of rGO (**Figure III.22 a**) do not reveal a trend, which is confirmed by the evolution of ± $Intensity^{1/2}$ as a function of d-CycloH (**Figure**

III.22 b), which does not show the linear dependency expected in the case of a successful CV-SANS experiment. The non-monotonic evolution between ± Intensity$^{1/2}$ and the percentage of d-CycloH in the solvent mixture suggests that the powder-rich domains may not contain enough solvent to fill the pores, a prerequisite for successful matching conditions. Therefore, the solid density of rGO could not be determined using this technique. **However, the density of GA and rGO in pellet form (pressed under 2T for 10 min) was found to be very close to each other at 1.38 and 1.41 g/cm^3 respectively**. These densities are likely to be closest to the solid density determined by SANS, as pressing removes the majority of the porosity. Since the pellets densities of GA and rGO are very close to each other, we can assume that this also applies to their solid densities. For the quantitative results, we have assumed that rGO and GA have the same solid density of 1.56 g/cm^3.

The SLD of rGO, calculated from its solid density and using the chemical formula obtained with the EA, is 4.7 10^{10} cm^{-2}.

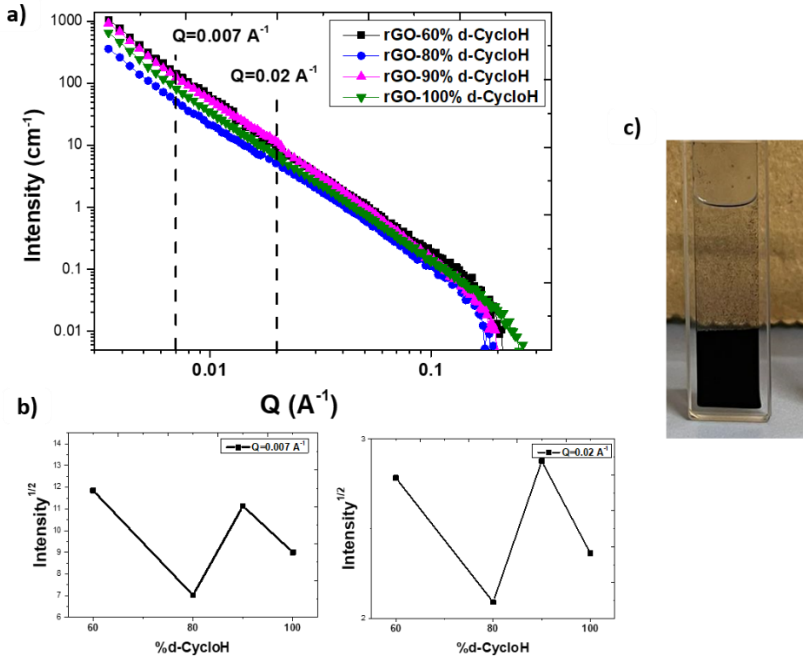

Figure III. 22 (a) CV-SANS profiles of rGO at different mixtures of cyclohexane/d-cyclohexane (b) Intensity$^{1/2}$ as a function of deuterated solvent at Q=0.007A^{-1} and Q=0.02A^{-1}showing the absence of a trend or a minimum intensity (c) image of rGO inside Hellma cell after 30 sec of the suspension.

The solid densities determined from the CV-SANS of the reference materials and their envelope densities (**Table III.6**) were used to calculate the porosity volume in these materials. The volume of the solid and envelope can be easily obtained by inverting the density, while the porosity volume is calculated as the difference between the volume of the envelope (V_A) and the volume of the solid phase (V_C). **Table III.6** shows that the pores in GA (24.3 cm^3/g) occupy

a larger volume than in rGO (4.3 cm^3/g). This large variation is attributed to the difference in their envelope volume ($V_{A(GA)}$~25 cm^3/g *vs* $V_{A(rGO)}$~ 5 cm^3/g), as it was hypothesized that they have similar solid density. This represents the total porosity of these materials, where the macroporosity might have a significant contribution in the case of GA. At this stage, the total pore volume is determined, but the distribution of pore volumes as a function of the scale is not yet determined**. Therefore, a quantitative assessment of this porosity is required. To do so, SAS techniques can be very valuable as long as quantitative analysis of the SAS measurements can be performed.**

Table III.6: Envelope and solid density as well as envelope, solid, and pores volumes of GA and rGO.

Material	Envelope density d_A (g/cm^3)	Solid density d_C (g/cm^3)	Envelope volume V_A (cm^3/g)	Solid volume V_C (cm^3/g)	Porosity volume (cm^3/g)
GA	0.04	1.56	25	0.64	**24.3**
rGO	0.2	1.56	5	0.64	**4.3**

6.3 Mesoporosity investigation

SAS is a powerful technique for estimating material porosity at the mesoscale [31]. In two-phase systems, Porod's invariant, denoted as INV, does not depend on the structure, but only on the volume fraction of each phase (solid/pores) and contrast. Therefore, determining the INV can help to calculate the proportion of pores within the probed length scale (more details in **Chapter II**). At this stage, it should be recalled that in this study the SANS profiles were measured on an extended scale from 3 to 210 nm. We therefore examine the mesoscale (from 3 to 50 nm) and part of the macroscale (from 50 to 210 nm). The INV is calculated using the absolute scattering intensity (cm^{-1}).

$$INV = \int_0^\infty I_{measured}(Q)Q^2 dQ = 2\pi^2\varphi(1-\varphi)\Delta\rho^2 \qquad (III.4)$$

Where:

$\Delta\rho$: the contrast = $SLD_{material}$ - SLD_{air} = $SLD_{material}$

φ: volume fraction of phase 1 (solid)

$(1-\varphi)$: volume fraction of phase 2 (pores)

The determination of the scattering invariant requires a measurement of the scattered intensity over a very large Q-range (from zero to infinity). However, in practice, this is not possible. The

porosity of the materials was calculated in the limited Q-range: 0.003-0.2 $Å^{-1}$. For the quantitative analysis, the intensity was normalized to the solid thickness (e_B), following the work of Spalla *et al* [31]. The porosity can be derived using equation (III.5):

$$INV^* = \int_{0.003}^{0.2} \frac{I_{abs}}{e_B}(Q)Q^2 dQ = 2\pi^2 \varphi^* \Delta\rho^2 \qquad (III.5)$$

The invariant INV* was calculated based on the area under the curve of the Kratky plots derived from the normalized SANS profiles (**Figure III.23**). The CV-SANS technique was used to determine the material's SLD, which was found to be 4.7 10^{10} cm^{-2} and 4.9 10^{10} cm^{-2} for rGO and GA respectively, as shown above. The solid thickness (e_B) was determined using the transmission and neutron attenuation coefficient (**Equation (III.6)**). **Table III.7** gathers the various parameters used to estimate the mesoporosity.

$$e_B = \frac{-\ln(T)}{\mu_{solid}} \qquad (III.6)$$

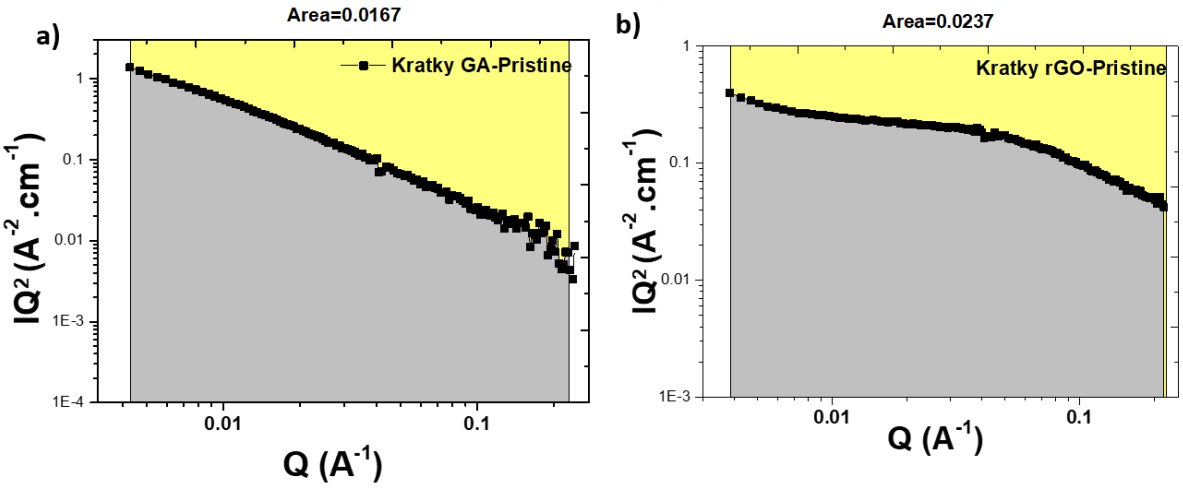

Figure III. 23 The invariant determination from the area under the Kratky curves of (a) GA and (b) rGO.

Table III.7: The different parameters used to estimate the mesoporosity of GA and rGO.

Material	Attenuation coefficient (cm^{-1})	Transmission	e_B (cm)	INV (10^{20} cm^{-4})	φ^*(%)
GA	0.494	0.97	0.0616	167	**35**
rGO	0.488	0.98	0.0413	237	**57**

There are only a few examples in the literature where this technique has been used to estimate the porosity and, to the best of our knowledge, none of them has been applied to carbon materials. The porosity of the Marcellus shells was investigated by a combination of USANS/SANS to cover an extended Q-range from 3.10^{-5} to 0.2 $Å^{-1}$ [32, 33]. The porosity ranged from ~0.4 % to 4 %. Gibaud *et al.* [34] explored the porosity of porous silica using SAXS and the invariant on a Q-range of 0.003 - 0.2 $Å^{-1}$, and estimated a porosity of approximately 40%.

Application of this method to both GA and rGO in a Q-range of 0.003-0.2 $Å^{-1}$ (corresponding to an extended length scale from 3 to 210 nm) **showed that rGO has a higher porosity of 57%, compared to 35% porosity for GA**. This finding highlights that the high total pore volume in GA, as shown in **Table III.6**, is not primarily due to its mesoporosity. Instead, it emphasizes a significant contribution from macropores, which is consistent with the SEM observations of GA.

To complete this analysis, our colleagues from CEMTHI laboratory in Orléans (Pr. Encarnacion Raymundo and DR. Conchi O. Ania) measured the **BET surface area for N_2 gas sorption at 77 K and found a SSA of 401 and 237 m^2/g for rGO and GA, respectively**. These values seems to be low compared to porous carbon-based materials such as activated carbon (SSA ~2000 m^2/g) [35]. Despite their low SSA, rGO-based materials showed comparable electrochemical performances to activated carbons, showing a well-optimized hierarchical porosity [9]. Furthermore, rGO shows a higher SSA than GA. Additionally, the N_2 pore size distribution (N_2-PSD) (**Figure III.24**) shows a **pore volume (in the scale ranging from 0.6 to 30 nm) of 0.86 and 0.24 cm^3/g in rGO and GA respectively, confirming the SANS porosity measurements.**

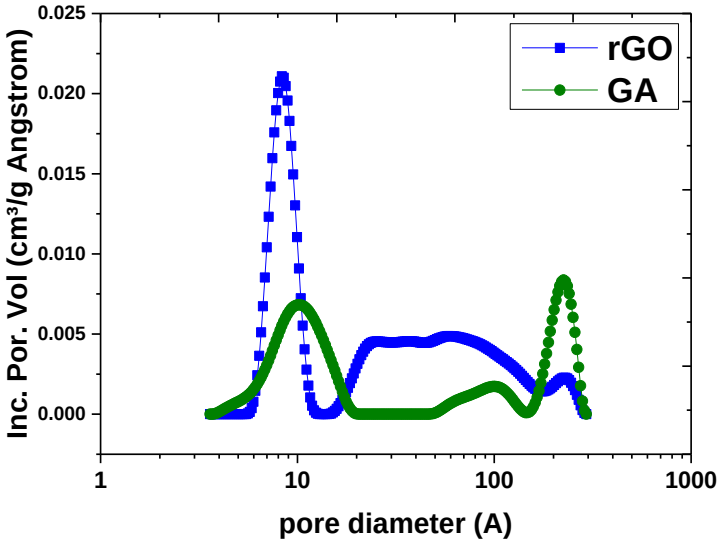

Figure III. 24 N_2-PSD of GA and rGO.

7 Conclusions

The methodology involved in this chapter consisted of studying graphene-based materials chemistry and their structure/porosity at different scales. The impact of the chosen reduction techniques on these parameters were evaluated and will be directly correlated to their electrochemical performance (**Chapter V**). As shown previously, the nano-, meso-, and macroscale structures of GA and rGO were very different, indicating that they were strongly influenced by the chosen reduction techniques. The nanoscale structure was mainly studied by XRD. This initially showed an efficient oxidation of graphite leading to a clean GO with no remaining graphitic component.

Second, XRD showed that GO reduction following both methods led to restacking of the graphene sheets (single G peak). A slight broadening of the G peak of rGO compared to GA was observed and shown using Sherrer equation and TEM observations to be due to a higher number of restacked graphene sheets per stack in GA. This lower number of restacked graphene sheets in rGO could lead to a more disordered material with higher porosity. In addition, XRD results showed efficient reduction of GO and indicate elimination of most oxygen functional groups, which was confirmed by the chemical analysis. XPS and EA indicated a higher C/O ratio for the reduced materials compared to GO in the order: rGO > GA > GO, confirming that rGO is more reduced than GA and contains a lower amount of oxygen functional groups, which was also established by TGA. Indeed, a weight loss of 10% was observed for rGO compared to 30% on GA (**Figure III.25**). In addition, the conductivity measurement on GO showed an

insulating behavior and a conductivity of 0 S/m. In turn, rGO and GA presented conductivities of 1662 ± 18 S/m and 108 ± 5 S/m respectively. All these results showed that hydrazine reduction was more efficient than hydrothermal reduction.

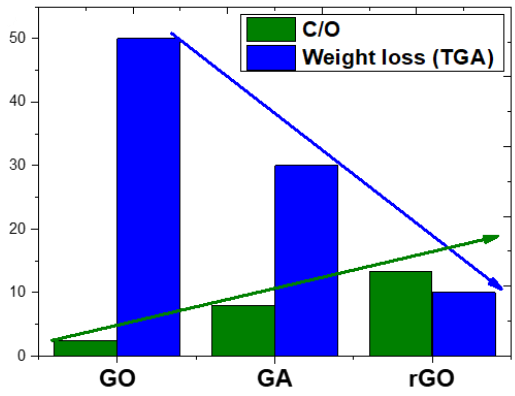

Figure III. 25 C/O evolution and TGA weight loss of GO, GA, and rGO.

The macroscale structure of these materials was investigated using SEM. SEM observation of all materials showed a structure consisting of an interconnected network of graphene sheets. This structure was characterized by self-similarity, regardless of the probed length scale and by the absence of individual objects with clearly defined dimensions within the materials, suggesting a fractal structure. The SEM images of GO showed a very large and flat morphology of graphene sheets with high macroporosity. Hydrothermal reduction results in a lightweight monolith with high porosity (GA). SEM observations on pristine GA showed that this material is indeed highly macroporous. On the other hand, rGO presented a very dense and crumpled graphene sheet structure, which could be due to the mode of synthesis (synthesis under stirring), and the stirring could favor the folding of the graphene sheets. These observations emphasize that the structure/morphology at the macroscale is strongly influenced by the chosen reduction technique, leading to two different macroassemblies.

The fractal mesoscale morphology of these materials was studied with SANS. **Figure III.26** summarizes the results of this study. The SANS profile of GO showed a single power-law decay with a slope of - 3.6 over the entire Q-range (0.003 - 0.2 $Å^{-1}$, corresponding to a scale of 3 to 210 nm), indicating that we studied the same structure without any change in this wide scale. In contrast, the SEM observations on GO revealed a structure with very large graphene sheets that explain the observed SANS profile, which indicates that only the rough solid/pore interfaces were probed (surface fractal dimension Ds~2.4 (**Figure III.26 a)**. After reduction, the SANS profiles of GA and rGO were characterized by a sequence of power-law decays,

separated by break in slopes. GA showed a break in slope observed at Q*~ 0.011 $Å^{-1}$ corresponding to a distance of d* ~ 57 nm (d*=2π/Q*), assigned to the bending length (R) of the crumpled graphene layers, which was confirmed by the SEM observations. In addition, GA exhibited a surface and mass fractal dimension of D_s= 2.6 and D_m= 3 respectively (**Figure III.26 b)**. In turn, the SANS profile of rGO showed two breaks in slopes at Q*=0.053 $Å^{-1}$ and Q**=0.006 $Å^{-1}$, associated to the bending length R and the persistence length Σ, which are about 12 nm and 105 nm, respectively. These values agreed with those on the SEM images at high magnification, showing good complementarity between the real space imaging and the scattering techniques. Additionally, rGO showed a surface and mass fractal dimension of D_s= 3 and D_m= 2 respectively (**Figure III.26 c)**.

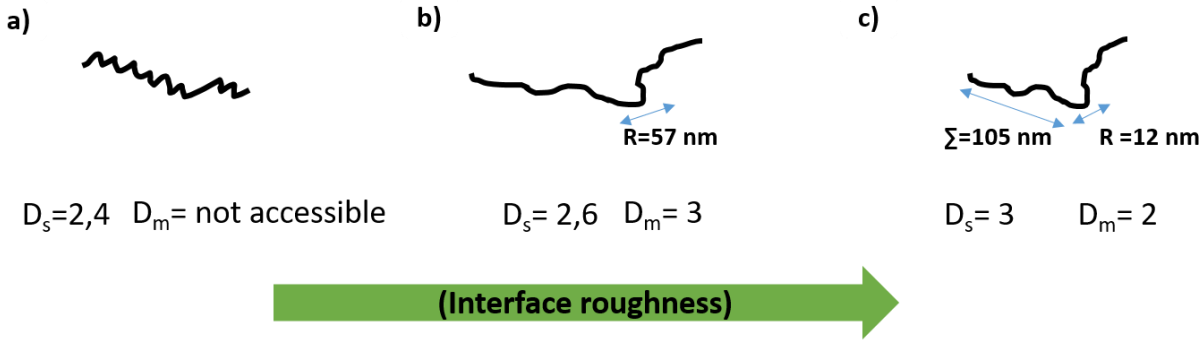

Figure III. 26 the morphologic model, the characteristic structural features (R, and Σ), and the mass and surface fractal dimensions determined from SANS of (a) GO, (b) GA, and (c) rGO.

Regarding porosity, the SANS porosity data extracted from the invariant INV show that rGO has higher mesoporosity than GA: 35 and 57% for GA and rGO respectively (**Figure III.27 a**). Furthermore, rGO showed a higher N_2 BET SSA of 401 m^2/g than GA with only 237 m^2/g (**Figure III.27 b)** and higher pore volume of 0.86 compared to 0.24 cm^3/g in GA in the 0.6 to 30 nm scale (**Figure III.27 c)**. These BET results further confirmed that the higher total pore volume in GA (24.3 cm^3/g) compared to that of rGO (4.3 cm^3/g), which was calculated from the difference between the envelope volume (V_A) and solid volume (V_A), was mainly due to its high macroporosity confirming the SEM observation.

All these quantitative results showed that rGO is more reduced than GA and has higher micro-/mesoporosity and lower macroporosity than GA. The chemical analysis and porosity measurements will be correlated to the electrochemical performances of these materials in **Chapter V**.

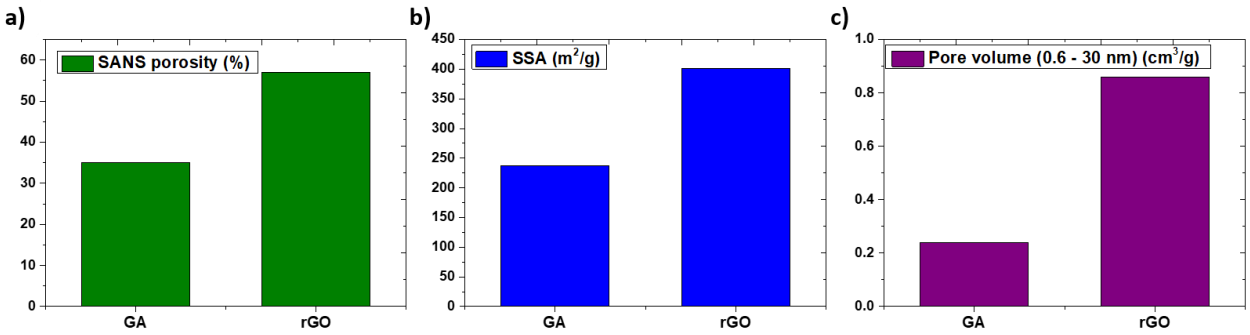

Figure III. 27 (a) SANS porosity, (b) N_2 SSA, and (c) pore volume in the scale 0.6 to 30 nm of GA and rGO.

8 References

[1] H. Banda *et al.*, "Sparsely Pillared Graphene Materials for High-Performance Supercapacitors: Improving Ion Transport and Storage Capacity," *ACS Nano*, vol. 13, no. 2, pp. 1443–1453, Feb. 2019, doi: 10.1021/acsnano.8b07102.

[2] H. Banda *et al.*, "Investigation of ion transport in chemically tuned pillared graphene materials through electrochemical impedance analysis," *Electrochimica Acta*, vol. 296, pp. 882–890, Feb. 2019, doi: 10.1016/j.electacta.2018.11.122.

[3] F. A. Suwaidi, H. Younes, V. Sreepal, R. R. Nair, C. Aubry, and L. Zou, "Strategies for tuning hierarchical porosity of 3D rGO to optimize ion electrosorption," *2D Mater.*, vol. 6, no. 4, p. 045010, Jul. 2019, doi: 10.1088/2053-1583/ab2927.

[4] S. Wang *et al.*, "Green Synthesis of Porous Cocoon-like rGO for Enhanced Microwave-Absorbing Performances," *ACS Appl. Mater. Interfaces*, vol. 10, no. 49, pp. 42865–42874, Dec. 2018, doi: 10.1021/acsami.8b15416.

[5] S. Pei and H.-M. Cheng, "The reduction of graphene oxide," *Carbon*, vol. 50, no. 9, pp. 3210–3228, Aug. 2012, doi: 10.1016/j.carbon.2011.11.010.

[6] L. G. Guex *et al.*, "Experimental review: chemical reduction of graphene oxide (GO) to reduced graphene oxide (rGO) by aqueous chemistry," *Nanoscale*, vol. 9, no. 27, pp. 9562–9571, 2017, doi: 10.1039/C7NR02943H.

[7] H. Khan, A. S. Yerramilli, A. D'Oliveira, T. L. Alford, D. C. Boffito, and G. S. Patience, "Experimental methods in chemical engineering: X-ray diffraction spectroscopy—XRD," *The Canadian Journal of Chemical Engineering*, vol. 98, no. 6, pp. 1255–1266, 2020, doi: 10.1002/cjce.23747.

[8] W. S. Hummers and R. E. Offeman, "Preparation of Graphitic Oxide," *J. Am. Chem. Soc.*, vol. 80, no. 6, pp. 1339–1339, Mar. 1958, doi: 10.1021/ja01539a017.

[9] H. Banda *et al.*, "One-step synthesis of highly reduced graphene hydrogels for high power supercapacitor applications," *Journal of Power Sources*, vol. 360, pp. 538–547, Aug. 2017, doi: 10.1016/j.jpowsour.2017.06.033.

[10] A. Monshi, M. R. Foroughi, and M. Monshi, "Modified Scherrer Equation to Estimate More Accurately Nano-Crystallite Size Using XRD," *World Journal of Nano Science and Engineering*, vol. 2, pp. 154–160, Sep. 2012, doi: 10.4236/wjnse.2012.23020.

[11] D. Foster *et al.*, "Comparative micromechanics assessment of high-carbon martensite/bainite bearing steel microstructures using in-situ synchrotron X-ray diffraction," *Materialia*, vol. 14, p. 100948, Dec. 2020, doi: 10.1016/j.mtla.2020.100948.

[12] Y. Yang *et al.*, "Graphene-based materials with tailored nanostructures for energy conversion and storage," *Materials Science and Engineering: R: Reports*, vol. 102, pp. 1–72, Apr. 2016, doi: 10.1016/j.mser.2015.12.003.

[13] M. Fathy, A. Gomaa, F. A. Taher, M. M. El-Fass, and A. E.-H. B. Kashyout, "Optimizing the preparation parameters of GO and rGO for large-scale production," *J Mater Sci*, vol. 51, no. 12, pp. 5664–5675, Jun. 2016, doi: 10.1007/s10853-016-9869-8.

[14] S. Stankovich *et al.*, "Synthesis of graphene-based nanosheets via chemical reduction of exfoliated graphite oxide," *Carbon*, vol. 45, no. 7, pp. 1558–1565, Jun. 2007, doi: 10.1016/j.carbon.2007.02.034.

[15] R. P. Rocha, M. F. R. Pereira, and J. L. Figueiredo, "Characterisation of the surface chemistry of carbon materials by temperature-programmed desorption: An assessment," *Catalysis Today*, vol. 418, p. 114136, Jun. 2023, doi: 10.1016/j.cattod.2023.114136.

[16] K. H. Kangasniemi, D. A. Condit, and T. D. Jarvi, "Characterization of Vulcan Electrochemically Oxidized under Simulated PEM Fuel Cell Conditions," *J. Electrochem. Soc.*, vol. 151, no. 4, p. E125, Feb. 2004, doi: 10.1149/1.1649756.

[17] W. Zhang, P. Feng, J. Chen, Z. Sun, and B. Zhao, "Electrically conductive hydrogels for flexible energy storage systems," *Progress in Polymer Science*, vol. 88, pp. 220–240, Jan. 2019, doi: 10.1016/j.progpolymsci.2018.09.001.

[18] L. M. Da Silva *et al.*, "Reviewing the fundamentals of supercapacitors and the difficulties involving the analysis of the electrochemical findings obtained for porous electrode materials," *Energy Storage Materials*, vol. 27, pp. 555–590, May 2020, doi: 10.1016/j.ensm.2019.12.015.

[19] R. Mendoza, J. Oliva, and V. Rodriguez-Gonzalez, "Effect of the micro-, meso- and macropores on the electrochemical performance of supercapacitors: A review," *International Journal of Energy Research*, vol. 46, no. 6, pp. 6989–7020, 2022, doi: 10.1002/er.7670.

[20] E. Lust *et al.*, "Influence of specific surface area and microporosity-mesoporosity of pristine and Pt-nanoclusters modified carbide derived carbon electrodes on the oxygen electroreduction," *Electrochimica Acta*, vol. 140, pp. 294–303, Sep. 2014, doi: 10.1016/j.electacta.2014.04.054.

[21] E. G. Iashina *et al.*, "Small-angle neutron scattering (SANS) and spin-echo SANS measurements reveal the logarithmic fractal structure of the large-scale chromatin organization in HeLa nuclei," *J Appl Cryst*, vol. 52, no. 4, pp. 844–853, Aug. 2019, doi: 10.1107/S160057671900921X.

[22] D. Saurel *et al.*, "A SAXS outlook on disordered carbonaceous materials for electrochemical energy storage," *Energy Storage Materials*, vol. 21, pp. 162–173, Sep. 2019, doi: 10.1016/j.ensm.2019.05.007.

[23] J. Teixeira, "Small-angle scattering by fractal systems," *J Appl Cryst*, vol. 21, no. 6, Art. no. 6, Dec. 1988, doi: 10.1107/S0021889888000263.

[24] P. W. Schmidt, "Small-angle scattering studies of disordered, porous and fractal systems," *J Appl Cryst*, vol. 24, no. 5, Art. no. 5, Oct. 1991, doi: 10.1107/S0021889891003400.

[25] B. Hammouda, "A new Guinier–Porod model," *J Appl Cryst*, vol. 43, no. 4, pp. 716–719, Aug. 2010, doi: 10.1107/S0021889810015773.

[26] E. M. Anitas, "Small-Angle Scattering from Fractals: Differentiating between Various Types of Structures," *Symmetry*, vol. 12, no. 1, Art. no. 1, Jan. 2020, doi: 10.3390/sym12010065.

[27] J. Bahadur, L. F. Ruppert, V. Pipich, R. Sakurovs, and Y. B. Melnichenko, "Porosity of the Marcellus Shale: A contrast matching small-angle neutron scattering study," *International Journal of Coal Geology*, vol. 188, pp. 156–164, Mar. 2018, doi: 10.1016/j.coal.2018.02.002.

[28] L. F. Ruppert *et al.*, "A USANS/SANS Study of the Accessibility of Pores in the Barnett Shale to Methane and Water," *Energy Fuels*, vol. 27, no. 2, pp. 772–779, Feb. 2013, doi: 10.1021/ef301859s.

[29] R. C. Hedden, H.-J. Lee, and B. J. Bauer, "Characterization of Nanoporous Low-k Thin Films by Small-Angle Neutron Scattering Contrast Variation," *Langmuir*, vol. 20, no. 2, pp. 416–422, Jan. 2004, doi: 10.1021/la035384w.

[30] Z. Mileeva, D. K. Ross, D. Wilkinson, S. M. King, T. A. Ryan, and H. Sharrock, "The use of small angle neutron scattering with contrast matching and variable adsorbate partial pressures in the study of porosity in activated carbons," *Carbon*, vol. 50, no. 14, pp. 5062–5075, Nov. 2012, doi: 10.1016/j.carbon.2012.06.046.

[31] O. Spalla, S. Lyonnard, and F. Testard, "Analysis of the small-angle intensity scattered by a porous and granular medium," *J Appl Cryst*, vol. 36, no. 2, Art. no. 2, Apr. 2003, doi: 10.1107/S0021889803002279.

[32] J. Bahadur, A. P. Radlinski, Y. B. Melnichenko, M. Mastalerz, and A. Schimmelmann, "Small-Angle and Ultrasmall-Angle Neutron Scattering (SANS/USANS) Study of New Albany Shale: A Treatise on Microporosity," *Energy Fuels*, vol. 29, no. 2, pp. 567–576, Feb. 2015, doi: 10.1021/ef502211w.

[33] "Pore characterization of shales: A review of small angle scattering technique," *Journal of Natural Gas Science and Engineering*, vol. 78, p. 103294, Jun. 2020, doi: 10.1016/j.jngse.2020.103294.

[34] E. A. Chavez Panduro *et al.*, "Small-angle X-ray scattering analysis of porous powders of CaCO3," *J Appl Cryst*, vol. 45, no. 5, pp. 881–889, Oct. 2012, doi: 10.1107/S0021889812032219.

[35] W. Gu and G. Yushin, "Review of nanostructured carbon materials for electrochemical capacitor applications: advantages and limitations of activated carbon, carbide-derived carbon, zeolite-templated carbon, carbon aerogels, carbon nanotubes, onion-like carbon, and graphene," *WIREs Energy and Environment*, vol. 3, no. 5, pp. 424–473, 2014, doi: 10.1002/wene.102.

CHAPTER IV:

Chemical and structural studies of pillared graphene materials

1 Objectives and approaches

As shown in **Chapter III**, the graphene sheets tend to restack after GO reduction due to the removal of the oxygen functional groups and π-π stacking interactions between rGO sheets. This restacking leads to an inter-graphene layer d-spacing of the reduced graphene materials (GA and rGO) of 0.36 nm, which is too narrow for electrolytic ion adsorption (cation size ~0.7 nm). To prevent the restacking issue of graphene sheets during reduction and increase the surface area accessible to ions, alkyl diamines (*i.e.* linear alkyl chain with 2 terminal amine functions) were used to space out graphene sheets and keep them apart. The amine function reacts with oxygen containing functionalities, resulting in covalent or electrostatic grafting [1]. When the alkyl chain length is long enough, both terminal amines can graft two graphene sheets, creating a bridging or cross-linking resulting in the formation of graphene galleries with a d-spacing or height that depends on the alkyl chain length (*i.e.* pillar) (**Figure IV.1**). This design allows for the creation of a new family of graphene-based materials that can be tailored to specific needs. This is achieved by incorporating alkyl-diamine linkers of varying lengths, resulting in increased porosity that is accessible to electrolytic ions. As a result, the electrochemically active surface area is increased , leading to improved storage performance of supercapacitors [2].

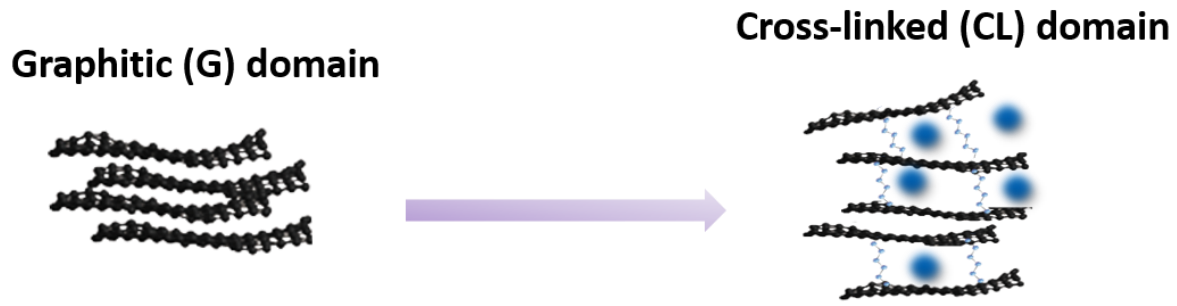

Figure IV.1 Schematic representation of graphitic and pillared domains showing ions adsorption within the galleries.

To unlock the full potential of the pillared graphene-based materials in SCs applications, it is imperative to adopt a comprehensive approach that integrate structural and morphological analysis, electrochemical investigation, and physicochemical characterization. Such a holistic perspective is crucial for gaining a profound understanding of the properties and behaviors exhibited by these materials. The structural and morphological analyses provide insights into the arrangement and configuration of graphene sheets. They shed light on factors such as restacking, pillaring and porosity at various scales. Electrochemical investigations offer

a deeper understanding of the materials' performance, elucidating their behavior in different electrolytes and shedding light on the factors that influence their capacitance.

As for the reference materials, depending on the synthesis method used (hydrothermal reaction or chemical reaction under stirring), pillared graphene-based materials can be prepared in two different pristine forms (aerogel or powder). To understand the impact of these two-synthesis method on the pillaring efficiency, it is necessary to characterize the multi-scale structure and porosity, as well as chemical properties. Therefore, this Chapter focuses on studies aiming to assess the physicochemical properties of the samples, as well as their morphological and structural features, including porosity at all relevant length scale ranging from nano- to macroscale. As for the characterization of the reference graphene samples, the characterization methodology includes physicochemical characterizations using TGA, XPS, EA and TPD-MS to gain insights into the reduction degree and successful functionalization as well as structural analysis using XRD, SANS, and SEM to understand the pillaring impact within an extended length scale (**Figure IV.2**).

The comparison with the reference materials GA and rGO will enable us to highlight the impact of pillaring on the structural and physicochemical. This work aims to gain a nuanced understanding of how pillaring affects the material's porosity and its relationship to the electrochemical performance, which will be presented in **Chapter V**.

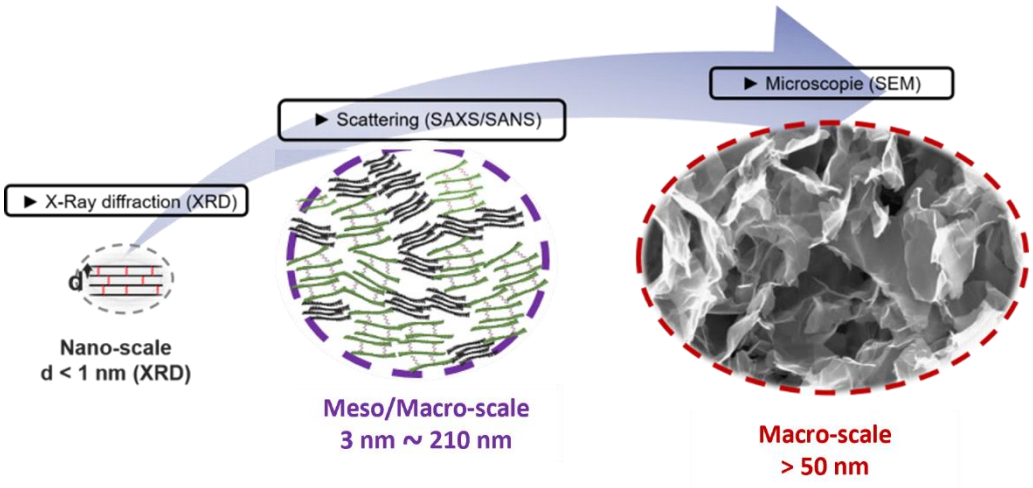

Figure IV.2 Conceptual scheme of the different level of porosity in pillared graphene materials

2 Overview on the studied pillared graphene materials

Figure IV.3 presents an overview of the two synthesis protocols used to prepare nGAs and nRPs, where 'n' represents the number of carbons in the alkyl chain, indicating the pillar length. The synthesis of nGAs involved a one-step hydrothermal process in the presence of alkyl diamine, conducted in an autoclave at 180°C for 17 hours, resulting in the formation of an aerogel. In contrast, the preparation of nRPs involved a two-step protocol that included functionalization and subsequent reduction using hydrazine hydrate. Both steps were carried out under stirring and heating conditions at 90°C for 24 hours, resulting in the production of a powder [2, 3]. For 6GAs, three distinct equivalent diamine numbers (0.05, 0.5, and 1) were used, while for 6RPs 0.2, 1, and 2 equivalents were studied (**Figure IV.3 c**). Furthermore, nGA-0.05 involved the study of four different pillars with various lengths of the alkyl chain (n = 6, 8, 10, or 12) (**Figure IV.3 d**).

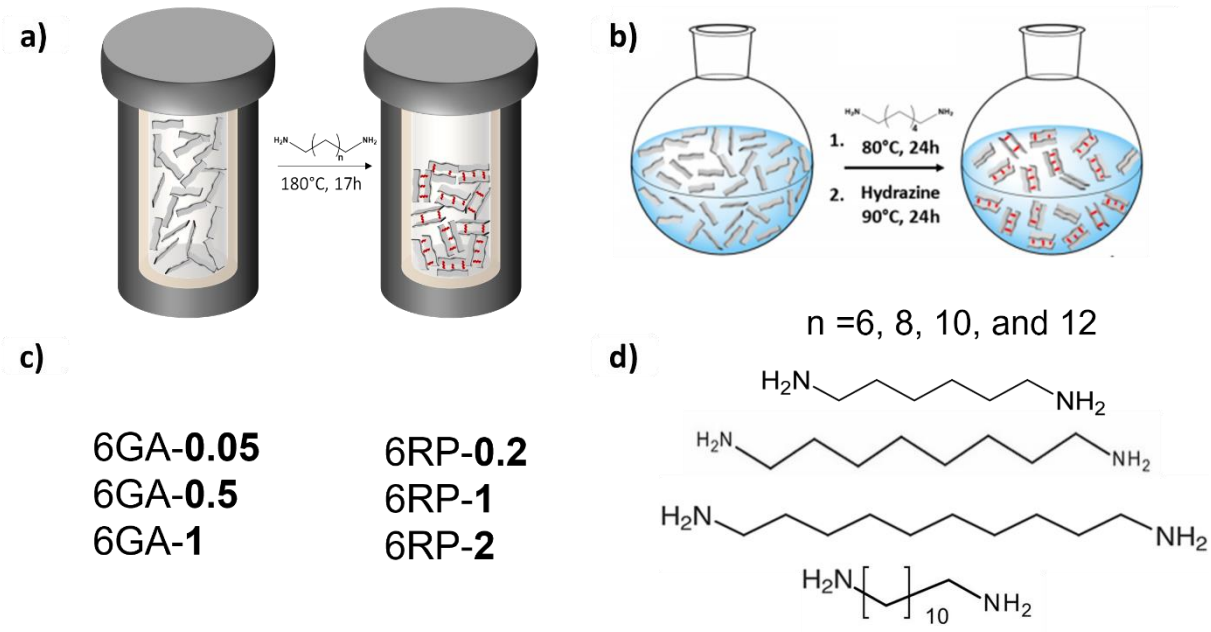

Figure IV.3 Synthesis protocol of (a) nGAs (b) nRPs (c) the pillars used in this work with the number of carbons in the alkyl chain and (d) the equivalent number used for 6GA and 6RP synthesis.

Regarding the corresponding reference materials (GA and rGO), the two distinct pillared graphene materials (nGAs and nRPs) exhibit different characteristics. Visually, these pristine materials present notable differences in terms of apparent density and shape. The nRPs are dense powders, while the nGAs appear as lightweight porous aerogels. To assess the complete difference between these materials, a comprehensive analysis of their physicochemical, structural and morphological properties will be presented in this chapter.

3 Reduction efficiency and chemical composition of 6RP-0.2 and 6GA-0.05

A prior investigation conducted in our laboratory [1] focused on various 6GAs and 6RPs with different equivalent numbers (alkyl diamine concentrations). This study revealed that 6GA-0.05 and 6RP-0.2 exhibited similar d-spacing and demonstrated superior electrochemical performances compared to other studied concentrations. Therefore, these materials were selected as the standard materials for our current study, except for the studies on the impact of the number of equivalents and pillar length

The success of functionalization and the reduction efficiency in 6GA-0.05 and 6RP-0.2 were investigated using TGA, XPS, EA. TGA was performed on all samples under N_2 atmosphere, with at a heating rate of 5°C/min from 30 to 800°C (**Figure IV.4 a**). As shown in **Chapter III Section 3**, GO undergoes three distinct weight loss processes. The first process is attributed to the desorption of adsorbed water molecules at around 100°C, while the second is associated with the elimination of surface oxygen functional groups at around 200°C. Beyond 200°C, a consistent decrease in weight is typically assigned to the slow elimination of stable oxygen containing functional groups [4], resulting in a total weight loss of 50%.

In contrast, the thermogram of pillared samples can be decomposed in two weight loss processes. The first one occurs between 312 and 570 °C is attributed to the degradation of the grafted molecules and the decomposition of surface oxygen groups. Beyond 550°C, a consistent decrease in weight is observed, which is assigned to the slow elimination of stable oxygen containing groups, as in the case of GO. 6RP-0.2 and 6GA-0.05 show a weight loss of 26 and 30% respectively, across the temperature spectrum. A more pronounced weight loss recorded for the 6GA-0.05 indicates that it may contain more grafted pillars or be less reduced than 6RP-0.2 or. **In order to understand this difference, the corresponding weight loss of pillars is calculated** by measuring the weight loss between the changes in slopes in the degradation profile before and after the degradation step of the pillars ($312 \leq T \leq 570$ °C). **Figure IV.15 b** shows that 6RP-0.2 exhibit a weight loss of 17 wt%, while 6GA-0.05 show a weight loss of 22 wt%.

This weight loss is adjusted by subtracting the weight loss of rGO and GA, which occurred in the same temperature range (3.2 wt% and 6.6 wt% respectively), to account for any oxygen losses taking place in such temperature range. The calculated weight loss of pillars gives 13.8 and 15.4 wt% for 6RP-0.2 and 6GA-0.05 respectively, **demonstrating that 6GA-0.05 contains more pillars than 6RP-0.2**. To determine the degree of reduction of both

materials, the weight loss percentage of pillars is subtracted from the total weight loss revealing 12.2 and 14.6 wt% for 6RP-0.2 and 6GA-0.05 respectively, indicating that **6RP-0.2 is more reduced than 6GA-0.05**. To further investigate these findings, XPS analysis is conducted on these samples.

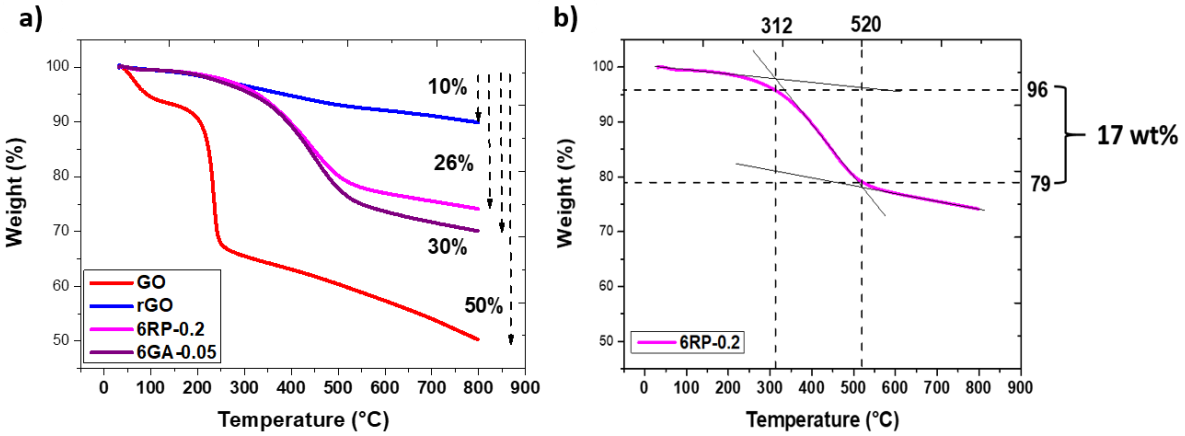

Figure IV.4 (a) TGA response performed under N_2 atmosphere of GO, rGO, 6RP-0.2, and 6GA-0.05 (b) TGA profile of the 6RP sample with the difference in weight % calculated from the changes in the slopes of the degradation profile before and after the degradation step.

The XPS survey spectra of the pillared materials (**Figure IV.5**) show the presence of the expected N1s signal at around 400 eV, which originates from the pillars. High resolution XPS C1s, O1s and N1s spectra were recorded and the atomic concentration of each element was determined. These data, along with the elemental mass concentration determined by elemental analysis performed on 6RP-0.2 and 6GA-0.05 are gathered in **Table IV.1**. Both techniques show similar trend: the nitrogen content in 6RP-0.2 is markedly higher than that of 6GA-0.05. Such observation can be explained by the incorporation of nitrogen in the graphene sheet backbone when hydrazine hydrate is used for its reduction. Additionally, both techniques show that the oxygen content of 6GA-0.05 is slightly higher than that of 6RP-0.2. Furthermore, the conductivity measurements performed using a four-probe system of pellets, reveal **an electrical conductivity of 124 ±5 S/m and 28 ±2 S/m for 6RP-0.2 and 6GA-0.05 respectively**. These results support the TGA observations, indicating that 6RP-0.2 is more reduced than 6GA-0.05, and confirm the presence of grafted molecules within the materials. To determine whether the pillars are covalently bonded or only adsorbed or intercalated within the graphene layers, TPD-MS was conducted.

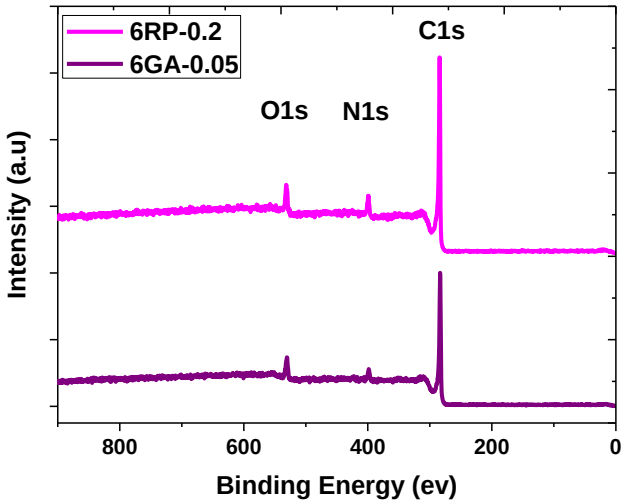

Figure IV.5 XPS survey scan of 6GA-0.05 and 6RP-0.2

Table IV.1: XPS atomic concentration extracted from and EA mass concentration of the 6GA-0.05 and 6RP-0.2

	Materials	%C	%H	%N	%O
XPS	**6GA-0.05**	87.02	-	4.89	8.09
	6RP-0.2	84.7	-	7.6	7.7
EA	**6GA-0.05**	77.49	3.72	5.82	12.95
	6RP-0.2	74.8	3.74	9.29	12.17

TPD-MS analysis were conducted by the CEMHTI Laboratory in Orléans. The comparison between the degradation temperatures of the bare molecules and grafter molecules within the materials can indicate whether they are adsorbed or covalently bonded to the graphene sheets. TPD-MS was performed under inert atmosphere (Ar) on a temperature range of 0 to 300°C for the bare pillar and 0 to 900°C for the pillared materials. **Figure IV6. a** demonstrates that the bare 1,6 diamonohexane pillar starts decomposing at a low temperature of around 30°C, releasing $–CH_2$-CH_2-NH_2 compounds. Additionally, distinct degradation peaks of the bare molecule (corresponding to -CH_2-NH_2, $–CH_2$-CH_2-NH_2, and –NH fragments) are recorded at 180°C, accompanied by a weight loss of 100%, indicating complete degradation of the pillars.

In turns, **Figure IV.6 b** shows the TPD-MS profile of the 6RP-0.2 material. Both 6GA-0.05 and 6RP-0.2 exhibit similar profiles. Interestingly, the peaks of the molecule's decomposition have shifted to higher temperatures: 300°C for $–CH_2$-CH_2-NH_2, 450°C for CH_2-NH_2, and 500°C for NH. Moreover, the broadness of these peaks indicates that the pillar is more stable and requires higher thermal energy for decomposition than the bare pillar. **These results confirm that the molecules are covalently bonded to the graphene sheets.** Additionally, the decomposition of molecules containing $–NH_2$ groups could only originate from the amines that did not react with the oxygen functional groups on the graphene oxide. **This finding suggests the presence of non-reacted amines, which may come from pillars that reacted only from one side with the graphene sheet**. These findings confirm the functionalization of the graphene. However, this study aims to open new porosity accessible to ions by bridging the graphene sheets with the pillars and preventing their restacking. Therefore, XRD was conducted to determine if the materials are pillared or only functionalized graphene-based materials.

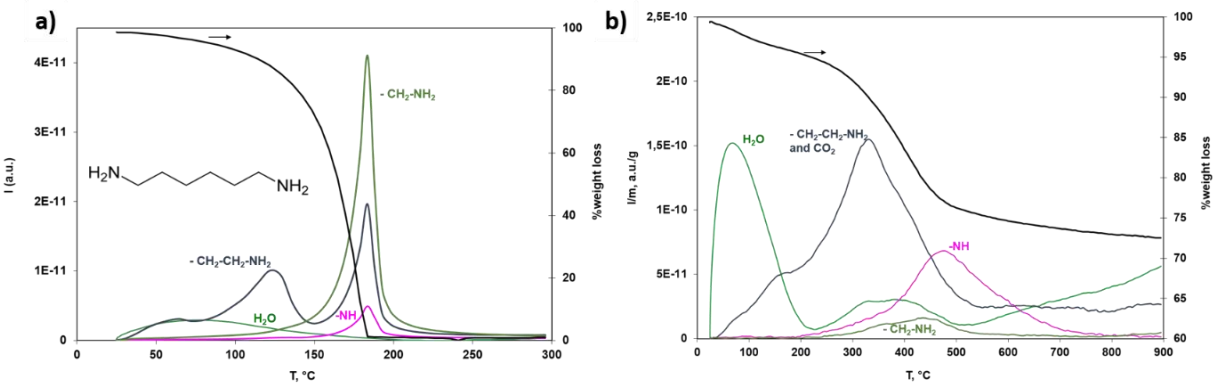

Figure IV.6 The decomposition products under heating evaluated by TPD-MS of (a) 1,6 diamonohexane and (b) 6RP-0.2.

4 Nano-porosity investigation

XRD was conducted to give evidence of successful pillaring and the creation of nanoporosity. In this study, the so called nanoporosity or galleries refer to the interlayer d-spacing created by the pillaring. The XRD patterns (**Figure IV.7**) of the two materials exhibit two distinct diffraction peaks compared to the reference materials, which only display a single peak (in the Q range 0 to 3 $Å^{-1}$). The peak observed at Q=1.6 $Å^{-1}$ corresponds to the restacked graphitic part (G peak) with an interlayer distance of 0.39 nm, showing a slight increase compared to their respective reference materials (0.36 nm). This difference may be due to either i) a lower degree of reduction of the pillared materials or ii) the presence of horizontally

intercalated pillars between the graphene sheets. The former explanation is more consistent with the chemical analysis, which indicated the presence of grafted molecules on only one side.

The new XRD peak appears at lower Q values (Q=0.82 $Å^{-1}$), featuring a d-spacing of 0.77 nm, attributed to a long-range order. **This peak is ascribed to the bridging of the rGO sheets together using the molecular pillars and is denoted as the CL (cross-linked) peak**. This attribution was further supported by the absence of this peak in rGO samples, confirming that the CL peak only appeared when pillaring was performed prior to reduction.

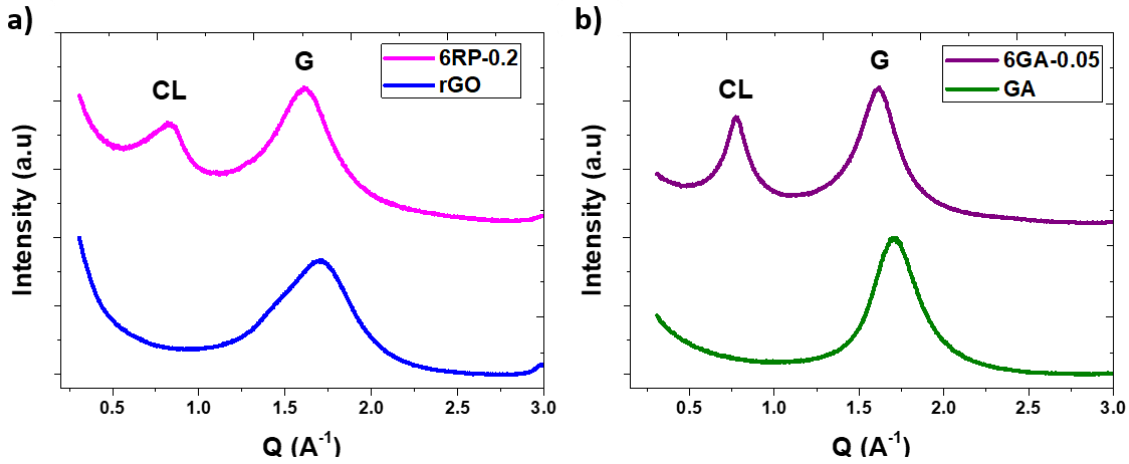

Figure IV.7 XRD patterns of (a) 6RP-0.2 and rGO, (b) 6GA-0.05 and GA.

The mean graphitic domains represented by the G peak exhibit a broad profile, similar to that of their reference materials, and broader than that of graphite. This observation is consistent for both 6GA-0.05 and 6RP-0.2, suggesting that the restacking process is comparable, regardless of the presence of pillars. Furthermore, the CL peak in 6RP-0.2 is broader than that of 6GA-0.05 and displays an asymmetric shape. This may be attributed to a lower number of bridged layers per stackor non-uniform pillaring across the sample, leading to a larger distribution of d-spacing in 6RP-0.2. To verify these hypotheses, the Scherrer equation was applied to estimate the stack height [5, 6]. The XRD fitting data and calculation results are presented in **Table IV.2.**

$$L_c = \frac{k_1 \lambda}{FWHM.cos\theta_1} \qquad (IV.1)$$

With:

ƛ radiation wavelength of cobalt (0.1789 nm)

K_1, form factor (k=1)

FWHM, width at half height of the diffraction peak (rad)

Table IV.2: XRD fitting data and the stack height calculated from Scherrer equation.

	CL peak			G peak				
Sample	**Position (°)**	**d-spacing (nm)**	**FWHM**	**Position (°)**	**d-spacing (nm)**	**FWHM**	**Stack Height (nm)**	
							CL	**G**
6GA-0.05	13.1±0.3	0.77±0.01	2.6	26.9	0.39	4.7	**3.5**	**2**
6RP-0.2	13.4±0.3	0.76±0.01	4	26.6	0.39	6.1	**2.3**	**1.5**

Both 6GA-0.05 and 6RP-0.2, exhibit similar number of layers per stack (stack height divided by d-spacing), with approximately 3-4 and 2-3 layers per stack, respectively. This result suggests that the broadness of the CL peak in 6RP-0.2 is not primarily due to the number of cross-linked layers per stack. Therefore, further investigations were conducted to track whether the broadness of the CL peak in 6RP-0.2 could result from a non-uniform pillaring distribution. Indeed, different samples from the same synthesis batch displayed different CL peak shapes (**Figure IV.8**), **revealing two dominant populations with d-spacing of 0.75 nm and 0.66 nm**. The former, present in both 6RP-0.2 and 6GA-0.05, could be considered as the stable pillar conformation. The latter, with a 0.66 nm d-spacing, may indicate the presence of tilted pillar conformation. Therefore, a grinding step was implemented after each synthesis to obtain a homogeneous powder and for relevant electrochemical and physicochemical results.

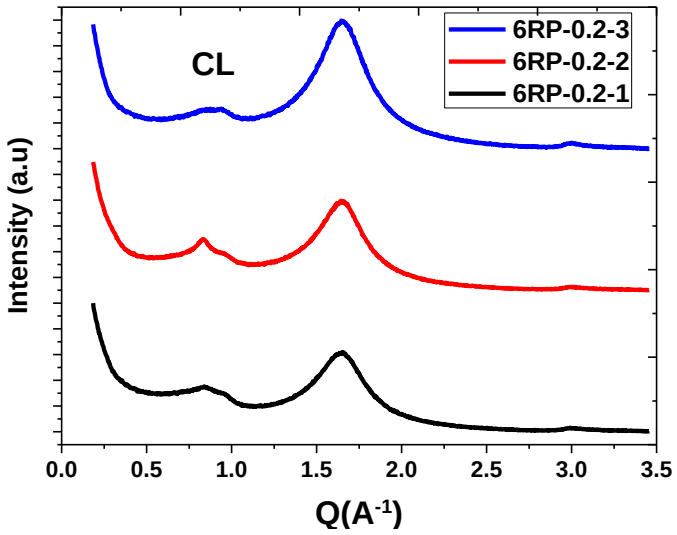

Figure IV.8 XRD patterns of different samples from the same 6RP-0.2 synthesis.

5 Pillaring homogeneity investigation

5.1 Pillaring homogeneity in 6RP-0.2

In an effort to understand the observed populations on the CL peak, we monitored the 6RP-0.2 reaction by extracting samples at different time points during the reaction and studying their nanostructure and chemical properties. As previously mentioned, the 6RP-0.2 synthesis involves a two-step process, with the first step being functionalization or pillaring, resulting in a product named 6P. Four samples were extracted at 2, 4, 8, and 24 hours after the first reaction step, washed, and subsequently dried to perform XRD and XPS analyses. The XRD results indicate that the GO peak shifted to smaller angles after two hours (**Figure IV.19**), indicating an increase in the interlayer distance due to diamine intercalation.

A small bump around 1 $Å^{-1}$ is observed (black circle), possibly resulting from diamine intercalation between the partially reduced graphene layers. Moreover, the presence of a G peak after only two hours is evident, indicating that a substantial portion of the material has undergone reduction and restacking, indicating that both functionalization and partial reduction occurred during this step. The early onset of reduction kinetics explains why a fully pillared material is never achieved, and a certain amount of restacked graphene is always present. After four hours of reaction, the GO peak exhibits two dominant interlayer distances, suggesting that the pre-intercalated diamine has started to react with the graphene sheets. Subsequently, after 8 and 24 hours, the GO peak shifts to higher angles, indicating a decrease in interlayer distances, ultimately reaching 0.93 nm by the end of the reaction. **Figure IV.10** illustrates the evolution of the functionalized graphene material (6Ps) during the first reaction step. In the initial stages of the reaction (6P-2H), the amines intercalate between the GO sheets and initiate reactions with the oxygen functional groups, causing an increase in the d-spacing. After 4 to 8 hours, the d-spacing starts to decrease and eventually stabilizes at 0.93 nm after 24 hours. Towards the end of the reaction, with such a high d-spacing compared to 6GA-0.05 for example with a d-spacing of 0.77 nm, it is expected that the pillars are vertically aligned.

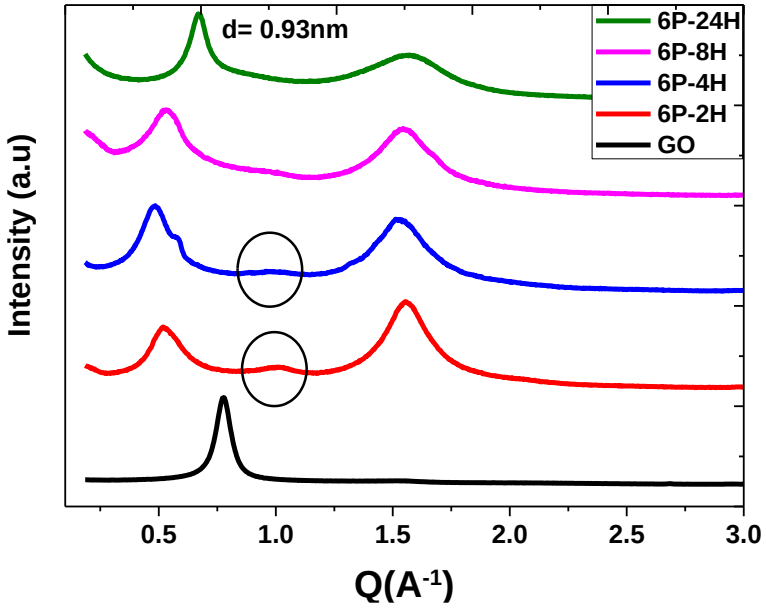

Figure IV.9 XRD patterns of GO and 6Ps after 2, 4, 8, and 24 hour of reaction.

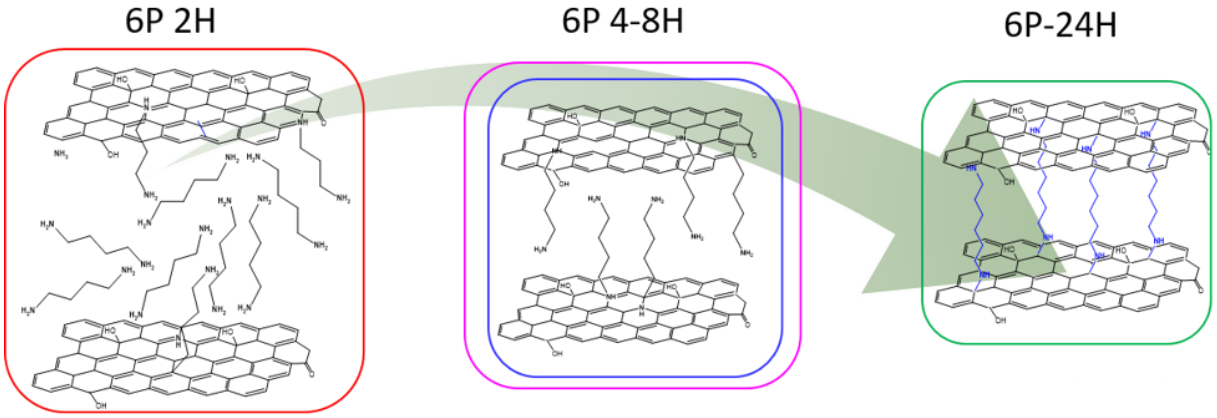

Figure IV.10 The proposed scheme of the functionalized and pillared graphene during this first reaction.

In the second step of the reaction, hydrazine hydrate was used to reduce the 6P-24H sample and remove the remaining oxygen groups, aiming to increase the conductivity of the material. **Figure IV.11** shows the evolution of the material's structure during this reduction step monitored by XRD. After two hours of 6P-24H reduction, the CL peak shifts to higher angles, resulting in a d-spacing of 0.82 nm. This shift is likely attributed to the removal of oxygen groups to finally lead to a decrease in the interlayer distance. This decrease in d-spacing may be due to a tilted pillar conformation. After 8 hours, the d-spacing continues to decrease, and a second peak begins to emerge, increasing the broadness of the CL peak. The broad double peak at the end of the reaction indicates the presence of two pillaring populations. The peak deformation observed after 8 hours of reduction suggests that the degree of reduction impacts

the pillaring. This effect may be due to differences in pillar conformation either arising from second amine grafting or further elimination of oxygen functional groups, leading to a deformation of the pillars and the creation of other stable conformation.

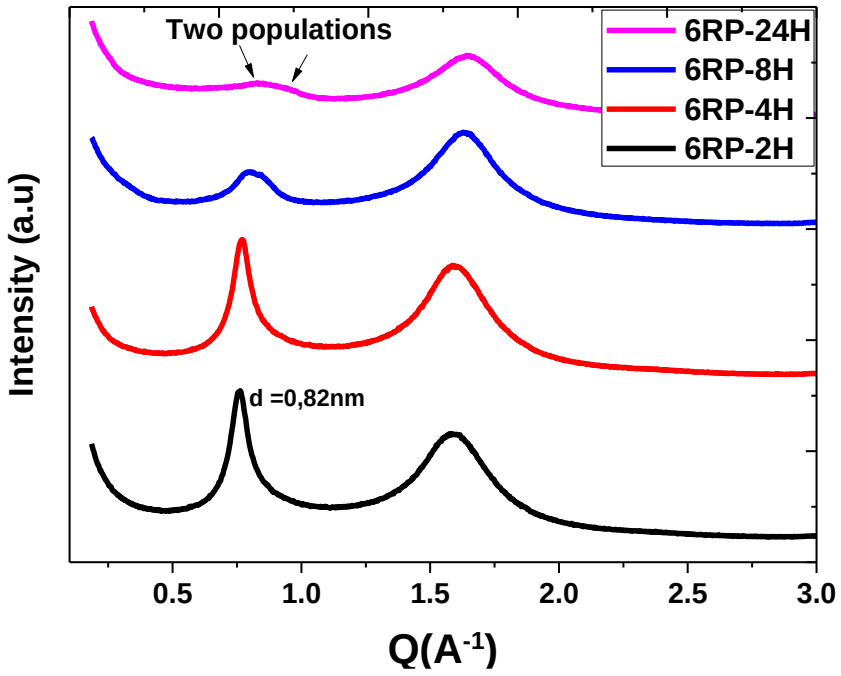

Figure IV.11 XRD patterns of 6RP-0.2 after 2, 4, 8, and 24 hour of 6P-24H reduction.

The two reactions were also monitored using XPS, providing insights into the evolution of nitrogen and oxygen content during the two reaction steps. Since the samples were washed and dried before the analysis, any non-intercalated or non-reacted diamine should have been removed, and the nitrogen percentage can provide insights on the intercalation/reaction process. **Figure IV.12** illustrates the nitrogen and oxygen evolution during the first reaction step. The nitrogen content increases from 0.3% in GO to approximately 6% after only 2 hours of reaction, **demonstrating the high reactivity of the diamines**. After 2 hours of reaction, the N content increases gradually, indicating that the reaction between the diamine and the graphene oxygen functional groups occurs progressively. In contrast, the oxygen evolution displays a sharp decrease after 2 hours of reaction, **decreasing from ~30% in GO to ~20% after two hours of functionalization**. This reduction represents the removal of 33% of the oxygen content in the material. After 4 hours, the oxygen amount further decreases from 20% to ~12%, representing a reduction of approximately 40% of the remaining oxygen content. The rapid removal of oxygen groups could be indeed responsible for the fast restacking kinetics observed by XRD. Additionally, the formation of a G peak after only 2 hours of

functionalization underscores the potent reduction capabilities of the 1,6-diaminohexane pillar. These results emphasize the fast reaction kinetics between the amines and the oxygen functional groups during the first two hours of the reaction. They also highlight the reduction ability of the diamines.

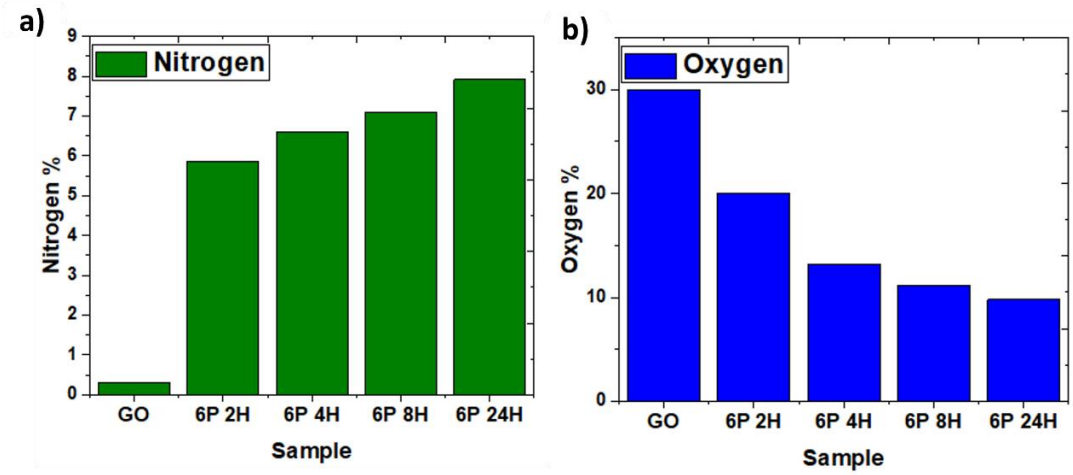

Figure IV.12 (a) Nitrogen and (b) oxygen evolution during the first reaction step determined by XPS.

During the reduction step using hydrazine (**Figure IV.13**), the nitrogen content increases due to the reaction between the hydrazine used for reduction and the graphene oxide sheets. A comparable increase in nitrogen was also observed in rGO using the same reducing agent without pillars, as nitrogen is incorporated into the graphene conjugated network, as shown in **Chapter III Section 3**. Additionally, a continuous decrease of the oxygen content is observed during reduction, reflecting the gradual elimination of the remaining oxygen functional groups. It appears that the reduction was more efficient during the initial step, when the majority of oxygen was removed. However, the conductivity measurements show that the electrical conductivity of 6P-24h (7 ±2 $S.m^{-1}$) is 20 times lower than that of 6RP-0.2 (124 ±5 $S.m^{-1}$). This indicates that the reduction step is crucial in restoring the conjugated network and ultimately enhancing the conductivity of the material.

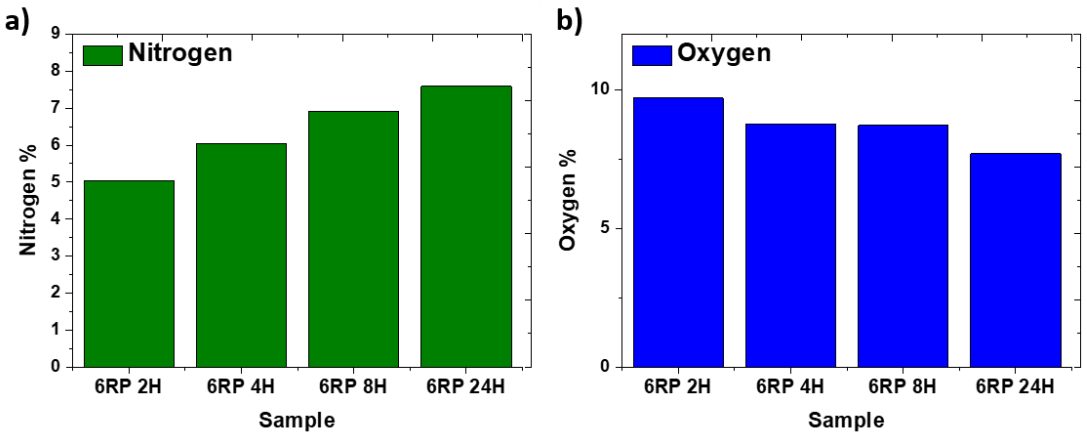

Figure IV.13 (a) Nitrogen and (b) oxygen evolution during the second reaction step determined by XPS.

5.2 Pillaring homogeneity in 6GA-0.05

For the 6GA-0.05, no deformation or asymmetry of the CL peak was observed. However, systematic XRD analysis and data fitting revealed a non-homogenous distribution of the ratio between cross-linked and graphitic domains. A study was conducted on different samples in order to identify the origin of this inhomogeneity. **Figure IV.14** displays the XRD patterns of various 6GA-0.05 samples prepared from the same synthesis batch. The samples were all prepared under identical conditions with a weight of 5 mg and pressed under 2 T for 10 min. The CL and G peaks were fitted using the same parameters and the same Q range (Q = 0.5-1.05 A^{-1} for CL peak and Q = 1.05-2.5 A^{-1} for G peak). The position of the CL peak remained constant, resulting in a unique d-spacing, unlike 6RP-0.2 (**Figure IV.8**). However, the CL/G peak ratio varies between samples, impacting the cross-linking percentage in the material (%CL). **Table IV.3** gathers the fitting XRD results, indicating a variation in cross-linked domain percentage from 19 to 34%. This suggests that the pillaring was not homogeneous across the sample during the synthesis.

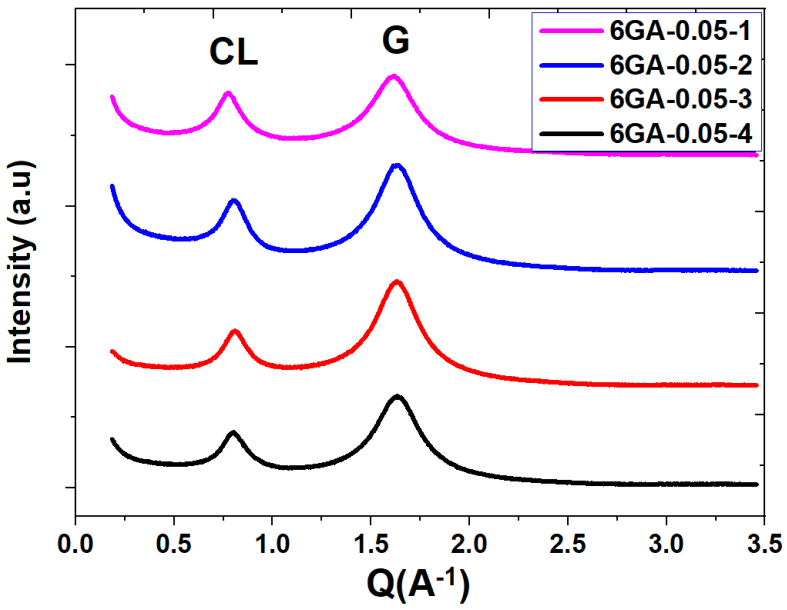

Figure IV.14 XRD patterns of different samples from the same 6GA-0.05 synthesis.

Table IV.3: XRD fitting data and the percentages of the cross-linked and the graphitic domains of 4 different samples of 6GA-0.05 single batch.

	CL		G		% CL	% G
	FWHM	Peak area	FWHM	Peak area		
6GA-0.05-1	2.5	56300	4.74	107900	**34**	**66**
6GA-0.05-2	2.5	45610	4.79	175075	**21**	**79**
6GA-0.05-3	2.46	36573	4.51	157601	**19**	**81**
6GA-0.05-4	2.44	53147	4.52	168810	**24**	**76**

To understand the inhomogeneity in pillaring of 6GA-0.05, we sought to investigate the core and shell of the aerogel based on the observed macrostructure between them as shown in **Figure IV.15 c**. Our aim was to gain insights into the evolution of cross-linking within the material. Two different samples from the core and two from the shell were examined using XRD (**Figure IV.15 a, b**). The two samples from the same aerogel part (core or shell) exhibited similar XRD patterns. After fitting the XRD curves, it was found that the core samples and the shell samples have a cross-linking percentage of 25% and 35% respectively, as shown in **Table IV.4**. These results indicate that the cross-linking is uniform within the core and shell of the aerogel. However, the study also reveal that the shell has a 40% higher cross-linked graphene

domain than the core. As it is technically challenging to separate shell from core for all analyses, a grinding step was implemented to obtain a homogeneous powder and prepare electrodes for relevant electrochemical and physicochemical results.

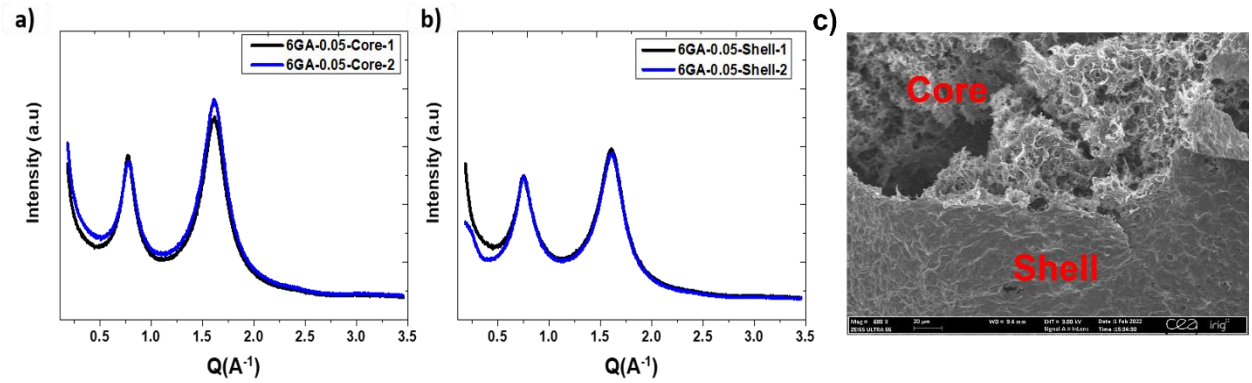

Figure IV.15 XRD patterns of two different samples from the (a) core and (b) shell of the 6GA-0.05 aerogel, (c) SEM image of the 6GA-0.05 aerogel showing the visual difference between the core and shell.

Table IV.4: XRD fitting data and the percentages of the cross-linked and the graphitic domains of different 6GA-0.05 samples extracted from the core and the shell of the aerogel.

	CL		G		% CL	% G
	FWHM	Peak area	FWHM	Peak area		
6GA-Core-1	2.6	44209	4.74	126350	**25**	**75**
6GA-Core-2	2.9	36576	4.79	111066	**25**	**75**
6GA-Shell-1	3.5	39033	4.66	71999	**35**	**65**
6GA-Shell-2	3.5	54209	4.95	105881	**34**	**66**

6 Investigation of impact of the equivalent number of pillars on the nanostructure and chemical properties of 6RP and 6GA

The impact of the equivalent number of the diamonohexane pillar used to prepare 6GAs and 6RPs on the grafted quantity within the materials was chemically investigated. Three different diamine equivalent numbers were used to prepare 6GAs (0.05, 0.5, and 1) and 6RPs (0.2, 1, and 2). **Table IV.5** gathers data from XPS and EA conducted on the different 6GAs. As previously mentioned, monitoring the evolution of nitrogen content could provide insights into the amount of grafted pillars in the material. Both XPS and EA show that the nitrogen amount

in 6GA-0.5 is approximately twice that found in 6GA-0.05. The nitrogen content was approximately doubled by increasing the diamine equivalent number by 10 from 0.05 to 0.5. However, both 6GA-0.5 and 6GA-1 contain the same nitrogen amount, which could be due to a functionalization saturation being reached below 0.5 equivalent number, meaning that any additional pillars were unable to react and were subsequently washed out of the material.

Table IV.5 Atomic percentages extracted from XPS and EA of the different 6GAs.

	Materials	**%C**	**%H**	**%N**	**%O**
XPS	**6GA-0.05**	87.02	-	**4.89**	8.09
	6GA-0.5	86.23	-	**8.65**	5.11
	6GA-1	84.95		**8.66**	6.39
EA	**6GA-0.05**	77.49	3.72	**5.82**	12.95
	6GA-0.5	71.8	5.9	**10.09**	12.21
	6GA-1	73.52	6	**10.02**	10.46

In contrast, the chemical analysis of 6RPs (**Table IV.6**) shows that increasing the pillars' equivalent number did not have a significant impact on the nitrogen content within the materials compared to 6GAs. This result suggests that the grafting saturation is already reached at 0.2 equivalent and that the additional pillars do not react.

Table IV.6 Atomic percentages extracted from XPS and EA of the 6RPs.

	Materials	**%C**	**%H**	**%N**	**%O**
XPS	**6RP-0.2**	84.7	-	**7.6**	7.7
	6RP-1	85.79	-	**6.46**	7.75
	6RP-2	84.28	-	**8.15**	7.57
EA	**6RP-0.2**	74.8	3.74	**9.29**	12.17
	6RP-1	71.7	3.7	**8.5**	16.1
	6RP-2	71.1	3.7	**8.1**	17.1

The impact of pillar density on the d-spacing was investigated using XRD. **Figure IV.16 a** displays the XRD patterns of the various 6GAs. Increasing the pillar density from 0.05 to 0.5 and then to 1 equivalent leads to an asymmetric and very large CL peak, indicating a

significant distribution of the interlayer distance. The peak's maximum was recorded at Q = 0.62 $Å^{-1}$, corresponding to a d-spacing of 1 nm. Additionally, the large d-spacing distribution suggests the presence of multiple stable pillar conformations within the material, including tilted and vertical pillars. This variability may be attributed to the high quantity of intercalated pillars that reacted with the graphene sheets. Furthermore, the stability of the CL peak above 0.5 equivalent corroborates the chemical analysis results, which showed a stable nitrogen percentage above 0.5 equivalent. This further confirms that the additional pillars could not react and were washed out from the material.

In turns, 6RPs XRD patterns are presented in **Figure IV.16 b**. Interestingly, increasing the pillar's equivalent number for 6RP synthesis did not exhibit a significant impact on the CL peak compared to 6GA. The CL peak position and shape of 6RP-1 resembled that of 6RP-0.2, while 6RP-2 showed a slight increase in the d-spacing to 0.8 nm (corresponding to Q = 0.78 $Å^{-1}$). These findings suggest that increasing the equivalent number in 6RP did not have a significant impact on the amount of grafted pillars. This finding is consistent with the chemical analysis, which indicated that grafting saturation occurred at 0.2 equivalent. These results confirm that 0.05 equivalent for 6GA and 0.2 equivalent for 6RP are the most suitable chemically and structurally.

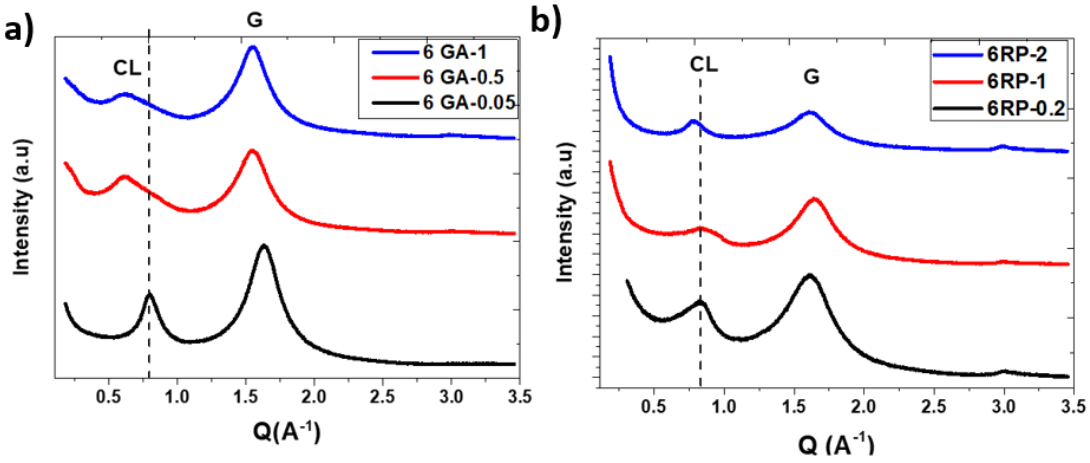

Figure IV.16 XRD patterns with different diamine equivalent numbers for (a) 6GA and (b) 6RP.

7 Pillars length impacts on the nanostructure and chemical properties of nGA-0.05

Four different graphene aerogels were synthesized using alkyl diamines with varying numbers of carbons in the alkyl chain (6, 8, 10, and 12) at an equivalent number (0.05). Chemical analyses were performed on the resulting pillared graphene aerogels (**Table IV.7**).

As all the pillar molecules contain the same number of nitrogen (2), the nitrogen content within the materials could be directly linked to the pillaring density and, therefore, to the pillaring efficiency. 6 and 8GA-0.05 have approximately the same nitrogen percentage. In turn, a slight decrease in the nitrogen percentage is noticed for 10 and 12GA-0.05. However, it is still comparable to that of the shorter alkyl diamines. This suggests that these pillars reacted with the graphene oxide with approximately the same yield as shorter diamines, from one or both sides, creating functionalized or pillared graphene materials. XRD analyses were performed on these samples to investigate the impact of the pillar length on the nanostructure.

Table IV.7 Atomic percentages extracted from XPS and EA of the different nGA-0.05 (n=6, 8, 10, and 12).

	Materials	**%C**	**%H**	**%N**	**%O**
XPS	**6GA-0.05**	87.02	-	**4.89**	8.09
	8GA-0.05	87.6	-	**6.3**	6.1
	10GA-0.05	88.89	-	**4.76**	6.35
	12GA-0.05	88.7	-	**3.2**	8.3
EA	**6GA-0.05**	77.49	3.72	**5.82**	12.95
	8GA-0.05	77.5	4.7	**5.7**	12.1
	10GA-0.05	73.7	4.7	**4.39**	17.2
	12GA-0.05	78.8	4.8	**3.95**	12.4

The impact of the pillar length on d-spacing was studied using XRD. **Figure IV.17** shows that increasing the alkyl chain length from 6 to 8 carbons (black and red curves) lead to an asymmetric and large CL peak, indicating a wide distribution of interlayer distances with two distinct populations at Q=0.73 $Å^{-1}$ and Q=0.63 $Å^{-1}$, corresponding to d-spacings of 0.86 and 0.99 nm respectively, compared to 0.77 nm for 6GA-0.05. These observations confirm that increasing the pillars length leads to an increase in the d-spacing. However, the pillared samples containing 10 and 12 carbons in the pillars do not show a clear CL peak. Two distinct bumps are noticed at approximately the same Q positions for both 10 and 12GA-0.05. The first bump, at Q=0.77 $Å^{-1}$, represents a d-spacing of 0.81 nm which is lower than that of 8GA-0.05. This could be attributed to the pillars that reacted from only one side and exhibit a tilted conformation. The second bump at Q=0.5 $Å^{-1}$ represents an interlayer distance of 1.25 nm, which is the highest d-spacing recorded for the pillared graphene materials. This bump could

be assigned to the reacted pillars that induce bridging between the graphene sheets. Moreover, the low peak intensity may be due to the low diamine equivalent used for their preparation, and increasing the equivalent number may improve the pillaring. These results indicate that 6GA-0.05 is the only sample with a well-defined d-spacing. This will allow a direct correlation between the nanoscale structure and the electrochemical properties, as it will not be affected by other factors, such as pillaring inhomogeneity.

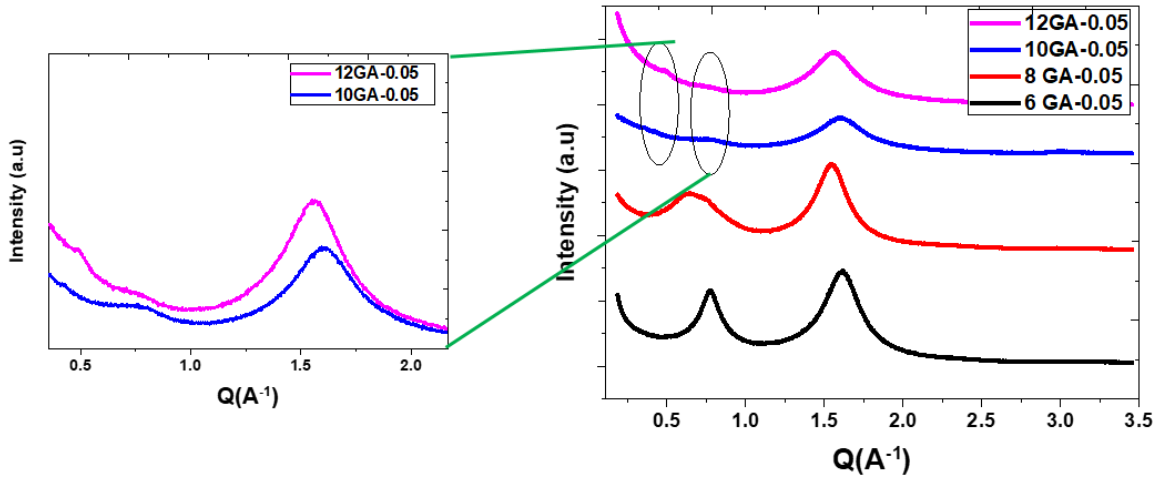

Figure IV.17 XRD patterns of the pillared graphene aerogels using different pillars with different lengths

8 Macro-structure investigation and its evolution compared to non-pillared materials

The macroscale morphologies of the graphene sheets within 6GA-0.05 and 6RP-0.2 materials were investigated using SEM (**Figure IV.18**). These images reveal that, unlike their references (GA and rGO), the macrostructures of both pristine pillared materials are not significantly different. **The 6GA-0.05 morphology is similar to that of GA, presenting a large connected graphene sheet structure with high macroporosity**. In contrast, **the morphology of 6RP-0.2 differs significantly from rGO.** This sample presents a less crumpled and aggregated structure, with higher macroporosity. Both pillared graphene-based materials present a highly connected fractal-like network, with no isolated objects of well-defined dimensions. This fractal structure exhibits self-similarity in the arrangement of graphene sheets across multiple magnifications scales. Even at low magnification, the materials exhibit a complex interconnected structure without any isolated entities. Additionally, 6RP-0.2 seems to be slightly denser than 6GA-0.05 with lower macroporosity. The pillaring of aerogels does not affect their macrostructure or morphology. Both 6GA-0.05 and GA exhibit the same aerogel

shape at the end of the reaction, as observed visually, and show similar macrostructure as shown by SEM. In turns, the pillaring process has a significant impact on the macrostructure of the reduced powders. At the end of the reaction, both rGO and 6RP-0.2 exhibited similar powder shapes. However, SEM observations revealed that the crumpled and dense structure of rGO was transformed into a less crumpled morphology with higher macroporosity by incorporating pillars in 6RP-0.2. These observations can be assigned to the additional functionalization step, which appears to affect the macrostructure of the graphene sheets. The presence of pillars may restrict the bending and folding of the graphene sheets promoted by the stirring. This limitation in motion could be attributed to an increase in the rigidity of the sheet assembly.

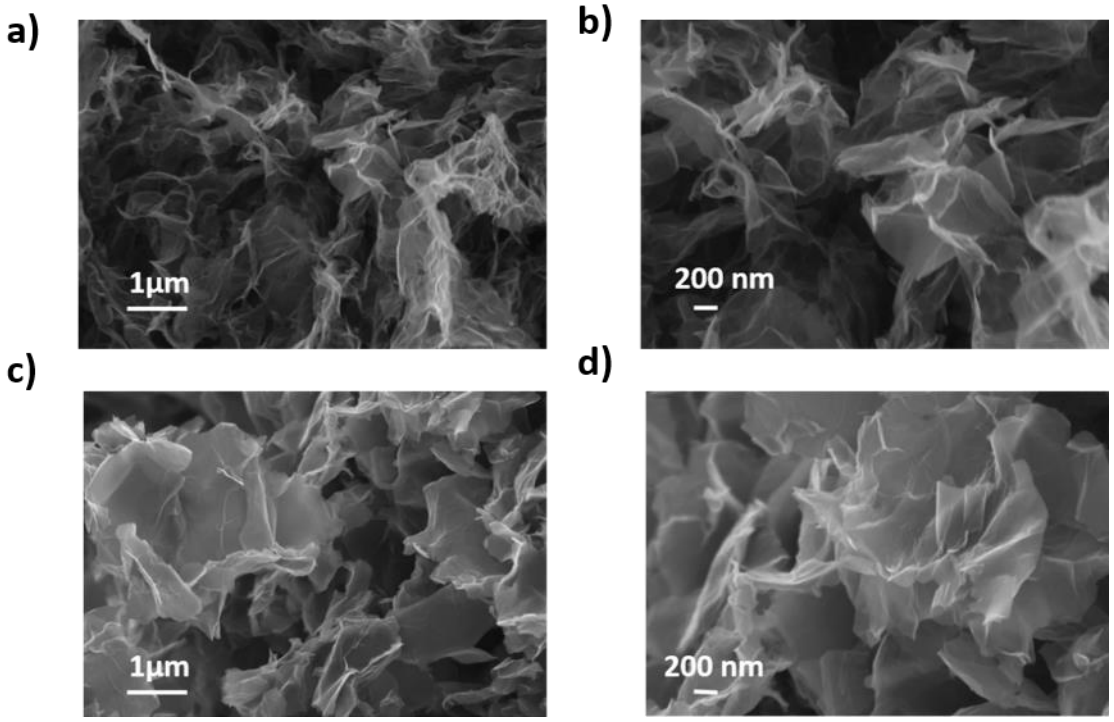

Figure IV.18 SEM images at different magnifications of (a,b) 6GA-0.05 and (c,d) 6RP-0.2.

As discussed previously in **Chapter III** and as will be shown in **Chapter V**, these materials will be used as electrodes for supercapacitors. For this purpose, a fine and homogeneous powder is needed to prepare good electrodes for better and reproducible electrochemical performances. Moreover, in the first part of this Chapter, the necessity of grinding to study a sample that accurately represent the entire batch was shown. Therefore, grinding becomes one of the most important steps for electrode preparation. The SEM analysis revealed that grinding has a similar impact on the macrostructure of 6GA-0.05 and GA. (**Figure IV.19**). Specially, the external macrostructure and porosity (> 1 µm) were destroyed, indicating that grinding significantly affects the macroscale structure and porosity of aerogels. The

external macroporosity was completely closed, forming a dense structure (**Figure IV.19 a, b)**. Surprisingly grinding did not alter the macrostructure of 6RP-0.2, and the pristine material morphology was preserved after grinding (**Figure IV.19 c, d)**. These observations confirm the hypothesis of the high graphene sheet rigidity in the 6RP-0.2 which may increase its resistant to grinding and explain the preservation of the macrostructure.

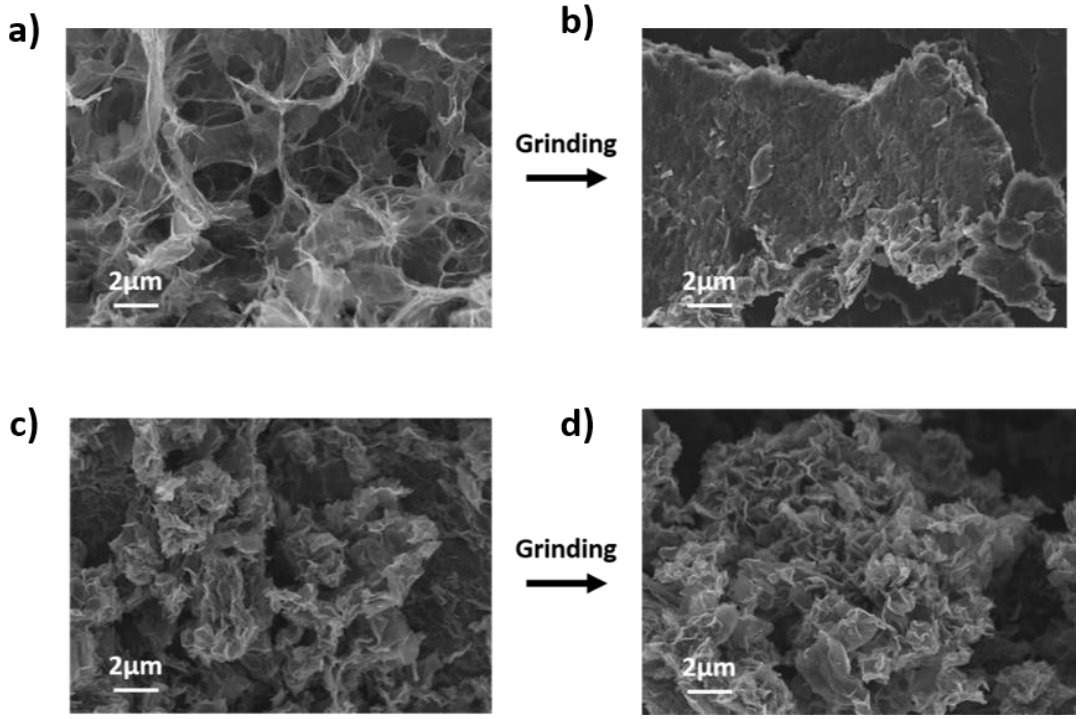

Figure IV.19 SEM images of (a) 6GA-0.05 before grinding (b) 6GA-0.05 after grinding (c) 6RP-0.2 before grinding (d) 6RP-0.2 after grinding.

This SEM analysis shows a slight difference regarding macroporosity (> 200 nm) between the pillared graphene samples that was highly modified for 6GA-0.05 and preserved for 6RP-0.2 after grinding. This difference may influence their capabilities to store ions, as macropororosity can be considered as an electrolytic ion reservoir. Still in the context of SCs, the meso-structure of the material plays a pivotal role. An optimal meso-scale structure ensures efficient ion transport and accessibility of active sites, contributing to superior electrochemical performances [7, 8]. Therefore, this macroscale study must be completed by a thorough characterization of the mesoscale, which will be presented in the following sections of this Chapter.

9 Understanding the meso structure and porosity of pillared graphene materials, interest of small angle scattering

9.1 Investigation of the meso-scale morphology of 6GA-0.05

As discussed in **Chapter III Section 5**, Small-Angle Neutron Scattering (SANS) is a well-adapted technique for capturing structure over a wide range of length scales (ranging from 3 to 210 nm in this study). Its complementarity with real space imaging was very helpful in understanding rGO-based materials. Therefore, the meso-scale morphology of pillared graphene materials is examined using SANS. As shown previously in **Section 8**, these materials exhibit a fractal structure, similar to that of GA and rGO. Therefore, their mass and surface fractal dimensions alongside their characteristic sizes (bending R and persistence Σ lengths) were investigated. It was observed that the SANS profiles of the reduced materials GA and rGO are characterized by a succession of power-law decays separated by break in slopes (**Chapter III Section 5.4**). Such shape of the scattering profile is characteristic of a porous two-phase system (carbon matrix and pores) with fractal structure [9 - 11].

The SANS profile of 6GA-0.05 (**Figure IV.20 a**) shows a break in slope at Q*~0.012 $Å^{-1}$, which is confirmed by the Kratky representation (**Figure IV.20 b**). **The characteristic distance is about d*~ 52 nm (d*=2π/Q*), which can be assigned to the bending length (R) of the crumpled graphene layers within 6GA-0.05**. In addition, a slope of ~-3.6 at high Q values is observed, indicating a surface fractal dimension D_s of 2.4. This indicates that air/particles interfaces in the 6GA-0.05 are rough. Additionally, a Q^{-3} slope is observed at small angle, which is attributed to **mass fractal scattering D_m of 3. This is assigned to the scattering from 3D crumpled graphene layers within the material**. Interestingly, this profile and the corresponding structural features (bending length, mass and surface fractal dimensions) are very similar between the two aerogels (GA and 6GA-0.05). Indeed, both aerogels exhibit the same break in slope position, and similar mass fractal scattering (Q^{-3}). However, 6GA-0.05 exhibit a slightly smoother interface (Ds=2.4) than GA (Ds=2.6). **These observations suggest that the pillaring does not influence significantly the meso-scale morphology of the aerogels.**

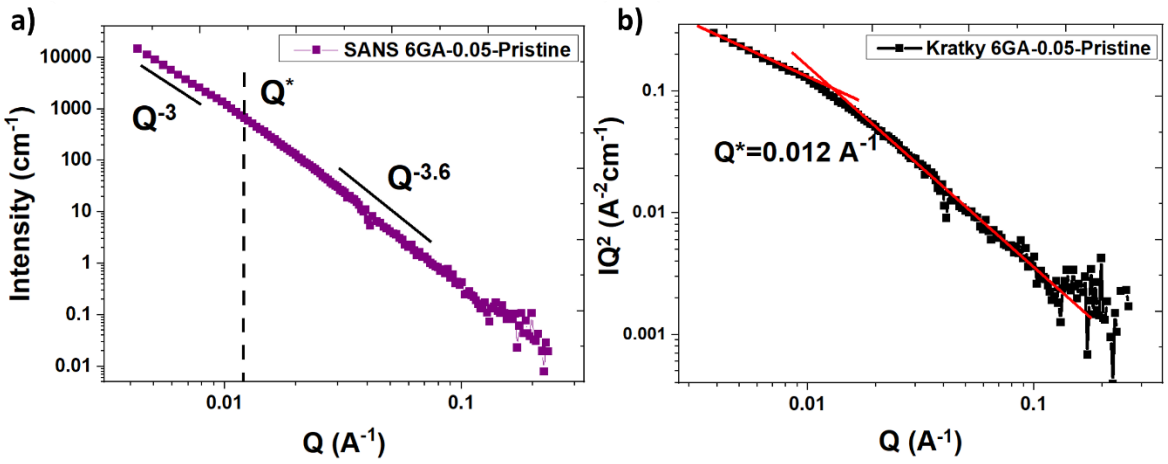

Figure IV.20 (a) SANS and (b) Kratky plot of 6GA-0.05.

9.2 Investigation of the mesoscale morphology of 6RP-0.2

In contrast, the 6RP-0.2 SANS profile (**Figure IV.21**) shows a single break in slopes at Q*~0.043 $Å^{-1}$, which is confirmed by the Kratky representation **(Figure IV.21 b)**. **The characteristic distance in this case is about d*~ 15 nm (d*=2π/Q*), which is assigned to the bending length (R) of the crumpled graphene layers within the 6RP-0.2**. In addition, a slope of ~-3.4 (Ds of 2.6) at high angles indicates a rough interface between air and particles in 6RP-0.2. Furthermore, a $Q^{-2.8}$ slope is observed at small angle, which is attributed to **mass fractal scattering D_m of 2.8. This is assigned to the scattering from a mixture of 3D crumpled particles and 2D flat restacked graphene domains**. In comparison to rGO, the 6RP-0.2 SANS profile lacks the second break in slope at small angles (Q=0.006 $Å^{-1}$ in rGO) that corresponds to the persistence length Σ. This persistence length may be beyond the probed scale (3 to 210 nm).

To confirm this hypothesis, a correlation between SANS and SEM was made. Unlike rGO, the SEM images of 6RP-0.2 showed a morphology of less crumpled graphene sheets with large graphene sheets, closely resembling that of graphene aerogels as shown in **Figure IV.18**. Therefore, as in the SANS profiles of aerogels, it can be concluded that the persistence length is indeed beyond the investigated scale for 6RP-0.2. Furthermore, 6RP-0.2 exhibits a smoother interface (Ds=2.6 in 6RP-0.2 *vs* Ds=3 in rGO). Interestingly, for both aerogels (6GA-0.05 and GA) and reduced powders (6RP-0.2 and rGO), the pillared materials showed smoother interfaces than the reference samples. **This can be attributed to the covalent bonding between the pillars and the GO sheets, along with the formation of galleries, which may hinder the folding of graphene sheets**. Consequently, the decrease in bend density within the

graphene sheets results in smoother interfaces. These results demonstrate that the pillaring induces a noticeable modification of the mesoscale structure of the reduced powders. The characteristic sizes and fractal dimension of the reference and pillared graphene-based materials are summarized in **Table IV.8.**

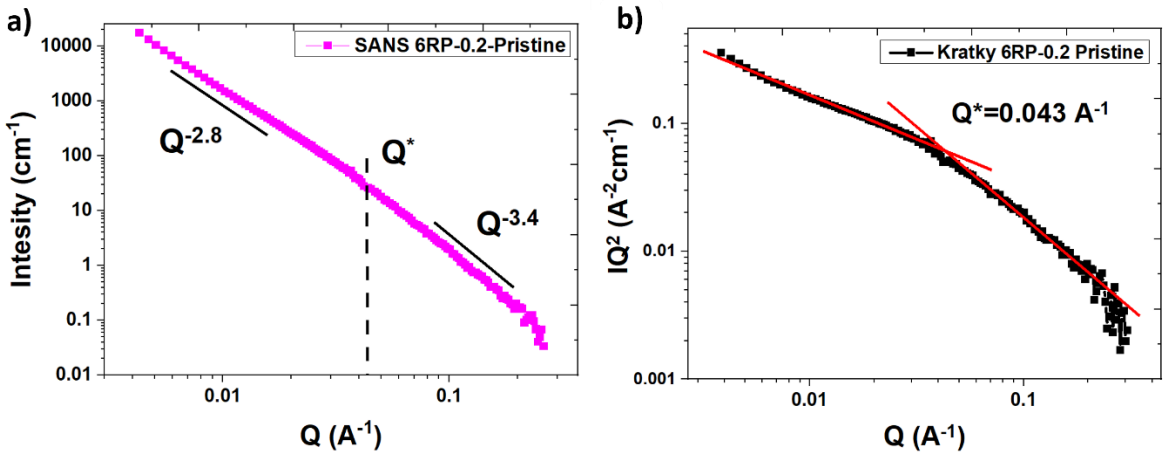

Figure IV.21 (a) SANS and (b) Kratky plot of 6RP-0.2.

Table IV.8: Summary of characteristic sizes and mass/surface fractal dimension of the graphene-based materials determined by SANS**.**

Materials	R (nm)	Σ (nm)	D_m	Ds
6GA-0.05	52	-	3	2.4
6RP-0.2	15	-	2.8	2.6
GA	57	-	3	2.6
rGO	12	105	2	3

9.3 Impact of grinding on the meso-scale morphology

As explained before, these materials will be used as electrode materials for supercapacitors, and undergo a grinding process during electrode preparation. Therefore, it is crucial to study the evolution of their meso-structure and porosity after the grinding. The effect of grinding on the meso-structure was investigated using SANS. Remarkably, the SANS profiles of all samples (**Figure IV.22**) remained almost unchanged after grinding, indicating the preservation of the materials' mesoscale morphology and structure, including the bending length (R), mass and surface fractal dimensions (Ds and D_m). This finding holds significance as the mesoscale structure and porosity play pivotal roles in electrochemical storage [7].

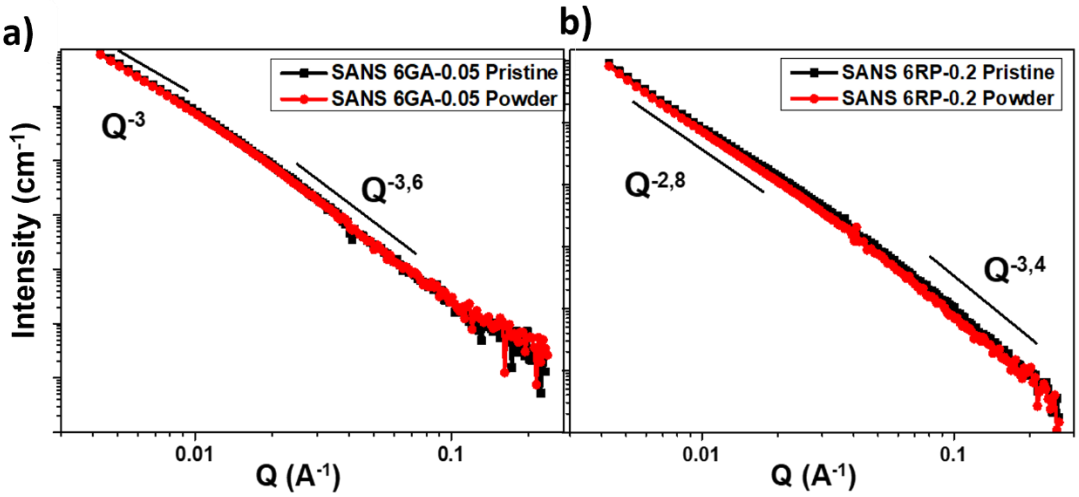

Figure IV. 22 Grinding impact on the meso-structure studied by SANS for (a) 6GA-0.05 and (b) 6RP-0.2 before (black) and after (red) grinding

9.4 Impact of pillars density and length on the meso-scale morphology of pillared samples

The impact of the equivalent number and length of pillars on the nanoscale structure (galleries) and materials chemistry was clearly pronounced as shown previously using XRD, XPS and EA (**Section 4**). It was worth investigating whether these factors also affect the mesoscale structure. The impact of the pillars equivalent number was studied on the mesoscale of both pillared materials (6GAs and 6RPs) using SANS (**Figure IV.23**). It is worth reminding here the different equivalent numbers used for the preparation of the pillared graphene materials. Three different diamine equivalent numbers were used for each material: 0.05, 0.5, and 1 for 6GA, and 0.2, 1, and 2 for 6RP. As shown in **Figure IV.23**, the shape of the SANS profiles was clearly modified with an increase in the number of pillars for both materials. However, no discernible trend could be identified. When increasing the equivalent number, the scattering profiles of the pillared materials with a high equivalent number of diamines showed regions both above and below those of 6GA-0.05 and 6RP-0.2. Furthermore, the breaks in slopes were not consistently preserved, and the slopes varied arbitrarily without a discernible trend, in contrast to XRD where trends were easily identified.

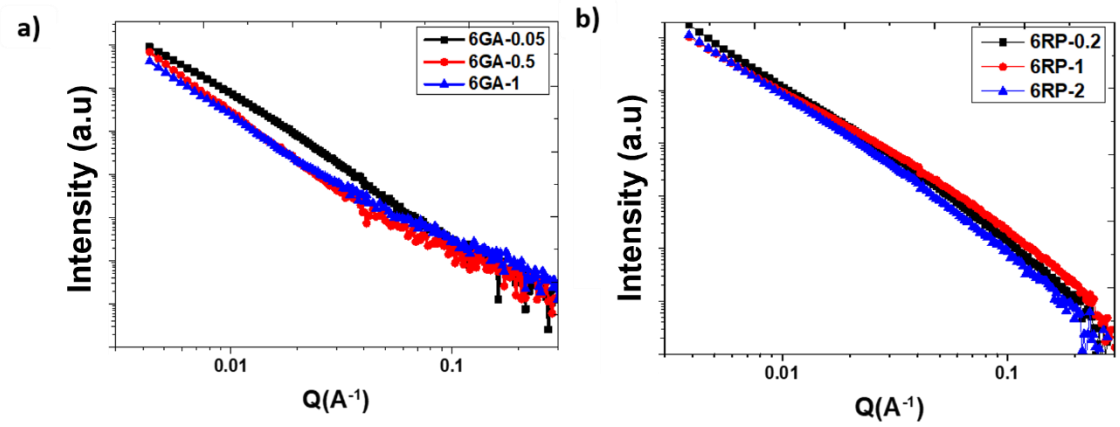

Figure IV. 23 SANS profiles of (a) 6GA and (b) 6RP with different equivalent number.

Regarding the impact of pillar length on the mesoscale structure, **Figure IV.24 a** shows that 6GA-0.05 and 8GA-0.05 present similar scattering profiles. Both materials display the same break in slope position (Q= 0.012 $Å^{-1}$) and slopes (Ds=2.4 and D_m=3), indicating that the mesoscale morphology was preserved despite the increase in the number of carbons in the pillar alkyl chain from 6 to 8 carbons. However, the 10 and 12GAs present single power-law decay profiles (**Figure IV.24 b)**, that are not superimposed and do not follow any trend compared to 6 and 8GA-0.05 This suggests that the same structure is probed across the whole scale range without any modification, and the structural features may be beyond the observation scale as in the case of GO (**Chapter III Section 5.3**).

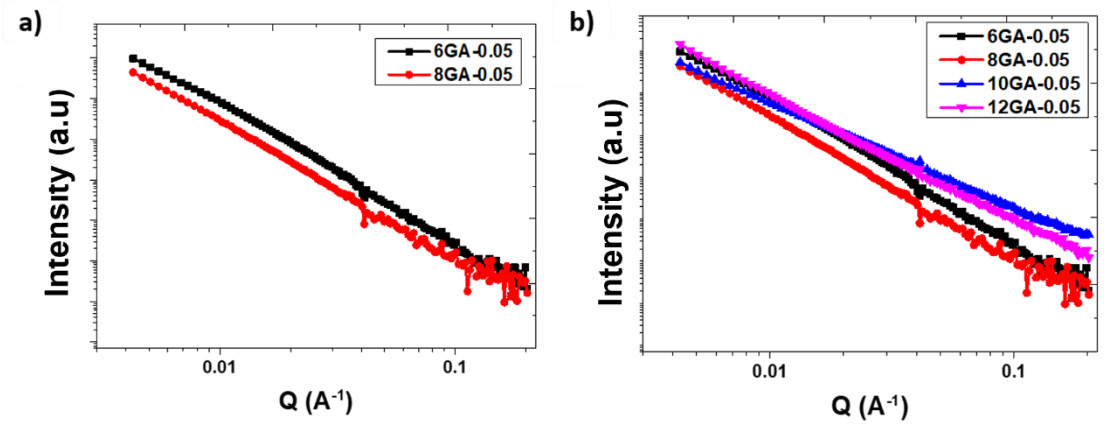

Figure IV. 24 SANS profiles of nGA-0.05 with (a) n =6 and 8, and (b) n=6,8, 10, and 12.

10 Density and porosity investigation

10.1 Envelope density

As stated in in **Chapter III Section 6**, the materials density is very important in energy storage applications. Higher material density enables the storage of more energy within a given volume, allowing for the design of more compact energy storage devices. At this stage, it is worth reminding the different volumes investigated in **Chapter III** for reference materials, as the same methodology will be applied for pillared materials. **Figure.IV.21** illustrates the three different volumes and densities that can be measured in porous materials and used to estimate their porosity.

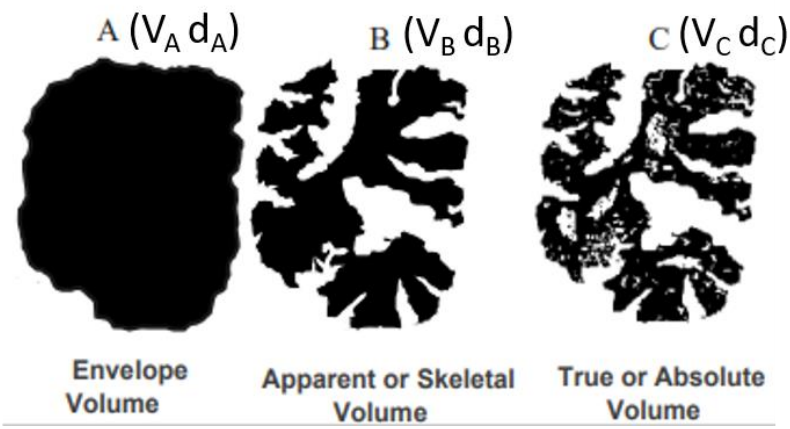

Figure IV. 25 The various volumes that can be quantified in a porous carbon sample

The volume (V_A) of the envelope was determined by completely filling a Hellma 1 mm quartz cell with the pristine material. Grinding was avoided to preserve the macroporosity of the materials. The envelope density was calculated by weighing the materials within the cell and using the known volume of the cell (**Table IV.9**).

Table IV.9: The envelope density pillared and reference graphene-based materials.

Material	**Envelope density (d_A) (g/cm^3)**
6GA-0.05	0.025 ±0.005
6RP-0.2	0.05 ±0.002
GA	0.04 ±0.005
rGO	0.2 ±0.02

The envelope densities of the pillared materials differ significantly from the reference materials (0.04 g/cm^3 for GA and 0.2 g/cm^3 for rGO). **The pillared materials exhibit lower envelope densities**. Additionally, the pillared aerogel (6GA-0.05) show a lower density than 6RP-0.2, which is consistent with the trend observed between GA and rGO. These results emphasize that i) pillared materials inherently possess a higher envelope volume, which implies greater porosity compared to the reference materials, ii) aerogels display higher porosity than reduced powders.

10.2 Solid density, interest of neutrons

Determining the solid density d_C is crucial in quantifying the overall porosity of the material (open *vs* closed). Contrast Variation-SANS (CV-SANS) is one of the most suitable technique for determining this density [12] (more details can be found in **Chapter II**). Our initial CV-SANS study was performed on pristine materials at the SANS-I spectrometer (Paul Scherrer Institut (PSI)-Villigen) and complementary measurements were conducted on D22 at ILL. The pristine materials were placed in Hellma 1 mm quartz cells and immersed in various mixtures of cyclohexane (CycloH) and deuterated cyclohexane (d-CycloH) (**Table IV.10**) to adjust the scattering contrast between the solid and the solvent.

Table IV.10: The solvent mixtures used for CV-SANS and the corresponding SLD.

% d - cyclohexane	**SLD 10^{10} cm^{-2}**
60	3.89
80	5.2
90	5.9
100	6.68

10.2.1 Solid density of 6GA-0.05 investigated by CV-SANS

The combined CV-SANS profiles recorded at PSI and ILL of pristine 6GA-0.05 (**Figure IV.26 a**) show a gradual decrease in the intensity as the amount of deuterated cyclohexane increases, with a **minimum intensity recorded at a mixture containing 50% of d-CycloH, the intensity then increases again above 50% of d-CycloH**. At 50% of d-CycloH), the intensity is almost zero in the high Q values domain (above Q=0.01 Å^{-1}) and shows a slight increase in small angles range (below Q=0.01 Å^{-1}).

A comprehensive study at multiple Q values (Q=0.007 $Å^{-1}$, Q=0.02 $Å^{-1}$, and Q=0.05 $Å^{-1}$) was conducted to demonstrate the uniformity of the evolution (more details in **Chapter II**). The intensity as a function of the percentage of deuterated solvent (%vol) reveals a uniform evolution of the intensity at all the Q values with a minimum intensity close to zero recorded at 50% of d-CycloH (matching point) (**Figure IV.26 b**). **This uniform relationship indicates a matching point at 50% deuterated solvent**, which corresponds to a Scattering Length Density (SLD) of 3.2 10^{10} cm^{-2}. The solid density of 6GA-0.05, determined from the matching SLD and the molecular weight calculated from the EA chemical formula is found to be d_C= 1.1 g/cm^3.

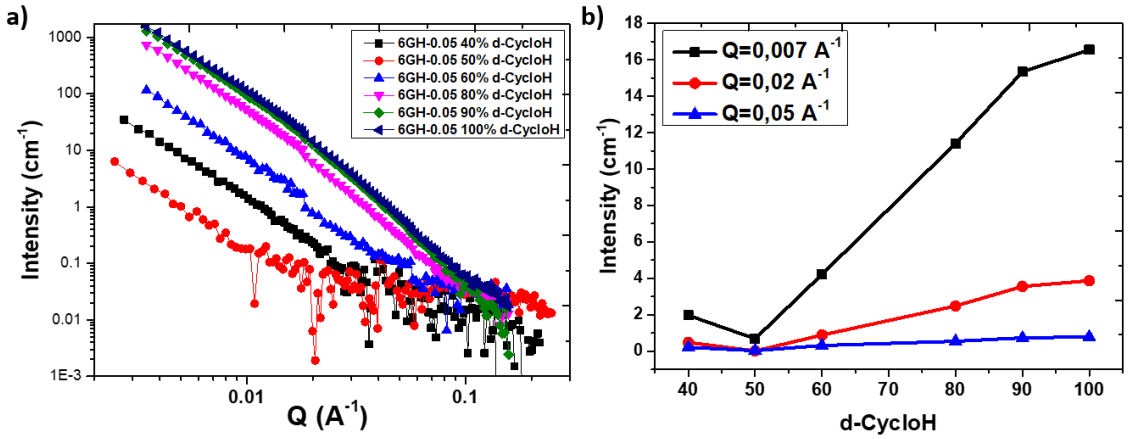

Figure IV. 26 (a) CV-SANS profiles of pristine 6GA-0.05 at different mixtures of cyclohexane/d-cyclohexane (b) the intensity as a function of the % of deuterated solvent at Q=0.007 A^{-1}, Q=0.02 A^{-1}, and Q=0.05 A^{-1}showing its uniform evolution at the different Q values and a minimum at 50% of d-CycloH

10.2.2 Solid density of 6RP-0.2 investigated by CV-SANS

For 6RP-0.2, the CV-SANS profiles (**Figure IV.27 a**) show a similar trend to 6GA-0.05: a **gradual decrease in the intensity as the amount of deuterated cyclohexane decreases, with a minimum intensity recorded at 50%.** The intensity then increases again below this percentage of d-CycloH. The comprehensive study at multiple Q values (Q=0.007 $Å^{-1}$, Q=0.02 $Å^{-1}$, and Q=0.05 $Å^{-1}$) was also conducted for this sample. The intensity as a function of the percentage of deuterated solvent (%vol) reveals a uniform evolution of the intensity at all the Q values with a minimum intensity close to zero recorded at 50% of d-CycloH (matching point) (**Figure IV.27 b**). **This uniform relationship implies a matching point at 50% deuterated solvent**, corresponding to a Scattering Length Density (SLD) of 3.2 10^{10} cm^{-2}. The 6RP-0.2 solid density determined from the matching SLD and the molecular weight calculated from the EA chemical formula is found to be d_C= 1.02 g/cm^3. These findings reveal that pillared graphene materials exhibit lower solid densities compared to reference materials, even though

both are composed of reduced graphene sheets. This observation suggests the presence of additional porosity below 3 nm in pillared graphene materials, which is not detectable using CV-SANS as the probed length scale is limited to 3 nm. This specific porosity below 3 nm corresponds to the galleries that contribute to a higher measured volume in pillared graphene materials, as illustrated in **Figure IV.28**.

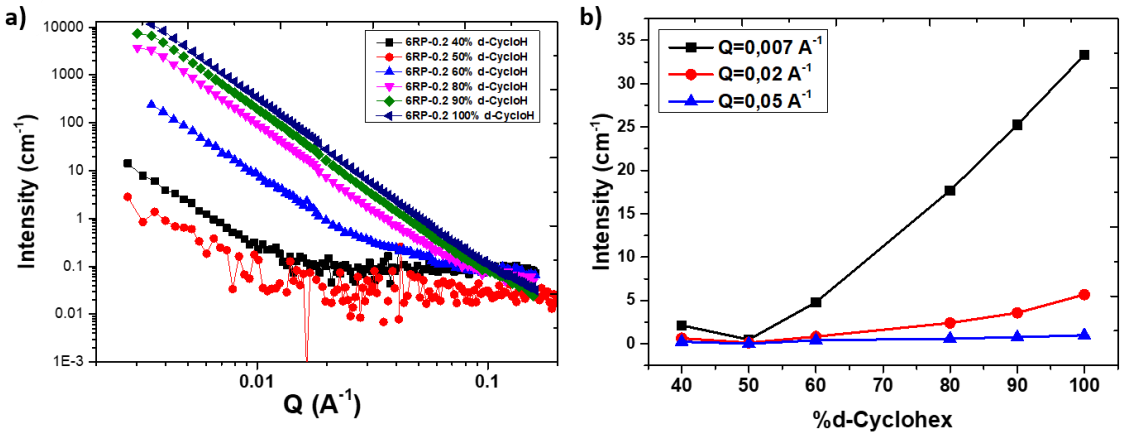

Figure IV. 27 (a) CV-SANS profiles of pristine 6RP0.2 at different mixtures of cyclohexane/d-cyclohexane (b) the intensity as a function of the deuterated solvent at Q=0.007 A^{-1}, Q=0.02 A^{-1}, and Q=0.05 A^{-1}showing its uniform evolution at the different Q values and a minimum at 50% of d-CycloH

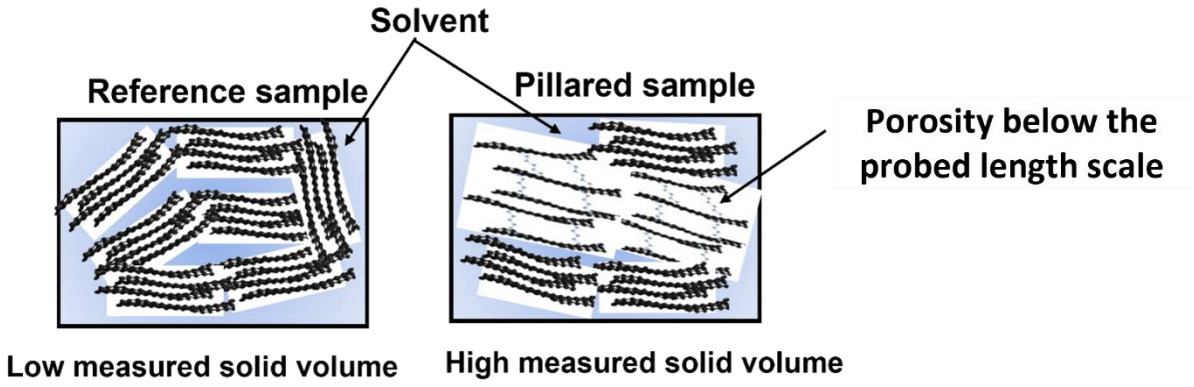

Figure IV. 28 Schematic representation of the impact of galleries on the measured solid volume in CV-SANS.

The solid density d_C obtained from the CV-SANS of the pillared materials and their envelope density d_A (**Table IV.10**) were used to calculate the porosity volume within these materials. The solid and envelope volumes were obtained by taking the inverse of the density, while the porosity volume was calculated as the difference between the envelope volume (V_A) and the solid volume (V_C). **Table IV.10** shows that the pores occupy a larger volume in 6GA-0.05 (39 cm^3/g) compared to 6RP-0.2 (19 cm^3/g). Furthermore, the pillared materials exhibit higher pore volume compared to the references (24.3 cm^3/g in GA and 4.3 cm^3/g in rGO). **This**

result highlights that the pillaring induces an expansion of the materials by creating an additional microporosity.

Table IV.10: Solid, envelope, and pores volumes of the pillared and reference graphene-based materials.

Material	Envelope density d_A (g/cm^3)	Solid density d_C (g/cm^3)	Envelope volume V_A (cm^3/g)	Solid volume V_C (cm^3/g)	Porosity volume (cm^3/g)
6GA-0.05	0.025	1.1	40	0.9	**39.1**
6RP-0.2	0.05	1.02	20	0.98	**19**
GA	0.04	25	1.56	0.64	**24.3**
rGO	0.2	5	1.56	0.64	**4.3**

At this stage of the analysis, the total pore volume is determined but the distribution of pore volumes in function of the scale is not yet possible. The pillaring showed an opening of new porosity at the nanoscale (galleries). However, the mesoporosity of these materials is still unknown. Therefore, a quantitative assessment of this porosity is needed. To do so, SAS techniques can be very valuable as long as quantitative analysis of the SAS measurements can be performed.

10.3 Mesoporosity investigation

As shown in **Chapter III Section 6.3**, the SANS profiles were measured in a limited Q-range: 0.003-0.2 $Å^{-1}$ which corresponds to an extended probed length scale ranging from 3 to 210 nm. Therefore, , the intensity was normalized to the solid thickness (e_B) for the quantitative analysis, as described in work by Spalla *et al* [6]. The porosity can be derived from the invariant using **Equation (IV.2):**

$$INV^* = \int_{0.003}^{0.2} \frac{I_{abs}}{e_B}(Q)Q^2 dQ = 2\pi^2 \varphi^* \Delta\rho^2 \qquad (IV.2)$$

The invariant INV* was calculated based on the area under the curve of the Kratky plots derived from the normalized SANS profiles (**Figure IV.29**). The CV-SANS technique was used to determine the SLD of the material, which was found to be 3.2 10^{10} cm^{-2} for both

6GA-0.05 and 6RP-0.2, as shown previously shown. The solid thickness (e_B) was determined using the transmission and neutron attenuation coefficient (**Equation (IV.3)**). **Table IV.11** gathers the various parameters used to estimate mesoporosity.

$$e_B = \frac{-\ln(T)}{\mu_{solid}} \qquad (IV.3)$$

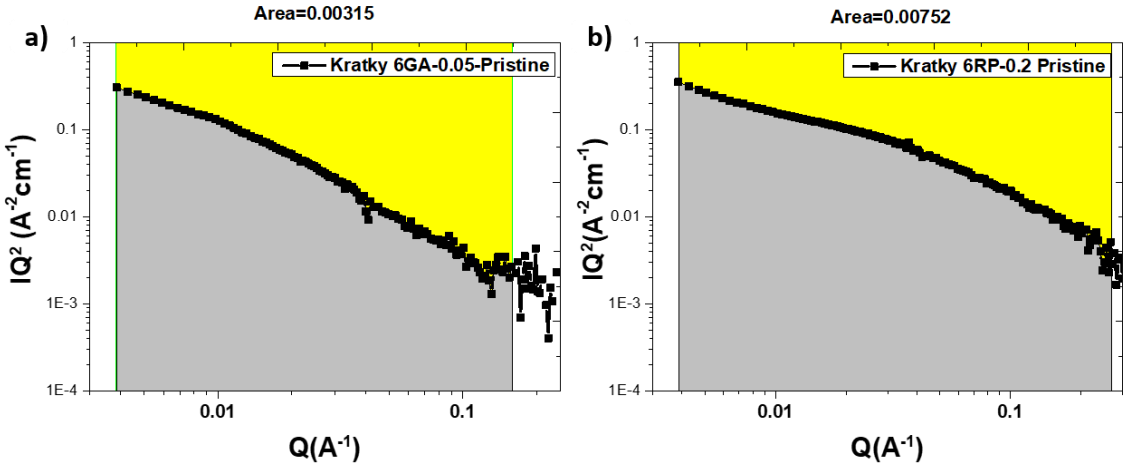

Figure IV. 29 The invariant determination from the area under the Kratky curves of (a) 6GA-0.05 and (b) 6RP-0.2.

Table IV.11: The different parameters used to estimate the mesoporosity of pillared and reference graphene-based materials.

Material	Attenuation coefficient (cm^{-1})	Transmission	e_B (cm)	INV (10^{20} cm^{-4})	φ^*(%)
6GA-0.05	0.386	0.97	0.0789	31.5	**15**
6RP-0.2	0.299	0.98	0.0674	75.2	**37**
GA	0.494	0.97	0.0616	167	**35**
rGO	0.488	0.98	0.0413	237	**57**

These results show that in this Q-range (0.003-0.2 $Å^{-1}$), **6RP-0.2 has a higher porosity (37%) than 6GA-0.05 (15%)**. Interestingly, **the pillared materials have lower porosity at this scale compared to the reference materials (57% in rGO and 35% in GA)**, although they have a higher total pore volume (see **Table IV.10**). This result indicates that the high total pore volume in pillared graphene materials is not primarily due to mesoporosity. Instead, it emphasizes a significant contribution of micro/nano pores and confirms the contribution of the

galleries in the volume extension. To complete this analysis, our colleagues from CEMTHI laboratory in Orléans (Pr. Encarnacion Raymundo and DR. Conchi O. Ania) carried out N_2 gaz sorption **BET surface area measurements at 77K, revealing a SSA of 93 and 26 m^2/g for 6RP-0.2 and 6GA-0.05 respectively**. In addition, the N_2 pore size distribution (N_2-PSD) (**Figure IV.29**) shows a pore volume (within the length scale ranging from 0.6 to 30 nm) of 0.23 and 0.06 cm^3/g in 6RP-0.2 and 6GA-0.05, respectively, showing a very low porosity compared to rGO (0.8 cm^3/g), which is consistent with their lower SANS porosity. The low porosity observed in both pillared samples, especially in 6GA-0.05, when examined by N_2 at 77K, raises the question of whether this phenomenon arises from steric restrictions (closed porosity) or whether it is influenced by the low adsorption kinetics of nitrogen at 77K in pores with dimensions close to the kinetic diameter of nitrogen (kinetic restrictions). Therefore, H_2 adsorption isotherms at 77K were conducted on all samples. Supposedly, H_2 is able to penetrate into pores with small dimensions (where the nitrogen adsorption is hindered), thereby demonstrating whether the sample has micropores (or not).

Interestingly, the highest hydrogen uptake at 77K was observed in sample 6GA-0.05 (H_2 SSA of 479 m^2/g), the one with the lower nitrogen uptake (N_2 SSA of 26 m^2/g). This suggests the presence of small micropores in this sample which are inaccessible to nitrogen. In addition, the hydrogen uptake of sample 6GA-0.05 is considerably higher than that of rGO and GA which had a H_2 SSA of 181 and 240 m^2/g respectively. Conversely, the hydrogen uptake of 6RP-0.2 is very low (H_2 SSA of 92 m^2/g), and thus the lowest among the series, despite showing a relatively high nitrogen uptake compared to 6GA-0.05. This indicates that the porosity of this sample is dominated by a proportion of pores in the 0.1-1 nm range. All these results corroborate the SANS porosity, which shows lower mesoporosity of pillared materials than that of the reference materials and emphasizes the high microporosity of these pillared materials.

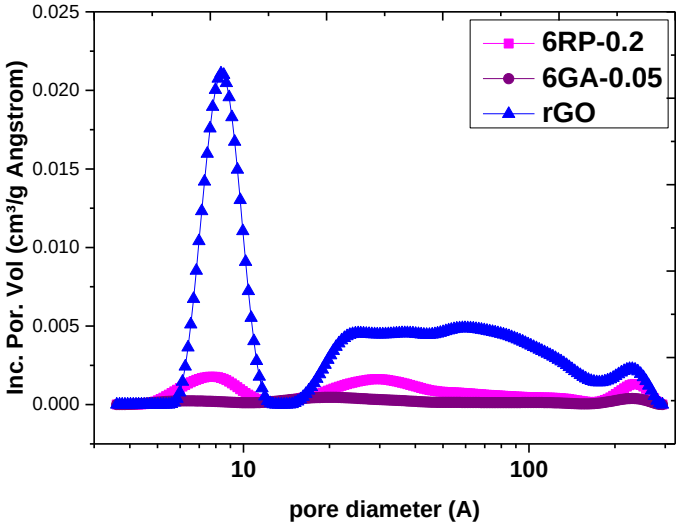

Figure IV. 30 N_2-PSD of 6GA-0.05, 6RP-0.2 and rGO

11 Conclusion:

This Chapter delved into the exploration of pillared graphene-based materials using alkyl-diamine pillars. The primary goal of this pillaring is to mitigate graphene sheet restacking issues during reduction, thereby increasing the electrochemically active surface area accessible to ions. The approach involved in this work consisted in studying their chemistry and their structure/porosity at different scales. Two different pillared graphene-based materials were studied, pillared graphene aerogel 6GA-0.05, and pillared reduced powder 6RP-0.2. The impact of the chosen synthesis method on these properties as well as a comprehensive comparison with the reference materials (GA and rGO) was investigated and will be directly correlated to their electrochemical performances in **Chapter V**.

Chemical analyses by TGA showed that 6RP-0.2 and 6GA-0.05 exhibited weight losses of 26% and 30%, respectively. The more pronounced weight loss in 6GA-0.05 suggested a potential higher content of grafted pillars or lower reduction degree compared to 6RP-0.2. To assess this difference, the total weight loss was adjusted by subtracting the corresponding weight loss of the pillars. The weight loss originating from pillars was 13.8% and 15.4% for 6RP-0.2 and 6GA-0.05, respectively. Showing firstly that 6GA-0.05 contain more pillars than 6RP-0.2. Additionally, by subtracting it from the total weight loss, it was determined that 6RP-0.2 was slightly more reduced (weight loss of oxygen groups 12.2%) compared to 6GA-0.05 (weight loss of oxygen groups 14.6%). Furthermore, XPS, and EA confirmed the good reduction of GO after pillaring and evidenced the presence of nitrogen within the material,

which confirmed the presence of the pillars. The nature of bonding between pillars and graphene sheets was assessed using TPD-MS. 6GA-0.05 and 6RP-0.2 showed a decomposition of the pillar at higher temperature than when the bare pillar itself was subjected to high temperatures, indicating covalent bonding.

XRD analysis showed that the nanoscale structure of the two pillared samples, 6GA-0.05 and 6RP-0.2, exhibited remarkable similarity. Both materials exhibited a distinct CL peak with a d-spacing of 0.77 nm, indicating the successful creation of a new porosity within the materials. The percentage of pillared portion (%CL) within the materials was approximately 20 to 30%, demonstrating that despite the successful pillaring, the majority of the materials comprised restacked graphitic domains, constituting approximately 70 to 80% of the overall structure.

The macroscale structure of the pillared materials was investigated using SEM. This macrostructure was very similar to that of non-pillared samples, revealing an interconnected network of graphene sheets characterized by self-similarity across different length scales. The absence of individual objects with clearly defined dimensions within the materials suggested a fractal structure. Contrary to reference materials (GA and rGO), both pristine pillared materials exhibited approximately similar macrostructures. Furthermore, the morphology of 6GA-0.05 resembled that of GA, featuring a large connected graphene sheet structure with high macroporosity. On the other hand, the morphology of 6RP-0.2 was significantly different from rGO, displaying a less crumpled and aggregated structure with higher macroporosity.

The fractal mesoscale morphology of the pillared materials was studied with SANS. The SANS profile of 6GA-0.05 was very similar to that of GA, showing a break in slope observed at $Q^* \sim 0.012$ $Å^{-1}$ corresponding to a distance of $d^* \sim 52$ nm ($d^*=2\pi/Q^*$), assigned to the bending length (R) of the crumpled graphene layers. In addition, 6GA-0.05 exhibited a surface fractal dimension of $D_s= 2.4$, showing a slightly smoother interface compared to GA (Ds=2.6) and a mass fractal dimension of $D_m= 3$. In turn, the SANS profile 6RP-0.2 showed a single break in slopes at $Q^*=0.043$ $Å^{-1}$ associated to the bending length R which was about 12 nm very close to that of rGO (R=15 nm). Additionally, 6RP-0.2 showed a surface fractal dimension of $D_s= 2.6$, showing a slightly smoother interface compared to RGO (Ds=3), and a mass fractal dimension of $D_m= 2.8$.

Regarding porosity, the SANS porosity data extracted from the invariant INV showed that 6RP-0.2 exhibit higher mesoporosity than 6GA-0.05: 37% and 15% for 6RP-0.2 and 6GA-

0.05 respectively. Furthermore, 6RP-0.2 showed a higher N_2 BET SSA of 93 compared to 26 m^2/g for 6GA-0.05. In addition, the N_2 pore size distribution (N_2-PSD) shows a pore volume (within the length scale ranging from 0.6 to 30 nm) of 0.23 cm^3/g and 0.06 cm^3/g in 6RP-0.2 and 6GA-0.05, respectively. The comparison with the reference non-pillared samples is displayed in **Figure IV.31**. The pillared materials show a very low mesoporosity compared to the non-pillared samples. Despite the opening of the new microporosity, the pillaring seems to partially close the mesoporosity, which may influence the electrochemical performances. This reduced mesoporosity in pillared samples might be due to the connection of the restacked or pillared domains via pillars. Indeed, the pillars showed high reactivity with the oxygen functional groups leading to pillaring between the graphene sheets. However, there is a possibility of random reactions of pillars on the surface of the restacked or pillared, connecting them to each other. This random connection will reduce the inter particle distances and, consequently, mesoporosity. **Figure IV.32** shows the proposed schematic presentation of a non-pillared and a pillared sample. In reference samples (**Figure IV.32 a**) high mesoporosity (blue circles) is evident as shown previously. After pillaring (**Figure IV.32 b**), the graphitic domain (black) and pillared domain (green) may be connected via pillars (indicated by the red lines for clarity), which reduce their mesoporosity.

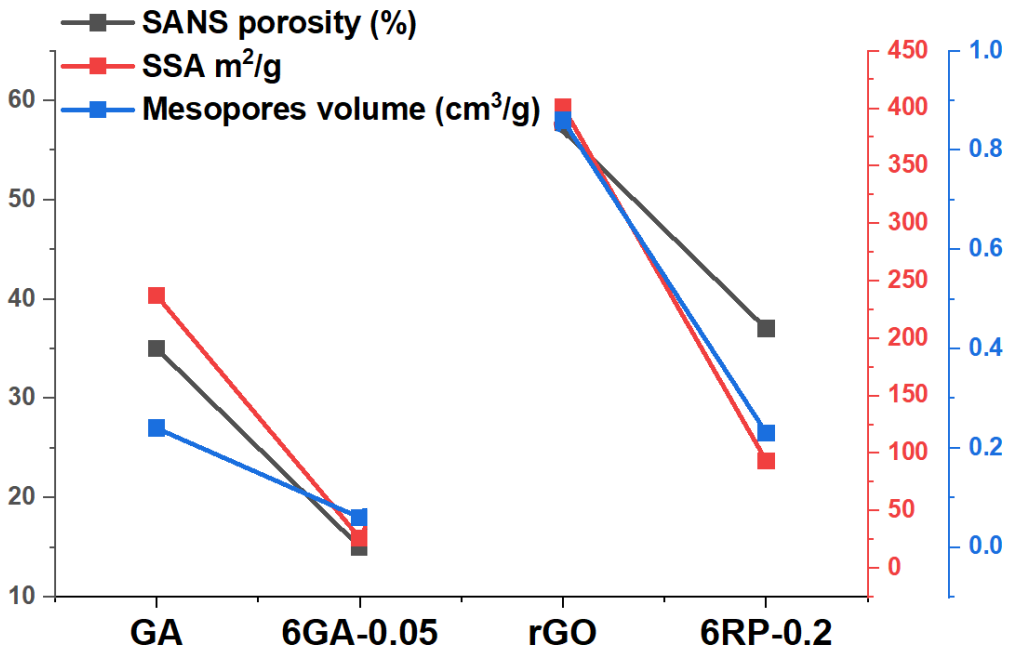

Figure IV. 31 SANS porosity, N_2 BET SSA, and the mesopores volume for GA, 6GA-0.05, rGO, and 6RP-0.2.

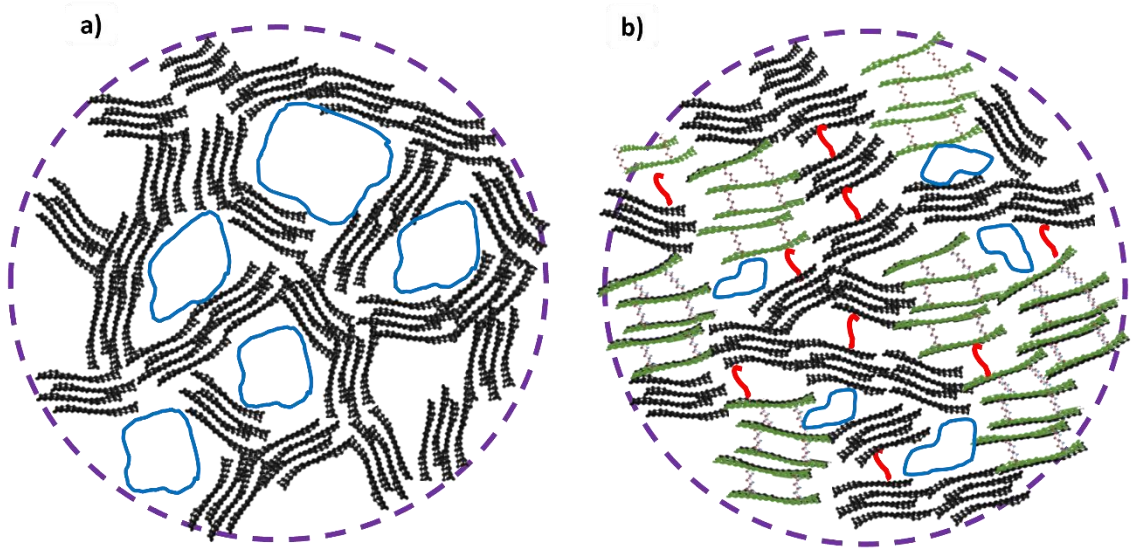

Figure IV. 32 schematic representation of (a) non-pillared sample and (b) pillared sample.

12 References:

[1] H. Banda *et al.*, « Sparsely Pillared Graphene Materials for High-Performance Supercapacitors: Improving Ion Transport and Storage Capacity », *ACS Nano*, vol. 13, nº 2, p. 1443-1453, févr. 2019, doi: 10.1021/acsnano.8b07102.

[2] H. Banda *et al.*, « Ion Sieving Effects in Chemically Tuned Pillared Graphene Materials for Electrochemical Capacitors », *Chem. Mater.*, vol. 30, nº 9, p. 3040-3047, mai 2018, doi: 10.1021/acs.chemmater.8b00759.

[3] H. Banda *et al.*, « Investigation of ion transport in chemically tuned pillared graphene materials through electrochemical impedance analysis », *Electrochimica Acta*, vol. 296, p. 882-890, févr. 2019, doi: 10.1016/j.electacta.2018.11.122.

[4] S. Stankovich *et al.*, « Synthesis of graphene-based nanosheets via chemical reduction of exfoliated graphite oxide », *Carbon*, vol. 45, nº 7, Art. nº 7, juin 2007, doi: 10.1016/j.carbon.2007.02.034.

[5] A. Monshi, M. R. Foroughi, et M. Monshi, « Modified Scherrer Equation to Estimate More Accurately Nano-Crystallite Size Using XRD », *World J. Nano Sci. Eng.*, vol. 2, p. 154-160, sept. 2012, doi: 10.4236/wjnse.2012.23020.

[6] O. Spalla, S. Lyonnard, et F. Testard, « Analysis of the small-angle intensity scattered by a porous and granular medium », *J. Appl. Crystallogr.*, vol. 36, nº 2, Art. nº 2, avr. 2003, doi: 10.1107/S0021889803002279.

[7] R. Mendoza, J. Oliva, et V. Rodriguez-Gonzalez, « Effect of the micro-, meso- and macropores on the electrochemical performance of supercapacitors: A review », *Int. J. Energy Res.*, vol. 46, nº 6, p. 6989-7020, 2022, doi: 10.1002/er.7670.

[8] E. Lust *et al.*, « Influence of specific surface area and microporosity-mesoporosity of pristine and Pt-nanoclusters modified carbide derived carbon electrodes on the oxygen electroreduction », *Electrochimica Acta*, vol. 140, p. 294-303, sept. 2014, doi: 10.1016/j.electacta.2014.04.054.

[9] D. Saurel *et al.*, « A SAXS outlook on disordered carbonaceous materials for electrochemical energy storage », *Energy Storage Mater.*, vol. 21, p. 162-173, sept. 2019, doi: 10.1016/j.ensm.2019.05.007.

[10] J. Bahadur, L. F. Ruppert, V. Pipich, R. Sakurovs, et Y. B. Melnichenko, « Porosity of the Marcellus Shale: A contrast matching small-angle neutron scattering study », *Int. J. Coal Geol.*, vol. 188, p. 156-164, mars 2018, doi: 10.1016/j.coal.2018.02.002.

[11] L. F. Ruppert *et al.*, « A USANS/SANS Study of the Accessibility of Pores in the Barnett Shale to Methane and Water », *Energy Fuels*, vol. 27, nº 2, p. 772-779, févr. 2013, doi: 10.1021/ef301859s.

[12] R. C. Hedden, H.-J. Lee, et B. J. Bauer, « Characterization of Nanoporous Low-k Thin Films by Small-Angle Neutron Scattering Contrast Variation », *Langmuir*, vol. 20, nº 2, p. 416-422, janv. 2004, doi: 10.1021/la035384w.

CHAPTER V:

Insights into the electrochemical behavior of graphene-based materials

1 Objectives and approaches

Chapters III and **IV** were dedicated to the investigation of the chemical composition and multiscale structure/porosity of rGO-based materials and pillared graphene materials. These chapters highlighted the effectiveness of tuning the chemical and structural properties of the materials using different reduction techniques and pillaring processes. The aim of this project is to use these materials as electrode materials for SC. Therefore, it is necessary to investigate their electrochemical performances, and to correlated to them to their physicochemical and structural properties. This approach aims to gain a deeper understanding of the materials and pave the way for designing optimized graphene-based materials with properties precisely tailored for improved supercapacitor applications.

This chapter is divided into two main parts. The first part presents a fundamental electrochemical study performed on the materials formulated as SC electrodes, using cyclic voltammetry. The purpose of this study is to explore the influence of the physicochemical properties and structure or porosity of graphene-based materials on their performance as electrode materials for supercapacitors.

Both organic and aqueous electrolytes have been tested to highlight the impact of chemical properties on the pseudo-capacitive behavior of the sample. A comparative analysis of the performance between rGO and GA is carried out to evaluate the impact of the reduction degree (particularly the remaining oxygen content) and porosity on the improvement of the supercapacitor performance. Additionally, a comparison between the pillared graphene materials and rGO-based materials was conducted to investigate whether pillaring improves the electrochemical performances. In the second part of the chapter, the dedicated effort made to understand the real-time behavior of these materials as supercapacitor electrodes is discussed. The underlying objective of such fundamental study is to get insights into the adsorption/desorption mechanisms within the whole porosity scale of the sample.

Therefore, an advanced *in-situ/operando* SAXS/WAXS study using synchrotron radiation was performed to unveil the structural evolution during cycling and polarization of the graphene-based materials. Additionally, we took advantage of the SANS contrast modulation and performed an *in-situ* SANS experiment to uncover the localization of ions within pores of different sizes.

2 Electrochemical performances of graphene-based materials

As mentioned above, in order to understand and optimize the performances of these promising materials, it is essential to evaluate their electrochemical performances and to try to correlate them with their physicochemical properties, but also to follow their structural evolution in real time as a function of the operating parameters during charging and discharging. The multi-scale picture of the sample will allow an efficient differentiation of the structural evolutions between pristine and cycled samples, thereby enabling to extract pore-size dependent information within graphene-based electrodes to understand the mechanisms of ion diffusion and electro-adsorption. To achieve these specific objectives, a series of *in-situ* and *operando* SAS measurements were performed.

Since the synchrotron experiment is performed in transmission geometry, all parts of the cell, contribute to the scattered signal. In order to increase the resolution of the data, it is necessary to avoid the maximum of residual interaction between the beam and other components of the electrochemical cell. Therefore, free-standing electrodes (FSE) were developed to avoid the contribution of the stainless-steel current collector to the signal. These FSE were used for both the macroscopic electrochemical performance analysis as well as for the *in-situ* and *operando* SAS measurements. They consisted of grinding 80% of the active material with 15% acetylene black (AB) and 5% PTFE (binder) in ethanol. After 30-45 min of grinding, a paste was formed which was spread on a glass window and dried at 80°C for 24 hours. The FSE were cut into discs and used directly after drying.

2.1 The electrochemical performances of reference materials: rGO and GA

Three-electrode Teflon Swagelok® cells (**Figure V.1**) were used for the electrochemical testing. The working electrode (WE) consists of the FSE prepared with the graphene-based materials as active material. The counter electrode (CE) is a FSE with YP50 (activated carbon) as active material, ten times the mass of the WE so that it is not limiting in term of adsorption capacity. The reference electrode (RE) is a pseudo-reference silver wire thinly coated with AgCl. The Cyclic Voltammetry (CV) analyses were carried out in two electrolytes 3M H_2SO_4 within a potential window ranging from -0.4 to 0.6 V *vs* Ag and 1M $TEABF_4$ in acetonitrile (AN) within a potential window ranging from -1.3 to 1.5 V *vs* Ag and at different scan rates: 5, 10, 20, 50, and 100 mV/s.

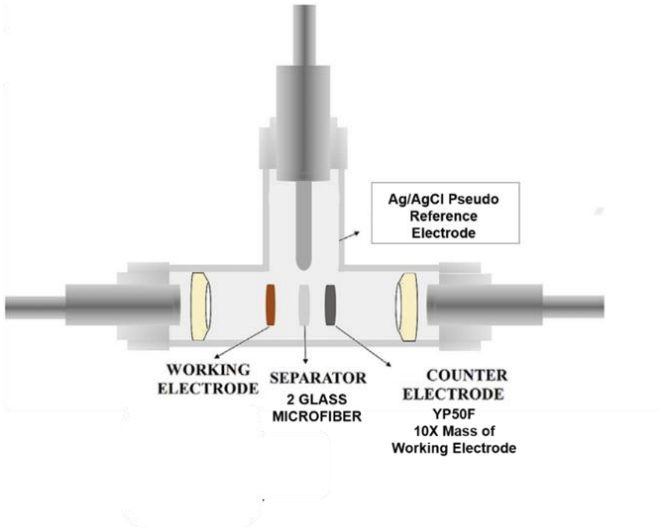

Figure V. 1 A three-electrode Swagelok® cell configuration

The electrochemical performance of the FSE, recorded in the standard Swagelok cell, was first studied in an organic electrolyte (1M $TEABF_4$ /AN). The cyclic voltammetry (CV) curves of the rGO and GA (**Figure V.2**) present quasi-rectangular EDLC shapes [1]. A slight deformation of the rectangular shape was recorded at high scan rate (100 mV/s), which could be due to a resistive behavior caused by the imperfect electrical contact between the FSE and the current collector. The capacitance achieved was 88 ± 4 $F.g^{-1}$ for rGO and 78 ± 4 $F.g^{-1}$ for GA at 10 $mv.s^{-1}$.

The FSE were also cycled in an aqueous electrolyte (3M H_2SO_4) to study their pseudo-capacitive behavior. Indeed, in this acidic medium, electrochemical reactions involving redox-active oxygen-containing functionalities should play a role in the overall storage process mechanism. This allows a fundamental study on the influence of the chemical properties on the electrochemical performances. Compared to the organic electrolyte, the CV curves show a pseudo-capacitive peak, which is more pronounced in GA than in rGO (**Figure V.3**). Both materials showed an increase in the overall electrochemical capacitance. In addition, GA showed a capacitance of 149 ± 6 $F.g^{-1}$, higher than that of rGO with 96 ± 4 $F.g^{-1}$ at 10 $mv.s^{-1}$.

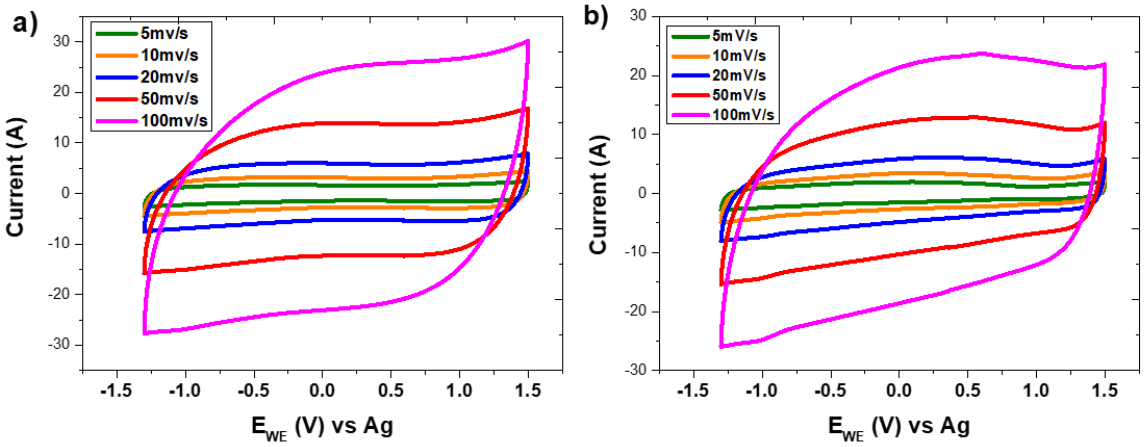

Figure V. 2 CV curves of (a) rGO (b) GA cycled at different scan rate in 1M $TEABF_4$ in acetonitrile

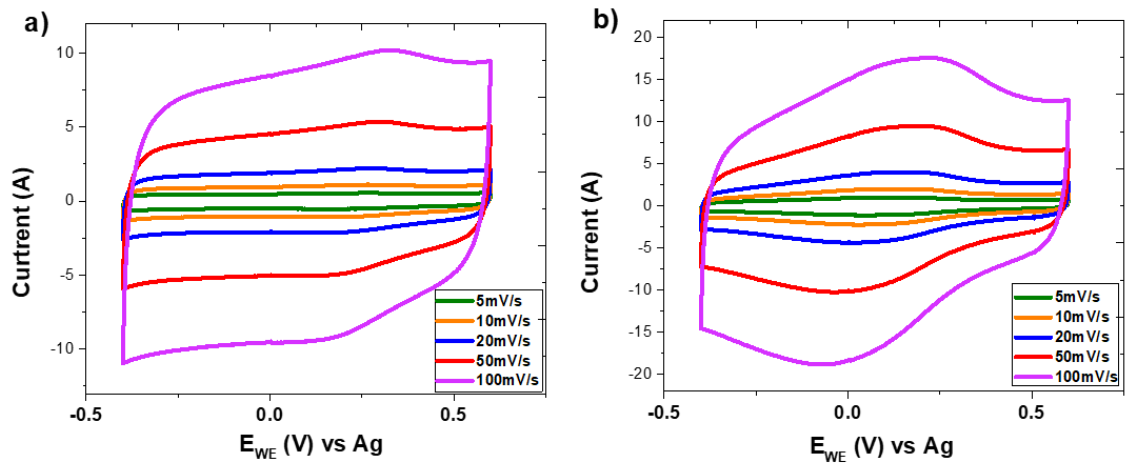

Figure V. 3 CV curves of (a) rGO (b) GA cycled at different scan rate in 3M H_2SO_4

In the organic electrolyte (1M $TEABF_4$ /AN), the electrochemical performances were evaluated and show a capacitance of 88 ± 4 $F.g^{-1}$ for rGO and 78 4 $F.g^{-1}$ ± 4 $F.g^{-1}$ for GA at a scan rate of 10 $mV.s^{-1}$ **(Figure V.4 a)**. It is evident that rGO slightly outperforms GA. In organic electrolyte, pseudo-capacitive behavior is mostly absent, so in this case the storage mechanism relies mainly on the adsorption and desorption of ions within the porosity of the materials [2]. As shown in **Chapter III**, the micro, meso, and macroscale morphology was very different between GA and rGO, showing the strong influence of the chosen reduction technique. In addition, in terms of porosity, the SANS porosity data extracted from the invariant showed that rGO had a higher mesoporosity than GA: 35% and 57% for GA and rGO respectively. Furthermore, N_2 gas sorption BET showed that rGO has a higher SSA of 401 m^2/g than GA with only 237 m^2/g and higher mesopore volume of 0.86 cm^3/g compared to 0.24 cm^3/g in GA in the mesoscale from 0.6 to 30 nm. Thus, the mesoporosity amount of rGO exceeds that of

GA, as evidenced by SANS and N_2 gas adsorption, while the higher total pore volumes of GA (24.3 cm^3/g) determined from the difference between its envelope and solid volumes originates from a significant contribution of its macroporosity, which does not contribute significantly to electrochemical storage (**Figure V.4 b**).

Although the conductivity of rGO is 15 times higher than that of GA, it is worth noting that the addition of 15% conductive agent during electrode preparation can mitigate the effect of intrinsic conductivity differences between the materials. Therefore, the superior electrochemical performances of rGO in the organic electrolyte can be attributed to its higher mesoporosity, underscoring its importance in high performance SC.

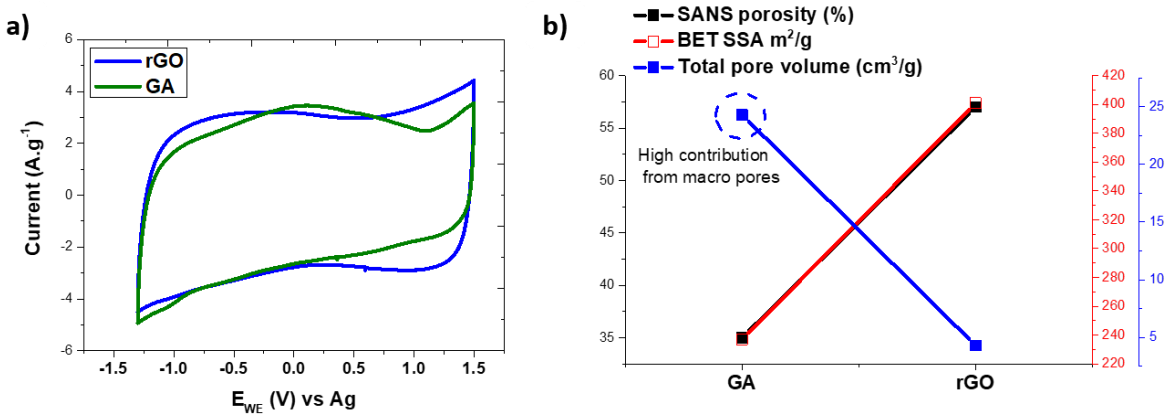

Figure V. 4 (a) CV curves of rGO and GA in organic electrolyte 1M $TEABF_4$ in acetonitrile at 10 $mV.s^{-1}$ (b) SANS porosity, N_2 BET SSA, and total pore volume representation.

In aqueous electrolyte (3M H_2SO_4), a pseudo-capacitive peak was recorded on the CV curves, more pronounced in GA than in rGO (**Figure V.5 a)**. Interestingly, the trends were reversed: **GA showed a capacitance of 149 ± 4 $F.g^{-1}$, higher than rGO with 96 ± 4 $F.g^{-1}$ at 10 $mv.s^{-1}$**. It is noteworthy that both capacitances were higher than in the organic electrolyte, due to the additional pseudo-capacitive behavior associated with the adsorption/desorption mechanism. Additional contributions, such as the smaller size of ions in the aqueous electrolyte, which can be more easily adsorbed in small porosities, could play a role in enhancing the capacitance. However, considering that rGO exhibits higher specific surface area (SSA) and higher mesoporosity, this reversal of trend cannot be explained by the structure and porosity of the samples. The **chemical properties** of the materials could play a **key role** in explaining this opposite trend. As shown in **Chapter III**, GA is less reduced than rGO. The C/O ratio of rGO (8.2) was twice that of GA (4.4). Additionally, TGA showed a weight loss of 30% for GA compared to 10% for rGO, indicating a higher amount of oxygen functional groups present in GA **(Figure V.5 b**). Indeed, the pseudo-capacitive peaks observed on the CV curves indicate

highly reversible surface or near-surface faradaic processes occurring between the electrode and the electrolyte. The remaining oxygen-containing groups, such as alcohol, carbonyl, and carboxylic acid groups, can undergo reactions with the aqueous electrolyte, according to the following equation: $C_xO + H^+ \leftrightarrow C_xOH$ [2]. Thus, the higher abundance of oxygen functional groups in GA results in a higher pseudo-capacitance stemming from faradic processes, shedding light on the superior electrochemical performances of GA in the aqueous electrolyte.

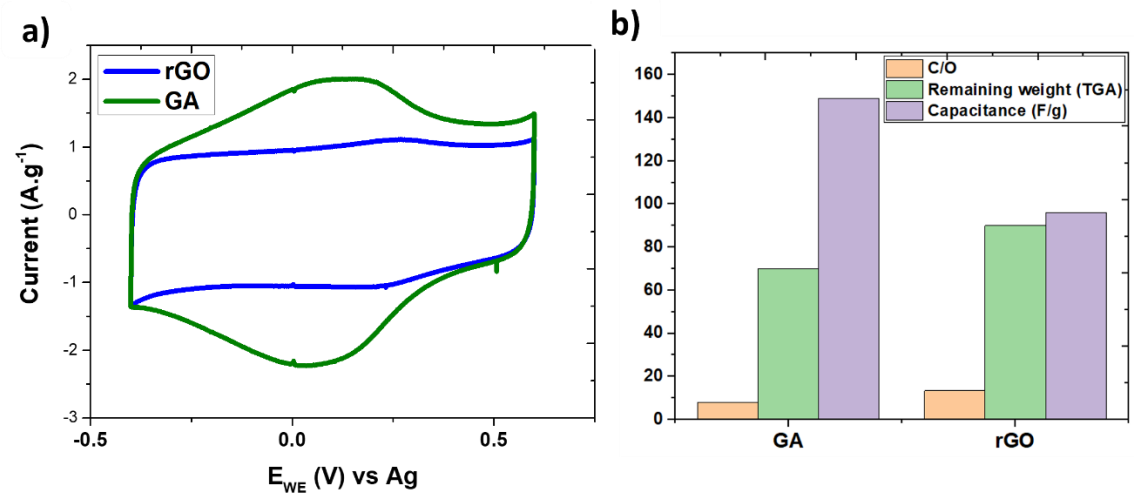

Figure V. 5 (a) CV curves of rGO and GA in aqueous electrolyte 3M H_2SO_4 at 10 mV.s^{-1} (b) C/O evolution, TGA remaining weight after GO reduction, and electrochemical capacitance in the aqueous electrolyte.

2.2 The electrochemical performances of pillared graphene materials: 6RP-0.2 and 6GA-0.05

As in the case of the reference materials (GA and rGO), FSE were also prepared to study the electrochemical performances of the pillared graphene materials. The electrochemical analysis of the FSE was carried out in organic (1M $TEABF_4$ /AN) and aqueous (3M H_2SO_4) electrolytes. In organic electrolyte, the CV curves of 6GA.0.05 and 6RP-0.2 (**Figure V.6**) show a slight deformation compared to the rectangular EDLC shape. Moreover, the achieved capacitance was 88 ± 4 F.g^{-1} for 6GA-0.05 and 101 ± 4 F.g^{-1} for 6RP-0.2 at 10 mV.s^{-1}, showing a slight increase compared to non-pillared graphene materials (78 ± 4 F.g^{-1} for GA and 88 ± 4 F.g^{-1} for rGO). In aqueous electrolyte, the CV curves of the pillared samples do not present a pronounced pseudo-capacitive peak (**Figure V.7**) compared to the reference materials. Furthermore, 6GA-0.05 showed a capacitance of 105 ± 4 F.g^{-1} slightly lower than 6RP-0.2 with 116 ± 4 F.g^{-1} at 10 mV.s^{-1}.

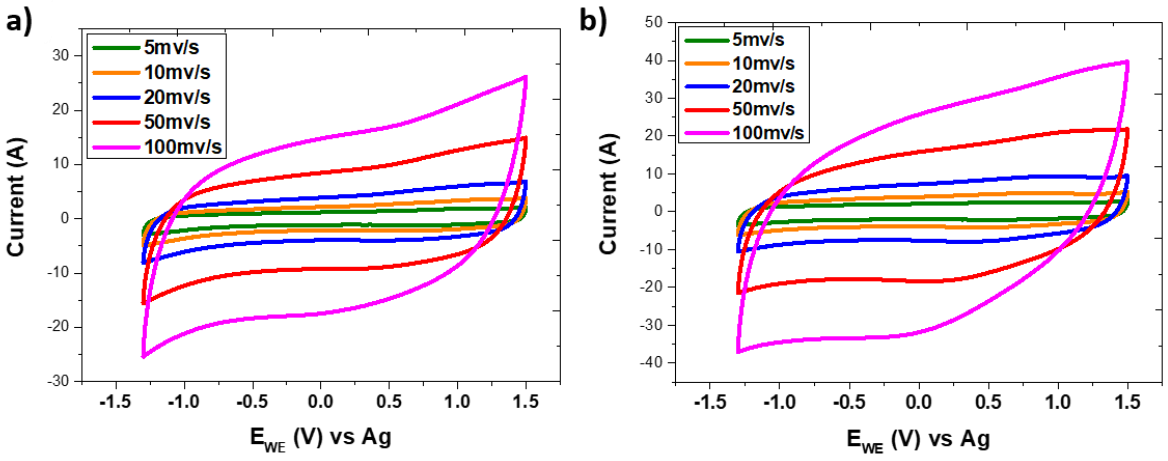

Figure V. 6 CV curves of (a) 6GA-0.05 and (b) 6RP-0.2 cycled at different scan rate in 1M $TEABF_4$ in acetonitrile.

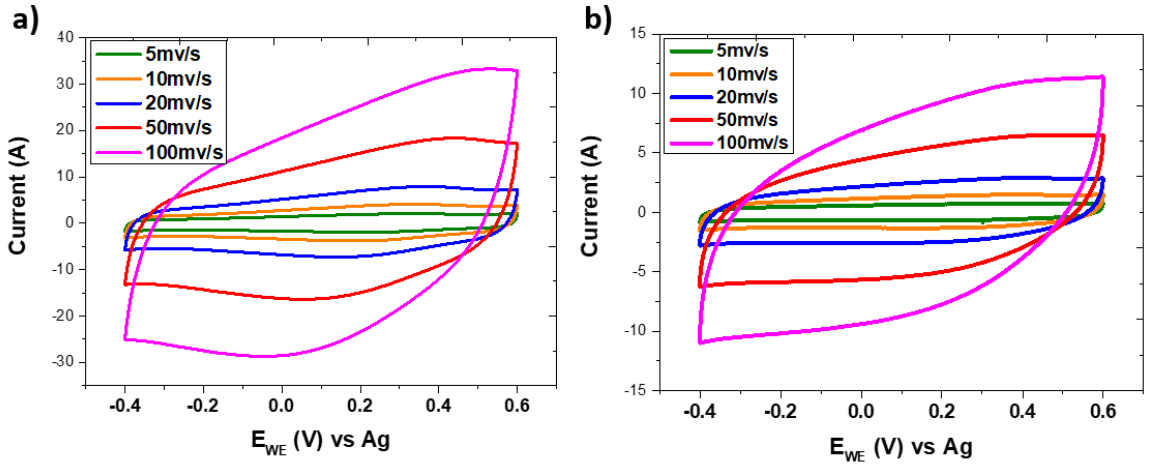

Figure V. 7 CV curves of (a) 6GA-0.05 and (b) 6RP-0.2 cycled at different scan rate in 3M H_2SO_4 electrolyte.

As shown in **Chapter IV**, the SANS mesoporosity of the pillared materials is 15% and 37% for 6GA-0.05 and 6RP-0.2 respectively, which is lower than that of the non-pillared samples (35% for GA and 57% for rGO respectively). Their N_2 BET SSA are also lower than those of GA and rGO. **Despite these lower mesoporosity and SSA, pillared materials showed higher electrochemical capacitances than the reference materials in organic electrolyte.** These results underline the participation of the newly formed graphene galleries in the electrochemical process. Indeed, this new microporosity provides additional adsorption sites for ions, and enhances the overall capacitance. **These results highlight the importance of the micropores in the electrochemical storage in SCs**. Moreover, despite the higher mesoporosity in reference materials, their electrochemical performances are limited because of the restacking of the graphene sheets which must strongly influence their microporosity and,

consequently, their electrochemical capacitance in an organic electrolyte as shown in **Figure V.8**.

N_2 gas sorption BET surface area measurements at 77K revealed a SSA of 26 and 93 m^2/g for 6GA-0.05 and 6RP-0.2 respectively (**Figure V.8**). Therefore**, 6RP-0.2 shows a higher SSA, higher mesoporosity and a comparable size of the new microporosity** (close d-spacings 0.77 nm and pillars densities within the materials) **than that observed for 6GA-0.05**. Accordingly, 6RP-0.2 shows slightly higher capacitance than 6GA-0.05 in organic electrolyte.

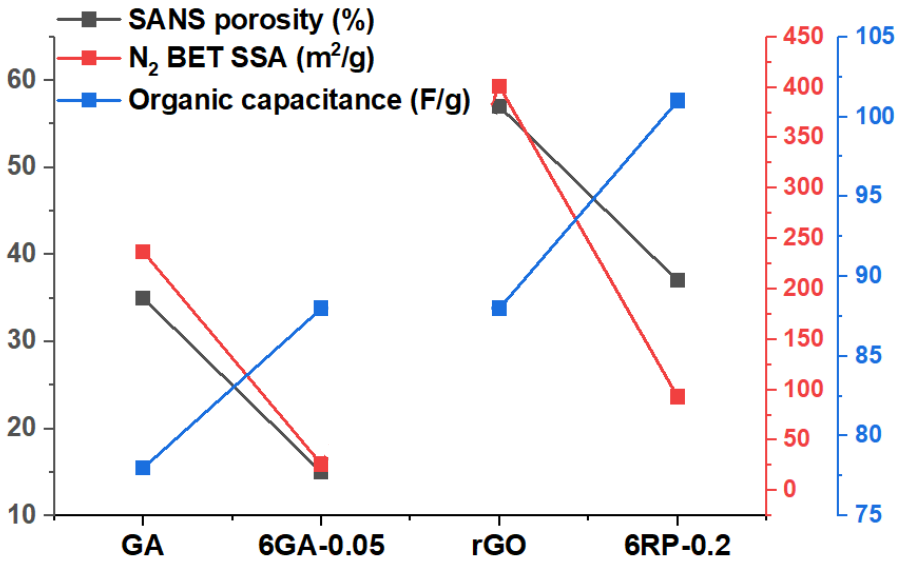

Figure V. 8 SANS porosity, N_2 BET SSA, and the electrochemical capacitance in organic electrolyte for GA, 6GA-0.05, rGO, and 6RP-0.2.

In the aqueous electrolyte, both materials showed an increase in their electrochemical capacitances of about ~20% compared to the organic electrolyte. This increase could be due to the pseudo-capacitive behavior resulting from reversible surface or near-surface faradaic processes occurring between the remaining oxygen-containing groups in the electrode and the electrolyte. As shown in **Chapter IV**, chemical analysis of the pillared samples showed that they have a similar oxygen content (12% by EA), which could justify the comparable increase in capacitance. **Despite the introduction of pillaring, non-pillared GA remains the most efficient sample in the aqueous electrolyte.**

This performance is attributed to the high oxygen content in this material (17.6%), providing additional confirmation of the **high contribution of the pseudo-capacitance to the electrochemical performances in aqueous media**. Furthermore, pillared and non-pillared graphene-based materials showed good and **similar** rate capabilities in the **organic** electrolyte

as shown in **Figure V.9 a**. However, in the **aqueous** electrolytes (**Figure V.9 b**), **pillared samples showed lower rate capabilities performances than non-pillared samples**. This loss in capacitance at high scan rates could be attributed to two possible factors: i) reduced ion adsorption within the porosity, or ii) the absence of pseudo-capacitive reactions at high scan rates. The CV curves of pillared samples at high scan rates in the aqueous electrolyte (**Figure V.7**) do not exhibit a pseudo-capacitive peak compared to non-pillared samples (**Figure V.3**). These observations suggest that, at high scan rates, the oxygen functional groups in pillared materials may be less accessible and may be obstructed by the pillars, supporting the second hypothesis.

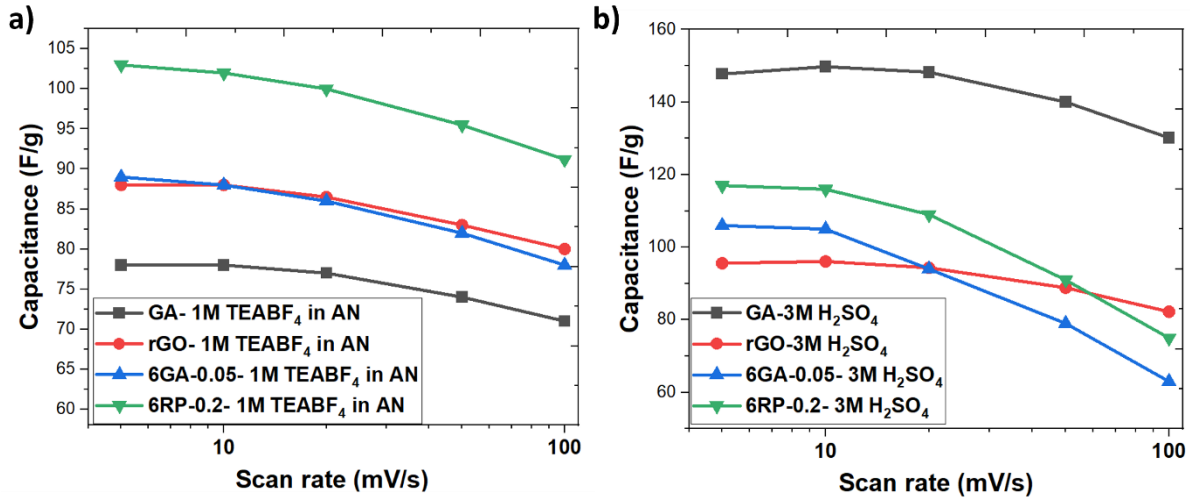

Figure V. 9 Rate capability of pillared and non-pillared graphene samples in (a) 1M $TEABF_4$ / AN and (b) 3M H_2SO_4 electrolytes.

To verify the participation of the galleries in the electrochemical performances of pillared materials, 6RP-0.2 and rGO FSE were cycled in a second organic electrolyte with a larger cation size (1M $THABF_4$). rGO showed comparable electrochemical performances in both electrolytes (**Figure V.10 a**). The CV shape was not significantly impacted by increasing the cation size. This result confirms that for non-pillared samples, the adsorption process occurs within the mesoporosity, which is well developed and optimized in these samples. The large cation (THA^+) could reach the same adsorption sites than the smaller one (TEA^+). In turn, the electrochemical capacitance of 6RP-0.2 decreased from 101 ± 4 $F.g^{-1}$ in 1M $TEABF_4$ /AN electrolyte to 61 ± 4 $F.g^{-1}$ in 1M $THABF_4$ /AN electrolyte. As shown in **Figure V.10 b**, the shape of the CV curve at negative potential (cation adsorption at -1.3 V) was strongly influenced by the increase in cation size. The large cation THA^+ showed less adsorption than TEA^+.

There are two possibilities for such a situation: i) the large cation may not be able to access the newly created galleries because its diameter (1 nm) is larger than the d-spacing in pillared samples (0.7 nm), or ii) the large cation may be blocked at higher porosity scale (mesoporosity). The substantial difference in mesoporosity between non-pillared and pillared samples adds complexity to this phenomenon. If they exhibited similar mesoporosity, then the conclusion of the inaccessibility of THA^+ to the galleries would be more straightforward. Therefore, the low mesoporosity of pillared samples may also be partly responsible for this phenomenon. In order to answer this question and to understand how the different porosity scales in graphene-based materials contribute to the adsorption/desorption process in supercapacitors, an *in-situ* SANS experiment was performed.

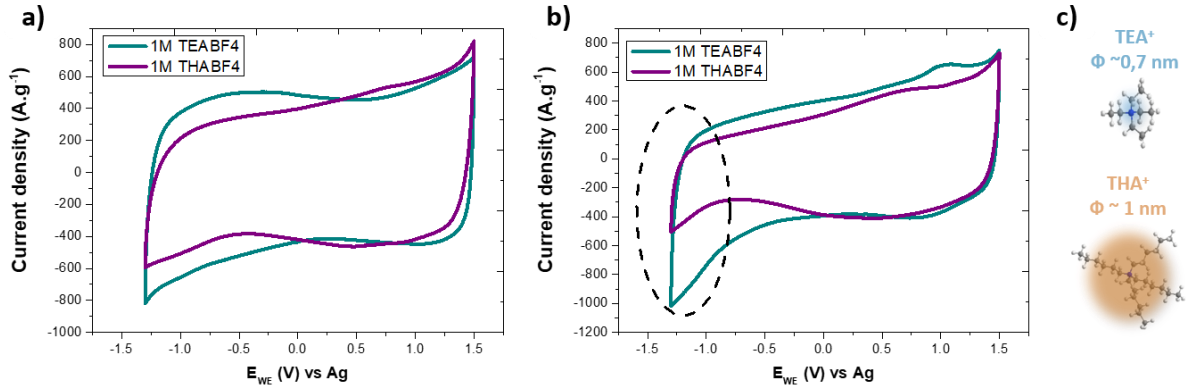

Figure V. 10 (a) rGO (b) 6RP-0.2 cycled in 1M $TEABF_4$ and $THABF_4$ /AN at a scan rate of 10 mV/s (c) the two cations and their approximate diameter [3]

3 Understanding the adsorption/desorption mechanisms in graphene-based materials

The sensitivity of neutrons to the variations in nuclear scattering lengths makes SANS a powerful technique to probe the variation in the nature and amount of adsorbed species and their concentration within the porosity of the material. It is worth reminding at this stage that for a two-phase system, the equation of the small-angle scattered intensity is:

$$I(Q) = \varphi V p \Delta\rho^2 P(Q) S(Q) \qquad (V.1)$$

The study discussed further in this chapter, involved the investigation of the difference in contrast ($\Delta\rho$) between polarized and non-polarized samples originating from an evolution of location and amount of electrolytic ions within the probed mesoporosity scale. For relevant interpretations, the structural evolution (P(q)S(q)) during electrochemical cycling must be insignificant compared to the variation in contrast between the two samples. To verify this

absence of significant structural evolution, an *in-situ* and *operando* SAXS/WAXS experiment was first conducted. In SANS experiments, counting times of more than 10 min are often required to achieve a good signal-to-noise ratio. However, the charging process of a supercapacitor is very fast, typically around 20 seconds. This fast charging makes *operando* cycling experiments in SANS impossible due to the mismatch in time scales between the SANS measurements and the fast charging process of the supercapacitor. Therefore, *in-situ* SANS was performed under polarization of the electrodes at different potentials at the D22 beam line at ILL. We have been able to monitor the structural evolution of materials in real time under cyclic conditions (*operando* SAXS/WAXS) thanks to the temporal resolution available at ESRF. The *in-situ* and *operando* SAXS/WAXS analyses were performed at the D2AM beamline (ESRF) and aimed at investigating the potential structural evolution of graphene-based materials during SC operation within an extended scale from 0.2 to 210 nm.

These experiments required an electrochemical cell adapted with transmission measurements. For this purpose, an *ad hoc* electrochemical cell for small angle scattering experiment was developed in our laboratory during this PhD. **Figure V.11 a** shows the conceptual scheme of the cell. It consists in a three-electrode electrochemical cell with two aluminum windows acting as current collectors, two holes for injecting electrolyte and removing air bubbles, and a silver reference electrode. The beam entrance window has a thinner section at the center, with a diameter of 4 mm and a thickness of 200 µm. This design is used to facilitate beam centering and reduce beam attenuation. Inside the cell, the counter electrode and separators have a 4 mm diameter hole to prevent any interaction with the beam. This ensures that the beam only interacts with the working electrode (**Figure V.11 b**).

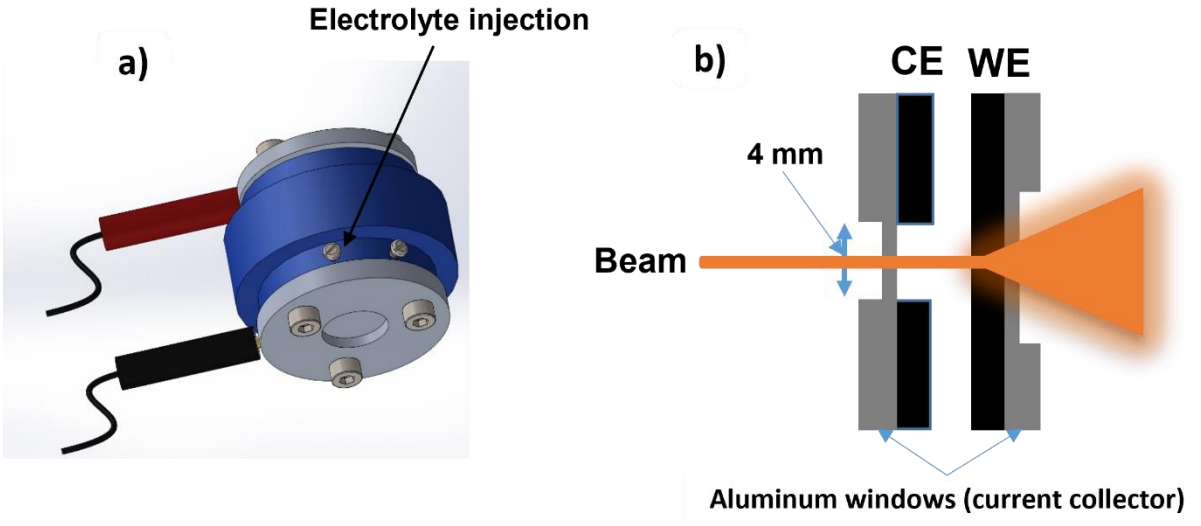

Figure V. 11 (a) The prototype of the operando electrochemical cell (b) the configuration of the electrodes and separator inside the cell, the beam interact only with the WE.

3.1 Unveiling the structural evolution of graphene-based materials during SC operation by *in-situ/operando* SAXS-WAXS study

It is worth introducing at this stage that the *in-situ* and *operando* SAS measurements were conducted **two years after the SANS results** discussed in **Chapters III** and **IV**. Consequently, the FSE were prepared using a different batch of GO. The resulting SAXS profiles of 6RP-0.2 and rGO showed noticeable variations compared to the previous SANS profiles, particularly in the positions of the breaks in slopes (as SAXS and SANS are expected to deliver similar structural features). The SAXS profile of rGO (**Figure V.12 b**) showed a single break in slope at Q*=0.043 $Å^{-1}$, compared to two in SANS (**Figure V.12 a)**. This break in slope could be attributed to the bending length within the crumpled graphene sheets (R_{SAXS}=14 nm, which is very close to that of the other batch used for SANS R_{SANS}=12 nm). The absence of a second break in slope indicates that, in this batch of synthesis, the graphene sheets are less crumpled, and the persistence length may have increased, causing the associated break in slope to be beyond the scale of investigation. The SAXS profile of 6RP-0.2 showed a shifted break in slope towards small angles (Q*=0.0083 $Å^{-1}$) (**Figure V.13 b)** compared to the SANS profile (**Figure V.13 a)**. The difference could be attributed to a longer bending length within the graphene sheets in this synthesis batch (R_{SAXS}=75 nm) compared to the other batch (R_{SANS}=14 nm). Furthermore, due to the limited beam time access for the SAS experiments,

only 6RP-0.2 and rGO were studied because FSE are easier to prepare using reduced powders compared to hydrogels.

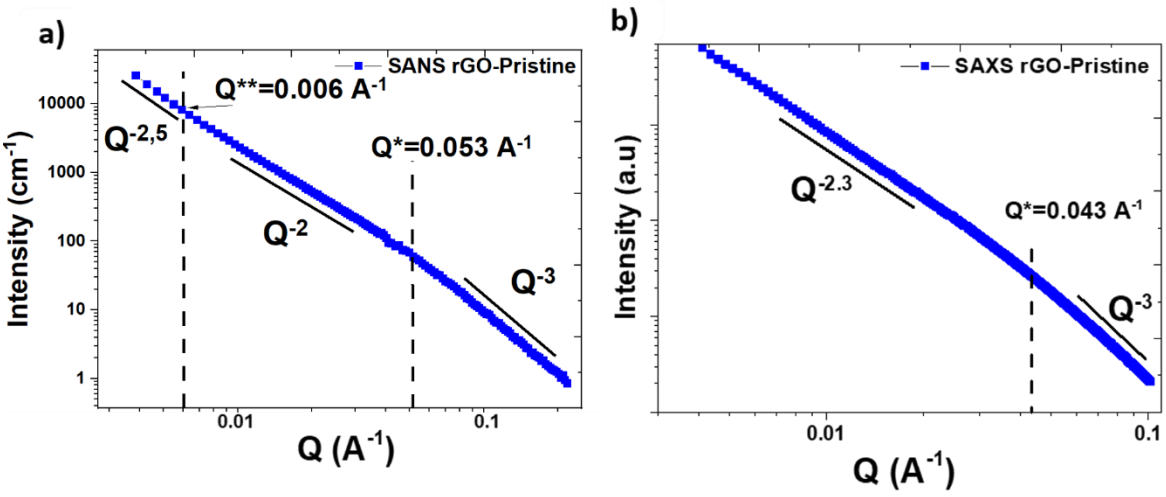

Figure V. 12 Comparison of (a) SANS and (b) SAXS profiles of pristine rGO

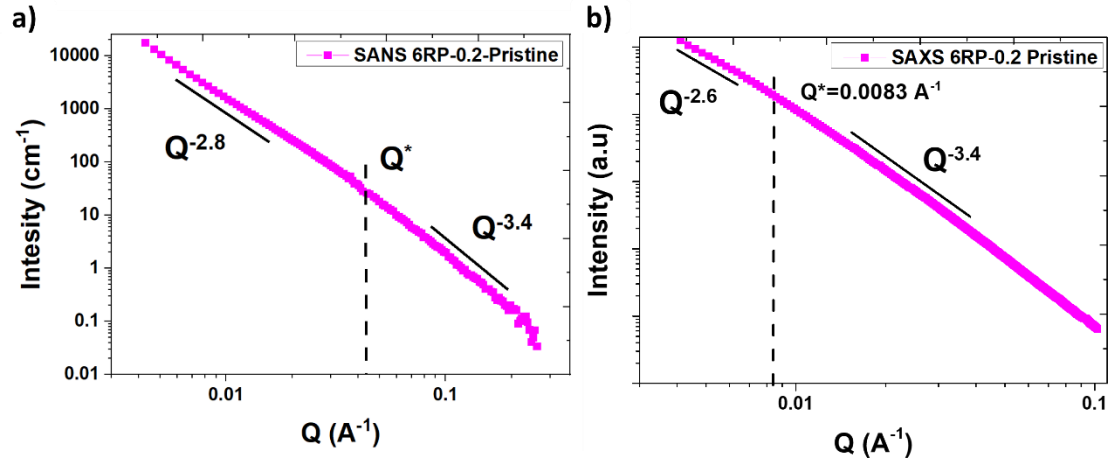

Figure V. 13 Comparison of (a) SANS and (b) SAXS profiles of pristine 6RP-0.2

Prior to analyzing the *in-situ* and *operando* results, it is essential to examine the scattering profiles of the FSE. The FSE preparation involves grinding 80 % wt of the active material with 15 % wt acetylene black (AB) and 5 % wt of PTFE. Consequently, all of these components may contribute to the scattering, which could potentially participate to the overall structural evolution. This could make it difficult to extract isolated information about the active material. Therefore, it is imperative to determine the actual contribution of the active material in the scattering profile of the FSE. The intensity depends on the volume fraction (φ) of the scattering particles (**Equation (V.1)**), which implies that the weight percentage of the different component of the FSE should be converted to volume percentage. For 6RP-0.2 FSE, the

calculated volume fraction for active material (6RP-0.2 powder), AB, and PTFE are 87.9%, 9.6%, and 2.5%, respectively.

Figure V.14 shows the SAXS profiles of the three components of the 6RP-0.2 FSE, the calculated SAXS profile of the FSE using these three components and their respective volume fraction, the measured SAXS profile of the 6RP-0.2 FSE, and its Kratky representation. Firstly, the linear combination of the SAXS profiles of each component (considering their volume fraction) produces a profile that is superimposed on that of the FSE (**Figure V.14 d**). This observation demonstrates that the formulation has maintained the morphology of each component and has not caused the formation of any additional porosity at this scale. This finding holds significant importance as it will help to understand the contribution of the different component in the structural evolution of the FSE during SC operation. Secondly, the three materials display a break in slope at small angles ($Q^*=0.0083$ $Å^{-1}$ in 6RP-0.2, $Q^{**}=0.0073$ $Å^{-1}$ in AB, and $Q^*=0.0065$ $Å^{-1}$ in PTFE). Notably, the Q^* for 6RP-0.2 powder is closest to that of the FSE ($Q^*=0.008$ $Å^{-1}$). Due to this proximity of the break, and considering that 6RP-0.2 powder constitutes more than 87 %v of the FSE, this break in slope is attributed to the bending length R within the graphene sheets in 6RP-0.2 powder. Similarly, the same analytical approach was applied to the rGO FSE, successfully reproducing its scattering profile from the three components (rGO powder, AB, and PTFE). However, the SAXS profile of rGO FSE exhibits two breaks in slopes (**Figure V.15**). The first one at $Q^*=0.043$ $Å^{-1}$ matches that of rGO powder (**Figure V.12),** indicating that it originates from the bending length within rGO graphene sheets. The presence of the signal related to the bending length in the rGO FSE SAXS profile implies that the Q^* in the 6RP-0.2 FSE SAXS profile also originates from the bending length within the graphene sheets in 6RP-0.2. Interestingly, the second break at $Q^{**}=0.013$ $Å^{-1}$ is not present in any of the scattering profiles of the three components recorded separately nor in the 6RP-0.2 FSE profile. This suggests that it does not stem from an interaction between the different materials. Moreover, this break in slope is persistent in all the SAXS profiles of the various studied rGO FSE, possibly indicating a new characteristic structural feature within the FSE. **These results highlight the complexity of the electrode structures.** Therefore, the structural evolution of the materials within the SAXS scale will be explored by monitoring the positions of the breaks in slopes (bending lengths) and the slopes at both small and high Q values (mass and surface fractal dimensions).

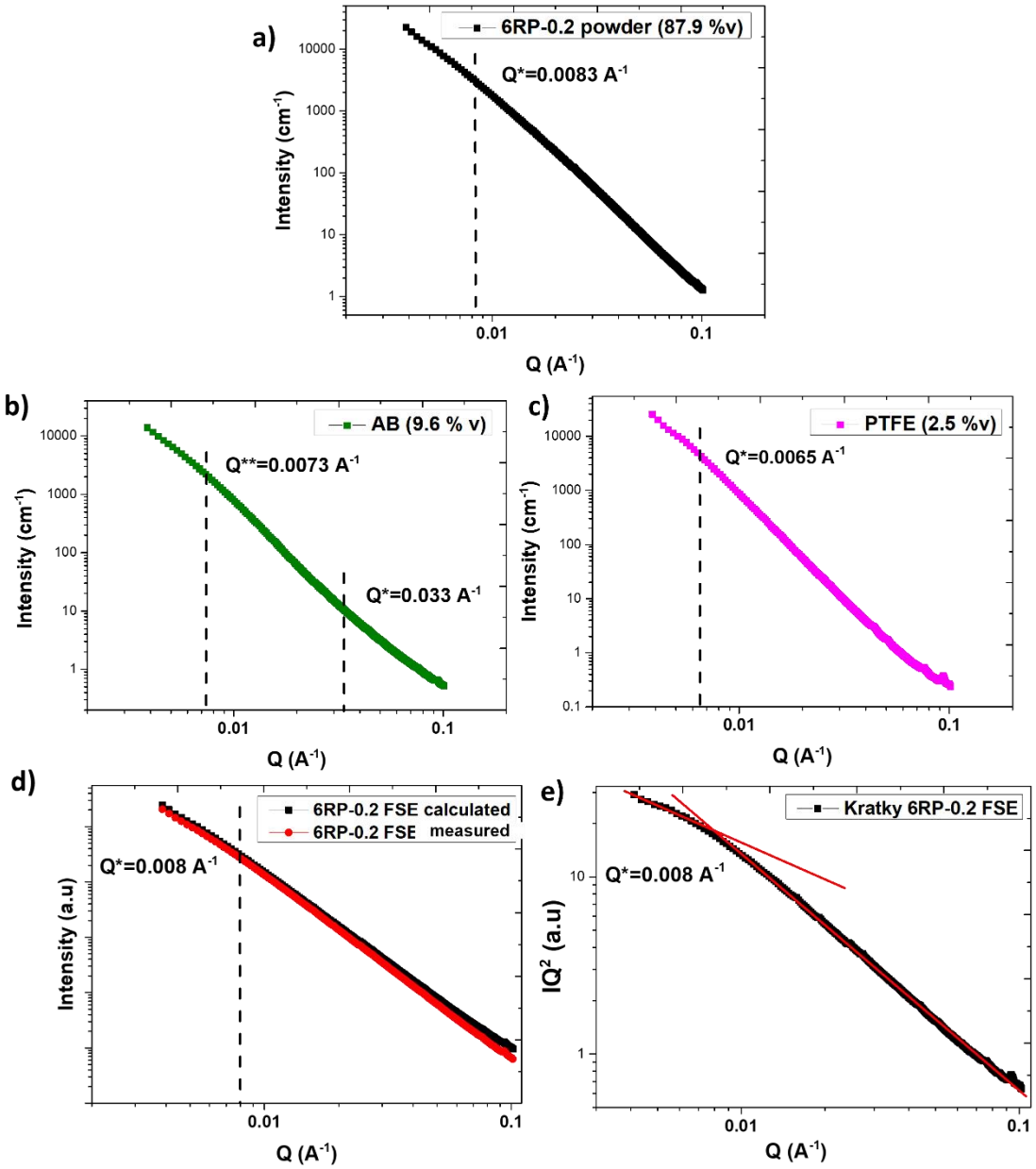

Figure V. 14 SAXS profile of (a) 6RP-0.2 powder, (b) AB, (c) PTFE, (d) 6RP-0.2 FSE calculated from the different volume fraction of the three materials (e) Kratky plot of 6RP-0.2 FSE

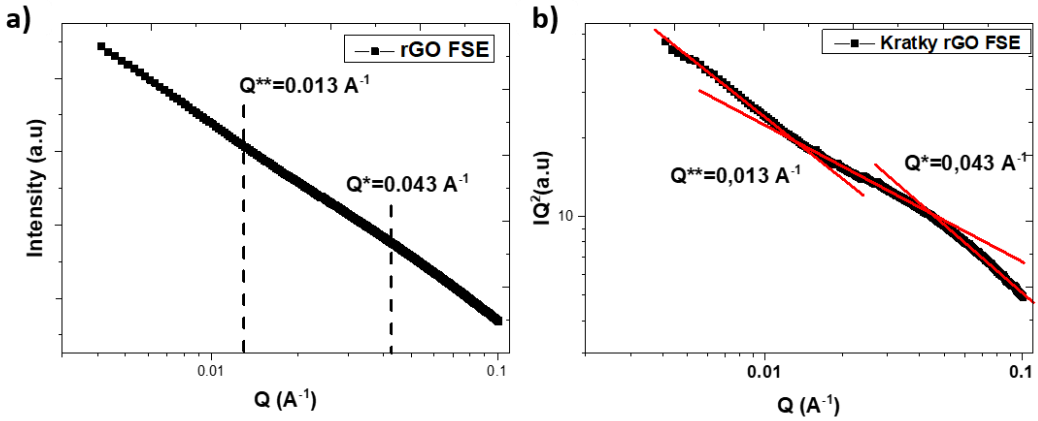

Figure V. 15 (a) SAXS profile and (b) Kratky plot of rGO FSE

The XRD profiles (XRD and WAXS refer to the measurement performed at the laboratory in reflection modes and at the ESRF in transmission mode, respectively) of 6RP-0.2 FSE and rGO FSE (**Figure V.16**) show the typical signal of pillared graphene materials (CL and G peaks) and non-pillared materials (G peak). In addition, both FSEs display a PTFE peak at Q=1.3 $Å^{-1}$ and a small contribution of AB on the G peak at high Q values (between Q=1.75 $Å^{-1}$ and Q=2 $Å^{-1}$) are recorded. The corresponding WAXS profiles were also recorded (**Figure V.17**). However, due to the high energy used for the SAXS/WAXS experiment (16 keV), the resolution of the WAXS profiles was considerably lower compared to XRD (**Figure V.17**).

Still, this energy was chosen as the most adapted compromise between resolution and optimal beam penetration through the aluminum windows of the electrochemical cell. The aluminum windows were chosen to enable the cell's use in both SAXS and SANS, as aluminum is transparent to neutrons. The two FSE WAXS profiles (**Figure V.17 a, b**) show a peak at small angles originating from the diffraction of the beam stop. The PTFE, CL and G peaks are also visible but with the expected low intensity arising from the high beam energy. These profiles were measured *ex-situ*, which means that the peaks of interest would have lower intensity due to the strong diffraction from the aluminum windows inside the electrochemical cell. Therefore, a quantitative analysis measuring the evolution of the full width at half-maximum (FWHM) and peak positions was not possible. Nevertheless, variations within the background intensity at the peaks position offer insights into the influence of the electrochemical process on the microscale structure.

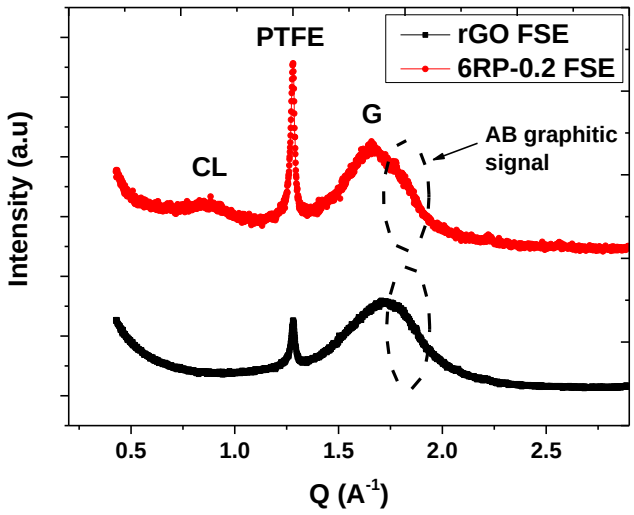

Figure V. 16 XRD profiles of rGO and 6RP-0.2 FSEs

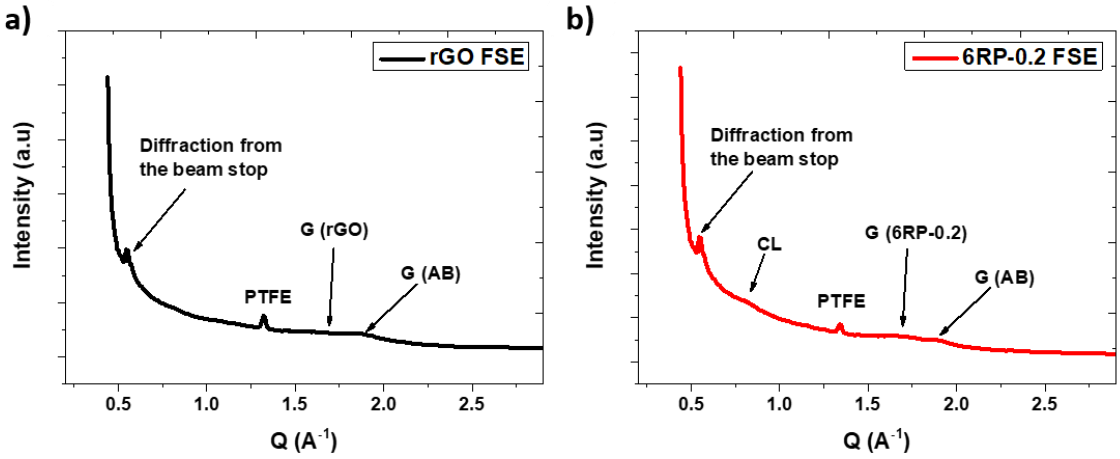

Figure V. 17 WAXS profiles of (a) rGO and (b) 6RP-0.2 FSEs

3.1.1 *Operando* SAXS-WAXS study on 6RP-0.2 FSE during cycling

The *operando* and *in-situ* SAXS/WAXS measurements were performed using the two organic electrolytes, 1M $TEABF_4$ and $THABF_4$ /AN. The *operando* measurements were performed under cycling within a potential window ranging from -1.3 to 1.5 V *vs* Ag and at various scan rates. The cycling program started with a stabilization step (300 cycle at 50 mV/s), followed by 10 cycles at 5, 10, 20, 50, and 100 mV/s, and ended with an aging step consisting of 10000 cycles at 1000 mV/s. The SAXS/WAXS profiles were collected continuously at a rate of 1 scan per second. Due to limited beam time, *operando* measurements were limited to 6RP-0.2 FSE. **Figure V.18** displays the SAXS and WAXS profiles of 6RP-0.2 FSE during cycling. It is important to note that the subtraction of the empty cell signal was not made on the WAXS profiles because it was found to increase the background, which hindered meaningful

observations. In addition, the SAXS/WAXS evolutions were examined during a single cycle, across various cycles at the same scan rate, and throughout the entire cycling program to detect any structural changes. In addition, for the sake of clarity, only profiles with significant changes have been plotted in **Figure V.18 d**. due to the large amount of data obtained.

Figure V.18 a, c shows the SAXS profiles of 6RP-0.2 FSE during cycling. The SAXS profiles exhibited no discernible evolution, indicating that the structure within the 3 to 210 nm length scale remained unaffected by cycling in both electrolytes, even with the presence of the large cation (THA^+). On the other hand, **Figure V.18 b, d** shows the WAXS profile evolution of 6RP-0.2 FSE. The positions of the CL and G peaks were marked on the plots. It is essential to note that the bump within the G peak position originates from the empty cell signal. Interestingly, with the small cation (TEA^+) no significant evolution was observed in the CL and G peaks This indicates that cycling in 1M $TEABF_4$ /AN electrolyte did not cause any structural modifications within this extended SAXS/WAXS scale (0.2 to 210 nm).

In turn, cycling in 1M $THABF_4$ /AN electrolyte results in a noticeable impact on the G peak position (**Figure V.18 d**) while no remarkable evolution in the CL peak was observed despite the cation size (1 nm) being larger than the d-spacing (0.77 nm). To emphasize this change, **Figure V.19** shows the result of subtracting the final scattering profile from the initial one.

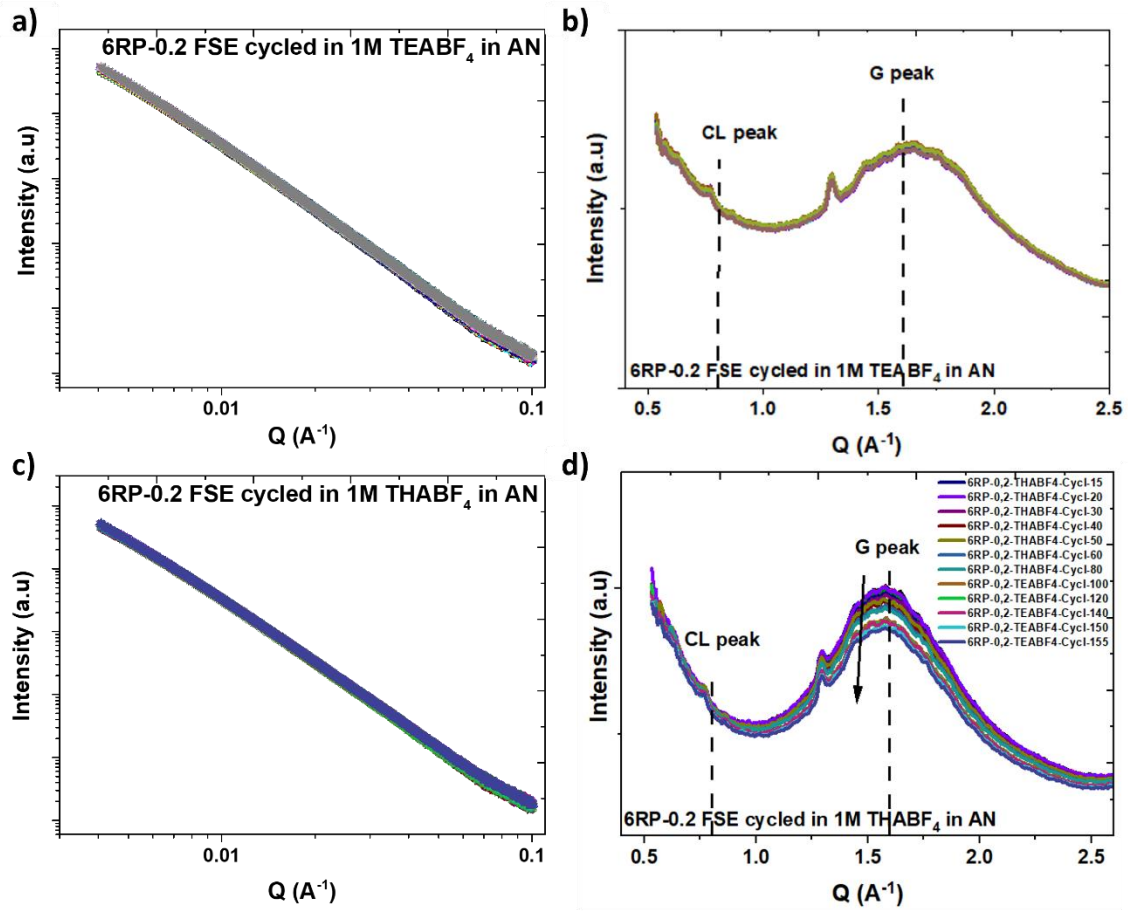

Figure V. 18 (a) SAXS and (b) WAXS profiles of 6RP-0.2 FSE recorded during cycling in 1M $TEABF_4$ /AN, (C) SAXS and (d) WAXS profiles of 6RP-0.2 FSE recorded during cycling in 1M $THABF_4$ /AN

Figure V.19 confirms that this evolution has occurred only within the G peak, and no modification of the CL peak is observed. The intensity of the G peak decreased, which may be due to a decrease in the graphitic domains size (number of stacked layers) or a modification of the orientation of these domains. The first hypothesis suggests that there is an exfoliation of the graphitic domain within the material. However, electrochemically exfoliating graphite requires aggressive condition with an applied potential of +10 V [4]. In addition, the observed low adsorption of the THA^+ cation (with a characteristic size d~1 nm) within the material porosity, as evidenced by the CV curves (refer to **Figure V.10 b**) reduces the possibility of its adsorption between the restacked sheets (with a d-spacing of 0.39 nm). This subsequently reduces the probability of the electrochemical exfoliation.

The latter hypothesis appears more suitable in these conditions. Indeed, in a flexible material such as graphene, the presence of large cations, driven by diffusion and adsorption within the porosity, can potentially influence the orientation of graphene sheets. Flexible materials like graphene are prone to undergo dynamic structural changes in response to external

stimuli [5], and the presence of large cations may induce variations in the arrangement of the restacked domains.

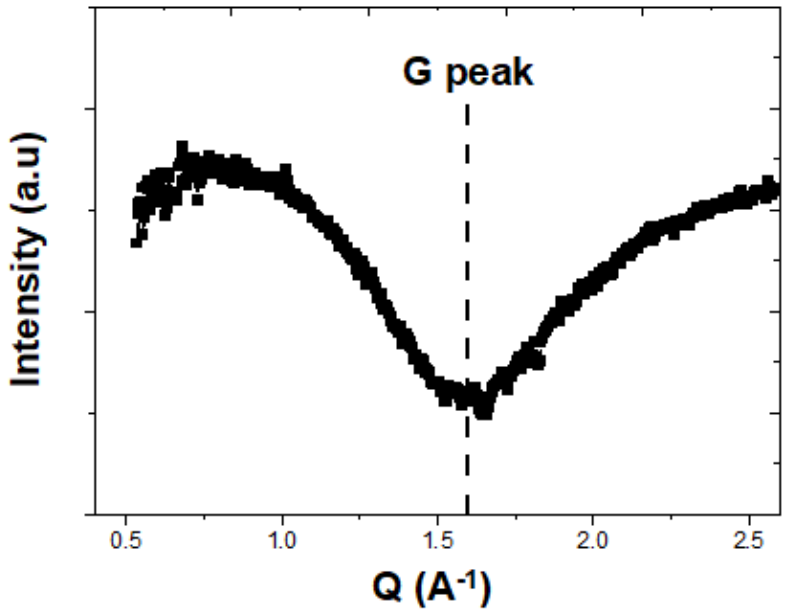

Figure V. 19 Subtraction of the first WAXS profile from the last one of 6RP-0.2 FSE cycled in 1M THABF₄ / AN.

3.1.2 *In-situ* SAXS-WAXS study on 6RP-0.2 FSE during polarization

The *in-situ* analyses were conducted on both 6RP-0.2 and rGO under polarization. To favor cation adsorption on the working electrode, a fixed potential of -1.3 V *vs* Ag was applied, considering that both electrolytes shared the same anion. The most significant difference in cycling behavior was observed at negative potentials (*i.e.* ion-sieving with THA^+) (**Figure V.10**). The initial three SAXS/WAXS profiles were acquired prior to polarization, and the subsequent ones were recorded every minute during the 90-min polarization at -1.3 V. **Figure V.20** presents the SAXS/WAXS profiles obtained for 6RP-0.2 acquired during polarization in both 1M $TEABF_4$ and $THABF_4$ /AN. As observed during cycling, the SAXS/WAXS profiles recorded during polarization in 1M TEABF4 /AN electrolyte showed no significant changes (**Figure V.20 a, b**). This indicates that the adsorption of the small cation (TEA^+) did not affect the structure at the SAXS/WAXS scale. In contrast, **polarization in 1M $THABF_4$ /AN electrolyte resulted in a distinct evolution of both SAXS and WAXS profiles** (**Figure V.20 c, d**). The SAXS profile exhibited a noticeable decrease in intensity as indicated by the black arrow (**Figure V.20 c**). The WAXS profile displayed a significant increase in intensity at the position of the G peak (**Figure V.20 c)**. To understand the origin of these evolutions, Kratky

plots for the initial and final SAXS profiles were examined (**Figure V.21. a**). Additionally, for WAXS, the final scattering profile was subtracted from the initial one to emphasize the variation within the G peak (**Figure V.21 b**).

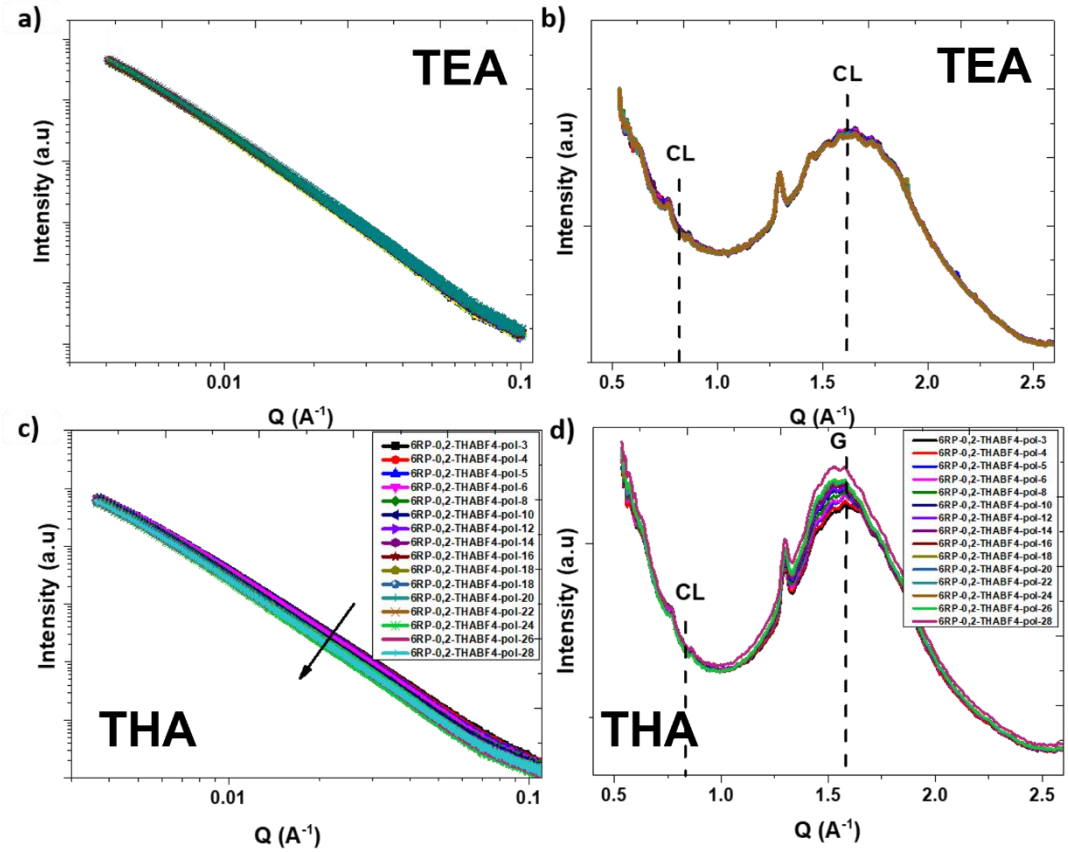

Figure V. 20 (a) SAXS and (b) WAXS profiles of 6RP-0.2 FSE recorded during polarization at -1.3V vs Ag in 1M $TEABF_4$/ AN, (c) SAXS and (d) WAXS profiles of 6RP-0.2 FSE recorded during polarization at -1.3V vs Ag in 1M $THABF_4$/ AN.

Notably the evolution within the SAXS profiles corresponds to a shift of the Q* break in slope (associated to the bending length within the graphene sheets in 6RP-0.2) at high Q values (**Figure V.21 a**). The initial position of this break was recorded at Q*= 0.008 $Å^{-1}$ (red curve), and after polarization, a shift towards smaller angles was observed, reaching a final position at Q*=0.006 $Å^{-1}$ (black curve). The initial bending length R was calculated to be 78 nm, which increased to 105 nm at the end of the polarization. **Figure V.21 b** shows the evolution of the WAXS profile within the G peak position area, indicating a clear increase in the intensity of the G peak itself. An increase in the intensity of a peak in XRD indicates an increase in the amount or ordering of the crystalline structure associated with that specific peak. Here, the increase in the amount of graphitic stacks entities suggests that electrochemical reduction of the remaining oxygen groups has occurred, increasing the amount of restacked graphene sheets within this 6RP-0.2 FSE polarized with $THABF_4$. However, this phenomenon

was not evident in the case of TEA^+, which is expected to be more accessible to the porosity than THA^+. Therefore, this increase in G peak intensity is most probably associated with the enhancement of ordering. Indeed, the observed evolutions in both SAXS and WAXS might be correlated. The SAXS results show a significant flattening of R, from 78 nm for non-polarized 6RP-0.2 FSE to 105 nm for polarized 6RP-0.2 FSE with THA^+. This could be due to an unfolding of the crumpled graphene sheets, which increases the number of oriented graphitic stacks within the beam direction, thereby contributing to the increase in the intensity of the G peak.

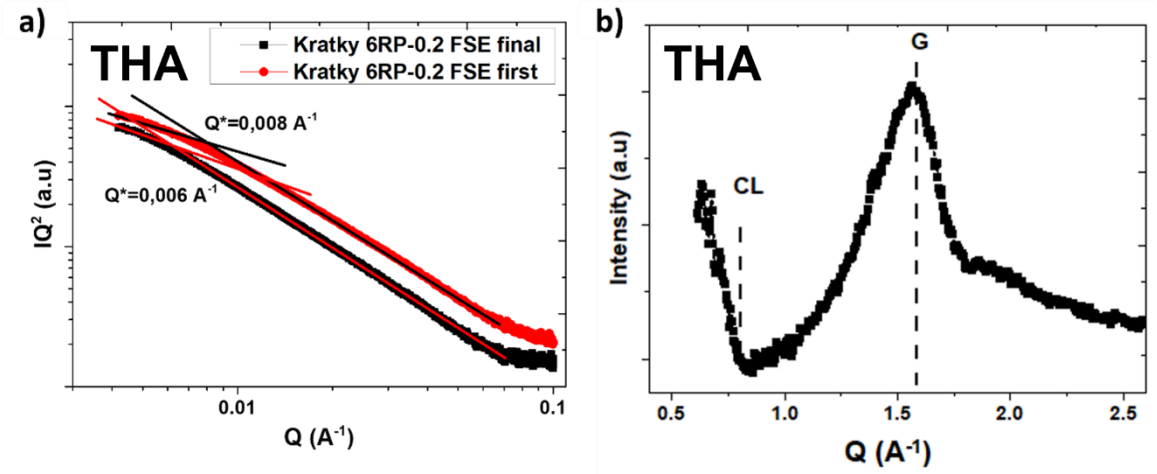

Figure V. 21 (a) Kratky plots of the first and last SAXS profiles of the polarization of 6RP-0.2 FSE at -1.3V vs Ag in 1M $THABF_4$ /AN (b) subtraction of the first WAXS profile from the last one for 6RP-0.2 FSE polarized at -1.3V vs Ag in 1M $THABF_4$ /AN

3.1.3 *In-situ* SAXS-WAXS study on rGO FSE during polarization

The SAXS/WAXS profiles of rGO-FSE during polarization in both 1M $TEABF_4$ and $THABF_4$ /AN electrolytes are presented in **Figure V.22.** The polarization in both electrolytes induced similar evolutions of the SAXS and WAXS profiles of rGO FSE. **Figure V.22 a, c** shows a slight shift of the scattering profile toward higher intensities, in the high Q region, as indicated by the arrow on the curves. This intensity evolution occurred to the same extent and **independently of the cation size**. On the other hand, **Figure V.22 b, d** show a significant increase in the intensity of the WAXS curves, particularly around the G peak position, in both electrolytes. However, it is important to note that these profiles also exhibited a slight shift in the background, which may affect the clarity of this evolution. To understand the origin of these changes, Kratky representation of SAXS profiles were plotted for the initial and final profiles

(**Figure V.23 a, c**). Additionally, for WAXS, the final scattering profile was subtracted from the initial one to emphasize changes within the WAXS scale (**Figure V.23 b, d)**.

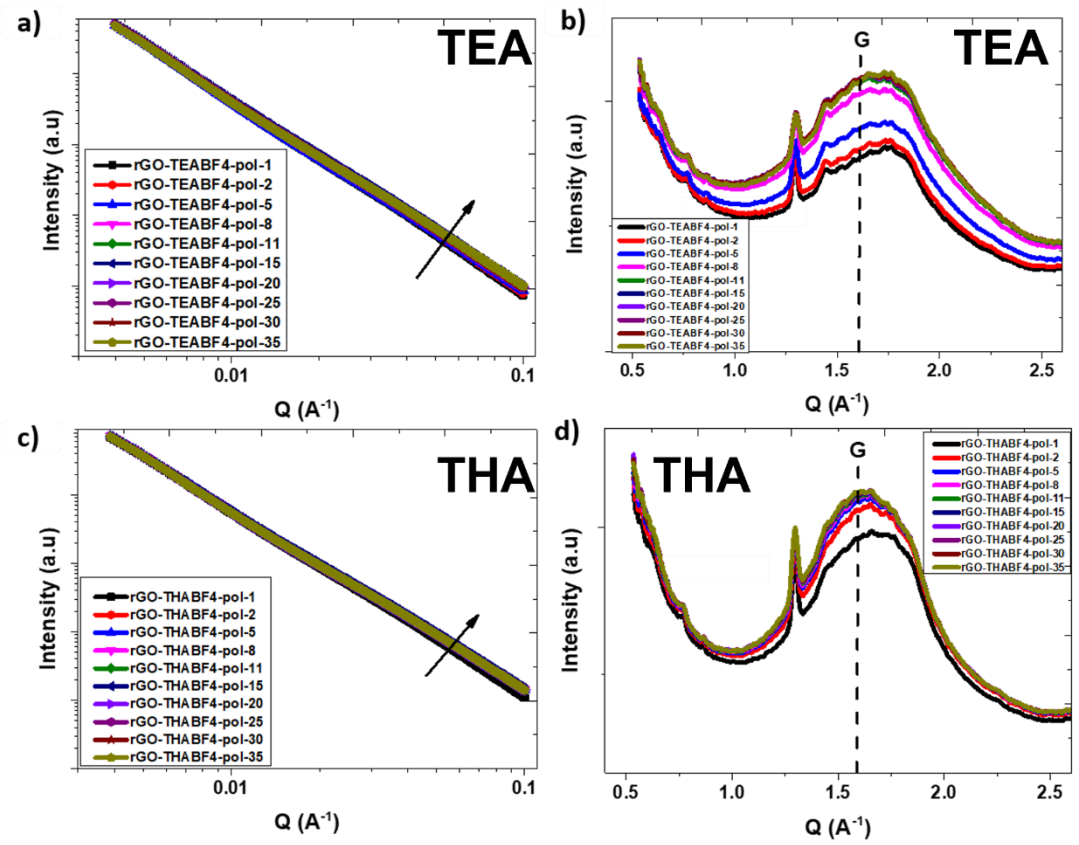

Figure V. 22 (a) SAXS and (b) WAXS profiles of rGO FSE during polarization at -1.3V vs Ag in 1M $TEABF_4$ /AN, (c) SAXS and (d) WAXS profiles of rGO FSE during polarization at -1.3V vs Ag in 1M $THABF_4$ /AN.

Similarly to 6RP-0.2, the evolution of the SAXS profiles corresponds to a shift of the break in slope at high Q values (Q*) (**Figure V.23 a, c**). The initial position of this break was observed at Q*= 0.043 $Å^{-1}$ (black curves). After polarization, a shift towards smaller angles was observed, resulting in a final position at Q*=0.03 $Å^{-1}$ and Q*= 0.036 $Å^{-1}$ for TEA^+ and THA^+ respectively (red curves). The initial bending length was calculated to be 14 nm, which increased to 21 and 18 nm in the case of TEA^+ and THA^+ respectively at the end of polarization. The new R values are very close to each other, so increasing the cation size (from TEA+ to THA+) does not seem to induce any further structural evolution within the SAXS scale. This is likely due to the size of the bending length itself. As the bending length is much smaller than that of 6RP-0.2, both cations caused the graphene sheet to flatten. In turns, **Figure V.23 b, d** shows that a significant evolution in the WAXS profiles occurred within the background. This background evolution is evidenced by the presence of the PTFE peak. In this case, it is not possible to attribute this evolution to the G peak.

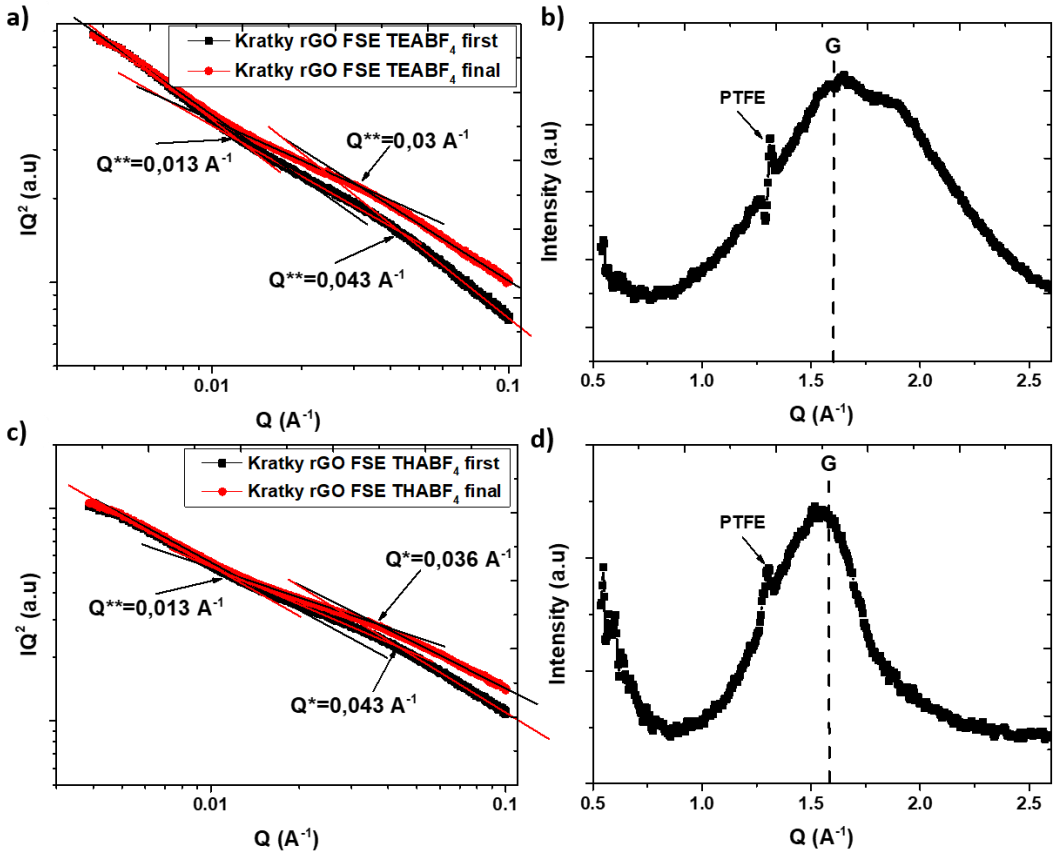

Figure V. 23 (a) Kratky plots of the first and last SAXS profiles of the polarization of rGO FSE at -1.3V vs Ag in 1M $TEABF_4$ /AN, (b) subtraction of the first WAXS profile from the last one of rGO FSE polarized at -1.3V vs Ag in 1M $TEABF_4$ /AN, (c) Kratky plots of the first and last SAXS profiles of the polarization of rGO FSE at -1.3V vs Ag in 1M $THABF_4$ /AN (d) subtraction of the first WAXS profile from the last one of rGO FSE polarized at -1.3V vs Ag in 1M $THABF_4$ /AN.

In summary, *operando* and *in-situ* SAXS/WAXS measurements were used to investigate the structural changes in graphene-based materials during cycling and polarization in two different organic electrolytes with varying cation sizes, 1M $TEABF_4$ and $THABF_4$ /AN. These measurements, conducted under various cycling conditions or constant potential, provided valuable insights into the structural evolution of the materials during supercapacitor operation.

Operando cycling experiments on 6RP-0.2 FSE showed that mesoscale structure (3 to 210 nm) remained unchanged even in the presence of a large cation (THA^+), as indicated by the unchanged SAXS profiles. In contrast, WAXS profiles showed significant evolution, particularly on the G peaks and in the presence of THA^+, suggesting a modification in the arrangement of restacked domains.

Further examination of the material's evolution during **polarization** provided valuable insights. For 6RP-0.2, polarization in 1M $TEABF_4$ did not result in any observable

modifications in the SAXS/WAXS profiles, indicating that the small cation (TEA^+) had no impact on the material's structure at the studied scale. However, in the presence of THA^+, distinct shifts were observed in both SAXS and WAXS profiles. The analysis of SAXS revealed a shift in the break in slope, which was attributed to a flattening of the graphene sheets. The WAXS analysis indicated an increase in the intensity of the G peak, suggesting an orientation of the graphitic domains.

Similar investigations were carried out on rGO, where SAXS/WAXS profiles showed significant changes during polarization in both electrolytes. The SAXS profiles showed similar evolution regardless of the cation size, which is likely due to the smaller bending length compared to 6RP-0.2 (R=14 nm in rGO and R= 78 nm in 6RP-0.2). However, the interpretation of the WAXS profiles was hindered by a noticeable shift in the profiles background. This shift complicates the attribution of specific structural changes to the material upon polarization.

3.2 Unveiling the localization of ions within the porosity of graphene-based materials during SC operation by *in-situ* SANS study

As discussed in the beginning of this chapter, the aim of this fundamental study is to gain insights into the adsorption and desorption mechanisms within an extended range of porosity (3 nm to 210 nm) in graphene-based materials. To achieve this goal, it is necessary to determine the location of the adsorbed ions within this range porosity scale. We used *in-situ* SANS to **selectively** investigate the pore size dependencies of the adsorption of hydrogen-containing (TEA^+ and THA^+) and boron-containing (BF_4) ions [6] by taking advantage of the high cross-section of neutron scattering on hydrogen (H) and the high neutron absorption cross-section of boron (B).To attribute the variations in intensity to the adsorbed species, it is crucial to ensure that the only source of hydrogen comes from cations within the electrolytic media. Therefore, deuterated acetonitrile was used as a solvent. The adsorption of hydrogen-rich cations (TEA^+ ($N^+(C_2H_5)_4$) and THA^+ ($N^+CH_3(CH_2)_5)_4$) is expected to be associated with an increase in the scattering intensity. Similarly, the adsorption of boron-rich anion is expected to be associated to a decrease in the scattered intensity (BF_4^- anions contain approximately 20% of neutron-absorbing ^{10}B). It is worth mentioning at this stage that at the adsorption interface (solid/electrolyte), **the polarization is supposed to create a concertation gradient of ions within the electrolyte**. This concentration gradient added complexity to the studied system as it is no more considered as a simple two-phase system. Herein, a qualitative study is carried out considering a two-phase system composed of the solid and: i) the electrolyte at the open circuit voltage (OCV), ii) the cation-rich electrolyte at negative polarisation, iii) the anion rich-

electrolyte at positive polarization as shown in **Figure V.24**. **In this case the relative quantities of the adsorbed ions will be marked by the variation of the contrast between the reference and polarized samples.**

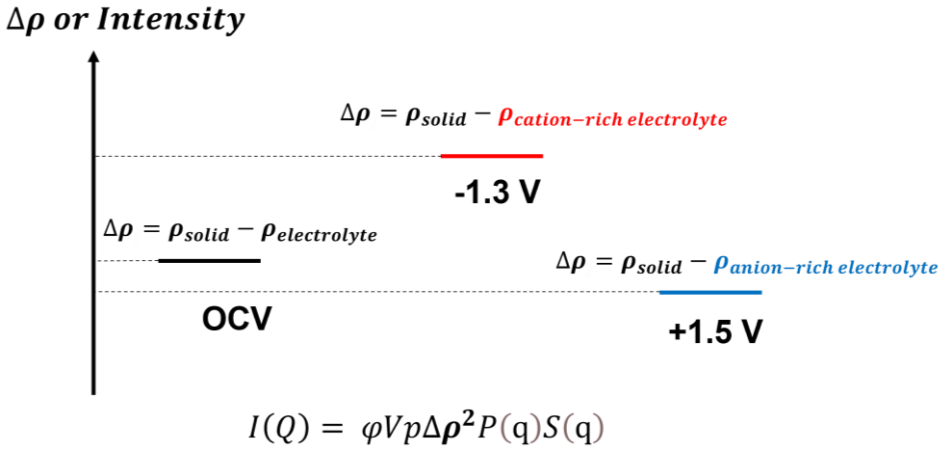

Figure V. 24 The expected variations in contrast Δρ or intensity after anions and cations adsorption within the porosity.

In this experiment, three profiles were recorded for each sample under three conditions: i) at the open circuit voltage (OCV), which served as a reference, ii) at -1.3 V *vs* Ag to promote cation adsorption, and iii) at +1.5 V *vs* Ag to promote anion adsorption.

Another set of experiments was conducted by reversing the order of polarizations, involving first the positive polarization at +1.5 V followed by the negative at -1.3 V. Each set was performed on a pristine FSE-electrode. This approach aims to understand the process of desorption of the adsorbed ions and their replacement by the ions of opposite charge during reverse polarization.

Such sequencing can help to identify the importance of cycling history of the. **The evolution of the scattering profiles during polarization was emphasized by normalizing the profiles to the one recorded at the open circuit voltage (OCV)** (the reference profile). Comparing the amount of adsorbed ions between samples can be qualitative inferred by examining the level of the normalized curves of the polarized samples. The normalized profiles presented in this chapter were smoothed for clarity purpose. This signal processing was made without any modification of the observed trends as shown in **Figure V.25**.

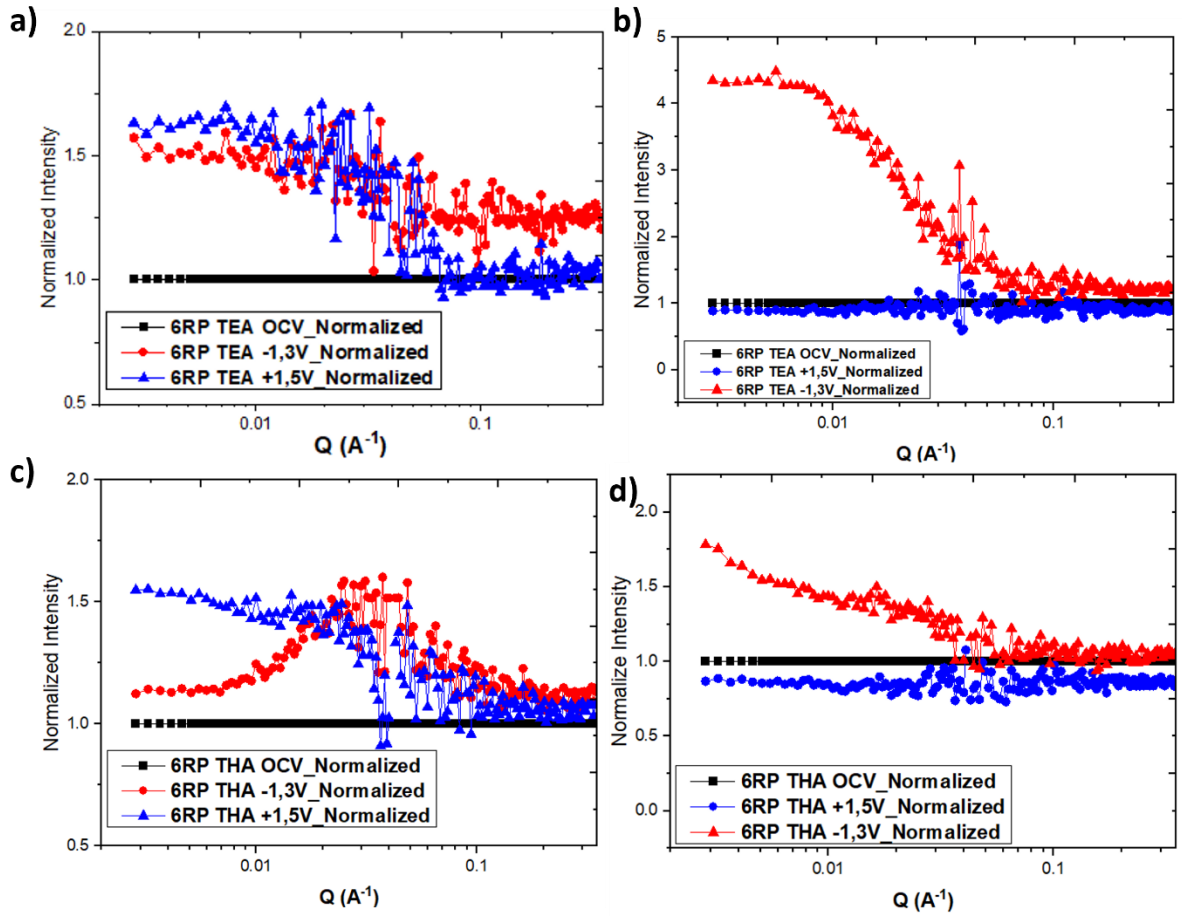

Figure V. 25 the normalized scattering profiles to the OCV without signal processing of 6RP-02 FSE polarized in 1M $TEABF_4$ /AN at (a) -1.3V followed by +1.5V, (b) +1.5 V followed by -1.3V, and in 1M $THABF_4$ /AN at (c) -1.3V followed by +1.5V, (d) +1.5 V followed by -1.3V.

3.2.1 *In-situ* SANS on 6RP-0.2 during polarization in 1M $TEABF_4$ /AN

As showed in the previous section, the polarization of 6RP-0.2 FSE in 1M $TEABF_4$ /AN did not result in any observable modifications in the SAXS profiles. In this case, any changes observed in the SANS profiles during polarization can **be attributed to a variation in contrast** ($\Delta\rho$) resulting from the evolution of the relative proportion of cations and anions within the different porosity scale under these specific polarization conditions. **Figure V.26** displays the SANS profiles of 6RP-0.2 FSE polarized at -1.3 V and +1.5 V in 1M $TEABF_4$ in deuterated acetonitrile (d-AN), along with the normalized profiles to the reference (OCV). As shown in **Figure V.26 a, b**, the order of polarization has a significant influence on the evolution of the scattering profiles after polarization. This suggests that the initial polarization state strongly influences the desorption of ions and the adsorption of ions of opposite charge when the polarization is reversed.

Figure V.26 c shows the normalized scattering profiles after polarization at -1.3 V followed by polarization at +1.5 V. Such plot follows the contrast evolution resulting from changes in the respective amounts of cations and anions over the probed scale. The polarization at -1.3 V (red curve) induces an increase in normalized intensity compared to that recorded at the OCV across the entire scale (3 nm to 210 nm). This increase is attributed to the electrolyte enrichment of H-rich cations (TEA^+) throughout all the porosity scales. This can be explained by the fact that, at potentials below the OCV cations are more involved in the diffusion and adsorption processes. It is worth mentioning that this increase could also be due to an anion desorption. However, BF_4^- (with a size of 0.3 nm [7]) are small enough to travel throughout the all porosity, and hence cannot be the limiting factor in these systems. We make this assumption and resonate with the intensity evolution originating from the evolution of the relative amount of cations. Furthermore, a decrease in the normalized intensity is observed above Q=0.02 $Å^{-1}$ (corresponding to 32 nm), stabilizing above Q=0.08 $Å^{-1}$, which corresponds to 8 nm. This decrease indicates that the smaller porosity (below 32 nm) accommodates a lower relative quantity of cations than the larger porosity. Conversely, polarization at +1.5 V (blue curve) induces a decrease in normalized intensity, reaching the OCV profile's level at high Q values (Q >0.08 $Å^{-1}$ corresponding to a pore size higher 8 nm). Below this point, the normalized intensity increases again compared to the OCV curve, surpassing that of -1.3 V at small angles. The decrease in normalized intensity observed at the small porosity scale (below 8 nm) may be attributed to the desorption of cations and the adsorption of anions (BF_4^-) as expected when polarizing at potential above OCV. Furthermore, the increase in normalized intensity above 8

nm may be attributed to the enrichment of this porosity by the cations that are either desorbed or diffusing from the small pores (below 8 nm).

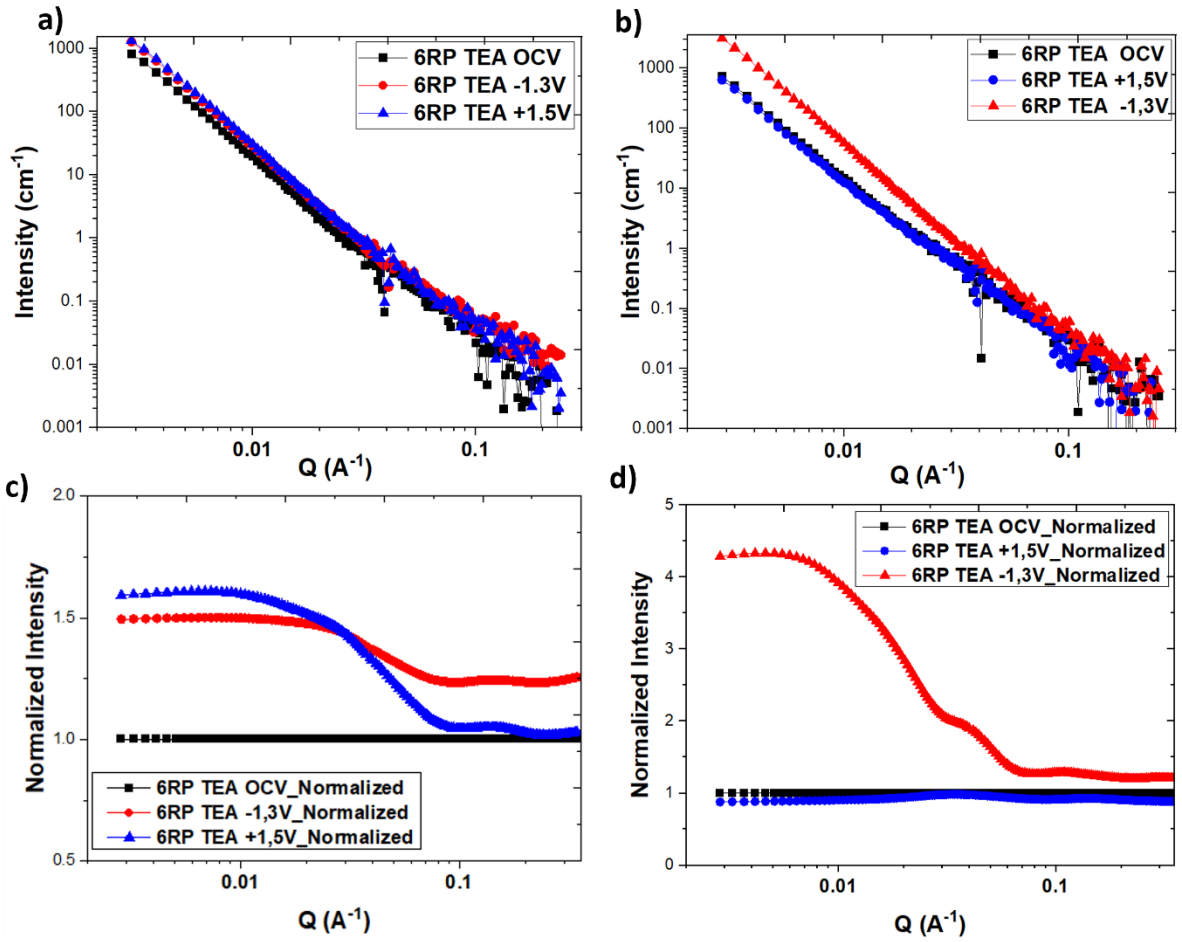

Figure V. 26 SANS profiles of 6RP-02 FSE polarized in 1M $TEABF_4$ / d-AN at (a) -1.3V followed by +1.5V and (b) +1.5V followed by -1.3V, and the normalized scattering profiles to the OCV of 6RP-02 FSE polarized in 1M $TEABF_4$ /d-AN at (c) -1.3V followed by +1.5V and (d) +1.5V followed by -1.3V.

On the other hand, **Figure V.26 d** shows the normalized scattering profiles after polarization at +1.5 V followed by polarization at -1.3 V. Interestingly, a significant difference between the results of the two sets of experiments is observed. The initial polarization at +1.5 V (blue curve) results in a slight decrease in normalized intensity compared to that at the OCV across the entire scale (3 nm to 210 nm). This decrease in normalized intensity may be due to the relative adsorption of more neutrons absorbing anions (BF_4^-) and from the relative desorption or diffusion of cations towards porosity of larger size than the probed scale. Compared to when a negative potential is applied first (**Figure V.26 c**), the signal did not increase at any scale. This confirms the absence of any pre-adsorbed cations within the pores, as expected when the potential applied is higher than the OCV.

At -1.3 V (red curve) polarization, the signal increases across the entire scale (3 nm to 210 nm) similar to the case when negative polarization is applied first. This increase is likely due to the desorption or diffusion of anions towards porosity of higher size than the probed scale, combined with the adsorption of H-rich cations (TEA^+) inducing higher contrast. Furthermore, at high Q values, similarly to when a negative potential is applied first, the normalized intensity remains constant (1.25) (above ~Q=0.08 $Å^{-1}$, below ~8 nm), indicating that independently of the first applied potential, the small porosity (below ~8 nm) accommodates the same quantity of cations, suggesting adsorption saturation. Moreover, a substantial increase in normalized intensity at small angles is observed above this scale (9~nm). The achieved normalized intensity level (4.2) is significantly higher than that observed when the negative potential is applied first (1.5). This increase is attributed to the low content of cations within the pores, as evidenced by the normalized intensity below OCV curve) when the positive potential is shifted to the negative one, it triggers a significant amount of cations towards the accessible pores to neutralize the charge. The scale of porosity does not appear to suffer from saturation. In the 6RP-0.2-FSE material, ions are distributed across the entire porosity scale. The diffusion of ions encounters entanglement within the scale of approximately 8 nm to 210 nm, below which a quantized amount of ions is stored mainly due to geometrical restriction.

3.2.2 *In-situ* SANS on 6RP-0.2 during polarization in 1M $THABF_4$ /AN

Figure V.27 displays the scattering profiles of 6RP-0.2 FSE polarized at -1.3 V and +1.5 V in 1M $THABF_4$ /d-AN, as well as the normalized profiles to the reference (OCV). Contrary to TEA^+, the order of polarization in THA^+ does not significantly impact the evolution of the scattering profiles after polarization as shown in **Figure V.27 a, b.** This provides preliminary evidence that THA^+ may be less adsorbed TEA^+.

Figure V.27 c shows the normalized scattering profiles after polarization at -1.3 V followed by polarization at +1.5 V. The polarization at -1.3 V (red curve) shows an increase in normalized intensity compared to that at the OCV across the entire scale (3 nm to 210 nm). This increase is due to the adsorption of H-rich cations (THA^+) within this scale, as expected when polarizing at such negative potential. In addition, a clear bump is recorded in the middle of the normalized profile between 0.01 $Å^{-1}$ < Q < 0.08 $Å^{-1}$ corresponding to a porosity ranging from ~ 8 nm to ~ 63 nm. This bump is likely caused by the accumulation of large cations (THA^+) within this porosity scale, impeding their diffusion to smaller pores. At high Q values, above Q=0.08

$Å^{-1}$ (*i.e.* 8 nm), the normalized intensity reaches 0.6, which is lower than the case of TEA^+ despite the higher hydrogen content in THA compared to TEA.

This indicates that less THA^+ are present in the pores with a size lower than 8 nm. Then, when the FSE is polarized sequentially at +1.5 V (blue curve), there is a slight decrease in intensity at high Q values (Q > 0.1 $Å^{-1}$). Unlike FSE cycled in TEA at +1.5V (**Figure V.27 c**), the normalized intensity does not reach the OCV level in this region, suggesting that some adsorbed THA^+ is trapped in this porosity scale and cannot be desorbed. The intensity gradually increases below Q=0.1 $Å^{-1}$, but it remains below the red curve (-1.3 V) and it rises above it at Q=0.02 $Å^{-1}$ (*ie*. 32 nm). It then reaches a plateau, similar to the case when the 6RP-FSE is cycle in TEA^+. This could be explained by the release of THA^+ cations from their accumulation at the intermediate porosity range upon positive potential polarization. This intensity level above ~32 nm illustrates the enrichment of this porosity with these cations.

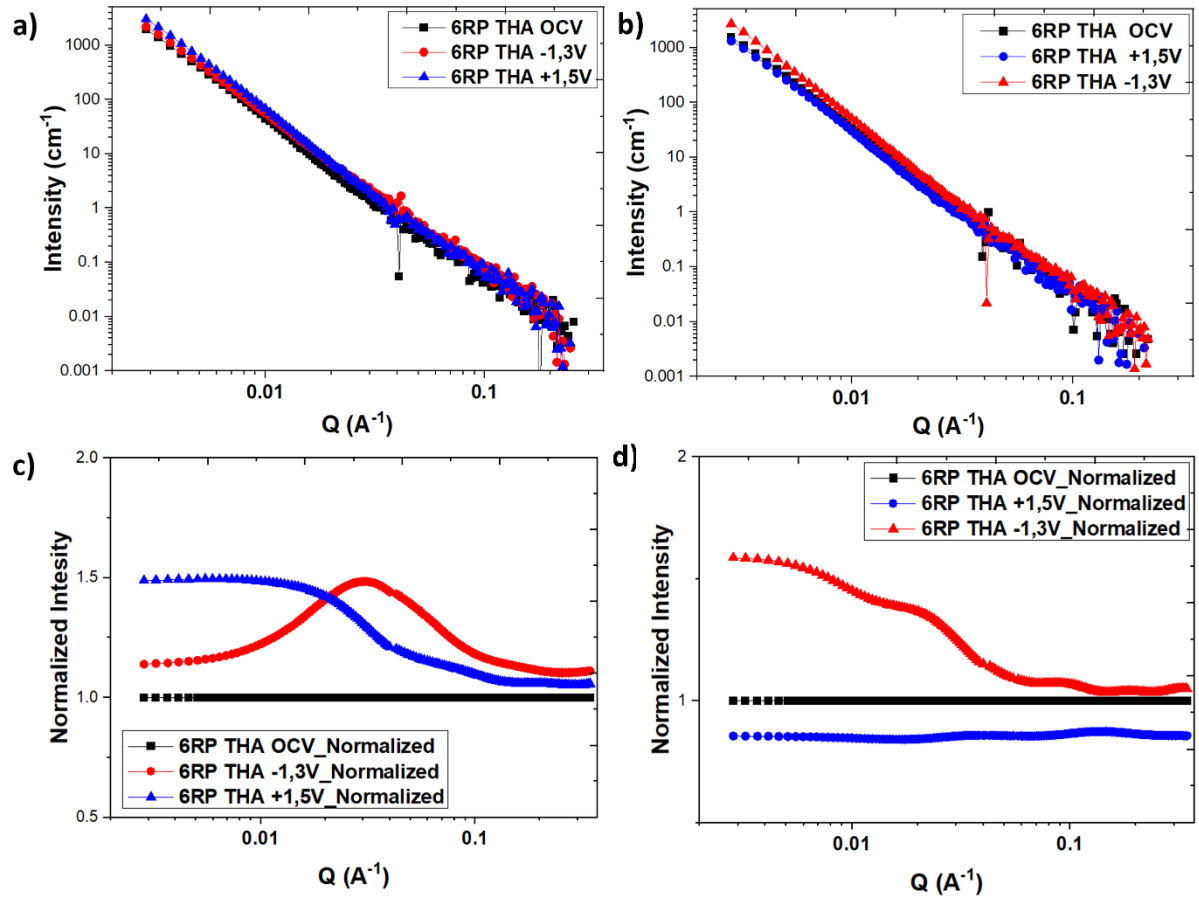

Figure V. 27 SANS profiles of 6RP-02 FSE polarized in 1M $THABF_4$ /d-AN at (a) -1.3V followed by +1.5V and (b) +1.5V followed by -1.3V, and the normalized scattering profiles to the OCV of 6RP-02 FSE polarized in 1M $THABF_4$ /d-AN at (c) -1.3V followed by +1.5V and (d) +1.5V followed by -1.3V.

On the other hand, **Figure V.27 d** displays the normalized scattering profiles after initial polarization at +1.5 V followed by polarization at -1.3 V. The polarization at +1.5 V (blue curve) indicates a slight decrease in intensity compared to the OCV across the entire scale (3 nm to 210 nm), reaching the same level as in the case of TEA. This decrease in the intensity results from the adsorption of anions (BF_4^-) that absorb neutrons as expected when polarizing at positive potentials. In turns, the polarization at -1.3 V (red curve) induces an increase in intensity within the Q range 0.003 $Å^{-1}$ < Q< 0.1 $Å^{-1}$. This increase may be due to the desorption of anions and adsorption or diffusion of H-rich cations (THA^+) within this wider scale of 6 to 210 nm. Additionally, a small bump is observed in the intermediate Q range, s indicating cations accumulation. However, the normalized intensity below Q=0.1 $Å^{-1}$ is slightly impacted by the negative polarization (back to the OCV level), suggesting that the cations are less adsorbed at this scale in this case. This slight evolution might be due to the initial occupation of this porosity by the anions and to the limited diffusion of the large sterically hindered THA^+ within or to the small pores (below ~6 nm). Furthermore, a pronounced increase in the relative intensity at small angles is observed starting at Q=0.02 $Å^{-1}$ compared to when the negative potential is applied first. This increase is attributed to the low concentration of cations within the pores when the potential is switched to negative potential, which causes a significant amount of cations to move towards these depleted pores.

This fundamental study provides valuable insights into the behavior of ions within the pores of pillared graphene material under various conditions. The observations show that upon polarization, THA^+ is less adsorbed in the small pores (< 8 nm) than TEA^+ and tends to agglomerate within the mesoscale porosity. These results are valuable and show that the previously observed ion-sieving (**Figure V.10**) is influenced by the lower adsorption of THA^+ in the mesoscale pores before reaching the galleries. Unfortunately, the probed scale is limited to 3 nm and does not allow for visualization of the micropores (*i.e.*, galleries d~0.7 nm) to verify the adsorption capabilities of THA^+ and TEA^+ within this scale. To complete this study, ***in-situ*** WANS are needed. The probed length scale in WANS (< 0.5 nm) is well adapted to investigate the ions adsorption within the galleries.

3.2.3 *In-situ* SANS on 6RP-0.2 during polarization at different potentials in 1M $TEABF_4$ /AN

The selected polarization potentials (-1.3 V and +1.5 V) do not fully capture the mechanisms at intermediate potentials or during cycling. To gain further insights into the cation adsorption and desorption mechanisms under conditions closer to cycling, we investigated the

evolution of scattering profiles of 6RP-0.2 FSE during polarization in 1M $TEABF_4$/ d-AN at different potentials *vs* Ag: OCV, -0.65 V, -1.3 V, and the return to OCV: -0.65 V (R), finally reaching the OCV (R) as displayed in **Figure V.28 a**. These experiments were conducted on the same electrode, under conditions that closely resemble the cycling process. **Figure V.28 b** shows the scattering profiles normalized to the OCV. At -0.65 V (red curve), a slight increase of the normalized intensity was recorded at small angles ($Q < 0.08$ $Å^{-1}$, *i.e.* ~8 nm), indicating that cations started to diffuse in large porosity without reaching the smaller one.

At -1.3 V (blue curve), the normalized intensity increases at high Q values ($Q > 0.08$ $Å^{-1}$, *i.e.* 8 nm), indicating that cations are adsorbed in the small porosity. Furthermore, a significant increase in the relative intensity at small angles is observed. This increase can be interpreted as a large amount of cations diffusing within the large pores and becoming blocked by adsorption saturation in smaller pores. After reversing potential, at -0.65 V (green curve), the relative intensity at high Q values ($Q > 0.08$ $Å^{-1}$, *i.e.* 8 nm) remains constant, suggesting that cations do not desorb within this scale. Furthermore, a decrease in normalized intensity at small angles is observed, indicating a back-diffusion of cations from the larger pores. A similar trend is observed at 0V (purple curve), indicating that cations may remain trapped in small pores. It seems that unless a positive potential is applied, these ions are not compelled to diffuse back to higher porosity and be replaced by anions.

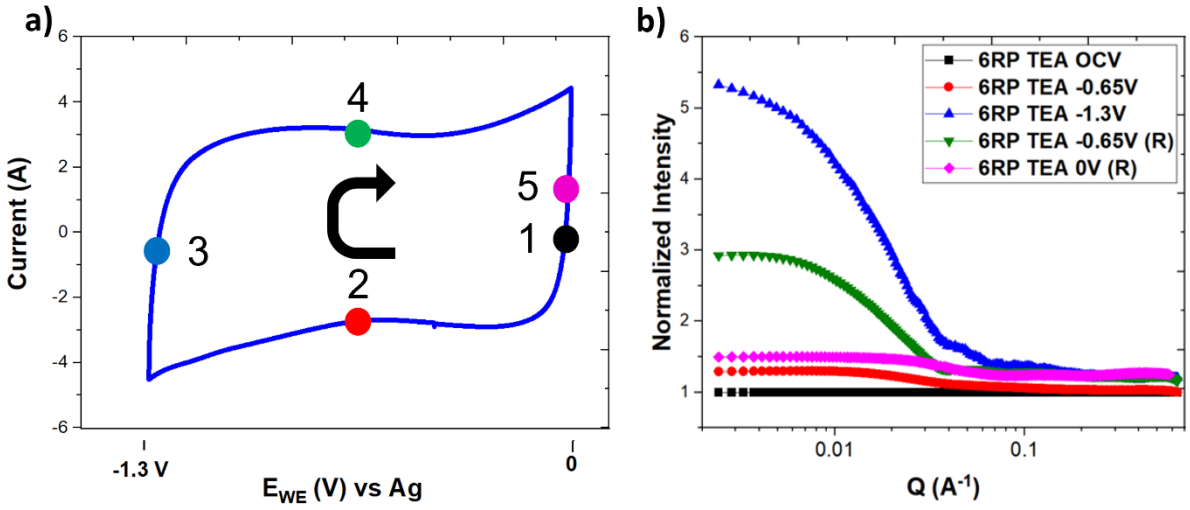

Figure V. 28 (a) The different polarization potentials displayed on a CV curve, (b) the normalized scattering profiles to the OCV of 6RP-0.2 FSE polarized at these different potentials, R refer to return.

Unfortunately, rGO showed a significant structural evolution upon polarization, which prevented the attribution of the changes in the intensity to the contrast. The study with rGO

aimed to compare the impact of the mesoporosity on the adsorption/desorption mechanisms of ions within this scale, as rGO showed a well-developed mesoporosity compared to 6RP-0.2.

4 Conclusion

This chapter was dedicated to study the electrochemical performance of graphene-based materials and to understand their behavior in real time as a supercapacitor electrode, thereby, it was divided into two main parts. The first part involved a fundamental electrochemical study using Cyclic Voltammetry (CV) of reference and pillared samples formulated as a free-standing electrode (FSE) for SC. This study aims to understand the influence of physicochemical properties, structure, and porosity of graphene-based materials on their electrochemical performance. Both organic and aqueous electrolytes were tested to highlight the impact of chemical properties on the pseudo-capacitive behavior.

In the organic electrolyte (1M TEABF4 /AN), the pillared samples exhibited higher capacitances compared to the reference materials. Specifically, 6GA-0.05 demonstrated a capacitance of 88 F/g, surpassing GA at 78 F/g, and 6RP-0.2 exhibited a capacitance of 101 F/g, outperforming rGO at 88 F/g at 10 mV/s. Despite the lower mesoporosity, mesopore volume, and N_2 specific surface area (SSA) observed in pillared materials, as discussed in **Chapter IV**, they displayed enhanced electrochemical capacitances compared to the reference materials. This discrepancy underscores the significant involvement of the newly formed graphene galleries in the electrochemical process. These results suggest that the newly created microporosity in pillared materials provides additional adsorption sites for ions, contributing to an overall increase in capacitance. This emphasizes the importance of micropores in electrochemical storage within SCs. Moreover, despite higher mesoporosity in reference materials, their electrochemical performances are limited due to the restacking of graphene sheets, which likely influences their microporosity and, consequently, their capacitance in an organic electrolyte.

In the aqueous electrolyte (3M H_2SO_4), CV curves of reference and pillared samples exhibited a pseudo-capacitive peak, notably more pronounced in reference samples especially in GA. Surprisingly, the capacitance trends were reversed, in reference samples, with GA showing a capacitance of 149 F/g, surpassing rGO with 96 F/g at 10 mV/s. In pillared samples, both capacitances were higher than those in the organic electrolyte, revealing 105 F/g and 116 F/g for 6GA-0.05 and 6RP-0.2 respectively. This increase in the capacitance is attributed to the additional pseudo-capacitive behavior associated with highly reversible surface or near-surface

faradaic processes between the electrode and the electrolyte. This process is directly correlated to the oxygen content within the materials. The higher abundance of oxygen functional groups in GA results in a higher pseudo-capacitance from faradic processes, elucidating the superior electrochemical performances of this sample in the aqueous electrolyte outperforming the pillared samples.

In the second part of this chapter, the effort was dedicated understand the real-time behavior of these materials as SC electrodes. An advanced *in-situ/operando* Small-Angle X-ray Scattering (SAXS) and Wide-Angle X-ray Scattering (WAXS) study using synchrotron radiation was carried out to unveil the structural evolution during cycling and polarization of graphene-based materials. Additionally, an *in-situ* Small-Angle Neutron Scattering (SANS) experiment was performed to reveal the qualitative location of ions within pores of different sizes, aiming to gain insights into the adsorption/desorption mechanisms across the entire porosity scale of the samples.

Operando and *in-situ* SAXS/WAXS measurements were performed in two distinct organic electrolytes, 1M $TEABF_4$ and $THABF_4$ /AN. *Operando* SAXS experiments on 6RP-0.2 FSE under cycling revealed that the structure within a length scale of 3 nm to 210 nm remained unchanged even in the presence of a large cation (THA^+). However, a significant evolution was observed in WAXS profiles only in the presence of THA^+, particularly on the G peaks, indicating a modification in the arrangement of restacked domains. During polarization in 1M $TEABF_4$ /AN, *in-situ* SAXS/WAXS studies 6RP-0.2 did not result in observable modifications, suggesting that the small cation (TEA^+) had no impact on the material's structure at the studied scale. In the presence of THA^+, distinct shifts were observed in both SAXS and WAXS profiles. SAXS revealed a shift in the break in slope (R) toward small angles, attributed to a flattening of the graphene sheets, while WAXS indicated an increase in the intensity of the G peak, suggesting an orientation of the graphitic domains. Similar investigations on rGO showed significant changes in SAXS/WAXS profiles during polarization in both electrolytes. SAXS profiles exhibited similar evolution, showing a decrease in the bending length (R) regardless of cation size, likely due to the smaller bending length compared to 6RP-0.2 (R=14 nm in rGO and R= 78 nm in 6RP-0.2). However, interpretation of WAXS profiles was not possible due to a noticeable shift in the background, hindering the attribution of specific structural changes to the material.

In-situ SANS experiments were conducted on 6RP-0.2 FSE under polarization in both 1M $TEABF_4$ and $THABF_4$ /AN. The results were qualitatively discussed considering a two-

phase system composed of the solid and: i) the electrolyte at the OCV, ii) the cation-rich electrolyte at -1.3 V, iii) the anion-rich electrolyte at +1.5 V. The relative quantities of the adsorbed ions were assessed by the variation of the contrast between the reference and polarized samples.

In $TEABF_4$/AN electrolyte, when a negative polarization was applied first, an increase in normalized intensity across the entire scale (3 nm to 210 nm) was observed at -1.3 V, indicating the electrolyte enrichment of H-rich cations (TEA^+), showing their involvement in diffusion and adsorption processes. A slight decrease in normalized intensity above 32 nm suggested that smaller porosity accommodates a lower relative quantity of cations. Conversely, at +1.5 V, a decrease in normalized intensity was observed at high Q values indicating desorption of cations and adsorption of anions (BF_4^-) at the small porosity (< 8nm). Interestingly, when reversing the polarization order, a significant difference was observed. The initial polarization at +1.5 V resulted in a slight decrease in normalized intensity, all over the probed Q-range, likely due to the diffusion of anions toward the working electrode and the diffusion of cations towards the counter electrode. At -1.3 V, the normalized intensity increased across the entire scale, similarly to the case when a negative potential was applied first, indicating adsorption and diffusion of cations towards smaller pores. In the 6RP-0.2-FSE material, TEA^+ and BF_4^- were distributed across the entire porosity scale, with saturation observed in small pores (below 8 nm), likely due to geometrical restrictions.

Furthermore, 6RP-0.2 FSE showed similar behaviors in the presence of THA^+ with a clear accumulation of this cation within the pore in the length scale between 8 nm and 63 nm. Overall, THA^+ showed lower adsorption capability in small pores (< 8 nm) than TEA^+ and tends to agglomerate within mesoscale porosity. These observations suggested that the observed ion-sieving phenomenon was influenced by the lower adsorption of THA^+ in the mesoporosity before reaching the galleries. To further investigate ions' adsorption within galleries, *in-situ* WANS with a probed length scale below 0.5 nm is recommended.

5 References

[1] W. Yang *et al.*, "Graphene in Supercapacitor Applications," *Current Opinion in Colloid & Interface Science*, vol. 20, no. 5, pp. 416–428, Oct. 2015, doi: 10.1016/j.cocis.2015.10.009.

[2] "Tunable Sub-nanopores of Graphene Flake Interlayers with Conductive Molecular Linkers for Supercapacitors | ACS Nano." Accessed: Nov. 19, 2023. [Online]. Available: https://pubs.acs.org/doi/full/10.1021/acsnano.6b02415

[3] H. Banda *et al.*, "Ion Sieving Effects in Chemically Tuned Pillared Graphene Materials for Electrochemical Capacitors," *Chem. Mater.*, vol. 30, no. 9, Art. no. 9, May 2018, doi: 10.1021/acs.chemmater.8b00759.

[4] P. Yu, S. E. Lowe, G. P. Simon, and Y. L. Zhong, "Electrochemical exfoliation of graphite and production of functional graphene," *Current Opinion in Colloid & Interface Science*, vol. 20, no. 5, pp. 329–338, Oct. 2015, doi: 10.1016/j.cocis.2015.10.007.

[5] H. Dai, Z. Xu, and X. Yang, "Water Permeation and Ion Rejection in Layer-by-Layer Stacked Graphene Oxide Nanochannels: A Molecular Dynamics Simulation," *J. Phys. Chem. C*, vol. 120, no. 39, pp. 22585–22596, Oct. 2016, doi: 10.1021/acs.jpcc.6b05337.

[6] S. Boukhalfa *et al.*, "*In Situ* Small Angle Neutron Scattering Revealing Ion Sorption in Microporous Carbon Electrical Double Layer Capacitors," *ACS Nano*, vol. 8, no. 3, Art. no. 3, Mar. 2014, doi: 10.1021/nn406077n.

[7] J. N. Neal, K. L. Van Aken, Y. Gogotsi, D. J. Wesolowski, and J. Wu, "Self-Amplified Surface Charging and Partitioning of Ionic Liquids in Nanopores," *Phys. Rev. Applied*, vol. 8, no. 3, p. 034018, Sep. 2017, doi: 10.1103/PhysRevApplied.8.034018.

General conclusion and Perspectives

Graphene-based materials have been widely examined as electrodes materials for supercapacitors. The ability to control the structure and the chemical properties of these materials is a significant advantage, that was addressed by using specific reduction methods allowing to fine-tune the oxygen content, and by incorporating pillars allowing to space-out graphene sheets. The electrochemical performances of these materials are highly dependent on the structural features, notably the porosity of the electrode materials. However, and to the best of our knowledge, a multi-scale comprehensive characterization of graphene-based materials has not yet been addressed in the literature, particularly in terms of their mesostructural and morphological properties.

This emphasizes the need for a holistic approach enabling to unlock the full potential of graphene-based materials in supercapacitor technology. A comprehensive strategy integrating complementary structural and morphological analysis, physicochemical characterizations, and electrochemical investigations is deemed essential. Such an approach would aim not only to enhance the current understanding of these materials but also to highlight the importance of a multidisciplinary methodology to optimize the design and performance of graphene-based materials, ultimately contributing to the development of supercapacitors.

Therefore, in this thesis, the effort has been dedicated to the study of graphene-based materials following a methodology that includes i) the study of the effect of reduction on the physicochemical and multi-scale structural properties of rGO using two reduction methods, hydrothermal reduction and reduction using hydrazine hydrate, ii) the study of the influence of functionalization/pillaring on the multi-scale structure, morphology, and porosity of pillared graphene materials, highlighting their properties at different scales, iii) the understanding of the electrochemical properties of both reference (non-pillared) and pillared graphene materials by establishing a correlation between their structural or chemical properties and their electrochemical performances, and finally iv) partially unveiling the real-time behaviours of these materials as electrode for SC *via in-situ* and *operando* advanced characterizations.

i) Chemistry and multi-scale structure of rGO-based materials:

In this study, two reduction methods, hydrothermal reduction and chemical reduction using hydrazine hydrate, were employed to reduce graphene oxide (GO). XRD revealed that

both reduction methods led to restacking of graphene sheets. A slightly broader G peak was observed for rGO compared to GA, suggesting a higher number of graphene sheets per restacked aggregate in GA. These observations were confirmed by TEM, showing a higher number of restacked graphene sheets per stack in GA. The chemical analyses using XPS and EA showed a higher carbon-to-oxygen (C/O) ratio in the reduced materials compared to GO, confirming their efficient reduction. In addition, rGO showed higher C/O (13.4) ratio than GA (7.9) and lower weight loss as evidenced by TGA (10% and 30% in rGO and GA respectively), confirming the higher reduction level of rGO compared to GA. Furthermore, SANS showed that the mesoporosity of rGO (57%) was greater than that of GA (35%) in the 3 nm to 210 nm range. Moreover, N_2 BET surface area and pore volume measurements further confirmed the higher micro/mesoporosity in rGO (N_2 BET SSA of 401 m^2/g and 237 m^2/g in rGO and GA respectively, as well as a pore volume within the 0.6 to 30 nm length scale of 0.86 cm^3/g and 0.24 cm^3/g in rGO and GA respectively). All these quantitative results showed that **rGO is more reduced than GA and has higher micro/mesoporosity**.

This work, goes from materials development to in-depth studies, provides valuable understanding of the multiscale structure of rGO-based materials and their tunable chemistry via the reduction processes.

ii) Chemistry and multi-scale structure of pillared graphene-based materials:

The chemical analyses of 6RP-0.2 and 6GA-0.05 performed by TGA revealed weight losses of 26% and 30%, respectively, showing good GO reduction. The higher weight loss observed in 6GA-0.05 was shown to be due to a higher content of grafted pillars and a lower reduction degree compared to 6RP-0.2. The effectiveness of the reduction was further confirmed by XPS and EA, which also highlighted the presence of nitrogen within the material, confirming the incorporation of pillar molecules within the samples.

The nature of the bonding between pillars and graphene sheets was assessed using TPD-MS, revealing that covalent bonding occurred in both 6GA-0.05 and 6RP-0.2. Furthermore, XRD analysis revealed a remarkable similarity in the nanoscale structure of the two-pillared samples. Both materials exhibited a distinct CL peak with a d-spacing of 0.77 nm, indicating the successful creation of a new porosity within the materials. The proportion of the pillared domains (% CL) within the materials was determined from the XRD data showing approximately 20 to 30%. This indicated that despite successful pillaring, the majority of the

materials still consisted of restacked graphitic domains, accounting for approximately 70 to 80% of the overall structure.

SANS showed that 6RP-0.2 had a higher mesoporosity than 6GA-0.05, with a porosity of 37% and 15%, respectively. Additionally, 6RP-0.2 showed a higher N_2 BET SSA of 93 m^2/g compared to 26 m^2/g for 6GA-0.05. The N_2 pore size distribution (N_2-PSD) also showed a higher pore volume (within the length scale ranging from 0.6 to 30 nm) in 6RP-0.2 (0.23 cm^3/g) compared to 6GA-0.05 (0.06 cm^3/g). Clearly, despite the opening of new microporosity, the pillaring process seemed to partially close the mesoporosity in the pillared samples. This reduction in mesoporosity in the pillared samples was attributed to the **potential connection of restacked or pillared domains via pillars**. Indeed, the reactivity of pillars with oxygen functional groups can lead to a bridging between the different domains, resulting in random connections and reduced interparticle distances and decreasing mesoporosity. The work presented here shows the effect of **pillaring** on the microscale porosity, and chemistry of pillared graphene materials, highlighting its impact on **reducing the mesoporosity**.

iii) Understanding the electrochemical performances of graphene based-materials:

In the **organic electrolyte** (1M $TEABF_4$ in AN), the **pillared samples**, 6GA-0.05 and 6RP-0.2, exhibited **higher capacitances** compared to the reference materials. Specifically, 6GA-0.05 had a capacitance of 88 F/g, surpassing GA 78 F/g, and 6RP-0.2 had a capacitance of 101 F/g, outperforming rGO 88 F/g at 10 mV/s. Despite having lower SANS mesoporosity, mesopore volume, and N_2 BET SSA, **pillared materials, displayed enhanced electrochemical capacitances compared to the reference materials**. This discrepancy highlights the **significant role of the newly formed graphene galleries in the electrochemical process**. The results showed that the microporosity in pillared materials provided additional adsorption sites for ions, contributing to an overall increase in capacitance. This underscores the importance of micropores in the electrochemical storage of supercapacitors. Additionally, the limited electrochemical performances of reference materials with higher mesoporosity are attributed to the restacking of graphene sheets, which affects their microporosity and, consequently their capacitance.

In the aqueous electrolyte (3M H_2SO_4), both the reference and pillared samples showed an increase in capacitance compared to when cycled in the organic electrolyte. In addition, all samples exhibited a pseudo-capacitive peak on the CV curves, which was more

pronounced for the reference samples, particularly in GA. Interestingly, the capacitance trends were reversed in reference samples, with GA showing a capacitance of 149 F/g, surpassing rGO capacitance of 96 F/g at 10 mV/s. **In pillared samples, both capacitances were higher than those in the organic electrolyte**, reaching 105 F/g for 6GA-0.05 and 116 F/g for 6RP-0.2. This increase in capacitance was attributed to **additional pseudo-capacitive** behavior associated with highly reversible surface or near-surface faradaic processes between the electrode and the electrolyte as evidenced by the presence of pseudo-capacitive peaks. This process was directly correlated with the oxygen content within the materials. The higher abundance of oxygen functional groups in GA results in a higher pseudo-capacitance from faradic processes, elucidating the superior electrochemical performances of this sample in the aqueous electrolyte, outperforming the pillared samples. This work contributes to the understanding the **high importance of the microporosity in SC, showing that, even at small quantities (20-30%), their contribution in enhancing the capacitance of pillared samples was evident.**

iv) Unveiling the real-time behaviours of graphene based-materials as electrode for SC

The fundamental study carried out during this thesis was divided into two parts: i) the study of the structural evolution of graphene-based materials during SC operating by performing an *in-situ* and *operando* SAXS/WAXS analysis, ii) the unveiling of the ions location within the material porosity at different applied potentials using an *in-situ* SANS study. The two studies were performed in two different organic electrolytes, 1M $TEABF_4$ and $THABF_4$ in AN to highlight the impact of the ion size on the adsorption capabilities of the materials porosity.

a) Structural evolution of graphene-based materials during SC operation:

Operando SAXS measurements on 6RP-0.2 FSE during cycling revealed that the mesoscale structure (3 to 210 nm) remained unchanged even in the presence of a large cation (THA^+). However, significant evolution was observed in WAXS profiles in the presence of THA^+, particularly on the G peaks. A modification in the arrangement of restacked domains was observed during cycling. Furthermore, *in-situ* SAXS/WAXS studies on 6RP-0.2 during polarization at -1.3 V in 1M $TEABF_4$ in AN, did not show observable modifications, suggesting that the small cation (TEA^+) had no impact on the material's structure. In contrast, **polarization at -1.3 V in the presence of THA^+ showed a distinct shift in both SAXS and WAXS profiles.** SAXS revealed a shift in the break in slope (R) towards small angles, indicating a flattening of the graphene sheets, while WAXS showed an increase in the intensity of the G peak, suggesting

an orientation of the graphitic domains. Similar investigations were carried out on reduced rGO, showing significant changes in SAXS/WAXS profiles during polarization in both electrolytes. SAXS profiles, regardless of cation size, exhibited similar evolution, showing a decrease in the bending length (R), likely due to the smaller bending length compared to 6RP-0.2 (R=14 nm in rGO and R= 78 nm in 6RP-0.2). However, the interpretation of the WAXS profiles was hindered by a noticeable shift in the background, which prevented the attribution of specific structural changes to the material.

a) Understanding the ion adsorption and desorption mechanisms:

In-situ SANS experiments were conducted on 6RP-0.2 FSE under polarization in both 1M $TEABF_4$ and $THABF_4$ in AN. The results were qualitatively discussed, considering a two-phase system composed of the solid and: i) the electrolyte at OCV, ii) the cation-rich electrolyte at -1.3 V, iii) the anion-rich electrolyte at +1.5 V. The relative quantities of the diffusing ions were assessed by analyzing the contrast variation between the reference and polarized samples.

In the $TEABF_4$/AN electrolyte, when a negative polarization was applied first (-1.3 V), an increase in normalized intensity across the entire length scale (3 nm to 210 nm) indicated the enrichment of the pores by H-rich cations (TEA^+), highlighting their involvement in diffusion and adsorption processes. A slight decrease in normalized intensity below 32 nm was observed, suggesting that smaller porosity accommodates a lower relative quantity of cations. Conversely, at +1.5 V, a decrease in normalized intensity at high Q values indicated desorption of cations and adsorption of anions ($BF4^-$) at small porosity (< 8 nm). Reversing the polarization order resulted in a significant difference. With the initial polarization at +1.5 V a slight decrease in normalized intensity across the probed Q-range was observed, indicating a depletion of cations in the electrolyte. At -1.3 V, the normalized intensity increased across the entire scale, indicating adsorption and diffusion of cations towards smaller pores.

In the presence of THA^+, 6RP-0.2 FSE exhibited significantly different behavior with a clear accumulation of THA^+ within the pores in the length scale between 8 nm and 63 nm at -1.3 V. Furthermore, THA^+ showed lower adsorption capability in small pores (< 8 nm) than TEA^+ and tended to agglomerate within mesoscale porosity. **These findings suggested that the observed ion-sieving phenomenon was influenced by the lower adsorption of THA^+ in the mesoporosity before reaching the galleries.**

Perspectives:

The SAS results presented in **Chapters III, IV**, and **V** were discussed by considering only the contribution of the form factor (P(Q)). This decision was justified by the hierarchical porosity of graphene-based samples, where the distance between the objects is non-uniform at the probed scale. In such cases, the contribution of the structure factor S(Q) is expected to be potentially hindered by that of P(Q). However, it is always recommended to assess the contribution of S(Q). To address this point, this is essential to measure the SAS profiles of diluted samples. This experiment allows for a comparison of SAS profiles of diluted and dense samples, enabling the evaluation of changes occurring within the scattering profiles. If diluted samples exhibit a different scattering profile than non-diluted ones, then it indicates that there is a non-negligible contribution from the structure factor. In such cases, the consideration of the structure factor becomes crucial in the interpretation of the results. Preliminary experiments have been conducted out to verify this point as shown in **Chapter II**. However, the samples suffer from precipitation due to the long acquisition time. Hence, experiments with other solvent, or under a continuous flux of solvent to maintain the dispersion have to be carried out.

The CV-SANS experiments provided valuable information on the real SLD of the graphene-based materials as well as their solid densities. However, this solid density accommodates all the porosity below the probed length scale (< 3 nm). This factor limits our understanding of the accessible porosity within these materials. Investigating the porosity below 3 nm is essential to complete our understanding on the accessible microporosity. To complete this study, CV-WANS is of prime interest. The probes length scale in WANS is similar to that of WAXS, exceeding the G peak. This would allow the visualization of the accessibility of the solvents to this porosity, and consequently quantifying the real solid density of the graphene-based materials.

As shown in **Chapter V**, *in-situ* SANS provided valuable insights on the adsorption mechanisms under different potentials, highlighting an adsorption saturation at small porosity below 8 nm in 6RP-0.2. Furthermore, this experiment showed that THA^+ was less adsorbed in small pores (< 8 nm) compared to TEA^+. Considering the higher mesoporosity in non-pillared samples compared to pillared samples, it is important to study the ion location within this scale by performing in-situ SANS for non-pillared samples. This will assess the impact of mesoporosity in the adsorption capabilities between pillared and non-pillared samples.

Furthermore, *in-situ* SANS showed that the ion-sieving phenomenon was influenced by the lower adsorption of THA^+ in the mesoporosity before reaching the galleries. To further investigate ion adsorption within galleries, *in-situ* WANS with a probed length scale below 0.3 nm is needed. The adsorption within the microscale, notably the galleries, will be assessed through the variation of the contrast at this scale, which is expected to be evident from the variation of the intensity of the CL peak.

This thesis highlighted the importance of advanced characterization techniques, namely WAXS, SAXS, and SANS, in understanding the structure and their complementarity to basic characterization techniques (SEM, XRD). Moreover, the possibility to investigate the mechanisms in supercapacitors by *in-situ* and *operando* measurements was emphasized. These advantages show the necessity to address other advanced characterization techniques for deeper understanding SC. Indeed, Quasielastic Neutron Scattering (QENS) is a sophisticated technique that enables to the study the dynamics of ions within the electrodes and electrolyte, providing insights into ion transport mechanisms and diffusion processes. Fleischmann, S. *et al*. explained that it is necessary to study *in-situ* the diffusion of electrolytic species in the porosity of carbonaceous material at the very local scale QENS analysis, alongside solid-state NMR [1]. Additionally, the Electrochemical Quartz Crystal Microbalance (EQCM) offers real-time monitoring of mass changes during electrochemical processes. This technique helps in elucidating the intricate interplay between electrode materials and electrolytes. Moreover, SECM [2] analysis, would enable identifying the nature of the species involved in the charge storage mechanism and relating macro-scale performances to local dynamics. Atomic Force Microscopy (AFM) and dilatometry can be combined to investigate the relation between the electrochemistry and the mechanics of such samples. *In-situ* and *operando* AFM can also be used to investigate local electrochemical processes [3]. Raman spectroscopy can be utilized to probe the electrode electrolyte interface under dynamic conditions [4].

References:

[1] S. Fleischmann, M. A. Spencer, et V. Augustyn, « Electrochemical Reactivity under Confinement Enabled by Molecularly Pillared 2D and Layered Materials », *Chem. Mater.*, vol. 32, n° 8, p. 3325-3334, avr. 2020, doi: 10.1021/acs.chemmater.0c00648.

[2] A. Sumboja, U. M. Tefashe, G. Wittstock, et P. S. Lee, « Investigation of Charge Transfer Kinetics of Polyaniline Supercapacitor Electrodes by Scanning Electrochemical Microscopy », *Adv. Mater. Interfaces*, vol. 2, n° 1, p. 1400154, 2015, doi: 10.1002/admi.201400154.

[3] Q. Gao, W.-Y. Tsai, et N. Balke, « In situ and operando force-based atomic force microscopy for probing local functionality in energy storage materials », *Electrochem. Sci. Adv.*, vol. 2, n° 1, p. e2100038, 2022, doi: 10.1002/elsa.202100038.

[4] R. Vicentini *et al.*, « Raman probing carbon & aqueous electrolytes interfaces and molecular dynamics simulations towards understanding electrochemical properties under polarization conditions in supercapacitors », *J. Energy Chem.*, vol. 60, p. 279-292, sept. 2021, doi: 10.1016/j.jechem.2021.01.003.